Holography, black holes and condensed matter physics

SIMON ADAM GENTLE

Holography, black holes and condensed matter physics

Simon Adam Gentle

A thesis presented for the degree of
Doctor of Philosophy

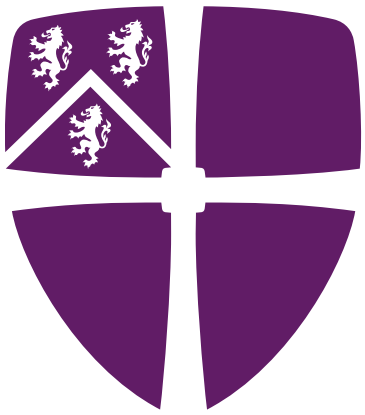

Department of Mathematical Sciences
University of Durham

March 2013

Holography, black holes and condensed matter physics

Simon Adam Gentle

A thesis presented for the degree of
Doctor of Philosophy

Abstract

In this thesis we employ holographic techniques to explore strongly-coupled quantum field theories at non-zero temperature and density. First we consider a state dual to a charged black hole with planar horizon and compute retarded Green's functions for conserved currents in the shear channel. We demonstrate the intricate motion of their poles and stress the importance of the residues at the poles beyond the hydrodynamic regime. We then explore the collective excitations of holographic quantum liquids arising on D3/D5 and D3/D7 brane intersections as a function of temperature and magnetic field in the probe limit. We observe a crossover from hydrodynamic charge diffusion to a sound mode similar to the zero sound mode in the collisionless regime of a Landau Fermi liquid. The location of this crossover is approximately independent of the magnetic field. The sound mode has a gap proportional to the magnetic field, leading to strong suppression of spectral weight for intermediate frequencies and sufficiently large magnetic fields.

In the second part we explore the solution space of AdS gravity in the hope of learning general lessons about such theories. First we study charged scalar solitons in global AdS_4. These solutions have a rich phase space and exhibit critical behaviour as a function of the scalar charge and scalar boundary conditions. We demonstrate how the planar limit of global solitons coincides generically with the zero-temperature limit of black branes with charged scalar hair. We exhibit these features in both phenomenological models and consistent truncations of eleven-dimensional supergravity. We then discover new branches of hairy black brane in $SO(6)$ gauged supergravity. Despite the imbalance provided by three chemical potentials conjugate to the three R-charges, there is always at least one branch with charged scalar hair, emerging at a temperature where the normal phase is locally thermodynamically stable.

Declaration

The research described in this thesis was carried out in the Department of Mathematical Sciences at the University of Durham between October 2009 and March 2013. Except where reference is made to the work of others, all the results are original and based on the following collaborative works of mine:

- D. K. Brattan, R. A. Davison, S. A. Gentle and A. O'Bannon, *Collective excitations of holographic quantum liquids in a magnetic field*, *JHEP* **1211** (2012) 084, arXiv:1209.0009 [hep-th].
- S. A. Gentle and B. Withers, *Superconducting instabilities of R-charged black branes*, *JHEP* **1210** (2012) 006, arXiv:1207.3086 [hep-th].
- S. A. Gentle, M. Rangamani and B. Withers, *A soliton menagerie in AdS*, *JHEP* **1205** (2012) 106, arXiv:1112.3979 [hep-th].
- D. K. Brattan and S. A. Gentle, *Shear channel correlators from hot charged black holes*, *JHEP* **1104** (2011) 082, arXiv:1012.1280 [hep-th].

None of the original works contained in this thesis have been submitted by me for any other degree, diploma or similar qualification.

Acknowledgements

First and foremost I would like to thank my supervisor Mukund Rangamani for his motivation and guidance throughout my graduate studies, and for suggesting my first project. I have benefited greatly from his vast knowledge, and his high standards have driven me to constantly challenge my own work and that of others.

Benjamin Withers has been an endless source of energy and inspiration, and I am deeply thankful for all I have learned from him. His enthusiasm, skill and flair (combined with his patience for those who code like chumps) were essential to my PhD. Our eureka moment with Mukund when all the solitons came together remains one of my fondest memories of my time at Durham. Special thanks also go to my academic brother Daniel Brattan for two enjoyable collaborations and for much moral support. We made a good team by the end.

I am very grateful to my collaborators Richard Davison and Andy O'Bannon for all they have taught me. It is also a pleasure to thank Joan Camps, Pau Figueras, Sean Hartnoll, Juan Jottar, Patrick Kerner, Keun-Young Kim, Matthew Lippert, James Lucietti, John McGreevy, Harvey Reall, Simon Ross, Jorge Santos, Julian Sonner and Sandip Trivedi for valuable discussions, comments and correspondence.

I am indebted to my housemates Luke Stanbra and Steven Wells for their support, brotherhood, a shared love of toffee muffins and many exciting adventures. I would also like to thank the inimitable Gurdeep Sehmbi and my officemates Harry Braviner and Craig Robertson for jokes and many good times.

My research was supported by an STFC studentship.

This thesis is dedicated to my parents Michael and Sarah and my big sister Claire. Thank you for your love, your unwavering support and your belief in me.

Contents

Chapter 1

Unusual uses for black holes

Black holes are arguably the most interesting objects in theoretical physics. On the one hand they can be simple: once the mass, charge and angular momentum of a black hole are prescribed, its properties are often fixed completely. However, they are also mysterious. A black hole curves spacetime so strongly that not even light can escape. For this reason, we can never directly observe the supermassive black hole we believe lurks at the centre of our galaxy, and must instead infer its presence from the motion of objects in orbit [1, 2].

In addition, black holes lie at the heart of the biggest contradiction in modern physics. Two of our most successful theories — quantum mechanics and Einstein's theory of general relativity — are inherently incompatible. However, black holes are gravitating objects that can be shown to have a quantum nature, and so provide a theoretical playground for studying quantum theories of gravity.

In recent years they have once again shown their utility, albeit in a rather unexpected way. In this thesis we will show how black holes can shed light on the most pressing problems in condensed matter physics. Along the way, we will encounter new kinds of black hole and other novel gravitational solutions that play a crucial role in this story.

1.1 Introduction

To make the surprising connection between black holes and condensed matter physics, first we need a rather remarkable tool. This tool is holography.

Put simply, holography maps an ordinary quantum field theory into a theory of gravity. As the name suggests, this map is holographic: the gravitational system lives in

(typically) one higher dimension. The gravitational dynamics of the fields in the 'bulk' is completely encoded in a field theory with a non-dynamical metric on the 'boundary'. The two theories in question are said to be dual to one another.

Examples of holography typically take the form

$$\begin{array}{c}\text{CFT in}\\ d \text{ dimensions}\end{array} \quad \leftrightsquigarrow \quad \begin{array}{c}\text{Theory of gravity}\\ \text{on } \mathrm{AdS}_{d+1}\end{array} \,. \tag{1.1}$$

Anti-de Sitter (AdS) space is the maximally symmetric solution to Einstein's equations in vacuum with a negative cosmological constant. A conformal field theory (CFT) is invariant under Poincaré, special conformal and scaling transformations at the quantum level. Thus, holography often goes by the name of the AdS/CFT correspondence. However, it is believed to be a much more general principle. Some intuition for why this should be the case can be found in [3, 4].

But what do we mean by 'gravity on AdS_{d+1}'? As will be made more precise in the following subsection, AdS space has a boundary. In some sense, the field theory 'lives' on this boundary. One of our boundary conditions will be that the dynamical metric in the gravity theory is asymptotically AdS_{d+1}. And what can we say about the field theory? If nothing else, one might expect it to be highly quantum. Perturbation theory would surely reveal the presence of an extra dimension, and classical CFT is very different to gravity. We will soon see that holography offers a powerful insight into the nature of strongly-coupled quantum field theories.

So far we have been rather vague. What kind of theories appear in (1.1)? When is this conjecture valid? How can we use it to compute observables? In the following subsections we develop a more precise dictionary between the two theories in a given dual pair and discuss its application to condensed matter systems. We then move on to the two main problems addressed in this thesis: (i) the real-time response of strongly-correlated states of quantum matter and (ii) the exploration of the space of solutions to AdS gravity and its bearing on the superconducting instability of such states.

1.1.1 A dictionary

The first concrete realisation of holography was put forward by Maldacena in [5]. He proposed that maximally supersymmetric Yang-Mills (SYM) theory with gauge group $SU(N_c)$ in (3+1) dimensions is dual to Type IIB string theory with $\mathrm{AdS}_5 \times S^5$ boundary conditions. His conjecture was inspired by the observation that D3-branes in Type IIB

string theory have two equivalent descriptions: one as end-points for open strings and another as sources for closed strings.

These two theories and the detailed mapping between them are fascinating subjects in their own right. We refer the reader to [5, 6, 7, 8, 3, 9] and references therein for more details and for Maldacena's original argument. Here we simply state the results we need and use them to set the scene for the work reported in this thesis.

Both theories enjoy a lot of symmetry, as we will describe further in chapter 3. As an example, SYM is a CFT and therefore invariant under global $SO(4,2)$ transformations. This is matched by the group of isometries of AdS_5. In general, a global symmetry in the field theory is realised as a local symmetry in the bulk. This feature is a minimal check on the conjecture and is often used as a guide when constructing new dualities.

Here we will consider a specific limit of this correspondence that has been studied extensively. The gauge theory has two dimensionless parameters: the Yang-Mills coupling g_{YM} and the number of colours N_c. Suppose we take the limit of large N_c with the 't Hooft coupling $\lambda \equiv g_{YM}^2 N_c$ held fixed, then follow this up with the limit of large coupling, $\lambda \gg 1$. In this limit, the quantum string theory reduces to classical Type IIB supergravity. This is a generic feature of all known examples of holography: the gravity theory becomes classical when the field theory has many degrees of freedom per point.

In this thesis we want to use this duality and others like it to ask tough questions in field theories at strong coupling. Correlation functions are the basic objects in a quantum field theory: they tell us everything we want to know about that theory. However, they are hard to extract when we do not have access to a perturbative regime. Holography provides the powerful machinery we need to tackle this problem.

A one-to-one mapping between gauge-invariant operators $\mathcal{O}$ of the field theory and fields ϕ in the bulk was proposed in [10, 11]. We are instructed to identify the generating functional of correlation functions in the field theory with the string theory partition function:

$$\left\langle e^{\int \delta\phi_{(0)}\mathcal{O}} \right\rangle_{\text{CFT}} = Z_{\text{string}} \left[\delta\phi \sim \delta\phi_{(0)}\right] . \tag{1.2}$$

On the left-hand-side we have deformed the CFT by a source $\delta\phi_{(0)}$ for the operator $\mathcal{O}$. The boundary condition on the fluctuation $\delta\phi$ of the corresponding bulk field is that it 'tends to' the value $\delta\phi_{(0)}$ at the boundary of AdS.

In general, we do not know what the full string theory partition function is, or even means. One could view (1.2) as its definition. However, in the limit of classical supergravity it is simply given by the dominant classical saddle. Taking logs we obtain

a prescription for the generating functional of connected correlation functions at large N_c and large λ:

$$W[\delta\phi_{(0)}] = S_{\text{gravity}}^{\text{on-shell}}\left[\delta\phi_{(0)}\right], \tag{1.3}$$

where the gravity action has been evaluated on a solution to the bulk equations of motion for $\delta\phi$. In this thesis we will assume that a relation of this form holds for any given dual pair.

We have glossed over many subtleties in this prescription. Let us confront these now by considering the example of a general scalar operator in d spacetime dimensions. The conformal dimension Δ of this operator is defined through its behaviour under the scaling transformation

$$x^\mu \to \xi x^\mu, \quad \mathcal{O}(x) \to \xi^\Delta \mathcal{O}\left(\xi^{-1}x\right) \tag{1.4}$$

and will generically receive quantum corrections unless protected by symmetry. Here, x^μ with $\mu = 0, 1, \ldots, d-1$ denote the coordinates of the field theory.

The first step in applying (1.3) is to identify the dual bulk field that lies in the same representation of the symmetry algebra as the corresponding operator. Here this is a massive scalar field ϕ. For a specific scalar operator in SYM, the mass m_ϕ of the bulk field will be fixed by the Kaluza-Klein harmonic on the S^5, but here we keep it arbitrary to demonstrate its relation to Δ.

The next step is to write down the appropriate gravity action for fluctuations of the scalar and solve its equation of motion subject to the right boundary conditions. Here we restrict to the calculation of two-point functions for simplicity, for which a quadratic action is sufficient:

$$S_\phi = K \int d^{d+1}x \sqrt{g}\left(g^{ab}\partial_a\phi\partial_b\phi + m_\phi^2\phi^2\right). \tag{1.5}$$

For the Maldacena duality, with $d = 4$, the coefficient K is proportional to the volume of the S^5. Altogether the action will be proportional to N_c^2 and so dominate the partition function, as discussed earlier.

In holography, the bulk solution is dual to a state in the field theory. Here we consider fluctuations ϕ about AdS_{d+1}, which has $\phi = 0$, in order to find correlation functions of $\mathcal{O}$ in the vacuum. In later chapters we will consider more complicated backgrounds with other bulk fields turned on, which corresponds to studying a field theory with a non-trivial density matrix.

To determine the right boundary conditions, first we need to know more about AdS

space. One can obtain AdS_{d+1} as a hyperboloid embedded in $\mathbb{R}^{d,2}$. Different solutions to the embedding equation yield different coordinate charts. These cover various fractions of the space and keep various subgroups of the full isometry group $SO(d,2)$ manifest. For example, consider the following metric:

$$ds^2 = g_{ab}\, dX^a dX^b = \frac{\ell^2}{\cos^2\theta}\left(-dt^2 + d\theta^2 + \sin^2\theta\, d\Omega_{d-1}^2\right), \quad 0 \le \theta < \pi/2, \tag{1.6}$$

where ℓ is the radius of curvature set by the cosmological constant and $d\Omega_{d-1}^2$ is the unit-radius round metric on S^{d-1}. These are global coordinates since they cover the whole space. They keep an $\mathbb{R} \times SO(d)$ manifest.[1]

Now we explain in what sense AdS space has a boundary. The above metric is conformal to the metric on (one-half of) the Einstein static universe, $\mathbb{R} \times S^d$. The boundary of AdS_{d+1} is the timelike surface $\{\theta = \pi/2\}$ on which the conformal factor has a double pole. Strictly speaking, points on this surface are not part of the original spacetime. We add them to give its conformal compactification, which is a new spactime. The boundary is at infinite proper distance from any point in the interior, but null geodesics can reach it in finite affine parameter. We say that AdS space in global coordinates is a covariant box.

The bulk metric does not yield a metric on the boundary due to the double pole. We need to strip this off. We define the conformal structure on the boundary via

$$\gamma_{\mu\nu}^{\infty} = f^2 \gamma_{\mu\nu}\big|_{\partial \mathrm{AdS}}, \quad \gamma_{\mu\nu} = \partial_\mu X^a \partial_\nu X^b g_{ab}, \tag{1.7}$$

where $f(X^a)$ is some function of the bulk coordinates that is positive in the interior and has a single zero on the boundary. Here, $\gamma_{\mu\nu}$ is the usual induced metric on the boundary, and is divergent. The conformal structure behaves like a metric for the most part, but is only defined up to conformal transformations because there is no natural choice for f.

This is exactly what we want: we identify this as the metric of the CFT. We say that a spacetime is asymptotically AdS_{d+1} if $\gamma_{\mu\nu}^{\infty}$ is conformal to $\mathbb{R} \times S^{d-1}$. Our correspondence is holographic in the sense that the boundary of conformally compactified AdS_{d+1} is identical to the conformal compactification of the spacetime on which the CFT is defined.

We will also find another set of coordinates useful, which keep the Poincaré group in d dimensions manifest:

$$ds^2 = \frac{r^2}{\ell^2}\, \eta_{\mu\nu}\, dx^\mu dx^\nu + \frac{\ell^2}{r^2}\, dr^2. \tag{1.8}$$

[1] Note that we have unwrapped the time circle and work with the universal covering space of the hyperboloid.

These are known as Poincaré, or planar, coordinates. The boundary is at $r \to \infty$ in this chart and has zero curvature. Bulk solutions whose metric asymptotes to this form are therefore used to model the physics of the dual CFT on Minkowski space $\mathbb{R}^{d-1,1}$.

Note that the timelike Killing vector becomes null at $r = 0$. This plane is known as the Poincaré horizon. Whilst these coordinates only cover one half of the hyperboloid, *i.e.* just a causal patch, one can analytically continue through the horizon to global coordinates. However, if the bulk solution contains a black hole horizon or matter fields then we expect no simple way of relating the two charts. The issue of whether a global solution admits a planar limit will be explored in detail in chapter 4.

The metric (1.8) also has an $SO(1,1)$ scaling symmetry:

$$x^\mu \to \xi x^\mu, \quad r \to r/\xi. \tag{1.9}$$

The first part corresponds to a dilatation (1.4) in the CFT. With this in mind, it was suggested in [5, 12, 13] that we should somehow associate r with the energy scale of the field theory. Going further we can interpret the radial flow in the bulk geometry as the renormalisation group (RG) flow of the boundary theory. The geometry in (1.8) represents an ultraviolet (UV) fixed point, whereas the behaviour of the solution (which may have other fields turned on besides the metric) in the interior of the spacetime will determine the low-energy physics. See [14] for a review of these ideas and for recent progress in finding an exact correspondence between the Wilsonian picture and the bulk integration of geometry.

Hidden in (1.2) is the fact that this prescription is formulated in Euclidean signature. Take the metric in (1.8) and rotate to Euclidean time $\tau = it$. These coordinates are in fact global in Euclidean signature and the boundary (of the conformal compactification) of this space is S^d. The main difference is in the interior: the geometry ends smoothly. We will consider the prescription for computing Lorentzian correlators in section 1.1.3.

Now back to the programme. We want to consider fluctuations ϕ, governed by the action (1.5), about the Euclidean version of the background (1.8). The equation of motion for these fluctuations is

$$\frac{1}{\sqrt{g}}\,\partial_a\left(\sqrt{g}g^{ab}\partial_b\phi\right) - m_\phi^2\phi = 0. \tag{1.10}$$

We choose the boundary condition of regularity in the interior because nothing special happens there. Next we turn to the boundary at $r \to \infty$ and postulate a power law

behaviour:

$$\phi(r,x) = r^{-\alpha}\phi(x) \quad \Rightarrow \quad \alpha_{\pm} = \frac{d}{2} \pm \sqrt{\frac{d^2}{4} + m_\phi^2 \ell^2}. \tag{1.11}$$

Note that $\alpha_+ \geq 0$. The general solution is a sum of two power series, with the leading fall-off set by $\alpha_- = d - \alpha_+$:[2]

$$\phi(r,x) = r^{-\alpha_-}\phi_{(0)}(x)\left(1 + O\left(r^{-2}\right)\right) + r^{-\alpha_+}\phi_{(2\Delta-d)}(x)\left(1 + O\left(r^{-2}\right)\right). \tag{1.12}$$

Generically, the first term is divergent as we approach the boundary; it is non-normalisable with respect to the standard Klein-Gordon norm. A property of Euclidean AdS space is that a solution to (1.10) is uniquely determined by the choice of $\phi_{(0)}$ and the requirement of regularity in the interior, as discussed in detail in [11]. By studying how the deformation in (1.2) transforms under scaling, we are led to identify $\phi_{(0)}$ as the source and $\Delta[\mathcal{O}] = \alpha_+$.

Once we have found a solution to (1.10) with these boundary conditions, we then evaluate (1.5) on this solution. This yields a boundary term that we must functionally differentiate twice with respect to $\phi_{(0)}$. We find the correct result for the two-point function of a scalar operator $\mathcal{O}$ in a CFT, as was first demonstrated in [10, 11]. This procedure generalises to n-point correlators (whose forms for $n > 3$ are not fixed by the conformal symmetry) once we have added appropriate interaction terms to the scalar action.

There are subtleties here too. The on-shell bulk action will generically diverge due to integration all the way to the AdS boundary. This long-distance divergence shows up as UV divergences in the field theory correlators. To compute renormalised correlation functions, we regulate the divergence by introducing a cut-off in r, introduce intrinsic covariant counter-terms localised on the cut-off surface, and then remove the regulator. A systematic treatment for scalars can be found in [15].

We interpret the coefficient of the normalisable mode $\phi_{(2\Delta-d)}$ as the expectation value of $\mathcal{O}$ generated by turning on the source $\phi_{(0)}$. According to (1.3) we extract this by differentiating the renormalised on-shell action once. Note that the first variation of the on-shell action with respect to the boundary value of a field goes by another name: the boundary value of the canonical momentum. This Hamiltonian approach, with r playing the role of time, was championed in [16], in which the emphasis was shifted to computing renormalised canonical momenta as arbitrary functionals of sources. Lorentzian correlators were computed in [17] using this approach.

[2] Note that if α_+ and α_- differ by an integer then logs may appear in this expansion.

The concept of operator relevance is encoded quite naturally in holography. Deforming a UV fixed point by a relevant operator does not destroy it; it merely triggers an RG flow to the infrared (IR). Likewise, turning on a bulk field in AdS that tends to zero at the boundary will not destroy the asymptotically AdS region of the geometry, but merely modify the interior. From (1.11) we learn that $\Delta < d$ is only possible if $m_\phi^2 < 0$. It was shown in [18] that a positive energy theorem still exists in AdS space as long as the following bound is satisfied:

$$m_\phi^2 \ell^2 \geq m_{BF}^2 \ell^2 \equiv -\frac{d^2}{4}. \tag{1.13}$$

This is known as the Breitenlohner-Freedman (BF) bound.

If the scalar mass falls within the window $m_{BF}^2 \ell^2 < m_\phi^2 \ell^2 < m_{BF}^2 \ell^2 + 1$ then both fall-offs in (1.12) are normalisable [18]. Here one has a choice of whether to fix $\phi_{(0)}$ or $\phi_{(2\Delta-d)}$ at the boundary; these are known as standard or alternate boundary conditions, respectively. This yields two inequivalent CFTs, with the source and expectation value switched, whose generating functionals are related by a Legendre transformation [19]. This choice is implemented by adding extrinsic terms to the bulk action to yield the correct variational principle. An analogy is provided by the Gibbons-Hawking term [20] in gravity, which must be added to the Einstein-Hilbert action if we only want to fix the induced metric on the boundary and not its first derivative too. Note that within this window, more general choices of boundary condition are possible; we will make use of this freedom in chapter 4.

1.1.2 From black holes to condensed matter physics

So far we have focused on the vacuum of the CFT. However, a typical system of condensed matter has a non-zero temperature and density. The application of holography to condensed matter phenomena has a brief but intense history: see [21, 22, 23, 24, 25] for recent reviews of these developments. We will encounter several examples in this thesis. We now describe how to incorporate these two ingredients in our holographic framework.

According to [11, 26], a temperature is introduced to the CFT by adding a black hole to the bulk. To see how this works, consider the following Euclidean action:

$$S_E = -\frac{1}{16\pi G_{d+1}} \int d^{d+1}x \sqrt{g} \left(R + \frac{d(d-1)}{\ell^2} \right) + S_{\partial \mathrm{AdS}} \tag{1.14}$$

with boundary action

$$S_{\partial\text{AdS}} = -\frac{1}{16\pi G_{d+1}} \int_{\partial\text{AdS}} d^d x \sqrt{\gamma} \left(2\mathcal{K} - \frac{2(d-1)}{\ell} \right). \tag{1.15}$$

The first boundary term is the aforementioned Gibbons-Hawking term, with $\mathcal{K}$ the trace of the extrinsic curvature of the AdS boundary, and the second is a counter-term required for a finite on-shell action. We choose the convention that the extrinsic curvature of the boundary is given by $\mathcal{K}_{\mu\nu} = \nabla_{(\mu} n_{\nu)}$, where the unit vector n^a is orthogonal to the boundary and outward-directed. Here, G_{d+1} is Newton's gravitational constant in $(d+1)$ dimensions. In every known example of holography, in the supergravity limit one can always truncate to this universal subsector of pure gravitational dynamics.

One solution to this theory is the Euclidean continuation of a Schwarzschild-AdS$_{d+1}$ black hole with planar horizon. Its metric can be written

$$ds^2 = \frac{r^2}{\ell^2} \left(f d\tau^2 + d\vec{x}_{d-1}^2 \right) + \frac{\ell^2}{r^2 f} dr^2, \quad f(r) = 1 - \left(\frac{r_+}{r} \right)^d, \tag{1.16}$$

where $d\vec{x}_{d-1}^2$ is the flat metric on $\mathbb{R}^{d-1}$. In Lorentzian signature this solution has a horizon at $r = r_+$. To prevent a conical singularity on this surface in Euclidean signature, we must periodically identify $\tau \sim \tau + \beta$, with

$$\beta = \frac{4\pi\ell^2}{r_+^2 |f'(r_+)|} = \frac{4\pi\ell^2}{dr_+}. \tag{1.17}$$

From (1.7), it follows that the field theory metric inherits this identification. Recall that a field theory with periodically identified Euclidean time, of period β, is equivalent to a field theory in equilibrium at temperature $T = 1/\beta$. Thus, in holography we identify the Schwarzschild-AdS$_{d+1}$ solution with a thermal state in the field theory.

We can extract the thermodynamic properties of this thermal field theory from S_E, which is given by

$$S_E = -\frac{\ell^{d-1}}{16\pi G_{d+1}} \left(\frac{4\pi}{d} \right)^d V_{d-1} T^{d-1}, \tag{1.18}$$

where V_{d-1} is the (divergent) spatial volume of the field theory. For the Maldacena duality, with $d = 4$, the prefactor $\ell^3/16\pi G_5 = N_c^2/8\pi^2$. Assuming our black hole is the dominant saddle of the bulk partition function and identifying the latter as in (1.2), we can express the free energy F of the field theory as

$$F = -T \log Z = T S_E. \tag{1.19}$$

We obtain the entropy of the field theory by taking the appropriate derivative of F or by applying the Bekenstein-Hawking formula directly:

$$S = -\frac{\partial F}{\partial T} = \frac{A_H}{4G_{d+1}} = \frac{\ell^{d-1}}{16\pi G_{d+1}} \frac{(4\pi)^d}{d^{d-1}} V_{d-1} T^{d-1} = \frac{\pi^2}{2} N_c^2 V_3 T^3, \tag{1.20}$$

where A_H is the area of the black hole horizon and the final equality is for SYM.

The stress tensor $T^{\mu\nu}$ of the CFT is dual to the metric g_{ab} in the bulk. By definition, the background metric of a field theory is a source for the stress tensor, so this fact is consistent with (1.7). This can be computed as in [27] and the result agrees with the thermodynamics found above.

We wish to consider field theories with a conserved current J^μ for a global $U(1)$ symmetry. In SYM, J^μ could be the diagonal Cartan generator of $U(1)^3 \subset SU(4)$, where the $SU(4) \cong SO(6)$ is the global R-symmetry dual to the isometry of the S^5. We introduce a finite density $\langle J^t \rangle \neq 0$ by holding the system at a fixed chemical potential μ. This corresponds to deforming the CFT Lagrangian by the term μJ^t. We identify this current with a Maxwell field A_a in the bulk. For a given bulk solution, the asymptotic expansion of the time component A_t near the AdS boundary is given by

$$A_t = \mu - \frac{\langle J^t \rangle}{r^{d-2}} + \dots . \tag{1.21}$$

In other words, the CFT has non-zero density if the bulk solution has electric flux at the boundary.

Holography is particularly well-suited to the study of strongly-coupled field theory at finite charge density. Here, lattice techniques fail due to the 'sign problem': at finite chemical potential the Euclidean action becomes complex, which results in a highly oscillatory path integral. Such problems arise when trying to solve even the simplest model describing electrons moving on a lattice with repulsive electron-electron interactions, known as the Hubbard model (see [28] for a recent review). Through AdS/CFT, the problem can be recast into studying solutions to Einstein-Maxwell theories.

In order to describe a strongly-correlated condensed matter system at non-zero temperature and density, the minimal gravitational ingredients are therefore a black hole in AdS and a non-zero electric flux at the boundary. A natural background is the electric Reissner-Nordström-AdS black hole, which will provide the starting point for much of the work described in this thesis. This solution was first explored in the context of holography in [29]. Note that the chemical potential and the temperature provide two

scales from which a dimensionless ratio can be formed, allowing for a non-trivial phase structure. This is indeed what we find, as we now describe, owing to the surprising properties of gravity in AdS spacetimes.

It turns out that hairy black holes are commonplace in AdS space. Loosely speaking, the negative cosmological constant means that the scalar potential is less restricted and so black holes in AdS are not burdened by the no-hair theorems that beset asymptotically flat black holes. In [30] it was shown that planar electric Reissner-Nordström-AdS black holes can be unstable to the formation of charged scalar hair at low temperatures. One can argue for this instability as follows. From the action for a minimally-coupled massive charged scalar (see (4.2) later), we can identify an effective mass

$$m_{\text{eff}}^2 \ell^2 = m_\phi^2 \ell^2 + q^2 g^{tt} A_t^2, \tag{1.22}$$

where q is the scalar charge. For sufficiently large scalar charge, and sufficiently close to the horizon, the negative contribution from the second term should be enough to drive this effective mass below the BF bound for the bulk spacetime. Once the scalar mass and charge are fixed, the critical temperature T_c at which the instability occurs is set by the only other scale in the problem: μ, the leading fall-off in (1.21).

Note that neutral scalars with $q = 0$ can also become unstable, indicating that a distinct mechanism is at play, as noted first in [31]. Given that a Reissner-Nordström black hole develops an AdS_2 throat at zero temperature, a sufficient condition (depending on m_ϕ and q) for instability is satisfied if the effective AdS_2 mass violates the $d = 1$ BF bound [32]. This AdS_2 has been the focus of much recent study: see *e.g.* [33]. Furthermore, it has been used as a diagnostic for exploring instabilities in other contexts too (see *e.g.* [34] for a discussion of finite momentum instabilities), though it cannot always be used, as we will show in chapter 5.

As alluded to, this instability corresponds to a continuous phase transition in the dual theory. Consider the generic case of $q \neq 0$. The operator dual to the bulk charged scalar develops an expectation value, which can be extracted from (1.12), and so spontaneously breaks the global $U(1)$ symmetry. Black branes with charged scalar hair, as first constructed nonlinearly in [31], can therefore be used to model the condensed phase of a superfluid. The phenomenology of such 'holographic superfluids' was explored further in [35, 36, 37, 38].

In fact, the phenomenology of superfluids has many similarities with that of superconductors. The application of a magnetic field results in the generation of supercurrents,

which underlie the Meissner effect (see [21] for a discussion). However, here there is no dynamical photon in the boundary theory and so these cannot generate their own magnetic field to cancel the applied one. One can 'weakly gauge' the boundary theory, as in [31], and show that the photon indeed gains a mass. In [39, 40] it was shown that the normal phase of the dual theory bears a striking resemblance to that of the cuprates when a lattice is added explicitly to the hairless black brane. There, as is typical in condensed matter physics, the response of the field theory to an electromagnetic source was found by turning on a background electromagnetic field. In this thesis we will use the terms holographic superfluid and superconductor interchangeably, and we will encounter such hairy black holes again in chapters 4 and 5.

We conclude this subsection with some brief remarks on the validity and applicability of holographic dualities. As hinted several times, (infinitely) many other dual pairs are known. Examples include those found by considering stacks of D-branes or M-branes on products of flat space and a Calabi-Yau cone over a Sasaki-Einstein base (see [41, 42, 43] and also [44] for examples). For this reason we are justified in the rather general approach to the holographic dictionary we have taken so far, giving explicit examples only where appropriate. In this thesis we will sometimes use these concrete dualities in which the dual field theory is known. At other times, however, we will choose the simplest bulk model with the ingredients necessary to model the phenomena of interest. In this pragmatic, 'bottom-up' approach the hope is that simple or common features will be robust and we will gain useful experience and intuition into a wide range of possible field theory duals. We must bear in mind however that we may miss some interesting features only visible from a 'top-down' perspective.

We will also work with consistent truncations of supergravity. Such a theory is found by reducing on a compact manifold then setting to zero a subset of Kaluza-Klein fields in such a way that they are not sourced by those remaining. For example, superfluid instabilities and the back-reacted black branes were embedded in this way into ten- and eleven-dimensional supergravity in [45, 32, 46]. Note that the existence of a consistent truncation does not imply that the dual field theory is known. Rather, it gives restricted information about the dual CFT spectrum: the quantum numbers of a few chiral operators at best. Whilst closer to a full dual pair than a phenomenological model, such setups can yield results that depend sensitively on the truncation employed, as we will see in chapter 4.

1.1.3 Linear response from black holes

Holography has become a powerful tool — in many cases, the only tool — for studying field theories at strong coupling. However, the prescription (1.2) for computing correlation functions was formulated in Euclidean signature. The true power of holography lies in its ability to encode the real-time evolution of the dual theory. In this subsection we show how to determine holographically the real-time response of a field theory at non-zero temperature and density to an external perturbation.

It is not always straightforward to analytically continue to Lorentzian signature, for the following reason. Thermal Euclidean correlators are periodic in imaginary time and so are only defined at discrete frequencies, known as Matsubara frequencies. The analytic continuation to arbitrary frequencies requires knowledge of the Euclidean correlator at all Matsubara frequencies, which is generally not available. Thus, it was necessary to devise a prescription for computing real-time correlators directly in holography. This was first done in [47], and we will review its generalisation to the case of coupled operators shortly.

There are several types of two-point correlators in Lorentzian signature. We can restrict attention to the retarded Green's function because all other two-point correlators can be constructed from this. To probe a many-body system experimentally, we can perturb the system by a source $\delta\phi_{i(0)}$ for some operator $\mathcal{O}_i$. Let us assume that the system has spacetime translational invariance so that we can work in Fourier space. The simplest perturbations to study have either a fixed frequency ω or a fixed momentum k. The retarded Green's function $G^R_{\mathcal{O}_i\mathcal{O}_j}$ characterises the response of the system at linear order in the source. The change in the expectation value of $\mathcal{O}_i$ is given by

$$\delta\left\langle\mathcal{O}_i\right\rangle(\omega,k) = G^R_{\mathcal{O}_i\mathcal{O}_j}(\omega,k)\,\delta\phi_{j(0)}(\omega,k). \tag{1.23}$$

We have allowed for the various operators in the theory to couple, which will be the case we are interested in. Note that we have suppressed any Lorentz indices for clarity. An equivalent definition is

$$G^R_{\mathcal{O}_i\mathcal{O}_j}(\omega,k) = -i\int dt d^{d-1}x\ \theta(t)\left\langle[\mathcal{O}_i(t,x),\mathcal{O}_j(0,0)]\right\rangle e^{i\omega t-ikx}. \tag{1.24}$$

We are interested in the retarded Green's function for three main reasons. Firstly, it gives us information about the excitation spectrum of a theory. In general, $G^R_{\mathcal{O}_i\mathcal{O}_j}$ is a complex function of the real variables ω and k. If we naively complexify either ω or k,

then often poles appear in $G^R_{\mathcal{O}_i\mathcal{O}_j}$, indicating a large response to an infinitesimal source. The position of each pole can be expressed as a function of the complex variable in terms of the real variable (as well as the other parameters of the system, such as temperature); this complex function is called the dispersion relation of the excitation corresponding to the pole. Henceforth we will abuse notation and write the dispersion relations simply as $\omega(k)$ or $k(\omega)$. Using the Fourier decomposition, we can interpret $\operatorname{Re}\omega(k)$ as the propagating frequency and $-\operatorname{Im}\omega(k)$ as the decay rate of the excitation, or alternatively $\operatorname{Re}k(\omega)$ as the propagating momentum and $\operatorname{Im}k(\omega)$ as the attenuation, or decay length, of the excitation.

The poles described above are not directly observable: in a real experiment, neither ω nor k can be complex. A common experimental technique for studying excitations of a many-body system is to measure the spectral function

$$\chi_{ij}(\omega,k) \equiv i\left[G^R_{\mathcal{O}_i\mathcal{O}_j}(\omega,k) - G^R_{\mathcal{O}_i\mathcal{O}_j}(\omega,k)^\dagger\right], \tag{1.25}$$

which is a real-valued function of real ω and k, and hence is observable. Physically, χ_{ij} determines the rate of work done on the system by the small external source $\delta\phi_{i(0)}$ (see, for example, [21]). A pole in $G^R_{\mathcal{O}_i\mathcal{O}_j}$ with sufficiently large residue will produce a large peak in χ_{ij}. We can thus identify excitations of the system from peaks in χ_{ij}. Note that we can reconstruct $\operatorname{Re}G^R_{\mathcal{O}_i\mathcal{O}_j}$ given χ_{ij} using the Kramers-Kronig relation, provided the large-ω and large-k asymptotics have been suitably regulated [21].

Secondly, the retarded Green's function can be used to compute transport coefficients of the field theory. These appear in the effective low-energy description of the system and govern its macroscopic properties. They can often be extracted via Kubo formulae [48] of the form

$$\eta_{ij} = -\lim_{\omega\to 0}\frac{1}{\omega}\operatorname{Im}G^R_{\mathcal{O}_i\mathcal{O}_j}(\omega,0). \tag{1.26}$$

The particular transport coefficient η_{ij} depends on which operators $\mathcal{O}_{i,j}$ the retarded Green's function refers to.

We are also interested in instabilities of the theory. It is easy to show that, when written in Fourier space, the retarded Green's function is analytic in the upper half-plane. Consider the following relation:

$$-i\theta(t)\left\langle[\mathcal{O}_i(t,x),\mathcal{O}_j(0,0)]\right\rangle = \int\frac{d\omega d^{d-1}k}{(2\pi)^d}\,e^{-i\omega t+ikx}G^R_{\mathcal{O}_i\mathcal{O}_j}(\omega,k). \tag{1.27}$$

The right hand side can be seen as a contour integral in the complex ω-plane. Since

$e^{-i\omega t} = e^{-i\,\mathrm{Re}\,\omega t}e^{\mathrm{Im}\,\omega t}$, the contour should be closed in the upper half-plane for $t < 0$. However, the left-hand side of this equation vanishes for $t < 0$. Thus, by Cauchy's theorem, $G^R_{\mathcal{O}_i\mathcal{O}_j}$ must be analytic in the upper half-plane. So if we compute $G^R_{\mathcal{O}_i\mathcal{O}_j}$ and find a pole in the upper half-plane, this tells us that the state in which it has been computed is unstable. We will have more to say about this soon.

We now give the details of the prescription presented in [49] for computing retarded Green's functions for coupled operators directly from AdS/CFT. As usual, first we must identify the bulk fields ϕ_i dual to the operators $\mathcal{O}_i$ of interest. Perturbing the CFT at equilibrium by sources $\delta\phi_{i(0)}$ for these operators corresponds in the gravity theory to fluctuating the dual bulk fields about the background solution: $\phi_i = \bar{\phi}_i + \delta\phi_i$, where a bar denotes the background value of the field. We obtain the equations of motion for these fluctuations by linearising about the bulk equations. We allow arbitrary Dirichlet data at the AdS boundary; in chapters 2 and 3 our bulk fields will have asymptotic expansions of the form

$$\delta\phi_i = \delta\phi_{i(0)} + \ldots \quad \text{as} \quad r \to \infty, \tag{1.28}$$

and thus we can identify the constant piece of the fluctuation at the AdS boundary as the source. (One can always work with rescaled fields such that this is the case.) Also, in these cases our backgrounds will possess spacetime translation invariance in the dual theory directions and so we can work in Fourier space, with the identification of ω, k in the bulk and the boundary.

There will be a regular future horizon in the interior of the background geometry in all cases considered in this thesis. We are instructed to solve the equations of motion for these fluctuations subject to (1.28) and the condition that the fluctuation is *ingoing* at this horizon. This second condition is natural from the bulk perspective because classically, information cannot reach asymptotic infinity from within an event horizon. It ensures that the retarded Green's function is causal, and thus characterises the *future* response of the dual theory to the external perturbation.

We then substitute ϕ_i into the renormalised bulk action, which reduces to a boundary term of the following form at quadratic order in $\delta\phi_i$:

$$S^{\text{on-shell}}_{(2)} = \lim_{r\to\infty} \int \frac{d\omega d^{d-1}k}{(2\pi)^d} \left[\delta\phi_i(r,-\omega,-k)\, C_{ij}(r,\omega,k)\, \partial_r \delta\phi_j(r,\omega,k) + \ldots\right]. \tag{1.29}$$

The ellipsis denotes terms with no radial derivatives. These give analytic contributions to the retarded Green's function, *i.e.* they lead only to contact terms in the final result,

which we will ignore in what follows. These terms also include the finite pieces of counter-terms. Defining the UV-normalised solution matrix F via

$$\delta\phi_i(r,\omega,k) \equiv F_{ij}(r,\omega,k)\,\delta\phi_{j(0)}(\omega,k), \tag{1.30}$$

the prescription of [49] then reads

$$G^R_{\mathcal{O}_i\mathcal{O}_j}(\omega,k) = -2\lim_{r\to\infty}\mathcal{F}_{ij}(r,\omega,k), \quad \text{with} \quad \mathcal{F}\equiv F^\dagger C\partial_r F. \tag{1.31}$$

We will show that this prescription yields the correct Ward identities for our retarded correlators.

The main motivation for the prescription for uncoupled operators, given in [47], was that it gave the correct results where independent verification was possible. This prescription is however limited to two-point correlators. It was subsequently shown to emerge from the complex time formalism of thermal field theory in [50] and further refined in [51, 52].

Before applying this prescription to study the real-time response of strongly-correlated states of quantum matter, we give a brief overview of the definition and physical importance of quasinormal modes. These are the characteristic oscillations of black objects and a recent comprehensive review can be found in [53]. They are directly related to the poles of retarded Green's functions in AdS/CFT field theory duals, as we now show.

Consider a minimally-coupled probe scalar field ϕ in an asymptotically AdS black hole spacetime. A quasinormal mode is a solution the equation of motion of the form $\phi \sim e^{-i\omega t}$ that describes an ingoing mode at the horizon and that vanishes at the AdS boundary. The resulting boundary value problem is non-Hermitian and the eigenfrequencies $\omega_\star$ are complex. This reflects the dissipative nature of the system, and the imaginary part of these frequencies gives a decay timescale for the perturbation. See [54] for early examples. It is straightforward to show (see [47] for example) that the retarded Green's function for the dual scalar operator $\mathcal{O}$ has the form

$$G^R_{\mathcal{O}\mathcal{O}} \sim \frac{\phi_{(2\Delta-d)}}{\phi_{(0)}}. \tag{1.32}$$

Here, $\phi_{(0)}, \phi_{(2\Delta-d)}$ are defined as in (1.12) but now ϕ is on a black hole background and is ingoing at the horizon. It follows directly that the quasinormal frequencies can be identified with the resonance frequencies of this retarded Green's function, as highlighted in [55, 47]. This identification, which is also true for coupled operators, will serve as a

valuable check on our calculations of retarded correlators in chapters 2 and 3.

Quasinormal modes typically decay exponentially in time. In contrast, modes whose frequencies have instead a positive imaginary part indicate a linear instability of the bulk theory. From the discussion around (1.27), this indicates a continuous phase transition in the boundary theory, as for holographic superfluids. This will form one motivation for our work in chapter 4 and the basis of chapter 5.

1.2 Real-time response of strongly-correlated systems

Consider a system with a global $U(1)$ symmetry, in a state with a net charge density of that $U(1)$. Such a state is said to be *compressible* if the charge density varies smoothly as a function of the chemical potential. The best-understood examples of compressible states are: solids, in which translational symmetry is spontaneously broken to a discrete subgroup; superfluids, in which the $U(1)$ is spontaneously broken; and Landau Fermi liquids (LFLs), in which neither translational symmetry nor the $U(1)$ are broken.

The degrees of freedom in an LFL include long-lived fermionic quasi-particle excitations about a Fermi surface. Two characteristic features of an LFL are that at temperatures T low compared to the Fermi energy, the heat capacity $c_V \propto T$ and the electrical resistivity $\mathscr{R} \propto T^2$. The spectrum of an LFL also includes collective charge density excitations, which produce poles in the retarded Green's function of the charge density operator. At sufficiently low T, in the so-called 'collisionless' regime in which quantum effects are more important than thermal effects, the spectrum of collective excitations includes 'zero sound', a fluctuation of the shape of the Fermi surface that has the dispersion relation of a sound wave [56, 57, 58]. In the opposite regime at sufficiently high T, the spectrum of collective excitations includes the expected hydrodynamic sound, shear and charge diffusion modes [58]. The transition between these two regimes as T increases is called the collisionless/hydrodynamic crossover.

Some real materials are compressible, break neither translational symmetry nor the $U(1)$, and exhibit Fermi surfaces, but the low-energy degrees of freedom are *not* those of an LFL. These materials are generically called 'non-Fermi liquids' (NFLs). A subset of these are the so-called 'strange metals', including the normal (non-superconducting) phase of high-T_c superconductors. The most prominent characteristic feature of a strange metal is a linear resistivity, $\mathscr{R} \propto T$. Experimental evidence indicates that, in many

cases, the strange metal phase is related to quantum criticality, *i.e.* a continuous phase transition at zero temperature [59]. In particular, the degrees of freedom at such a quantum critical point, when heated up to non-zero T, may give rise to a quantum critical region in which $\mathscr{R} \propto T$. Demonstrating this from first principles is difficult because generically quantum critical degrees of freedom are strongly interacting. The existence of strange metals and other NFLs raises a crucial question: can we classify compressible ground states?

Holography may help to answer this question. As discussed in section 1.1.2, in a given dual pair the conserved current of a global $U(1)$ symmetry of the CFT is dual to a $U(1)$ gauge field in the gravity theory. Compressible states can be described by asymptotically AdS spacetimes with non-zero electric flux at the boundary. Holography provides many examples of compressible states [60], but these are often not solids, superfluids or LFLs. The canonical example is the planar Reissner-Nordström-AdS solution of Einstein-Maxwell theory, as demonstrated in [61]. Holography has been used to describe both quantum criticality [62, 63, 64, 65, 66, 67, 68, 69] and compressible states with $\mathscr{R} \propto T$ [70, 71, 72] and, more generally, has the potential to reveal some guiding principles for classifying compressible states, as discussed in [73, 74].

In chapter 2 we will study the Reissner-Nordström-AdS$_4$ black hole with planar horizon. This describes a dual compressible state in (2+1) dimensions that is not a solid, a superfluid or an LFL. We compute the retarded Green's functions in full for conserved currents in the shear channel. We will work exclusively at non-zero temperature by studying a non-extremal black hole. This calculation extends the work of [75]. (See [76, 61] for results in the sound channel for this system.)

Many previous studies have restricted to calculating just the locations of poles in retarded Green's functions. As mentioned in the previous section, these are found by computing the quasinormal frequencies of the bulk theory. For example, the quasinormal frequencies for shear-type electromagnetic and gravitational perturbations of a Reissner-Nordström-AdS$_4$ black hole were computed in [75]. Note that no indication of an instability to these types of mode was found, though the same is not true for scalars, as discussed in section 1.1.2. Many studies, even those in which the retarded Green's functions themselves are computed, often restrict to the regime of long wavelengths and/or small frequencies. In this limit, the effective description is given by hydrodynamics and only the leading poles are significant [77]. Some examples are [78, 79] and [80].[3]

[3]See also [81] for a review of the recent developments in applying holographic methods to understand non-equilibrium physics in strongly-coupled field theories.

In chapter 2 we aim to go beyond these studies. We compute the shear channel correlators for arbitrary frequencies and momenta and explore the detailed structure of these correlators. We show that their poles have varying residues and that this information can be used to assess the dominance of these poles beyond the hydrodynamic regime. As well as analysing the properties of these correlators for large and small values of the boundary theory parameters, we also examine the curious and intricate motion of their poles at intermediate parameter values.

In chapter 3 we consider a similar type of crossover, related to that found in LFLs. We study two holographic systems describing compressible states that are however not solids, superfluids, LFLs or NFLs, as we soon explain. Our main goal is to study the effect of a non-zero magnetic field B on the collisionless/hydrodynamic crossover in these systems.

We will study the SYM theory introduced in section 1.1.1 coupled to a number N_f of $(n+1)$-dimensional massless hypermultiplets in the fundamental representation of $SU(N_c)$, *i.e.* flavour fields. Our two theories correspond to the choice $n = 2, 3$. In addition to the limit considered so far, we will work exclusively in the probe limit $N_f \ll N_c$. These field theories arise from the $(n+1)$-dimensional intersection of N_c D3-branes with N_f Dp-branes in Type IIB string theory, with $p = 2n + 1$ [82, 83, 84, 85]. We will refer to them as the D3/Dp theories.

Each D3/Dp theory enjoys a global $U(1)_B$ baryon number symmetry, with conserved current J^μ. To study compressible states of these theories, we will introduce a baryon number charge density $\langle J^t \rangle$, or equivalently a baryon number chemical potential μ. Recall that a hypermultiplet contains fermions and scalars, and that both are charged under $U(1)_B$. States with non-zero $\langle J^t \rangle$ and non-zero magnetic field B are dual holographically to probe Dp-branes embedded in $\mathrm{AdS}_5 \times S^5$ with non-zero worldvolume electric flux [85, 82, 86] and magnetic flux [87]. To add a temperature we replace the AdS_5 with a Schwarzschild-AdS_5 black brane.

For temperatures $T \ll \mu$, these compressible states have been studied extensively, using holography, in [88, 89, 90, 91, 92, 93, 94, 95, 96, 97]. Neither translational symmetry nor $U(1)_B$ are broken in these states, and to date no evidence of a Fermi surface in these systems has been found. In this sense, the evidence accumulated so far suggests that these states are not solids, superfluids, LFLs or NFLs. Indeed, these states exhibit various unusual properties, including an extensive $T = 0$ ground state degeneracy [89]. We will call these low-temperature compressible states 'holographic quantum liquids'.

The spectrum of excitations in these holographic quantum liquids at $T = 0$ includes

sound modes. These two modes produce poles in J^t's retarded Green's function $G^R_{tt}(\omega, k)$ whose dispersion relations, when expressed as complex frequencies ω, have real parts proportional to momentum k and imaginary parts $\propto k^2$ [89]. Due to their similarity with the zero sound modes in an LFL, we will call these modes 'holographic zero sound'.

As T increases, these holographic quantum liquids exhibit a collisionless/hydrodynamic crossover analogous to that in an LFL. For the D3/D7 system the crossover was studied in [94], and a similar crossover occurs in the D3/D5 system, as we will show.

Both systems exhibit quantum phase transitions for sufficiently large B, as we will review. We want to determine how B affects the holographic zero sound modes and the collisionless/hydrodynamic crossover in these holographic quantum liquids. Five scales appear in our problem: μ, T, B, which characterise the state of the system, and ω, k, which characterise perturbations of the state. We will work in the quantum liquid regime, where $\mu \gg T, \sqrt{B}$, and we always work with $\omega, k \ll \mu$. For the D3/D7 theory we choose the magnetic field to point in the direction orthogonal to the momentum. Furthermore, we will always work with values of B below any known phase transition, where we already find a rich story.

1.3 Solitons, black holes and superconductors

As has already been seen, gravity in AdS spacetimes is full of surprises. Some of these surprising features, such as black hole thermodynamics, can be understood using the AdS/CFT correspondence as a necessary consequence of the dual field theory dynamics. Nevertheless, in recent years various new surprises have been uncovered, mostly in the process of trying to model interesting exotic configurations in the boundary CFT using the gravitational description. Of primary interest in chapter 4 is the fact that asymptotically AdS spacetimes admit solitonic configurations with non-trivial matter profiles.

To motivate the discussion of solitons in AdS, recall the view of global AdS (1.6) as a covariant gravitational box and consider linearised matter fields in this geometry. It is straightforward to show that the eigenenergies of the single particle states are quantised as $\omega = \Delta + 2\,n + l$, where $n \in \mathbb{Z}_+$ denotes the harmonic level and $l \in \mathbb{Z}_+$ the rotational quantum number. Here, Δ is a zero-point energy from the bulk perspective that translates into the conformal dimension of the corresponding CFT operator on the boundary. One naively imagines that it would be impossible to macroscopically populate the single particle energy levels to form a coherent condensate of such fields (assuming

they are bosons); the harmonic gravitational potential will cause the particles to collapse to the centre of AdS and we should end up with a black hole.

Many examples prove this intuition to be incorrect. For one it is possible to balance the gravitational interaction by matter repulsion (*e.g.* by considering charged matter as we will discuss) or more simply by tuning the boundary conditions for fields at the AdS boundary. Since both of these ingredients will play a role in our work, we now briefly review previous discussions of solitons in AdS.

The earliest construction of solitons in AdS spacetimes was achieved in a very simple model of scalar fields coupled to gravity [98] by allowing for non-trivial boundary conditions for the scalar field. These boundary conditions correspond to deformations of the boundary CFT by multi-trace operators [99, 100]. Once one is willing to relax boundary conditions, solitons can be made to order: one demands that there is a soliton and works out which choice of boundary condition will allow it to exist. Such constructions go by the name of designer gravity [101] and have been extensively investigated in the context of positive energy theorems for AdS spacetimes with multi-trace boundary conditions [102, 103].

A different construction of solitons is to consider charged scalar fields in AdS and allow the charge repulsion to compensate against the gravitational attraction. In fact, the equations for BPS configurations preserving various fractions of supersymmetries in diverse dimensions have been known for a while [104] and admit charged supersymmetric solitonic solutions. More recently, charged solitons that asymptote to global AdS_5 were constructed in a perturbative expansion in the scalar amplitude in [105] within a simple phenomenological Einstein-Maxwell-scalar theory with negative cosmological constant. Subsequently, [106] and [107] constructed a family of charged scalar solitons within a particular five dimensional truncation of Type IIB supergravity to five dimensions (which is contained within the ansatz of [104]).[4]

Our interest in chapter 4 is with the global charged solitons in asymptotically AdS_4 spacetimes, motivated by many observations. First of all, an interesting question is whether global charged AdS solitons can become 'large'; in other words, is it possible for the soliton size to be parametrically larger than the length scale ℓ set by the cosmological constant? This question is not purely academic; one of the surprises about gravity in AdS is that when the characteristic size R of gravitational configurations (be they solitons or even black holes) becomes large compared to the AdS scale ℓ we can consider a scaling

[4]The truncation in question can equivalently be described as a truncation of $\mathcal{N} = 8$ $SO(6)$ gauged supergravity in (4+1) dimensions, where equal charges are turned on in $U(1)^3 \subset SO(6)$. We will study a truncation with non-equal charges in chapter 5.

regime that takes us to solutions in planar (Poincaré) AdS. This is of course well known in the context of asymptotically AdS black holes and plays an important role in modelling the thermal physics of the dual CFT on Minkowski space.

However, in many of the known examples of solitons in AdS this does not happen. For example, smooth charged solitons constructed in [106] are always at most of AdS scale and do not admit passage into the planar limit.[5] This behaviour seems at face value consistent with the known results for self-gravitating fluids in AdS [108, 109, 110, 111]. However, in the case of self-gravitating fluids it is known that there is a critical dimension beyond which the solitons can become parametrically large in AdS units [112, 113], indicating that weakening the gravitational attraction can lead to large solitons. A natural question then is whether one can have a different control parameter that allows solitons to get arbitrarily large. Indeed one such parameter presents itself: the charge of the bulk scalar field that controls the strength of the charge repulsion.

A second motivation comes from the tendency for charged scalar fields in AdS to condense, as discussed in section 1.1.2. It is widely believed that solitons provide the zero-temperature limit of superfluid black branes. For example, charged scalar configurations that asymptote to planar AdS_4 were constructed numerically for a restricted range of parameters in [114, 115] and were shown to back up this hunch. Once again we have a poser: if for a given choice of bulk Lagrangian one does not have a large global soliton, then how is it possible that we obtain a planar solution with a condensed scalar? One possibility is that the planar solution descends from a singular global soliton as for instance argued in [106], but it is not clear if this is generic. More to the point, we need to address what class of singular global solutions are admissible. After all, if we were only interested in constructing solutions with the desired AdS asymptotics and simply pick boundary data then integrate, such solutions will generically be singular. In chapter 4 we provide numerical and (some) analytical evidence to connect global and planar solitons with hairy black holes and branes more generally.

A further motivation comes from studies of superfluid black branes within consistent truncations of supergravity; the first examples of such in (3+1) dimensions were given in [46]. Many more truncations of $\mathcal{N} = 8$ $SO(8)$ gauged supergravity in (3+1) dimensions were studied recently in [116], where it was found that the behaviour and existence of solutions was highly dependent on the details of the truncation. For example, it was shown that within the truncation where equal charges were turned on in $U(1)^4 \subset$

[5] We are simplifying a little here; the statement is strictly true for solitons that carry equal charges under all three $U(1)^3 \subset SO(6)$. Solitons that are charged under a single $U(1)$ do become arbitrarily large. Here we are interested in understanding the circumstances under which this can happen.

$SO(8)$ (which is the AdS_4 analogue of the truncation studied in [106]), the hairless Reissner-Nordström-AdS_4 black brane dominates the grand canonical ensemble at low temperatures. This is despite the fact that one has a new branch of hairy black hole solutions; the latter turn out to be subdominant as they have larger free energy. This situation is in strong contrast to other truncations such as the one originally investigated in [46]. Such behaviour was noticed earlier in [117] (the author would like to thank Sean Hartnoll for alerting us to this) and has also been encountered in other AdS_5 gauged supergravity truncations [118]. These examples have an important lesson to impart: the linearised/probe analysis, as discussed for example in [32], is at best only useful to indicate where new solution branches exist. It cannot tell us whether the new branch of solutions is actually the true saddle point configuration. During our study of solitons in these truncations we will also find clues to help explain this behaviour.

One issue with consistent truncations is the lack of parameters that one can dial. However, the fact that we are interested in asymptotically AdS spacetimes comes to our rescue: we can relax boundary conditions on the scalar field to take advantage of multi-trace relevant operators (if the CFT admits such). For the examples we study this dial is present and as in the recent investigations of [119, 68] we can turn it to explore the solutions space of these theories and hence the phase diagram of the deformed CFT. To a certain extent we will see that relaxing the boundary condition on scalar fields is tantamount to reducing the effect of the gravitational attraction; its effect is qualitatively similar to increasing the charge repulsion or going up to higher dimensions.

In most applications of AdS/CFT to finite density systems, we are interested in the behaviour of the CFT in Minkowski spacetime in the grand canonical ensemble, *i.e.* at non-zero temperature and chemical potential, both of which are held fixed. On the other hand, investigating such theories with global AdS boundary conditions allows us to identify the CFT states corresponding to the condensation of bulk charged fields. Moreover, we can look at fixed charge sectors of the dual field theory and ask what the spectrum of CFT states looks like from the bulk viewpoint, and thus chart out the microcanonical phase diagram.

These considerations partly motivated the earlier work of [105, 106] on global charged solitons, wherein it was argued that the global solitons are the true ground states of the theory with fixed charge. Naively one would have expected that the ground state with fixed charge corresponds to a charged black hole in AdS, but the fact that the scalars can condense allows one to exit the black hole phase and enter the phase of the charged solitons below a critical mass.

However, the previous discussion of scalar solitons remaining bounded in size turns out to imply that the spectrum of smooth solitons terminates on a critical solution with maximal mass. (This happens even for the supersymmetric solitons of [106].) Equivalently, in the microcanonical phase diagram one has a critical charge for the CFT states. While one can certainly crank up the charge of the state beyond this value, it was conjectured in [106] that for larger values of CFT charge, one ends up with a singular global bulk soliton. Given our earlier observation regarding the strength of the bulk scalar interactions (equivalently the charge quantum number of the dual CFT operator), it is interesting to ask what happens to the microcanonical phase diagram as we dial this parameter, and also the scalar boundary conditions.

Whilst it is tempting to conjecture that the solitons we construct are the ground states for the CFT on $\mathbb{R} \times S^2$ at a fixed value of charge, this statement appears to depend sensitively on the theory in question. In particular, it can transpire in certain cases that one encounters global black holes with or without scalar hair that are lighter than a soliton at a given value of the charge [105, 120]. Our focus will be primarily on solitons and we only briefly touch upon the nature of global black holes.

This work can be viewed as part of a wider programme to explore the space of solutions to gravity theories with a negative cosmological constant in the hope of learning general lessons about strongly-coupled field theories. In the holographic approach to condensed matter physics there is great freedom in how a bulk theory is constructed. This has the advantage of allowing the construction of holographic models that capture a wide variety of physical phenomena. The drawback, of course, is that the detailed phenomenology of such constructions typically depends on the particular model employed. For this reason a desirable feature of any phenomenological holographic programme is the existence of some 'universal result', at least for a particular class of bulk theories. A celebrated example is the ratio of shear viscosity to entropy density for strongly-coupled, isotropic holographic plasmas arising from two derivative bulk Lagrangians [121, 122].

Holographic superconductivity on the other hand has no simple universal sector; in the minimal example of a single $U(1)$-charged bulk scalar field there is freedom to specify the potential and gauge field coupling. In a bottom-up approach, whilst the small-field expansion of these functions can be easily parametrised, the behaviour away from the critical temperature depends strongly on their nonlinear characteristics. Turning to a top-down approach one may hope to overcome such difficulties. However, as observed in [116], different consistent sub-truncations of a particular top-down model exhibit radically different results for the behaviour of the superconducting order parameter with

temperature. To understand if there are any generic features for the landscape of consistent holographic superconductors, one must delve deeper into larger families of consistent truncations. See [32, 116, 118, 123] for some interesting work along these lines, and also [39, 40, 124] for recent hints of universal behaviour that bears a tantalising resemblance to experimental observations of the cuprates.

In chapter 5 we take a step in this direction by considering a truncation of $\mathcal{N} = 8$ $SO(6)$ gauged supergravity in five dimensions containing 20 scalars and 15 gauge fields. This truncation contains a three-charge family of black branes [125], dual to a normal phase, about which we look for the emergence of new branches of superconductors. Such branches are indicated by the existence of marginal modes for the various charged scalar fields at finite temperature. This calculation can be viewed as a first step towards understanding the sequence of preferred phases of the full supergravity theory.

When cooled sufficiently the black branes we employ to model the normal phase become thermodynamically unstable. Note that in many cases the stable black brane simply ceases to exist at low temperatures, and so the system is largely immune to any $T = 0$ test of stability, such as BF bound violation for any near horizon $\mathrm{AdS}_2 \times \mathbb{R}^3$. We focus on superconducting instabilities that occur in the normal phase at sufficiently high temperatures where it is locally thermodynamically stable. We find that a superconducting black brane branch always exists in this region of the normal phase.

At high temperatures in the regime of local thermodynamic stability there are indications that this system is only metastable [126, 127, 128]. With the interpretation of the three R-charges as angular momenta of D3-branes spinning in the S^5 of the full ten-dimensional theory, this instability corresponds to the one-by-one fragmentation of D3-branes from the rotating stack. The superconducting branches we seek in this work are local instabilities of the black brane solutions, and whilst they may be subject to arguments vis-à-vis metastability, a study of the critical temperatures and chemical potential dependence is not directly affected by it. The family of black branes used here represents a convenient local minimum for our purposes.

In addition, the black brane solutions we employ for the normal phase have three R-charges, which allows us to explore the dependence of the various superconducting phase transitions on the conjugate chemical potentials. Some modes in the truncation are charged under a single $U(1)$ and do not couple to the other gauge fields at the linearised level. As such, turning on an additional chemical potential for another $U(1)$ provides an effective holographic description of a state with a density imbalance. An example in condensed matter physics is an imbalanced Fermi mixture in which there is a mismatch

of chemical potentials for spin-up and spin-down constituents [129]. Phenomenological holographic models of such mixtures were investigated in bottom-up bulk and probe brane constructions in [130, 131], where the additional $U(1)$ plays the role of up-down spin imbalance. One feature of these models is that the superconducting phase ceases to exist if the imbalance is too great.

Here we have an imbalance as a natural consequence of the three chemical potentials in our top-down setup. As the imbalance for a given superconducting mode is increased, its critical temperature decreases until it reaches the threshold of thermodynamic instability, at finite temperature. However, increasing the imbalance for one mode decreases the imbalance for another, and is a consequence of the $SO(6)$ symmetry. Surprisingly there is no set of chemical potentials for which the imbalance is simultaneously too great for all modes.

Chapter 2

Shear channel correlators from hot charged black holes

In this chapter, based on [132], we compute numerically the full retarded Green's functions for conserved currents in the shear channel of a (2+1)-dimensional field theory at non-zero temperature and density. In particular, we demonstrate the 'repulsion' and 'clover-leaf crossing' of their poles and stress the importance of the residues at the poles beyond the hydrodynamic regime.

This state is assumed to be holographically dual to a non-extremal, electric Reissner-Nordström-AdS_4 black hole with planar horizon. In the following section we present the bulk theory and the holographic prescription for computing the correlators of interest. We then obtain results for arbitrary frequencies and momenta and survey the detailed structure of these correlators. As a consistency check, we show that our results agree precisely with existing literature for the appropriate quasinormal frequencies of the bulk theory.

For comparison, we then demonstrate that we recover the hydrodynamics of this theory if we take the appropriate limit of our more general numerical results. We also illustrate how the effective theory provided by hydrodynamics breaks down for shorter wavelengths and larger frequencies.

Note that we have taken the opportunity to expand on some details of [132] and to correct a mistake. By using instead the prescription of [49], our retarded correlators manifestly satisfy the appropriate Ward identities.[1]

[1]The author would like to thank Richard Davison and particularly Juan Jottar for invaluable discussions on this issue.

2.1 Setup and extraction of correlators

An action for a $U(1)$ gauge field A coupled to gravity with a negative cosmological constant in four spacetime dimensions is

$$S_{\text{bulk}} = \frac{1}{16\pi G_4}\int d^4x\sqrt{-g}\left(R + \frac{6}{\ell^2} - \ell^2 F^2\right), \tag{2.1}$$

where ℓ is the curvature radius and $F = dA$. This is a consistent truncation of eleven-dimensional supergravity [29]. A solution to this theory describing an electric Reissner-Nordström-AdS$_4$ black hole with planar horizon can be written

$$ds^2 = \frac{r^2}{\ell^2}\left(-f dt^2 + dx^2 + dy^2\right) + \frac{\ell^2}{r^2 f}\,dr^2, \quad A = \mu\left(1 - \frac{r_+}{r}\right)dt, \tag{2.2}$$

where

$$f(r) = 1 - (1+Q^2)\left(\frac{r_+}{r}\right)^3 + Q^2\left(\frac{r_+}{r}\right)^4, \quad \mu = \frac{Qr_+}{\ell^2}. \tag{2.3}$$

The (outer) black hole horizon is at $r = r_+$ and has temperature

$$T = \frac{r_+^2 f'(r_+)}{4\pi\ell^2} = \frac{(3-Q^2)r_+}{4\pi\ell^2} = \frac{(3-Q^2)\mu}{4\pi Q}. \tag{2.4}$$

We identify T and μ as the temperature and chemical potential of the dual theory state, respectively, and work at $T > 0$ throughout.

Linearised fluctuations of the metric and gauge field about this background are dual to perturbations of the stress tensor $T_{\mu\nu}$ and $U(1)$ current J_μ, respectively. First we must isolate the relevant subsector of these fluctuations that will give us the correlators of interest. General fluctuations take the form

$$g_{ab} = \bar{g}_{ab} + h_{ab}, \quad A_b = \bar{A}_b + a_b, \tag{2.5}$$

where a bar denotes background quantities and the fluctuations h_{ab} and a_b depend *a priori* on all bulk coordinates. The background (2.2) preserves $SO(2)$ rotational symmetry in the (x, y) plane as well as translations in all three field theory directions t, x and y. We make use of these symmetries to perform the Fourier decomposition

$$\delta\phi_i(r,t,x) = \int \frac{d\omega dk}{(2\pi)^2}\,\delta\phi_i(r,\omega,k)\,e^{-i\omega t + ikx}, \quad \delta\phi_i = \{h_{ab}, a_b\}, \tag{2.6}$$

where we have used the $SO(2)$ invariance to set the y-momentum to zero.

With these choices, the fluctuations divide into two decoupled groups, depending on their behaviour under the parity transformation $y \to -y$. Here we focus on the odd-parity modes $\delta\phi_i = \{h_{yt}, h_{xy}, a_y\}$. In the dual theory, these correspond to perturbations at a given frequency ω and x-momentum k that are transverse to the direction of momentum flow. In other words, we seek the retarded Green's functions of operators T_{yt}, T_{xy} and J_y in the shear channel.

The equations for the odd-parity fluctuations are coupled in general. However, when these fluctuations are expressed in terms of gauge-invariant master fields $\Phi_\pm$ introduced in [133], the linearised equations of motion decouple. This greatly simplifies our task of extracting retarded Green's functions using the prescription outlined in section 1.1.3, as we shall see.

First we need the fluctuated on-shell bulk action. As emphasised in chapter 1, in general this action is divergent due to integration all the way to the AdS boundary. We add the following terms in order to give finite correlators:

$$S = S_{\text{bulk}} + \frac{1}{16\pi G_4}\int_{\partial\text{AdS}} d^3x\sqrt{-\gamma}\left(2\mathcal{K} - \frac{4}{\ell} - \ell\mathcal{R}\right), \tag{2.7}$$

where $\gamma_{\mu\nu}$, $\mathcal{K}$ and $\mathcal{R}$ are respectively the induced metric, the trace of the extrinsic curvature and the trace of the intrinsic curvature of the AdS boundary at $r \to \infty$.

Since we only need two-point functions, it is sufficient to fluctuate the action to quadratic order. Fluctuation of the Ricci scalars will yield terms of the form $h\partial^2 h$, which we must first integrate by parts. The resulting boundary terms from the second radial derivatives in the bulk Ricci scalar will be cancelled by the Gibbons-Hawking term. Terms with two t or x derivatives, or one of each, will vanish when integrated by parts since we choose the boundary condition that the fluctuations vanish at $t = \pm\infty$ and $x = \pm\infty$. Now we integrate terms of the form $(\partial h)^2$ and $(\partial a)^2$ by parts so that the remaining bulk piece yields the equations of motion for the fluctuations. The latter are given by

$$f\left[u^4 h^{y\prime\prime}{}_t + 4u^3 h^{y\prime}{}_t + \frac{4Q^2}{\mu}a'_y\right] - \frac{Q^2}{\mu^2}\partial_x\left(\partial_t h^x{}_y - \partial_x h^y{}_t\right) = 0 \tag{2.8a}$$

$$f\left[u^4 f h^{x\prime\prime}{}_y + (u^4 f)' h^{x\prime}{}_y\right] - \frac{Q^2}{\mu^2}\partial_t\left(\partial_t h^x{}_y - \partial_x h^y{}_t\right) = 0 \tag{2.8b}$$

$$f\left[u^4 f a''_y + u^2(u^2 f)' a'_y + \mu u^2 h^{y\prime}{}_t\right] - \frac{Q^2}{\mu^2}\left(\partial_t^2 a_y - f\partial_x^2 a_y\right) = 0, \tag{2.8c}$$

where we have introduced the rescaled radial coordinate $u = r/r_+$ (a prime denotes ∂_u)

and raised an index on the metric fluctuations for convenience. We also have a constraint equation that preserves the gauge choice $h_{r\mu} = 0$:

$$u^4 \left(\partial_t h^{y\prime}{}_t - f\partial_x h^{x\prime}{}_y\right) + \frac{4Q^2}{\mu}\partial_t a_y = 0. \tag{2.9}$$

Placing the resulting quadratic action on-shell we are left with the boundary action

$$\begin{aligned} S^{\text{on-shell}}_{(2)} = X \lim_{u\to\infty} \int d^3x \Bigg[& u^4 \left(h^y{}_t h^{y\prime}{}_t - f h^x{}_y h^{x\prime}{}_y\right) - \frac{4Q^2}{\mu^2}\left(u^2 f a_y a_y' + \mu a_y h^y{}_t\right) \\ & + 4u^3\left(1 - \frac{1}{\sqrt{f}}\right)\left(h^y{}_t h^y{}_t - f h^x{}_y h^x{}_y\right) \\ & - u^4 f' h^x{}_y h^x{}_y - \frac{Q^2}{\mu^2}\frac{u}{\sqrt{f}}\left(\partial_t h^x{}_y - \partial_x h^y{}_t\right)^2 \Bigg] \end{aligned} \tag{2.10}$$

with normalisation constant

$$X \equiv \frac{r_+^3}{32\pi G_4 \ell^4}. \tag{2.11}$$

Upon moving to Fourier space via (2.6), this action has the same form as (1.29):

$$\begin{aligned} S^{\text{on-shell}}_{(2)} = X\mu^2 \lim_{u\to\infty} \int dy \int \frac{d\mathfrak{w}\, d\mathfrak{q}}{(2\pi)^2} \Big[& u^4 h^y{}_t(u,-\mathfrak{w},\mathfrak{q})\, h^{y\prime}_t(u,\mathfrak{w},\mathfrak{q}) \\ & - u^4 f h^x{}_y(u,-\mathfrak{w},-\mathfrak{q})\, h^{x\prime}{}_y(u,\mathfrak{w},\mathfrak{q}) \\ & - \frac{4Q^2}{\mu^2} u^2 f a_y(u,-\mathfrak{w},-\mathfrak{q})\, a_y'(u,\mathfrak{w},\mathfrak{q}) + \ldots \Big]. \end{aligned} \tag{2.12}$$

For convenience we have defined the dimensionless frequency and x-momentum of the perturbation through $\mathfrak{w} \equiv \frac{\omega}{\mu}$ and $\mathfrak{q} \equiv \frac{k}{\mu}$ and relabelled $\delta\phi_i(u,\omega,k) \equiv \delta\phi_i(u,\mathfrak{w},\mathfrak{q})$. This means that the correlators we later extract will satisfy

$$G^R_{\mathcal{O}_i\mathcal{O}_j}(\omega,k) = \frac{1}{\mu^2} G^R_{\mathcal{O}_i\mathcal{O}_j}(\mathfrak{w},\mathfrak{q}). \tag{2.13}$$

As in section 1.1.3, the ellipsis denotes terms that do not contain radial derivatives and so lead only to contact terms in the final result.

As mentioned earlier, it is useful to move to the gauge-invariant master fields $\Phi_\pm$ defined in [75] via

$$\Phi_\pm \equiv -\mu \frac{u^3 f\mathfrak{q}}{\mathfrak{w}^2 - f\mathfrak{q}^2}\left(\mathfrak{w} h^{x\prime}{}_y + \mathfrak{q} h^{y\prime}{}_t\right) - \frac{2Q^2}{u}\left[\frac{2f\mathfrak{q}^2}{\mathfrak{w}^2 - f\mathfrak{q}^2} + u\, s_\pm(\mathfrak{q})\right] a_y, \tag{2.14}$$

with

$$s_\pm(\mathfrak{q}) \equiv \frac{3}{4}\left(1+\frac{1}{Q^2}\right)\left(1 \pm \sqrt{1+\frac{16}{9}\left(1+\frac{1}{Q^2}\right)^{-2}\mathfrak{q}^2}\right). \tag{2.15}$$

The system can then be recast in terms of two decoupled equations for these fields, given by

$$(u^2 f\,\Phi_\pm')' + \left[uf' + \frac{Q^2}{u^2 f}\left(\mathfrak{w}^2 - \mathfrak{q}^2 f\right) - \frac{2Q^2}{u^3}\,s_\pm(\mathfrak{q})\right]\Phi_\pm = 0. \tag{2.16}$$

Armed with these fields, we can express the matrix of retarded Green's functions in the shear channel in terms of two universal functions $\Pi_\pm(\mathfrak{w},\mathfrak{q})$. First we use (2.14) and (2.9) to express $h^{y'}{}_t, h^{x'}{}_y, a_y$ in terms of $\Phi_\pm$. Next we need the fall-offs as $u\to\infty$ of these fields:

$$\begin{aligned} h^y{}_t &= h^y{}_{t(0)} - \frac{Q^2\mathfrak{q}}{2u^2}\left(\mathfrak{w}\,h^x{}_{y(0)} + \mathfrak{q}\,h^y{}_{t(0)}\right) + \frac{\pi^y{}_t}{u^3} + \dots \\ h^x{}_y &= h^x{}_{y(0)} + \frac{Q^2\mathfrak{w}}{2u^2}\left(\mathfrak{w}\,h^x{}_{y(0)} + \mathfrak{q}\,h^y{}_{t(0)}\right) + \frac{\pi^x{}_y}{u^3} + \dots \\ a_y &= a_{y(0)} + \frac{\pi_y}{u} + \dots \end{aligned} \tag{2.17}$$

and

$$\Phi_\pm = \Phi_{\pm(0)}\left(1 + \frac{\Pi_\pm}{u} + \dots\right), \tag{2.18}$$

which all have the same form as (1.28). Using these relations and (2.8b) we can express $\Phi_{\pm(0)}$ in terms of the sources $\{h^y{}_{t(0)}, h^x{}_{y(0)}, a_{y(0)}\}$:

$$\Phi_{\pm(0)} = -2Q^2 s_\pm(\mathfrak{q})\,a_{y(0)} + \mu\mathfrak{q}Q^2\left(\mathfrak{w}\,h^x{}_{y(0)} + \mathfrak{q}\,h^y{}_{t(0)}\right). \tag{2.19}$$

Finally, we evaluate (2.12):

$$\begin{aligned} S^{\text{on-shell}}_{(2)} = X\mu^2\int dy\int\frac{d\mathfrak{w}\,d\mathfrak{q}}{(2\pi)^2}\Bigg\{&\frac{4Q^2\left(s_+\Pi_+ - s_-\Pi_-\right)}{\mu^2\left(s_+ - s_-\right)}\,a_{y(0)}\,a_{y(0)} \\ &- \frac{2Q^2\mathfrak{q}\left(\Pi_+ - \Pi_-\right)}{\mu\left(s_+ - s_-\right)}\left[a_{y(0)}\left(\mathfrak{w}\,h^x{}_{y(0)} + \mathfrak{q}\,h^y{}_{t(0)}\right) + \left(\mathfrak{w}\,h^x{}_{y(0)} + \mathfrak{q}\,h^y{}_{t(0)}\right)a_{y(0)}\right] \\ &- \frac{Q^2\left(s_-\Pi_+ - s_+\Pi_-\right)}{\left(s_+ - s_-\right)}\left(\mathfrak{w}\,h^x{}_{y(0)} + \mathfrak{q}\,h^y{}_{t(0)}\right)\left(\mathfrak{w}\,h^x{}_{y(0)} + \mathfrak{q}\,h^y{}_{t(0)}\right)\Bigg\}, \end{aligned} \tag{2.20}$$

where $\delta\phi_{i(0)}\,\delta\phi_{j(0)} \equiv \delta\phi_{i(0)}(-\mathfrak{w},-\mathfrak{q})\,\delta\phi_{j(0)}(\mathfrak{w},\mathfrak{q})$ and we have neglected a contact term. By design, the divergent pieces cancel precisely.

We now read off the matrix of retarded Green's functions using (1.31):[2]

$$G^R_{yt,yt} = \frac{2\mathfrak{q}^2 Q^2 X \mu^2 \left(s_- \Pi_+ - s_+ \Pi_-\right)}{\left(s_+ - s_-\right)} \tag{2.21a}$$

$$G^R_{xy,xy} = \frac{2\mathfrak{w}^2 Q^2 X \mu^2 \left(s_- \Pi_+ - s_+ \Pi_-\right)}{\left(s_+ - s_-\right)} \tag{2.21b}$$

$$G^R_{xy,yt} = G^R_{yt,xy} = -\frac{2\mathfrak{w}\mathfrak{q} Q^2 X \mu^2 \left(s_- \Pi_+ - s_+ \Pi_-\right)}{\left(s_+ - s_-\right)} \tag{2.21c}$$

$$G^R_{xy,y} = G^R_{y,xy} = \frac{4\mathfrak{w}\mathfrak{q} Q^2 X \mu \left(\Pi_+ - \Pi_-\right)}{\left(s_+ - s_-\right)} \tag{2.21d}$$

$$G^R_{yt,y} = G^R_{y,yt} = -\frac{4\mathfrak{q}^2 Q^2 X \mu \left(\Pi_+ - \Pi_-\right)}{\left(s_+ - s_-\right)} \tag{2.21e}$$

$$G^R_{y,y} = -\frac{8 Q^2 X (s_+ \Pi_+ - s_- \Pi_-)}{\left(s_+ - s_-\right)}. \tag{2.21f}$$

Note that all correlators are functions of $\mathfrak{w}$ and $\mathfrak{q}$ and satisfy the Ward identities given in [22]. In the rest of this chapter, we refer to $\Pi_\pm$ as 'the retarded Green's functions for $\Phi_\pm$' for brevity.

All that remains is to solve the equations of motion for the master fields numerically, subject to ingoing boundary conditions at the horizon, and extract $\Pi_\pm$. We now move on to the results, saving the details of our numerical method for appendix 2.B.

2.2 Results and discussion

To ensure that the retarded Green's functions for $\Phi_\pm$ have been calculated correctly, we must check that the locations of their poles match the quasinormal spectrum for the appropriate bulk fluctuations [55, 47]. In fig. 2.1 we demonstrate that this is indeed the case for our results. The quasinormal frequencies were computed using the method pioneered by Leaver in [134] and explained in detail in [135].[3] We find precise agreement with the quasinormal frequency plots for non-zero temperature shown in [75].

First, a note on our terminology. From the gravity perspective, modes with quasinormal frequencies on the negative $\mathrm{Im}\,\mathfrak{w}$ axis are associated with purely decaying perturbations of the black hole. We refer to these as 'on-axis' modes. The 'off-axis' modes have an additional oscillatory component.

[2] We have lowered the appropriate boundary indices using the flat Minkowski metric.

[3] The author would like to thank Sean Hartnoll for useful tips on generating these quasinormal spectra.

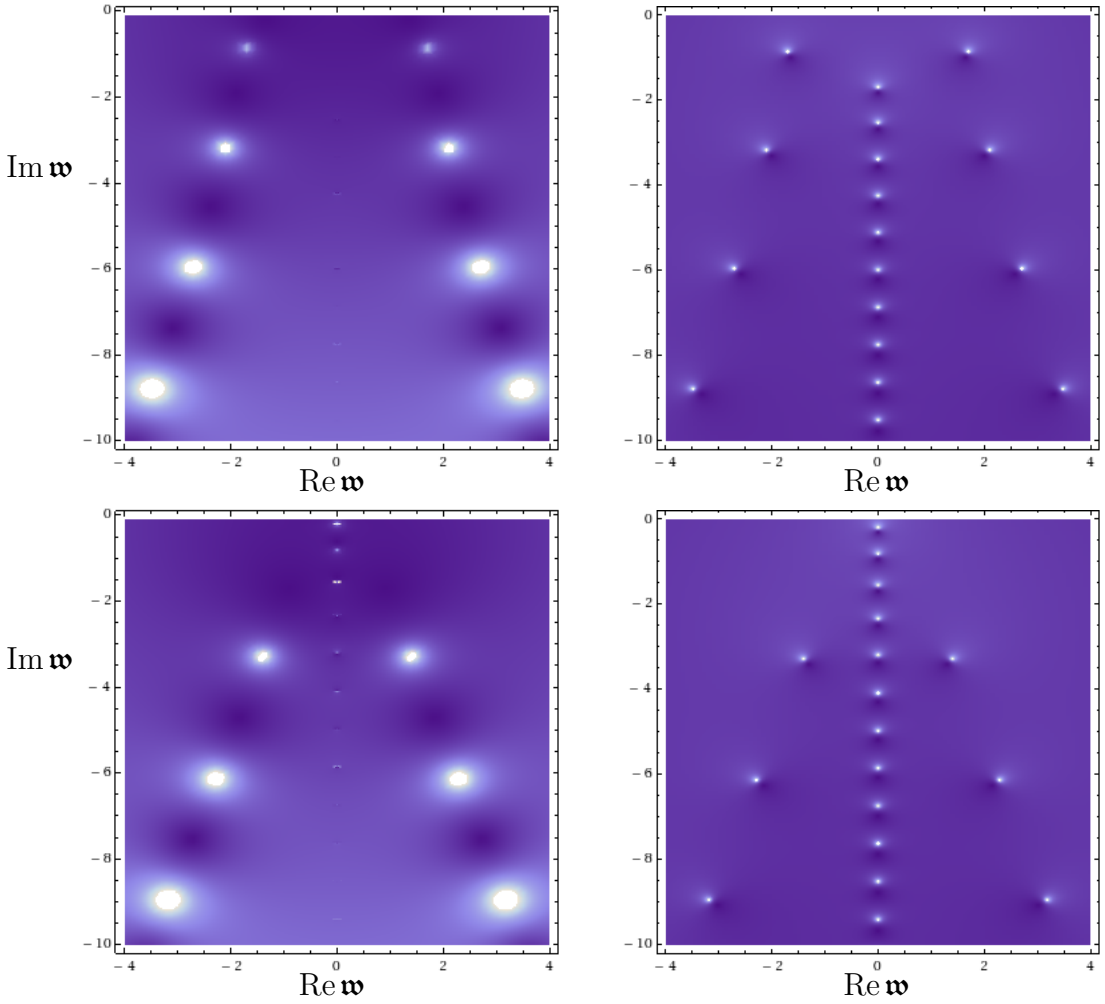

Fig. 2.1: A comparison between density plots of $|\Pi_\pm|$ on the complex $\mathfrak{w}$ plane (left panels) and the quasinormal frequencies for $\Phi_\pm$ (right panels). The top row is for Φ_+ and the bottom row is for Φ_-. All plots have $\mathfrak{q} = 1$ and $T/\mu = 0.09$. As we discuss later, the on-axis modes are weaker but have been tested thoroughly against the quasinormal spectrum in a finer plot.

As an example, we present in fig. 2.2 the full result for the $G^R_{xy,y}$ correlator, given in (2.21d). It can be seen from (2.21) and (2.15) that the poles in the various correlators are determined completely by $\Pi_\pm$, which we now study for various parameter ranges.

2.2.1 Residues

In fig. 2.3 we show surface plots of $\Pi_\pm$ on the complex $\mathfrak{w}$ plane. They exhibit the usual symmetries of retarded Green's functions, namely

$$\Pi_\pm(\mathfrak{w}, \mathfrak{q})^* = \Pi_\pm(-\mathfrak{w}^*, \mathfrak{q}), \tag{2.22}$$

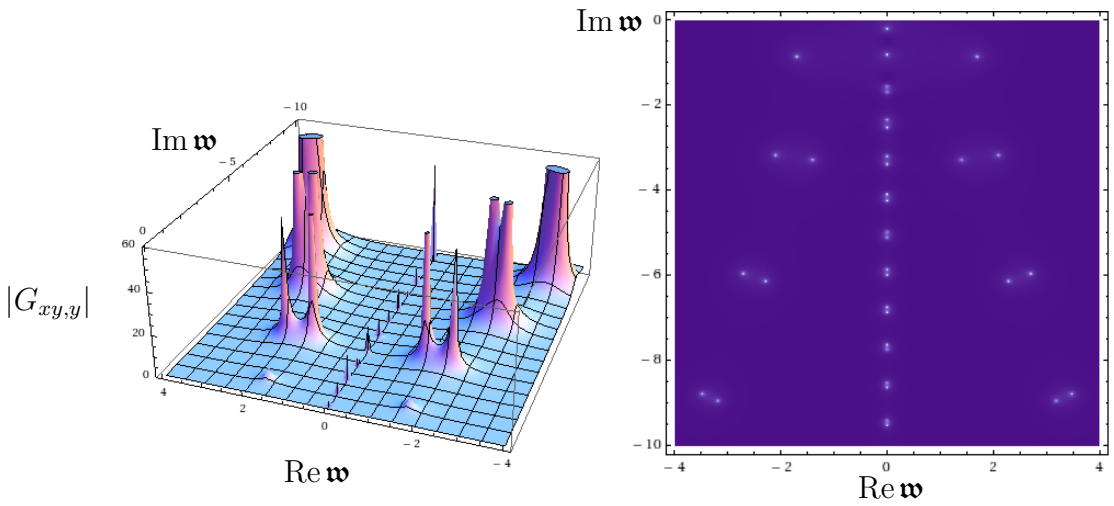

Fig. 2.2: A comparison between a surface plot of $|G_{xy,y}|$ on the complex $\mathfrak{w}$ plane (left) and the appropriate quasinormal frequencies (right). Both plots have $\mathfrak{q} = 1$ and $T/\mu = 0.09$.

which can be shown to follow from the $\mathfrak{w} \leftrightarrow -\mathfrak{w}^*$ symmetry of the equation of motion (2.16) and the ingoing boundary conditions.

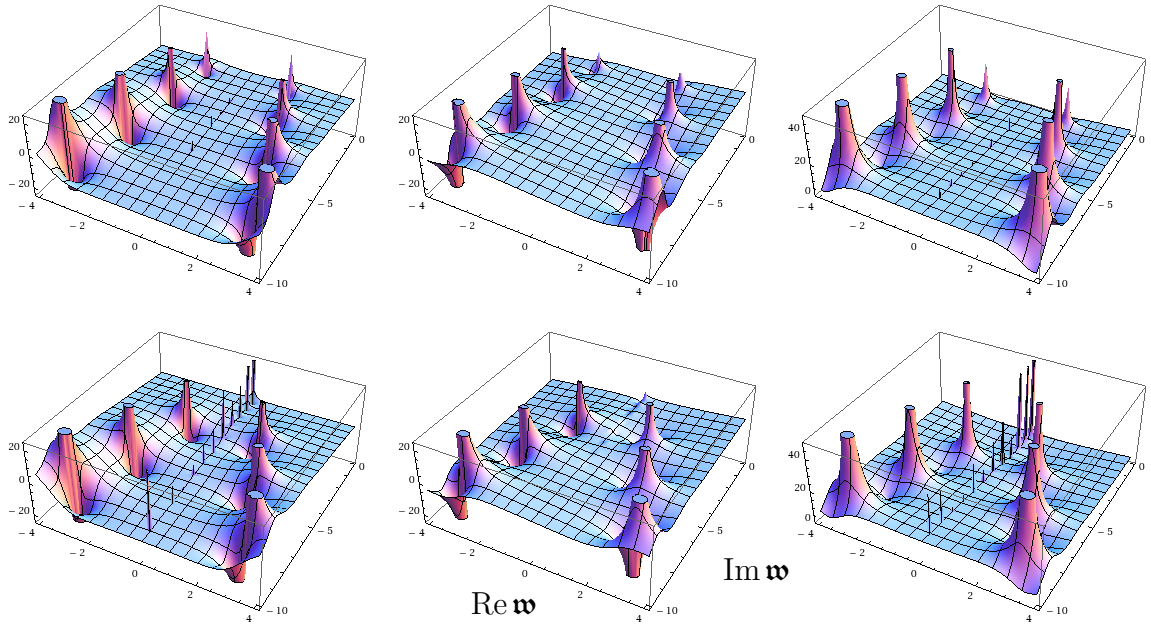

Fig. 2.3: Surface plots of Π_+ (top row) and Π_- (bottom row) on the complex $\mathfrak{w}$ plane at $\mathfrak{q} = 1$, $T/\mu = 0.09$. We show (from left to right) the real part, imaginary part and absolute value of each. All plots have the same orientation on the plane, as indicated.

Note that the off-axis poles have much wider peaks than those on-axis, indicating larger residues. We would like to understand how important these residues are in determining the behaviour of the boundary theory. Suppose we assume that $\Pi_\pm$ have only simple poles that are well-separated (an assumption we question in a later subsection).

Then they will have the form

$$\Pi_{\pm}(\mathfrak{w},\mathfrak{q}) = \sum_i \frac{R_i\left(\mathfrak{q};T/\mu\right)}{\mathfrak{w}-\mathfrak{w}_i\left(\mathfrak{q};T/\mu\right)} + \text{analytic pieces}, \tag{2.23}$$

where the locations of the poles $\mathfrak{w}_i$ in the complex $\mathfrak{w}$ plane have real part $\sigma_i(\mathfrak{q};T/\mu)$ and imaginary part $-\Gamma_i(\mathfrak{q};T/\mu)$. By performing a Fourier transform, we show in appendix 2.A that the quantity

$$R_i(\mathfrak{q};T/\mu)\, e^{-\mu\Gamma_i(\mathfrak{q};T/\mu)(t-t')}$$

determines the contribution of a given pole to $\Pi_{\pm}$. Beyond the hydrodynamic regime, *i.e.* for $t-t' \lesssim 1$, the residues can therefore be crucial in determining which poles dominate the linear response.

2.2.2 Behaviour at large frequency and momentum

At large $\mathfrak{w}$ and $\mathfrak{q}$ we can perform a WKB analysis of the equation of motion. This yields

$$\Pi = \pm iQ\sqrt{\mathfrak{w}^2-\mathfrak{q}^2} \tag{2.24}$$

for both $\Pi_{\pm}$, where we consider real $\mathfrak{w}$. So for $\mathfrak{w} \gg \mathfrak{q}$ or $\mathfrak{q} \gg \mathfrak{w}$ the growth of $|\Pi_{\pm}|$ is linear in the larger parameter, as demonstrated in fig. 2.4. We note the zeroes at $\mathfrak{w} = \pm\mathfrak{q}$ for large $\mathrm{Re}\,\mathfrak{w}$ and $\mathfrak{q}$ in confirmation of our result and also the strong presence of the hydrodynamic pole in Π_{-}, to be discussed in section 2.2.4.

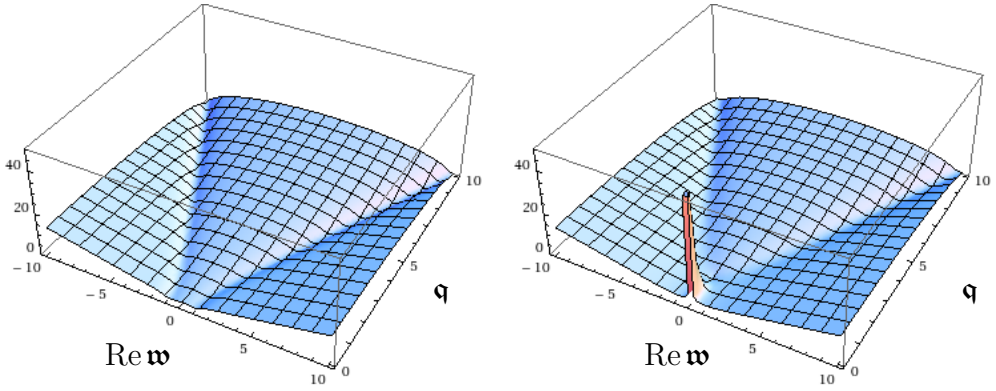

Fig. 2.4: Surface plots of $|\Pi_{+}|$ (left) and $|\Pi_{-}|$ (right) on the $(\mathrm{Re}\,\mathfrak{w},\mathfrak{q})$ plane at $T/\mu = 0.09$ to demonstrate the large $\mathfrak{w}$ and $\mathfrak{q}$ scaling. Note that we avoid $\mathfrak{q}=0$: in that case the symmetry is enhanced and so the master fields are different, as discussed in [75].

We have found the full retarded Green's functions for a non-trivial density matrix

in the boundary theory. To isolate the modification from the vacuum, *i.e.* the effect of adding the black hole to the bulk theory, one can subtract off the asymptotic behaviour found above. However, this comes at the price of introducing the square root branch cut shown above. The cut originates from the retarded Green's functions of the CFT dual to pure AdS_4, a fact which has been obscured somewhat by moving to master fields.

2.2.3 Spectral function

For a field theory in thermal equilibrium, the spectral function gives the number density of states in the ensemble with a particular $\mathfrak{w}$ and $\mathfrak{q}$. The spectral function is defined up to normalisation by

$$\chi_{ij}(\mathfrak{w},\mathfrak{q}) \equiv i\left[G^R_{\mathcal{O}_i\mathcal{O}_j}(\mathfrak{w},\mathfrak{q}) - G^R_{\mathcal{O}_i\mathcal{O}_j}(\mathfrak{w},\mathfrak{q})^\dagger\right] \tag{2.25}$$

for real $\mathfrak{w}$, where $G^R_{\mathcal{O}_i\mathcal{O}_j}$ is the appropriate retarded Green's function.

The features on the $\mathrm{Re}\,\mathfrak{w}$ axis can be explained by studying the general form (2.23). Making use of the symmetry (2.22) we consider a straightforward re-writing of this expression, with dependence on $\mathfrak{q}$ and T/μ suppressed:

$$\Pi_\pm(\mathfrak{w}) = \sum_i \left[\frac{a_i + ib_i}{\mathfrak{w} - |\sigma_i| + i\Gamma_i} - \frac{a_i - ib_i}{\mathfrak{w} + |\sigma_i| + i\Gamma_i}\right] + \sum_j \frac{ic_j}{\mathfrak{w} + i\Gamma_j} + \text{analytic}. \tag{2.26}$$

Here, i runs over one half of the off-axis poles and j runs over the on-axis poles. Taking real and imaginary parts of the above form we obtain

$$\mathrm{Re}\,\Pi_\pm = \sum_i \left[\frac{a_i\mathfrak{w} - (a_i|\sigma_i| - b_i\Gamma_i)}{(\mathfrak{w} - |\sigma_i|)^2 + \Gamma_i^2} - \frac{a_i\mathfrak{w} + (a_i|\sigma_i| - b_i\Gamma_i)}{(\mathfrak{w} + |\sigma_i|)^2 + \Gamma_i^2}\right] + \sum_j \frac{c_j\Gamma_j}{\mathfrak{w}^2 + \Gamma_j^2} \tag{2.27}$$

$$\mathrm{Im}\,\Pi_\pm = \sum_i \left[\frac{b_i\mathfrak{w} - (a_i\Gamma_i + b_i|\sigma_i|)}{(\mathfrak{w} - |\sigma_i|)^2 + \Gamma_i^2} + \frac{b_i\mathfrak{w} + (a_i\Gamma_i + b_i|\sigma_i|)}{(\mathfrak{w} + |\sigma_i|)^2 + \Gamma_i^2}\right] + \sum_j \frac{c_j\mathfrak{w}}{\mathfrak{w}^2 + \Gamma_j^2} \tag{2.28}$$

plus analytic pieces. In fig. 2.5 we have taken a slice of the $(\mathrm{Re}\,\mathfrak{w},\mathfrak{q})$ plane at $\mathfrak{q} = 10^{-6}$. The expressions above take their largest values whenever $\mathfrak{w} = 0$ or $\pm|\sigma_i|$, which is indeed what we find in fig. 2.5. In effect, the presence of poles lower down in the complex $\mathfrak{w}$ plane is 'projected' onto the retarded Green's functions at real $\mathfrak{w}$.

Note that in fig. 2.5 we have subtracted the large $\mathfrak{w}$ and $\mathfrak{q}$ behaviour discussed previously in order to reveal the peaks that occur away from $\mathfrak{w} = 0$. Our numerics confirm that the modified retarded Green's functions tend to zero as $\mathrm{Re}\,\mathfrak{w}$ increases. We

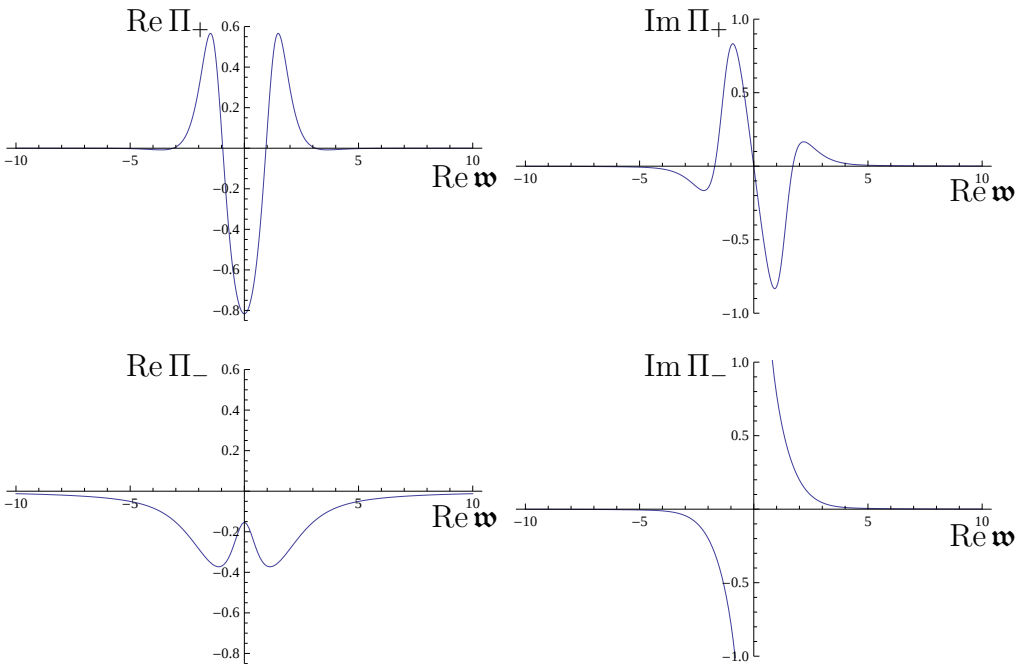

Fig. 2.5: Slices through the $(\mathrm{Re}\,\mathfrak{w}, \mathfrak{q})$ plane of Π_+ (top row) and Π_- (bottom row) at $\mathfrak{q} = 10^{-6}$ and $T/\mu = 0.09$. The left and right panels show the real and imaginary parts, respectively.

have chosen to subtract off the positive branch.

By considering $\mathfrak{q} \ll 1$ we are working in the long-wavelength regime. If instead we consider $\mathfrak{q} \gg 1$, for which the spatial perturbations are much smaller than the scales in the boundary theory, the poles on the $\mathrm{Im}\,\mathfrak{w}$ axis move much further down the complex $\mathfrak{w}$ plane and their effect on the spectral function will diminish.

2.2.4 Pole motion

As noted in [75], the lowest quasinormal frequency for Φ_- approaches zero as $\mathfrak{q} \to 0$. We found the same behaviour for the lowest pole in Π_-; as such, this can be identified as the hydrodynamic mode. The behaviour of the poles as $\mathfrak{q}$ and T/μ are varied is particularly rich; see also [136] for results in Schwarzschild-AdS$_4$.

The trajectories of the on-axis poles of Π_- at fixed T/μ are shown in fig. 2.6. As $\mathfrak{q}$ is increased, all these poles move down the $\mathrm{Im}\,\mathfrak{w}$ axis. The on-axis poles of Π_+ have very simple trajectories and so we focus on the behaviour of Π_-.

Firstly we note the apparent continuity of the white line that characterises the hydrodynamic pole. The physical implication of this behaviour is that in the hydrodynamic limit, where this is the only relevant pole, the dispersion relation of the quasi-particle

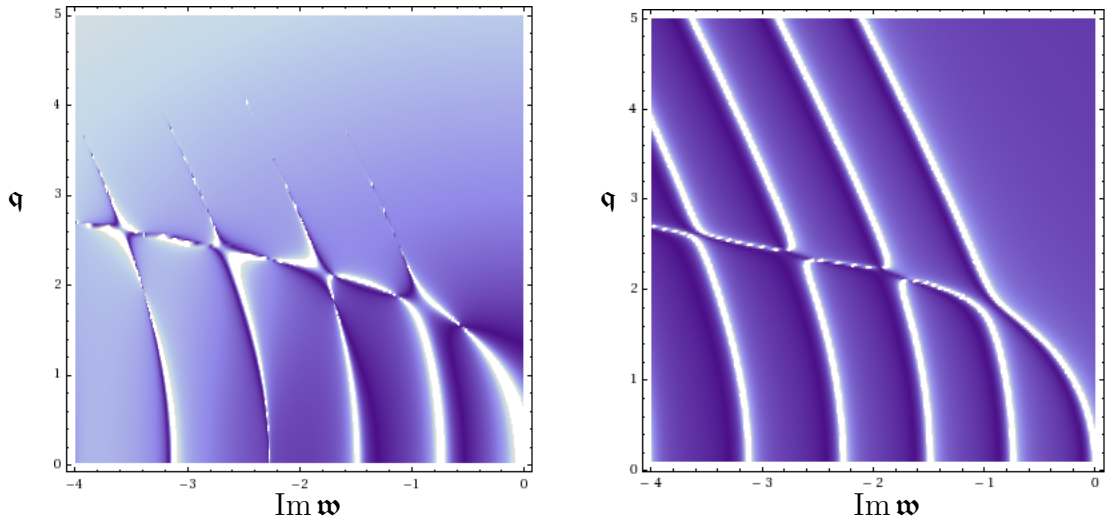

Fig. 2.6: Trajectories on the $(\mathrm{Im}\,\mathfrak{w}, \mathfrak{q})$ plane of the on-axis poles of Π_- (left) and the motion of the associated quasinormal frequencies (right). We fix $T/\mu = 0.09$ and consider $0.1 \leq \mathfrak{q} \leq 5$.

corresponding to this pole is a smooth function of $\mathfrak{q}$. This is given by

$$\mathfrak{w} = -i\mu D\,\mathfrak{q}^2 + O(\mathfrak{q}^4) \tag{2.29}$$

with diffusion constant D, discussed in the following section. In the left of fig. 2.6 we can see there are values of $\mathfrak{q}$ for which a given on-axis mode disappears, as indicated by a gap in the associated trajectory (for example at $\mathfrak{q} \approx 1.6$ and $\mathfrak{w} \approx -0.6i$). If (2.23) holds, then we must conclude that the residue vanishes at these $(\mathfrak{w}, \mathfrak{q})$. With this in mind we see that, for finely tuned $\mathfrak{q}$, it may be possible for a previously sub-leading pole to give the dominant contribution to Π_-. Note that whilst the quasinormal plots can show this continuity, full knowledge of the correlators is required to determine which pole dominates.[4]

Also, we observe that the trajectories of all on-axis poles become less pronounced as $\mathfrak{q}$ is increased, which indicates that the residues of the poles become smaller. Furthermore, there are no poles at small $|\mathfrak{w}|$ for sufficiently large $\mathfrak{q}$.

The 'interactions' between the poles of Π_- are quite intricate as T/μ and $\mathfrak{q}$ are varied. These features are best displayed in animations, but we give a brief summary here.[5] We observe two types of behaviour: 'repulsion' and 'clover-leaf crossing'. Suppose we fix

[4] The issue of which pole gives the dominant response will recur in detail in the following chapter.

[5] Animations are available at http://www.maths.dur.ac.uk/~rcqn58/research.html. These show the motion of the quasinormal frequencies for Φ_-. We observe the same behaviour for Π_- and as such it is not an artefact of using a matrix of finite size in the determinant method. These animations also show the behaviour of the off-axis poles, which remains to be understood.

T/μ and increase $\mathfrak{q}$. All poles on the $\mathrm{Im}\,\mathfrak{w}$ axis move downwards but the hydrodynamic pole moves down further for the same change in $\mathfrak{q}$, as shown in fig. 2.6. It slows down as it approaches the next pole and the latter speeds up but the two never touch, just as for two like magnetic poles being brought together. As this second pole approaches the third, the two coalesce into a single object, split and move off-axis, coalesce a second time then split and move on-axis in a clover-leaf pattern.

Now suppose we fix $\mathfrak{q}$ at some larger value and increase T/μ. Again, all the poles move downwards as T/μ is increased, except there is always one pole which moves upwards. An example of this is shown in fig. 2.7 and a sample crossing is depicted in fig. 2.8. We also see several repulsions, so it appears that a different pole moves upwards each time.

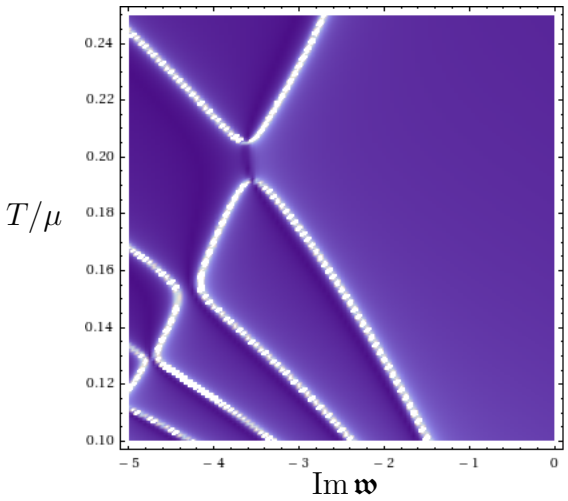

Fig. 2.7: Trajectories on the $(\mathrm{Im}\,\mathfrak{w}, T/\mu)$ plane of the on-axis quasinormal frequencies of Φ_-. We fix $\mathfrak{q} = 3$ and consider $0.1 \leq T/\mu \leq 0.25$.

We have so far not been able to tag the poles in a clover-leaf crossing and track their motion independently. The fact that the poles coalesce follows from the symmetry (2.22): the poles must be symmetric about the $\mathrm{Im}\,\mathfrak{w}$ axis, so they cannot move round each other but must cross. However, we do not know if this forms a sum of simple poles or a double pole. If the latter occurs then (2.23) must be modified, so it would be interesting to map the behaviour of Π_-, or even just the hydrodynamic pole, over a larger region of $(\mathfrak{q}, T/\mu)$ space.[6]

From the gravity perspective, we have shown that certain quasinormal modes switch from purely decaying to partially oscillatory behaviour as the parameters are varied. For example, for the central plot of fig. 2.8 there exist two modes degenerate in energy which move in opposite directions. Now, those modes closest to the $\mathrm{Re}\,\mathfrak{w}$ axis dominate the

[6] See also [137] for a discussion of similar behaviour in Schwarzschild-AdS$_4$.

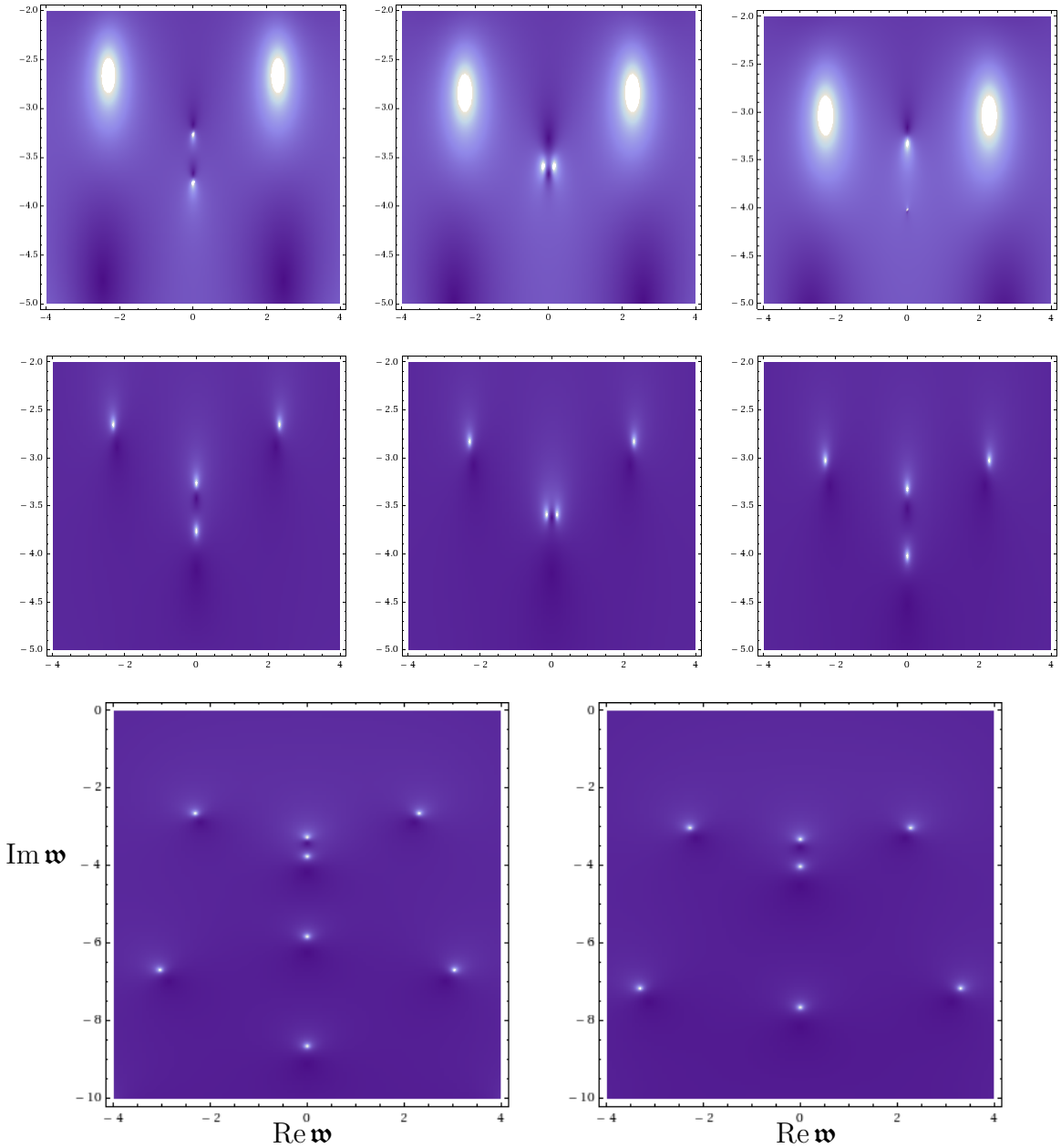

Fig. 2.8: Density plots of $|\Pi_-|$ on the complex $\mathfrak{w}$ plane at fixed $\mathfrak{q} = 3$ are shown in the upper row. The values of T/μ are (from left to right) 0.185, 0.2 and 0.215. These plots have been cropped to include only the poles which move off-axis and the leading poles. For comparison, the quasinormal frequencies at the same values of parameters are given in the second row. The final row contains two quasinormal frequency plots, one at $T/\mu = 0.185$ and one at $T/\mu = 0.215$. These show a larger region of the complex $\mathfrak{w}$ plane, including the origin, for orientation.

late-time response of the black hole. By studying this crossover we are exploring the intermediate response for perturbations of various $\mathfrak{q}$ of black holes with different T/μ. From the field theory perspective, the dispersion relation for the excitations associated with these poles develops a real part at this crossover.

2.3 Hydrodynamics

In this section we show that we recover the correct hydrodynamics if we take the appropriate limit of our numerical results. We begin by presenting the analytical expressions for $\Pi_\pm$ to leading order in $\mathfrak{w}$ and $\mathfrak{q}^2$, which we derive in appendix 2.C:

$$\Pi_+ = -\frac{4Q^2}{3(1+Q^2)} + i\mathfrak{w}\frac{Q\left(3-Q^2\right)^2}{9\left(1+Q^2\right)^2} - \mathfrak{q}^2\frac{Q^2\left(27+63Q^2+29Q^4+9Q^6\right)}{27\left(1+Q^2\right)^3} + O(\mathfrak{w}^2,\mathfrak{w}\mathfrak{q}^2) \tag{2.30}$$

$$\Pi_- = \frac{1+i\mathfrak{w}\frac{\mu}{4\pi T}d_1+\mathfrak{q}^2Q^2d_2}{-i\mathfrak{w}Q+\mathfrak{q}^2\frac{Q^2}{3(1+Q^2)}} + O(\mathfrak{w}^2,\mathfrak{w}\mathfrak{q}^2), \tag{2.31}$$

where $d_{1,2}$ are constants. Note that there can be no odd powers of $\mathfrak{q}$ due to parity.

In section 2.2.4 we identified the lowest pole of Π_- as belonging to the hydrodynamic mode. The location of the pole gives the dispersion relation for this mode. Fluctuations transverse to the direction of momentum flow, as in the shear channel we are studying, excite diffusive modes. As such, these have a dispersion relation of the form (2.29). This is indeed what we find in (2.31) if we identify

$$D = \frac{\ell^2}{3(1+Q^2)r_+}. \tag{2.32}$$

Before comparing with our numerics, we first perform a consistency check on these results. In a hydrodynamic system, we expect the following relation to hold for energy-momentum transport:

$$D = \frac{\eta}{\varepsilon+P}, \tag{2.33}$$

where η, ε, P are respectively the shear viscosity, energy density and pressure of the system. Our theory is conformal and so tracelessness of the energy-momentum tensor implies $\varepsilon = 2P$. The shear viscosity can be extracted from the Kubo formula

$$\eta = -\lim_{\omega\to 0}\frac{1}{\omega}\operatorname{Im}G^R_{xy,xy}(\omega,0). \tag{2.34}$$

Combining (2.13), (2.15), (2.21b) and (2.31) we obtain

$$\eta = \frac{1}{16\pi G_4}\left(\frac{r_+}{\ell}\right)^2. \tag{2.35}$$

To find the pressure we need to evaluate the Euclidean action $S_E = -iS$ on the background (2.2) in Euclidean time $\tau = it$ with $\tau \sim \tau + 1/T$:

$$S_E = -\frac{(1+Q^2)}{16\pi G_4}\frac{r_+^3}{\ell^4}\frac{V_2}{T} \tag{2.36}$$

where V_2 is the (divergent) spatial volume of the dual theory. Assuming our black hole is the dominant saddle of the bulk partition function Z and identifying the latter with the partition function of the dual theory, we can express the thermodynamic potential Ω of the grand canonical ensemble as

$$\Omega = -T\log Z = TS_E. \tag{2.37}$$

Finally, the pressure is found to be

$$P = -\frac{\Omega}{V_2} = \frac{(1+Q^2)}{16\pi G_4}\frac{r_+^3}{\ell^4}. \tag{2.38}$$

Combining this result with (2.35) and (2.32) we recover (2.33), as required.

A further consistency check makes use of the entropy density s of our black hole, given by

$$s = \frac{1}{4G_4}\left(\frac{r_+}{\ell}\right)^2. \tag{2.39}$$

This can be computed by taking the appropriate derivative of Ω or by applying the Bekenstein-Hawking formula directly. We thus obtain

$$\frac{\eta}{s} = \frac{1}{4\pi}, \tag{2.40}$$

as expected on general grounds for a theory dual to a two-derivative gravity theory with unbroken rotational symmetry [121, 122].

Note that this D can only be interpreted as the diffusion constant in the regime where hydrodynamics gives an effective description of the dynamics, *i.e.* for $T \gg \mu$. Outside this regime, we expect a different effective theory to be valid. In particular, we should not trust (2.32) for $T \ll \mu$: either the dispersion relation needs modifying, or the other poles in Π_- cannot be ignored, or both.

We can calculate the diffusion constant numerically by fitting the location of the lowest quasinormal frequency of Π_- to the form (2.29). Our numerical results agree with the analytical result in (2.32) for $T \gg \mu$, as shown in fig. 2.9. To reiterate: to calculate D we only need knowledge of the *lowest* quasinormal frequency and not our more complete numerical results for the correlators.

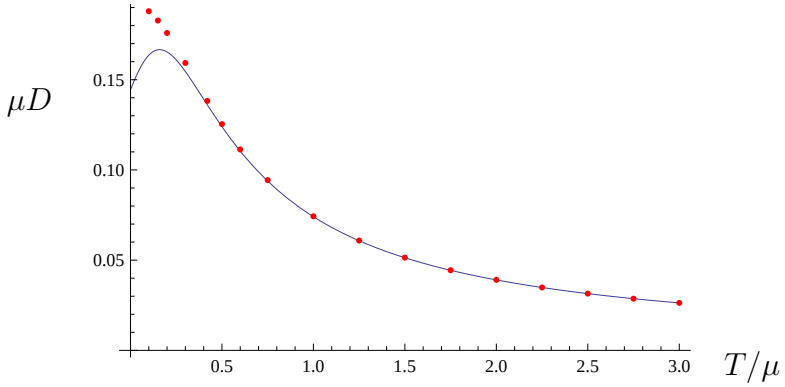

Fig. 2.9: Plot of μD as a function of T/μ. The solid curve is the analytical result from (2.32) and the points were extracted from the motion of the lowest quasinormal frequency.

Now we show how this agreement breaks down beyond the hydrodynamic regime, and as such our results are essential. In fig. 2.10 we get the correct contact term for Π_+ as in (2.30) and the results are in good agreement over a small range in $\mathfrak{w}$, but they soon deviate. The agreement persists over a larger range of $\mathfrak{w}$ if we work at a larger value of T/μ.[7]

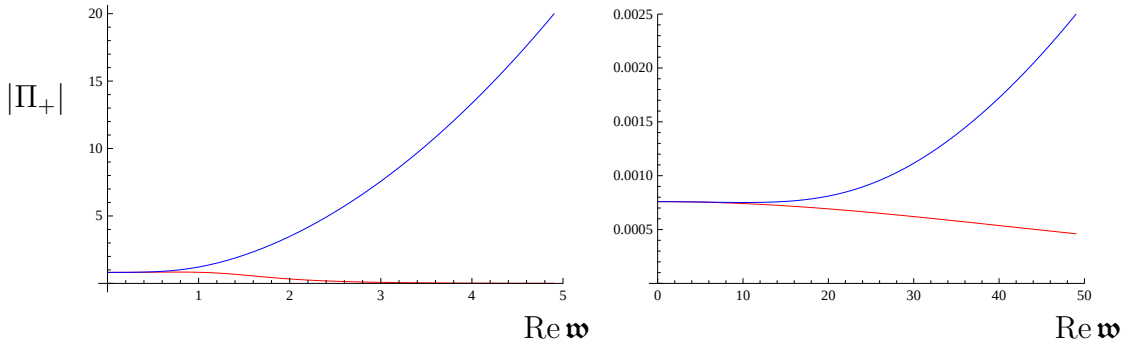

Fig. 2.10: A comparison between numerical (red) and analytical (blue) results for $|\Pi_+|$. The left plot is at $T/\mu = 0.09$, the right plot is at $T/\mu = 10$, and both have $\mathfrak{q} = 10^{-6}$. Note that we have subtracted off the large $\mathfrak{w}$ behaviour from all results, as discussed in section 2.2.2.

[7] We used numerical integration to obtain the $O(\mathfrak{w}^2)$ correction to (2.30).

2.A Retarded Green's functions in position space

In this appendix we derive the position space representation of the general form for $\Pi_\pm$ given in (2.23). First, consider the simpler function

$$\Pi_\pm(\mathfrak{w},\mathfrak{q}) = \frac{R(\mathfrak{q})}{\mathfrak{w} - \sigma(\mathfrak{q}) + i\Gamma(\mathfrak{q})}, \tag{2.41}$$

where we have suppressed the dependence on T/μ for clarity. Fourier transforming with respect to ω and k we find

$$\begin{aligned}\Pi_\pm(\Delta t,\Delta x) &= \mu\int\frac{d\omega dk}{(2\pi)^2}\,\frac{R(\mathfrak{q})}{\omega-\mu\sigma(\mathfrak{q})+i\mu\Gamma(\mathfrak{q})}\,e^{-i\omega\Delta t+ik\Delta x}\\ &= \mu\int\frac{da dk}{(2\pi)^2}\,\frac{R(\mathfrak{q})}{a}\,e^{-i(a+\mu\sigma(\mathfrak{q})-i\mu\Gamma(\mathfrak{q}))\Delta t+ik\Delta x}\\ &= \mu\int\frac{dk}{2\pi}\,R(\mathfrak{q})\,e^{-i(\mu\sigma(\mathfrak{q})-i\mu\Gamma(\mathfrak{q}))\Delta t+ik\Delta x}\int\frac{da}{2\pi}\,\frac{1}{a}\,e^{-ia\Delta t}.\end{aligned} \tag{2.42}$$

where $\Delta t = t - t'$ and $\Delta x = x - x'$. The integral over a yields the integral representation of the step function, as follows:

$$\lim_{\epsilon\to 0}\int\frac{da}{2\pi}\,\frac{1}{a+i\epsilon}\,e^{-ia\Delta t} = -i\theta(\Delta t). \tag{2.43}$$

Thus,

$$\Pi_\pm(\Delta t,\Delta x) = -i\mu\theta(\Delta t)\int\frac{dk}{(2\pi)}\,R(\mathfrak{q})\,e^{-\mu\Gamma(\mathfrak{q})\Delta t}e^{-i\mu\sigma(\mathfrak{q})\Delta t+ik\Delta x}. \tag{2.44}$$

The retarded Green's function of (2.23) is a sum over poles. We apply the above procedure to each term in that sum to obtain

$$\Pi_\pm(\Delta t,\Delta x) = -i\mu\theta(\Delta t)\int\frac{dk}{2\pi}\sum_i\left[R_i(\mathfrak{q})\,e^{-\mu\Gamma_i(\mathfrak{q})(t-t')}e^{-i\mu\sigma_i(\mathfrak{q})\Delta t}\right]e^{ik\Delta x}. \tag{2.45}$$

It is clear from this result that the contribution of each pole to $\Pi_\pm$ is characterised by the quantity $R_i(\mathfrak{q})\,e^{-\mu\Gamma_i(\mathfrak{q})(t-t')}$, as claimed in section 2.2.1.

2.B Numerical method

In this appendix we give details of the method used to numerically extract the retarded Green's functions for $\Phi_\pm$. We also note briefly a numerical issue that typically occurs in

such calculations, originating from the initial condition on the integration, as well as our strategy to overcome it.

To aid numerical work, it is convenient to introduce the bounded dimensionless coordinate $z = 1/u$. In this coordinate the AdS_4 boundary is at $z = 0$ and the black hole horizon is at $z = 1$. The master fields $\Phi_\pm$ satisfy

$$z^2 f(f\,\Phi_\pm')' + \left[-zff' + Q^2 z^2(\mathfrak{w}^2 - \mathfrak{q}^2 f) - 2Q^2 s_\pm(\mathfrak{q}) z^3 f\right]\Phi_\pm = 0, \tag{2.46}$$

where a prime denotes differentiation with respect to z. We must first solve this second-order, linear ODE numerically, subject to ingoing boundary conditions at the horizon. The latter is a regular singular point of the equation. We choose the following ansatz, where Φ denotes one of the $\Phi_\pm$:

$$\Phi(z) = (z-1)^{-i\mathfrak{w}\mu/4\pi T}\phi(z). \tag{2.47}$$

The first factor imposes the ingoing boundary condition at $z = 1$. A unique solution is then specified by $\phi(1)$, which we are free to choose because the equation is linear. We expand ϕ about $z = 1$ up to some order, $n_{\max}$, to generate the initial condition for a Runge-Kutta algorithm at some $z = 1 - \epsilon$. We then integrate out to the AdS_4 boundary and match this numerical solution to the small z expansion of $\Phi_\pm(z)$ near $z = 0$, given by

$$\Phi_\pm = \Phi_{\pm(0)}\left(1 + \Pi_\pm z + \ldots\right). \tag{2.48}$$

We extract $\Pi_\pm(\mathfrak{w}, \mathfrak{q})$ from this matching using a root-finding method. As described in detail in section 2.1, the matrix of retarded Green's functions in the shear channel can be built from these functions.

Naively, we would like to choose a small ϵ so that the series expansion of ϕ is accurate with only a few terms. However, we found that the pattern of poles was completely washed out below a certain line in the complex $\mathfrak{w}$ plane. This numerical instability appears if ϵ is small for $\mathrm{Im}\,\mathfrak{w}$ large and negative (and/or for T/μ small). To see why, note that the ansatz (2.47) for Φ at $z = 1 - \epsilon$ contains the factor

$$\epsilon^{-i\mathfrak{w}\mu/4\pi T}.$$

This factor becomes very large in these regimes if ϵ is small, leading to round-off errors.

Thus, a larger ϵ must be chosen in these regimes. As a consequence, a sufficiently large $n_{\max}$ must be chosen to offset the error from starting the integration further from

$z = 1$.[8] The values of $\epsilon, n_{\max}$ can be constrained by ensuring that the locations of the poles match the quasinormal spectrum for the appropriate bulk fluctuations, as stated in section 2.2.

2.C Correlators in the hydrodynamic limit

In this appendix we compute $\Pi_\pm$ to leading order in $\mathfrak{w}$ and $\mathfrak{q}^2$ in the spirit of [78]. We follow the strategy of [139] closely.

Firstly, we consider the following field redefinition, where Φ denotes one of the $\Phi_\pm$:

$$\Phi(z) = (z-1)^{-i\mathfrak{w}\mu/4\pi T} F(z) G(z). \tag{2.49}$$

The aim is to choose G such that F tends to an $\mathfrak{w}$- and $\mathfrak{q}$-independent constant, F_0, in the hydrodynamic limit $\mathfrak{w}, \mathfrak{q} \to 0$. This choice greatly simplifies the subsequent analysis, as we will soon show, and (2.46) leads to the equation

$$zfG'' + zf'G' - (f' + 2Q^2 s_\pm(0) z^2) G = 0, \tag{2.50}$$

which has solutions of the form

$$G(z) = a(z+b), \quad \text{where} \quad b = \begin{cases} -\frac{3}{4}\left(1 + \frac{1}{Q^2}\right) & \text{for } \Phi_+, \\ 0 & \text{for } \Phi_-. \end{cases} \tag{2.51}$$

Here, a is a constant we can specify by a choice of FG at the horizon. The resulting equation for F is

$$F'' + \left(-\frac{2i\mathfrak{w}c}{z-1} + \frac{f'}{f} + \frac{2G'}{G}\right) F' + \left[-\frac{i\mathfrak{w}c}{z-1}\left(-\frac{i\mathfrak{w}c - 1}{z-1} + \frac{f'}{f} + \frac{2G'}{G}\right) + \frac{Q^2}{f^2}(\mathfrak{w}^2 - \mathfrak{q}^2 f) - 2Q^2 \hat{s}_\pm(\mathfrak{q}) \frac{z}{f}\right] F = 0, \tag{2.52}$$

where we have defined the following for brevity:

$$c \equiv \frac{\mu}{4\pi T} \quad \text{and} \quad \hat{s}_\pm(\mathfrak{q}) \equiv s_\pm(\mathfrak{q}) - s_\pm(0). \tag{2.53}$$

[8] The author would like to thank Patrick Kerner for discussions on this issue. See [138] for further evidence.

Now that we have defined G in this way, we can write F as a series in $\mathfrak{w}$ and $\mathfrak{q}^2$, *i.e.*

$$F(z) = F_0 + \mathfrak{w} F_1(z) + \mathfrak{q}^2 F_2(z) + O(\mathfrak{w}^2, \mathfrak{w}\mathfrak{q}^2), \tag{2.54}$$

then collect terms in (2.52) at each order. Before moving on to find F_1 and F_2, we note two points that guide the analysis. First, the ingoing boundary condition at $z = 1$ implies that F be regular there, and second, we only require the small z expansion of F in order to read off $\Pi_\pm$ (as described in appendix 2.B).

Collecting terms at $O(\mathfrak{w})$, the equation for F_1 is

$$F_1'' + \left(\frac{f'}{f} + \frac{2G'}{G}\right) F_1' - \frac{icF_0}{(z-1)}\left(-\frac{1}{z-1} + \frac{f'}{f} + \frac{2G'}{G}\right) = 0, \tag{2.55}$$

which can be integrated once to give

$$F_1' = icF_0\left(\frac{1}{z-1} + \frac{c_1 a^2}{fG^2}\right). \tag{2.56}$$

The constant c_1 is determined by demanding that the $O(z-1)^{-1}$ terms cancel, and is found to be

$$c_1 = \begin{cases} -\frac{(3-Q^2)^3}{16Q^4} & \text{for } \Phi_+, \\ (3-Q^2) & \text{for } \Phi_-. \end{cases} \tag{2.57}$$

The factor of a^2 has been extracted because F cannot depend on a.

Collecting terms at $O(\mathfrak{q}^2)$, the equation for F_2 is

$$F_2'' + \left(\frac{f'}{f} + \frac{2G'}{G}\right) F_2' - \frac{Q^2 F_0}{f}(1 + 2\hat{s}_\pm(1) z) = 0, \tag{2.58}$$

which can be integrated once to give

$$F_2' = \frac{Q^2 F_0}{f(z+b)^2}\left[c_2 + b\left(bz + z^2 + 2\hat{s}_\pm(1)\left(\frac{bz^2}{2} + \frac{2z^3}{3}\right)\right) + \frac{z^3}{3} + \frac{\hat{s}_\pm(1) z^4}{2}\right]. \tag{2.59}$$

The constant c_2 is determined by demanding that the $O(z-1)^{-1}$ terms cancel, and is found to be

$$c_2 = \begin{cases} -\frac{27+63Q^2+29Q^4+9Q^6}{48Q^4(1+Q^2)} & \text{for } \Phi_+, \\ -\frac{1}{3(1+Q^2)} & \text{for } \Phi_-. \end{cases} \tag{2.60}$$

To extract $\Pi_\pm$, we need only keep terms up to $O(z)$ in $\Phi_\pm$. Let's focus on Π_+ for

now. Expanding each factor to this order we obtain

$$\Phi_+ = (-1)^{-i\mathfrak{w}c}(1+i\mathfrak{w}cz)a\left[F_0+\mathfrak{w}(F_1(0)+F_1'(0)z)\right. \\ \left.+\mathfrak{q}^2(F_2(0)+F_2'(0)z)\right](z+b)+O(z^2,\mathfrak{w}^2,\mathfrak{w}\mathfrak{q}^2). \tag{2.61}$$

By comparison with (2.48) and substituting for b we obtain

$$\Pi_+ = -\frac{4Q^2}{3(1+Q^2)}+i\mathfrak{w}\left(\frac{Q}{3-Q^2}-\frac{iF_1'(0)}{F_0}\right)+\mathfrak{q}^2\frac{F_2'(0)}{F_0}+O(\mathfrak{w}^2,\mathfrak{w}\mathfrak{q}^2). \tag{2.62}$$

Substituting for $F_1'(0)$ and $F_2'(0)$ we obtain the final result

$$\Pi_+ = -\frac{4Q^2}{3(1+Q^2)}+i\mathfrak{w}\frac{Q\left(3-Q^2\right)^2}{9\left(1+Q^2\right)^2}-\mathfrak{q}^2\frac{Q^2\left(27+63Q^2+29Q^4+9Q^6\right)}{27\left(1+Q^2\right)^3} \\ +O(\mathfrak{w}^2,\mathfrak{w}\mathfrak{q}^2). \tag{2.63}$$

The case of Π_- is slightly different because the z-dependence of F_1 and F_2 is different. We find

$$F_1 = icF_0\left(\frac{Q^2-3}{z}+d_1\right)+O(z), \tag{2.64}$$

$$F_2 = Q^2F_0\left(\frac{1}{3(1+Q^2)z}+d_2\right)+O(z), \tag{2.65}$$

where $d_{1,2}$ are arbitrary integration constants. Using $b=0$ we obtain

$$\Phi_- = (-1)^{-i\mathfrak{w}c}aF_0\left[-i\mathfrak{w}c(3-Q^2)+\frac{\mathfrak{q}^2Q^2}{3(1+Q^2)}+(1+i\mathfrak{w}cd_1+\mathfrak{q}^2Q^2d_2)z\right] \\ +O(z^2,\mathfrak{w}^2,\mathfrak{w}\mathfrak{q}^2) \tag{2.66}$$

and thus

$$\Pi_- = \frac{1+i\mathfrak{w}cd_1+\mathfrak{q}^2Q^2d_2}{-i\mathfrak{w}c(3-Q^2)+\mathfrak{q}^2\frac{Q^2}{3(1+Q^2)}}+O(\mathfrak{w}^2,\mathfrak{w}\mathfrak{q}^2). \tag{2.67}$$

Chapter 3

Collective excitations of holographic quantum liquids in a magnetic field

In this chapter, based on [140], we explore the collective excitations of holographic quantum liquids arising on D3/D5 and D3/D7 brane intersections as a function of temperature and magnetic field in the probe limit. We compute the spectrum of poles of the charge density retarded Green's function and the associated peaks in the spectral function in the presence of a chemical potential much larger than all other dimensionful scales.

In the following section we introduce our holographic systems and review their thermodynamics at finite density. We then move on to discuss an appropriate method for organising our calculation of the retarded Green's function. We focus on the evolution of the collective excitations as we increase the frequency relative to the temperature, *i.e.* the collisionless/hydrodynamic crossover. In section 3.3 we discuss this crossover in our systems at zero magnetic field, which for the D3/D7 system is a review but for the D3/D5 system includes novel results, then we study in detail the effect of a magnetic field in section 3.4.

We find that for all magnetic fields studied, at low frequencies the tallest peak in the spectral function is associated with hydrodynamic charge diffusion. At high frequencies the tallest peak is associated with a sound mode similar to the zero sound mode in the collisionless regime of a Landau Fermi liquid (LFL). We find that the location of the crossover is approximately independent of the magnetic field. However, we show that the sound mode has a gap proportional to the magnetic field, and as a result the spectral weight is strongly suppressed for intermediate frequencies and for magnetic fields sufficiently large compared to the temperature.

3.1 Review of holographic quantum liquids

Our starting point is Type IIB string theory, in which we study the $(n{+}1)$-dimensional intersection of N_c D3-branes with N_f Dp-branes, with $p = 2n+1 = 5, 7$. After the initial conjecture of [82], the holographic dictionary for these systems was established in more detail in [83, 84, 85]. We will refer to these as the D3/Dp theories and summarise both in the following array:

	t	x	y	z	X^1	X^2	X^3	X^4	X^5	X^6
N_c D3	×	×	×	×						
N_f D5	×	×	×		×	×	×			
N_f D7	×	×	×	×	×	×	×	×		

(3.1)

where × indicates that the brane fills that direction. These systems have two equivalent low-energy descriptions: one in terms of open strings and the other in terms of closed strings. We will discuss each perspective in turn then focus on the compressible states found in these systems.

In each intersection the low-energy theory on the D3-brane worldvolume is (3+1)-dimensional $\mathcal{N} = 4$ supersymmetric Yang-Mills theory (SYM) with gauge group $SU(N_c)$, coupled to N_f $(n{+}1)$-dimensional massless flavour fields, *i.e.* hypermultiplets in the N_c representation of $SU(N_c)$.[1] The Yang-Mills coupling g_{YM} is related to the string coupling g_s via $g_{YM}^2 = 4\pi g_s$. In the $n = 2$ case the flavour fields propagate along a codimension-one defect, which we take to be the plane $z = 0$.

For later use we record the many symmetries enjoyed by these theories. To begin with, each theory has eight Poincaré supercharges. The $(n{+}1)$-dimensional flavour fields break the R-symmetry of $\mathcal{N} = 4$ SYM from $SO(6)$ to $SO(n+1) \times SO(5-n)$, corresponding to rotations in the transverse $(X^1, \ldots, X^{n+1})$ and $(X^{n+2}, \ldots, X^6)$ directions, respectively. In the $n = 2$ case the $SO(3) \times SO(3)$ is the R-symmetry of the remaining (2+1)-dimensional $\mathcal{N} = 4$ supersymmetry. In the $n = 3$ case an $SU(2) \times U(1)$ subgroup of $SO(4) \times U(1)$ is the R-symmetry of the remaining $\mathcal{N} = 2$ supersymmetry. The N_f hypermultiplets also possess a global $U(N_f)$ symmetry, and we identify the diagonal $U(1)_B$ subgroup as baryon number.

We take the 't Hooft limit of $N_c \to \infty$ and $g_{YM}^2 \to 0$ with the 't Hooft coupling $\lambda \equiv g_{YM}^2 N_c$ fixed, then follow this up with the large-coupling limit $\lambda \gg 1$. Furthermore,

[1] We have neglected the $U(1)$ part of the $U(N_c)$ gauge group. From the D-brane perspective, this $U(1)$ corresponds to the overall centre-of-mass motion of the entire stack of N_c D3-branes.

we will always work in the probe limit: we keep N_f fixed as $N_c \to \infty$, expand all observables in the small parameter N_f/N_c, and retain terms only up to order $N_f N_c$. (Generically the leading order term is N_c^2.) In other words, the full dynamics of the glue and its effect on the flavour is included, but the backreaction of the flavour on the glue is ignored.

We want to study thermal equilibrium states of these theories. From the closed string perspective, a thermal state of large-N_c, strongly-coupled $\mathcal{N} = 4$ SYM is given by the near-horizon limit of the non-extremal 3-brane solution of Type IIB supergravity: a Schwarzschild-AdS$_5$ black hole with planar horizon times an S^5 [26]. The metric can be written in the form

$$\begin{aligned} ds^2 &= g_{tt}(r)dt^2 + g_{xx}(r)\left(dx^2+dy^2+dz^2\right) + g_{rr}(r)dr^2 + \ell^2 d\Omega_5^2 \\ &= \frac{r^2}{\ell^2}\left(-f dt^2 + dx^2 + dy^2 + dz^2\right) + \frac{\ell^2}{r^2 f}\,dr^2 + \ell^2 d\Omega_5^2, \end{aligned} \tag{3.2}$$

where

$$f(r) = 1 - \frac{r_+^4}{r^4}. \tag{3.3}$$

The AdS$_5$ boundary is at $r \to \infty$ and ℓ is the curvature radius, fixed to be $\ell^4 = 4\pi g_s N_c \alpha'^2$, with α' the squared string length. The S^5 has round metric $d\Omega_5^2$ of unit radius and is threaded by N_c units of Ramond-Ramond (RR) five-form flux in the full supergravity solution. The black hole horizon is at $r = r_+$ and has temperature $T = r_+/\pi\ell^2$. We identify T as the temperature of the dual field theory state. Starting now, we use units in which $\ell \equiv 1$; in these units we can convert between supergravity and field theory quantities using $\alpha' = 1/\sqrt{\lambda}$.

The massless flavour fields are dual to Dp-branes in this background. We choose to embed them along the AdS$_{n+2} \times S^n$ inside the Schwarzschild-AdS$_5 \times S^5$, where the AdS$_{n+2}$ is spanned by (t, x, y, r) and for $n = 3$ also z, and the $S^n \in S^5$. The S^5 has an $SO(6)$ isometry, dual to the $SO(6)$ R-symmetry of $\mathcal{N} = 4$ SYM. The Dp-brane breaks this to $SO(n+1) \times SO(5-n)$, dual to the corresponding global symmetries in the field theory. The $SO(n+1)$ factor is the isometry of the S^n.

The backreaction of the Dp-branes is controlled by $g_s N_f$. Recall that we have taken the 't Hooft limit, so if N_f remains finite we have $g_s N_f \to 0$ and may therefore safely ignore the branes' effect on the metric. In other words, the branes can be treated as probes in the limit $N_f \ll N_c$.

The non-Abelian Dp-brane action is not known in full generality. However in what

follows we will only need the Abelian Dp-brane action, which consists of two types of term: a Dirac-Born-Infeld (DBI) term and Wess-Zumino (WZ) terms describing the coupling to background RR fields. The DBI term is given by

$$S_{\mathrm{D}p} = -N_f T_{\mathrm{D}p} \int d^{p+1}\xi \sqrt{-\det\left(\gamma_{ab} + F_{ab}\right)}, \tag{3.4}$$

where $T_{\mathrm{D}p} = (2\pi)^{-p} g_s^{-1} \alpha'^{-(p+1)/2}$ is the Dp-brane tension, ξ^a with $a, b = 0, 1, \ldots, p$ are the Dp-brane worldvolume coordinates, γ_{ab} is the induced metric on the Dp-brane and F_{ab} is the field strength of the $U(1)$ gauge field A_a on the Dp-brane.[2]

The (9–p) scalars propagating on the worldvolume of the Dp-brane, which describe the embedding of the Dp-brane in the background (3.2), enter $S_{\mathrm{D}p}$ via the induced metric γ_{ab}. In our cases, of the (9–p) scalars, the $5-n$ describing the position of the Dp-brane on the S^5 form a vector of $SO(5-n)$, one of which is holographically dual to the supersymmetric mass operator $\mathcal{O}_m$. We will always work with trivial worldvolume scalars,[3] and as a gauge choice we will identify the worldvolume coordinates with the background coordinates along the $\mathrm{AdS}_{n+2} \times S^n$ spanned by the Dp-brane. In that case, γ_{ab} coincides with the background metric in the $\mathrm{AdS}_{n+2} \times S^n$ subspace. Note that once we restrict to the fluctuations we are interested in about this trivial embedding, the WZ terms give no contribution to the equations of motion and so we omit their explicit forms.

The $U(N_f)$ flavour symmetry appears in the supergravity description as the $U(N_f)$ worldvolume gauge invariance of the N_f Dp-branes. The $U(1)_B$ current J^μ is dual to the $U(1)$ worldvolume gauge field A_a. We want to study states with non-zero change density $\langle J^t \rangle$ and magnetic field B. We will demand that these states preserve various symmetries: time translations, n-dimensional spatial translations, $SO(n+1) \times SO(5-n)$, and the reflection symmetry $z \to -z$. To describe non-zero $\langle J^t \rangle$ and preserve these symmetries, we introduce $A_t(r)$. Employing $A_r = 0$ gauge, we thus have a worldvolume electric flux $F_{rt}(r) = A_t'(r)$, where prime denotes ∂_r. To describe non-zero B and preserve these symmetries, we introduce the magnetic flux $F_{xy} = B$, which must be constant to satisfy the Bianchi identity. With these fluxes and with trivial worldvolume scalars, the Dp-brane action reduces to

$$S_{\mathrm{D}p} = -\mathcal{N}_p V_{\mathbb{R}^{n,1}} \int dr\, g_{xx}^{(n-2)/2} \sqrt{(g_{xx}^2 + B^2)\left(g_{rr}|g_{tt}| - A_t'^2\right)}, \tag{3.5}$$

[2] Notice that with respect to the usual conventions (such as those of [141]) we have absorbed a factor of $(2\pi\alpha')$ into the field strength.

[3] The one and only place where we discuss solutions with non-trivial worldvolume scalars is at the end of this section, when we briefly review the solutions of [62, 63, 64, 65].

where $\mathcal{N}_p \equiv N_f T_{\mathrm{D}p} V_{S^n}$, with V_{S^n} the volume of a unit-radius S^n. Explicitly,

$$\mathcal{N}_p \equiv N_f T_{\mathrm{D}p} V_{S^n} = \begin{cases} \frac{4\sqrt{\lambda}}{(2\pi)^3} N_f N_c, & p = 5, \\ \frac{\lambda}{(2\pi)^4} N_f N_c & p = 7, \end{cases} \tag{3.6}$$

where in the second equality we have converted to field theory quantities. In (3.5), $V_{\mathbb{R}^{n,1}}$ is the (divergent) volume of $\mathbb{R}^{n,1}$. Starting now, we will divide both sides of (3.5) by $V_{\mathbb{R}^{n,1}}$, and in an abuse of notation we will use $S_{\mathrm{D}p}$ to denote the resulting action density, $S_{\mathrm{D}p}/V_{\mathbb{R}^{n,1}} \to S_{\mathrm{D}p}$, which we will henceforth refer to as the Dp-brane action.

Since $S_{\mathrm{D}p}$ depends only on the derivative of $A_t(r)$, we obtain a constant of integration, $\frac{\delta S_{\mathrm{D}p}}{\delta A_t'}$, which as shown in [86, 88] determines the charge density in the field theory:

$$\langle J^t \rangle = (2\pi\alpha') \frac{\delta S_{\mathrm{D}p}}{\delta A_t'} = \mathcal{N}_p \, g_{xx}^{(n-2)/2} \sqrt{g_{xx}^2 + B^2} \frac{(2\pi\alpha') A_t'}{\sqrt{g_{rr}|g_{tt}| - A_t'^2}}. \tag{3.7}$$

Solving for A_t', we find

$$A_t'(r) = \frac{\rho \sqrt{g_{rr}|g_{tt}|}}{\sqrt{g_{xx}^{n-2}\left(g_{xx}^2 + B^2\right) + \rho^2}}, \tag{3.8}$$

where

$$\rho \equiv \frac{\langle J^t \rangle}{(2\pi\alpha')\mathcal{N}_p}. \tag{3.9}$$

We will use 'charge density' to refer to either $\langle J^t \rangle$ or ρ.

We will now review various properties that characterise the compressible states described by the solution in (3.8), as determined from holographic calculations. We begin with low but non-zero temperatures, $T \ll \rho^{1/n}$, and with $B = 0$. In this regime, in these compressible states neither n-dimensional translations nor $U(1)_B$ are broken. In the canonical ensemble, the chemical potential is [89]

$$\mu(T, \rho) = \frac{\Gamma\left(\frac{1}{2} - \frac{1}{2n}\right)\Gamma\left(1 + \frac{1}{2n}\right)}{\Gamma(1/2)} \rho^{1/n} - (\pi T)\left[1 + O\left(T^{2n}/\rho^2\right)\right]. \tag{3.10}$$

From (3.10), we see that when $T = 0$ the density $\rho^{1/n} \propto \mu$, so the density varies smoothly as a function of μ, *i.e.* these states are indeed compressible, and a large density implies a large chemical potential. For convenience, we will denote the value of the chemical potential at $T = 0$ as μ_0:

$$\mu_0 \equiv \frac{\Gamma\left(\frac{1}{2} - \frac{1}{2n}\right)\Gamma\left(1 + \frac{1}{2n}\right)}{\Gamma(1/2)} \rho^{1/n}. \tag{3.11}$$

At low temperatures, the leading density-dependent contribution to the heat capacity is $c_V \propto T^{2n}/\rho$ [89], which is markedly different from that of an LFL, where $c_V \propto T$, or a gas of free bosons, where $c_V \propto T^n$, while the leading contribution to the $U(1)_B$ resistivity is $\mathscr{R} \propto T^2$ [142], the same as in an LFL.

Next we consider $T = 0$, still with $B = 0$. The system actually has a non-zero $T = 0$ entropy density $s \propto \langle J^t \rangle / \sqrt{\lambda}$ [89], indicating some degeneracy of states, in stark contrast to solids, superfluids and LFLs, which are all unique ground states. Degeneracy suggests instability, since generically any perturbation will break the degeneracy and drive the system to a new, presumably unique, ground state. These states are known to be thermodynamically stable, in the sense that they are at least local minima of the free energy [143]. As shown for the $n = 3$ case in [93], these states are also stable against dynamical (non-zero ω and k) fluctuations. To date, no Fermi surfaces have been detected in these states [63, 93, 144]. Remarkably, these states are in fact merely isolated points in an entire moduli space of compressible states parametrised by the expectation values of certain scalar operators, as discussed in detail in [96, 97]. The existence of the moduli space may be related to the non-zero $T = 0$ entropy density [97].

All of the above facts together indicate that these states are not solids, superfluids, LFLs or NFLs. Indeed, as proposed in [89], these states may be examples of some new kind(s) of compressible matter. Some evidence even suggests that the low-energy theory describing excitations about these states may be a (0+1)-dimensional CFT [64, 92, 93, 144].

Now we turn to the thermodynamics of these states at non-zero B. For the $n = 3$ case, a non-zero B explicitly breaks parity and charge conjugation symmetries, and breaks rotational symmetry from $SO(3)$ down to $SO(2)$. Moreover, with $T = 0$ and non-zero $\langle J^t \rangle$, a sufficiently large B triggers a quantum phase transition [62, 63]. When B is below a critical value, $B < B_c$, in the ground state $\langle J^t \rangle$ is non-zero but $\langle \mathcal{O}_m \rangle$ is zero. When $B > B_c$, the ground state changes such that $\langle J^t \rangle$ and $\langle \mathcal{O}_m \rangle$ are both nonzero. In the bulk, the worldvolume scalar dual to $\mathcal{O}_m$ becomes nontrivial when $B \geq B_c$. The non-zero $\langle \mathcal{O}_m \rangle$ signals spontaneous breaking of the $SU(2) \times U(1)$ symmetry down to $SU(2)$. The system thus exhibits a quantum phase transition. Notice that $U(1)_B$ is unbroken for all B. A numerical analysis indicates that the critical value of B is $B_c \approx 2.138\, \rho^{2/3}$ and that the transition is not first order, *i.e.* is at least second order [63]. At non-zero T, the quantum critical point gives rise to a quantum critical region [62, 63].

For the $n = 2$ case, a non-zero B breaks parity and charge conjugation symmetries. Here again, with $T = 0$ and non-zero $\langle J^t \rangle$, a sufficiently large B triggers a quantum

phase transition [64, 65]: for $B < B_c$ $\langle J^t \rangle$ is non-zero and $\langle \mathcal{O}_m \rangle = 0$, while for $B > B_c$ both $\langle J^t \rangle$ and $\langle \mathcal{O}_m \rangle$ are non-zero, and the non-zero $\langle \mathcal{O}_m \rangle$ spontaneously breaks the $SO(3) \times SO(3)$ symmetry down to $SO(3) \times U(1)$. In the bulk, the worldvolume scalar dual to $\mathcal{O}_m$ becomes nontrivial when $B \geq B_c$. The critical value of B is known exactly, $B_c = \rho/\sqrt{7}$, and the transition is of BKT-type: schematically, as B increases past B_c, $\langle \mathcal{O}_m \rangle \propto e^{-\sqrt{\rho/B_c - \rho/B}}$ [64]. At any non-zero T the transition becomes second order, and the quantum critical point gives rise to a quantum critical region [64, 65].

We hasten to add that we have only reviewed the *currently-known* phase diagrams of these systems. For given values of T, B, and ρ, other states may exist with lower free energy than any of the states mentioned above. Indeed, in the $n = 3$ case, when B is non-zero an instability has been detected at a single point in the grand canonical phase diagram, $(T, \mu) = (\frac{\sqrt{2}}{4\pi}\sqrt{B}, \sqrt{B})$ [145], where the known ground state has non-zero $\langle J^t \rangle$ and $\langle \mathcal{O}_m \rangle = 0$. The instability has non-zero k, suggesting the existence of an *inhomogeneous* state with lower free energy than the known ground state [145]. In what follows, we always work in regions of the phase diagram where the known ground state has non-zero $\langle J^t \rangle$ and $\langle \mathcal{O}_m \rangle = 0$. In bulk terms, we exclusively consider values of T, B and ρ for which the only known solutions for the Dp-brane worldvolume scalars are the trivial solutions.

3.2 Spectral functions from holography

In this section we detail our method for computing the current-current retarded Green's function $G^R_{\mu\nu}(\omega, k)$ holographically. As described in section 1.1.3, we need to introduce fluctuations of all the Dp-brane worldvolume fields, evaluate the bulk on-shell action to quadratic order in these fluctuations then read off the matrix of correlators as in (1.31).

The fluctuations, including all components of A_a and all (9–p) scalars, form representations of the symmetry preserved by the background solution. At the linearised level different representations cannot couple. In our case the background solution (3.8) preserves $SO(n+1) \times SO(5-n)$ and the reflection symmetry $z \to -z$. Under $SO(n+1)$, the components of A_a on the S^n are in the $n+1$ while all other fluctuations are singlets. Under $SO(5-n)$, the worldvolume scalars describing the position of the Dp-brane on the S^5 are in the $5-n$ and all other fluctuations are singlets. We are interested only in J^ν, which is a singlet under $SO(n+1) \times SO(5-n)$, and so is dual to a fluctuation of A_ν that is also a singlet, and thus has no dependence on the S^n directions and will not couple to fluctuations of A_a on the S^n or to the worldvolume scalars describing the

position of the Dp-brane on the S^5. In the $n = 2$ case, under the $z \to -z$ symmetry the fluctuation of the worldvolume scalar describing the position of the D5-brane in the z direction is clearly odd, and hence does not couple to the a_ν, which are even. We thus only need to consider the fluctuations a_ν of A_ν:

$$A_\nu(r, x^\mu) = A_t(r)\, \delta^t{}_\nu + Bx\, \delta^y{}_\nu + a_\nu(r, x^\mu). \tag{3.12}$$

On the right-hand-side of (3.12) the first two terms produce the electric and magnetic fluxes $F_{rt}(r)$ and $F_{xy} = B$ of the background solution. We will consider fluctuations a_ν that depend on r, t, and x only. The background solution preserves time translations and n-dimensional spatial translations, allowing us to perform the Fourier decomposition

$$a_\nu(r, t, x) = \int \frac{d\omega dk}{(2\pi)^2}\, a_\nu(r, \omega, k)\, e^{-i\omega t + ikx}. \tag{3.13}$$

To preserve $A_r = 0$ gauge, we take $a_r = 0$.

The background solution preserves $SO(2)$ rotational symmetry in the (x, y) plane. Under this $SO(2)$, a_t is a singlet while a_x and a_y together form a doublet. Our choice of momentum only in x breaks this $SO(2)$. In the D3/D5 system we make that choice with no loss of generality, but in the D3/D7 system we are restricting to a special subset of fluctuations with momentum perpendicular to the magnetic field. In the D3/D7 system, our choice of momentum preserves the $z \to -z$ symmetry, under which a_z is odd and hence will not couple to a_t, a_x, or a_y, which are even. When $B = 0$, with our choice of momentum a_t and a_x can couple to one another, but parity forbids these from coupling to a_y. When B is non-zero and parity is broken, all three fluctuations may couple to one another, and indeed do, as we will see shortly.

If different components of a_ν in the bulk couple, then the dual operators will mix, and in particular the poles in different components of $G^R_{\mu\nu}(\omega, k)$ will mix. These poles will be shared by all the components of $G^R_{\mu\nu}(\omega, k)$ that mix, but the spectral functions can still be different since the *residues* of the poles may be different for each component.

First we need the quadratic action of the fluctuations, $S_{(2)}$, and the resulting equations of motion. The equation for a_r in the $a_r = 0$ gauge is a constraint on the other fluctuations:

$$\omega\, a_t' + u(r)^2 k\, a_x' = 0, \tag{3.14}$$

where we define

$$u(r)^2 \equiv \frac{|g_{tt}| g_{rr} - A_t'^2}{\frac{g_{rr}}{g_{xx}}\,(g_{xx}^2 + B^2)} = \frac{|g_{tt}| g_{xx}^{n-1}}{g_{xx}^{n-2}\,(g_{xx}^2 + B^2) + \rho^2} \tag{3.15}$$

and a prime denotes ∂_r. With our choice of momentum, the gauge-invariant fluctuations are a_y itself and also the electric field (in Fourier space) [80]

$$E(r,\omega,k) \equiv k\, a_t(r,\omega,k) + \omega\, a_x(r,\omega,k). \tag{3.16}$$

In terms of these gauge-invariant fluctuations, using (3.14) and performing an integration-by-parts, we can write $S_{(2)}$ as

$$\begin{aligned} S_{(2)} = \frac{\mathcal{N}_p}{2}\int dr \frac{d\omega dk}{(2\pi)^2}\frac{|g_{tt}|g_{xx}^{(n+1)/2}}{u(r)g_{rr}^{1/2}\left(g_{xx}^2+B^2\right)}\times \\ \left[\frac{1}{\omega^2-u(r)^2k^2}|E'|^2 - \frac{g_{rr}}{|g_{tt}|}|E|^2 - |a_y'|^2 + \frac{g_{rr}}{|g_{tt}|}\left(\omega^2-u(r)^2k^2\right)|a_y|^2\right. \\ \left. +iB\frac{u(r)g_{rr}^{1/2}\left(g_{xx}^2+B^2\right)}{|g_{tt}|g_{xx}^{(n+1)/2}}\partial_r\left(\frac{g_{xx}^{(n-1)/2}g_{rr}^{-1/2}A_t'}{u(r)\left(g_{xx}^2+B^2\right)}\right)\left(E\,a_y^* + a_y\,E^*\right)\right], \end{aligned} \tag{3.17}$$

where E^* and a_y^* denote complex conjugates. For the D7-brane, in (3.17) we have omitted a boundary term produced by the integration-by-parts since this boundary term vanishes on-shell. The equations of motion that follow from $S_{(2)}$ are

$$\begin{aligned} &E'' + \left[\partial_r \log\left(\frac{g_{xx}^{(n+1)/2}|g_{tt}|g_{rr}^{-1/2}}{\left(\omega^2-u(r)^2k^2\right)u(r)\left(g_{xx}^2+B^2\right)}\right)\right]E' + \frac{g_{rr}}{|g_{tt}|}\left(\omega^2-u(r)^2k^2\right)E \\ &\quad = +iB\left[\frac{u(r)\left(g_{xx}^2+B^2\right)g_{rr}^{1/2}}{|g_{tt}|g_{xx}^{(n+1)/2}}\right]\left[\partial_r\left(\frac{g_{xx}^{(n-1)/2}g_{rr}^{-1/2}A_t'}{u(r)\left(g_{xx}^2+B^2\right)}\right)\right]\left(\omega^2-u(r)^2k^2\right)a_y, \end{aligned} \tag{3.18a}$$

$$\begin{aligned} &a_y'' + \left[\partial_r \log\left(\frac{g_{xx}^{(n+1)/2}|g_{tt}|g_{rr}^{-1/2}}{u(r)\left(g_{xx}^2+B^2\right)}\right)\right]a_y' + \frac{g_{rr}}{|g_{tt}|}\left(\omega^2-u(r)^2k^2\right)a_y \\ &\quad = -iB\left[\frac{u(r)\left(g_{xx}^2+B^2\right)g_{rr}^{1/2}}{|g_{tt}|g_{xx}^{(n+1)/2}}\right]\left[\partial_r\left(\frac{g_{xx}^{(n-1)/2}g_{rr}^{-1/2}A_t'}{u(r)\left(g_{xx}^2+B^2\right)}\right)\right]E. \end{aligned} \tag{3.18b}$$

When $B=0$, these reduce to the equations of motion in [89, 146, 94], and when B is non-zero, these agree with the equations of motion in [147, 148, 144]. Notice in particular that non-zero B leads to couplings between E and a_y, as advertised.

All of our results will follow from solutions of (3.18). These equations are second-order, hence for each field, E and a_y, we need two boundary conditions to specify a solution completely. At the future horizon, a solution for E or a_y looks like a linear combination of ingoing and outgoing waves, with some normalisations. To obtain the *retarded* Green's function, we require that the fields are purely ingoing. For each field,

the normalisation then provides us with a second boundary condition.

As emphasised in chapter 1, generically the on-shell action is divergent due to integration all the way to the AdS boundary. In our cases, the only near-boundary divergence that appears is $\propto F_{\mu\nu}F^{\mu\nu}\log r$ in the $S_{(2)}$ of the D7-brane, which we cancel with a counter-term [63].

Most of our results will be numerical. We will use the numerical method of [49] to extract the locations of poles in $G^R_{tt}(\omega,k)$ and the corresponding spectral function $\chi_{tt}(\omega,k)$, as we now briefly review. Let us define a vector of fields

$$\vec{V}(r,\omega,k) \equiv \begin{pmatrix} E(r,\omega,k) \\ a_y(r,\omega,k) \end{pmatrix}. \tag{3.19}$$

We need four boundary conditions to specify a solution for $\vec{V}$ completely. As stated above, at the future horizon we choose solutions to be purely ingoing waves. We next need to fix the normalisations of these ingoing waves. Explicitly, the vector of near-horizon normalisation factors, $\vec{V}_{\rm nh}$, is

$$\vec{V}_{\rm nh} \equiv \lim_{r\to r_+} \exp\left(i\omega \int dr \sqrt{g_{rr}/|g_{tt}|}\right) \vec{V}(r,\omega,k) \tag{3.20}$$

when T is non-zero.[4] Notice that $\vec{V}_{\rm nh}$ is constant, independent of r, ω and k. On the right-hand-side of (3.20), the exponential factor is designed to *cancel* the exponential factor that represents an ingoing wave at the future horizon.

In the method of [49], we first pick any convenient value of $\vec{V}_{\rm nh}$ and solve the equations, then we pick another $\vec{V}_{\rm nh}$, linearly independent of the first, and solve the equations, thus constructing a basis of solutions. We can then write any solution in that basis. For example, suppose we solve the equations twice, with two normalisations $\vec{V}^{(1)}_{\rm nh} = (1,0)^T$ and $\vec{V}^{(2)}_{\rm nh} = (0,1)^T$. Let the corresponding solutions be $\vec{V}^{(1)}$ and $\vec{V}^{(2)}$. Using these solutions, we define a 2×2 matrix $P(r,\omega,k)$ as

$$P(r,\omega,k) \equiv \left(\vec{V}^{(1)}(r,\omega,k), \vec{V}^{(2)}(r,\omega,k)\right), \tag{3.21}$$

allowing us to write any solution as

$$\vec{V}(r,\omega,k) = P(r,\omega,k)\,\vec{V}_{\rm nh} \tag{3.22}$$

[4] We use non-zero T in all of our numerical analysis. In what follows, we consider $T=0$ only in section 3.4.1, where we compute the dispersion relation of holographic zero sound at $T=0$. In that case the near-horizon behavior of $\vec{V}(r,\omega,k)$ is different from that at non-zero T: see (3.36).

for some choice of $\vec{V}_{\rm nh}$. This IR-normalised solution matrix P is linearly related to its UV-normalised counterpart via

$$F(r,\omega,k) = P(r,\omega,k)\lim_{r\to\infty} P(r,\omega,k)^{-1}. \tag{3.23}$$

Inserting a solution of this form into $S_{(2)}$ and using (1.31), we can thus extract retarded Green's functions in terms of P:

$$G^R(\omega,k) = -\mathcal{N}_p \lim_{r\to\infty} r^n \left[\begin{pmatrix} (-\omega^2+k^2)^{-1} & 0 \\ 0 & 1 \end{pmatrix} P'(r,\omega,k)P^{-1}(r,\omega,k) \right]. \tag{3.24}$$

We extract G^R_{tt} via

$$G^R_{tt}(\omega,k) = k^2 G^R_{EE}(\omega,k), \tag{3.25}$$

where G^R_{EE} is the upper-left component of the matrix in (3.24), and G^R_{yy} is the lower-right component. Any pole in G^R_{EE} not of the form $1/k^2$ will produce a pole in G^R_{tt}.

Generically, a pole will occur in G^R when $\lim_{r\to\infty} \det P^{-1}(r,\omega,k) \to \infty$, or equivalently when $\lim_{r\to\infty} \det P(r,\omega,k) = 0$, and so we only need to compute the latter in order to locate the poles in the retarded Green's functions. A pole in G^R corresponds to a quasinormal mode in the bulk, as highlighted in section 1.1.3; that is, a non-trivial solution for a gauge-invariant fluctuation that is ingoing at the horizon and vanishes at the AdS boundary. Explicitly, imposing this condition at the AdS boundary means

$$\lim_{r\to\infty} \vec{V}(r,\omega,k) = \lim_{r\to\infty} P(r,\omega,k)\vec{V}_{\rm nh} = 0. \tag{3.26}$$

If the solution $\vec{V}(r,\omega,k)$, and hence $\vec{V}_{\rm nh}$, is non-trivial, then (3.26) is satisfied only when $\lim_{r\to\infty} \det P(r,\omega,k) = 0$.

Let us summarise our numerical procedure. First, we choose values of T, ρ, B, ω, and k. Next we solve the equations of motion (3.18) twice, with two linearly-independent values of $\vec{V}_{\rm nh}$. With the two resulting solutions we construct the matrix $P(r,\omega,k)$ as in (3.21). At this point we can test for the presence of a pole in G^R by checcing whether $\lim_{r\to\infty} \det P(r,\omega,k) = 0$. We obtain the spectral function $\chi_{tt}(\omega,k)$ via (3.24), (3.25) and (1.25). Repeating this process for various values of T, ρ, B, ω, and k, we obtain all of the numerical results that follow.

3.3 Crossover at zero magnetic field

In this section we study the collisionless/hydrodynamic crossover in the D3/D5 system, in the limit $B = 0$. The results are qualitatively similar to those in the D3/D7 theory [94]. We begin by reviewing the crossover in an LFL, which provides a useful reference point for studying the collective density excitations of our systems.

3.3.1 Collective modes in a Landau Fermi liquid

In an LFL at $T = 0$, the zero sound mode dispersion relation $k(\omega)$ at small ω/μ has

$$\mathrm{Re}\, k(\omega) \propto \omega, \qquad \mathrm{Im}\, k(\omega) \propto \omega^2. \tag{3.27}$$

If expressed instead as $\omega(k)$, then the dispersion relation at small k/μ has

$$\mathrm{Re}\, \omega(k) \propto k, \qquad \mathrm{Im}\, \omega(k) \propto k^2. \tag{3.28}$$

At non-zero T, the attenuation $\mathrm{Im}\, k(\omega)$ of the zero sound mode changes as T increases [58, 57]. The attenuation $\mathrm{Im}\, k(\omega) \propto \nu$, where ν is the quasiparticle collision frequency,

$$\nu \propto \frac{\omega^2 + \pi^2 T^2}{\mu\,(1 + e^{-\omega/T})}. \tag{3.29}$$

On the right-hand-side of (3.29), in the numerator the ω^2 term is due to quantum interactions between the quasiparticles whereas the T^2 term is due to thermal scattering. At very low temperatures, $T \ll \omega$, the quantum term dominates and thus $\mathrm{Im}\, k(\omega) \propto \omega^2/\mu$. This is called the 'collisionless quantum' regime. As T increases, the thermal term begins to dominate when $T \approx \omega$, at which point the system enters the 'collisionless thermal' regime, where $\mathrm{Im}\, k(\omega) \propto T^2/\mu$. At even higher temperatures, the collision frequency becomes significantly greater than the propagating frequency of the mode, $\nu \gg \omega$. In this regime, the mode is very short-lived and so does not contribute significantly to the low-energy properties of the system. However, in precisely this limit we expect hydrodynamic behaviour, such as hydrodynamic sound propagation and diffusion of charge, since the high frequency of thermal collisions brings about local thermal equilibrium. This collisionless/hydrodynamic crossover at $\omega \simeq T^2/\mu$ thus leads to a qualitative change in the response of the liquid to density perturbations. We summarise our discussion of the three regimes of an LFL with increasing T in fig. 3.1.

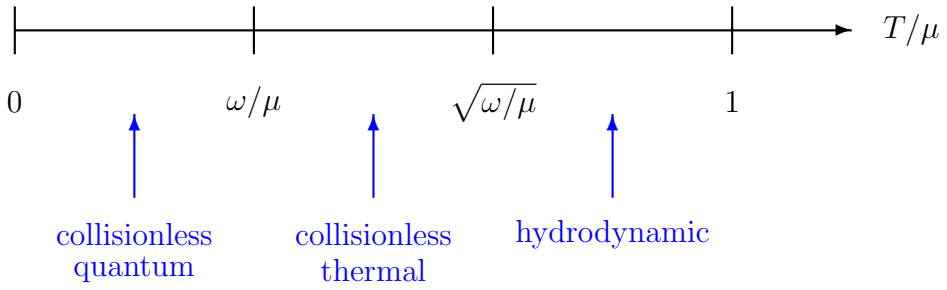

Fig. 3.1: The three regimes of charge density transport in a Landau Fermi liquid, with increasing T/μ.

3.3.2 Collective modes in holographic quantum liquids

We are interested in compressible states of the D3/Dp systems in the quantum liquid regime; that is, with a fixed, large density of matter present. We will thus normalise all dimensionful quantities by the appropriate power of the density, ρ, such that they are dimensionless. Specifically, we will define the dimensionless quantities

$$\bar{T} \equiv \frac{\pi T}{\rho^{1/n}}, \quad \bar{\omega} \equiv \frac{\omega}{\rho^{1/n}}, \quad \bar{k} \equiv \frac{k}{\rho^{1/n}}. \tag{3.30}$$

We will always work with $\bar{T}, \bar{\omega}, \bar{k} \ll 1$. Similarly, $\bar{\chi}_{\mu\nu}(\omega, k)$ will denote the spectral function normalised to be dimensionless by an appropriate power of ρ. Notice that since $\bar{T} \ll 1$, normalising dimensionful quantities by powers of ρ is equivalent, up to numerical factors, to normalising by appropriate powers of the chemical potential μ, via (3.10).

Both of our holographic quantum liquids support a holographic zero sound excitation at $T = 0$ [89]. For now, we will follow the convention of [89, 90, 92, 93, 94] and write the dispersion relation of the holographic zero sound in the form $\omega(k)$,

$$\bar{\omega} = \pm\frac{1}{\sqrt{n}}\bar{k} - i\frac{1}{2n}\frac{\rho^{1/n}}{\mu_0}\bar{k}^2 + O\left(\bar{k}^3\right). \tag{3.31}$$

(Recall that μ_0 was defined in (3.11).) These modes are called holographic zero sound because this $T = 0$ dispersion relation has $\mathrm{Re}\,\omega(k) \propto k$ and $\mathrm{Im}\,\omega(k) \propto k^2$, just like the zero sound excitation of an LFL, (3.28) [89].

The holographic zero sound mode persists at small but non-zero temperatures in the range $\bar{T}^2 \ll \bar{T} \ll \bar{k}$, with a dispersion relation described to a very good approximation by the $T = 0$ form, (3.31), as we show in fig. 3.2. This regime is analogous to the

collisionless quantum regime of an LFL, where quantum interactions of quasiparticles dominate thermal collisions and hence the decay rate of zero sound $-\mathrm{Im}\,\omega(k) \propto k^2$.

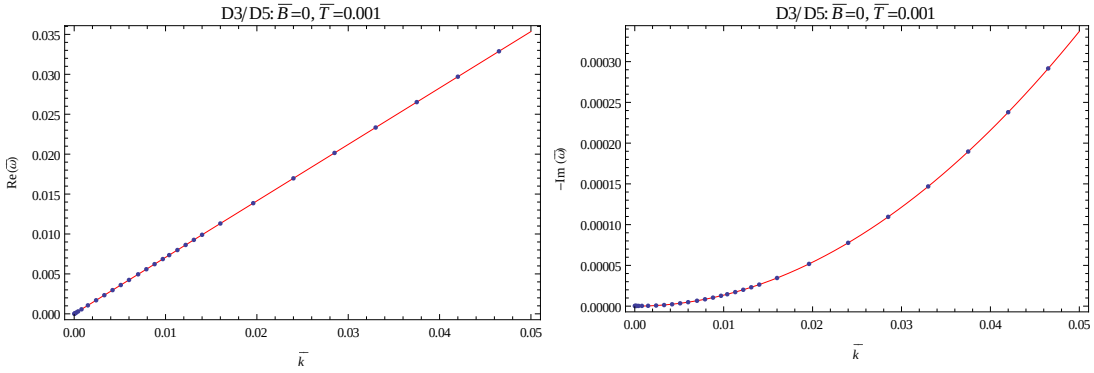

Fig. 3.2: *Left:* $\mathrm{Re}\,\bar{\omega}$ as a function of $\bar{k}$ for the holographic zero sound dispersion relation in the D3/D5 system at $B = 0$ and $\bar{T} = 0.001$, within the range $\bar{T}^2 \ll \bar{T} \ll \bar{k}$. *Right:* $-\mathrm{Im}\,\bar{\omega}$ versus $\bar{k}$ for the same mode at the same $\bar{T}$. In both figures the dots are our numerical results while the red lines come from the $T = 0$ dispersion relation in (3.31). Clearly the $T = 0$ result in (3.31) is a very good approximation to our numerical results for the low-temperature dispersion relation.

As $\bar{T}$ increases and enters the range $\bar{T}^2 \ll \bar{k} \ll \bar{T}$, the decay rate of the holographic zero sound mode increases as $-\mathrm{Im}\,\bar{\omega}(\bar{k}) \propto \bar{T}^2$, as shown in fig. 3.3. This is analogous to the collisionless thermal regime of an LFL, where thermal collisions of quasiparticles dominate quantum interactions, and the decay rate of zero sound $-\mathrm{Im}\,\omega(k) \propto T^2/\mu$.

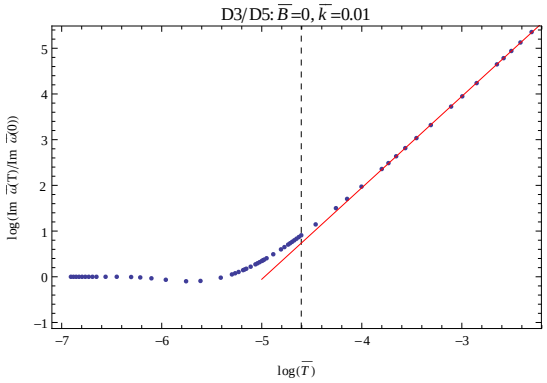

Fig. 3.3: Logarithm of the decay rate of the holographic zero sound mode in the D3/D5 system at $B = 0$, normalised to the $T = 0$ value, $\log\left(\mathrm{Im}\,\bar{\omega}(\bar{T})/\mathrm{Im}\,\bar{\omega}(0)\right)$, as a function of $\log\bar{T}$ for $\bar{k} = 0.01$, within the regime $\bar{T}^2 \ll \bar{k}$. The dots are our numerical results, the vertical dashed black line denotes $\bar{T} = \bar{k}$, and the solid red best-fit line has gradient 2, indicating that $\mathrm{Im}\,\bar{\omega}(\bar{k}) \propto \bar{T}^2$ for $\bar{T} \gtrsim \bar{k}$.

As $\bar{T}$ increases further still, the two holographic zero sound modes, viewed as poles of $G^R_{tt}(\omega, k)$ in the complex $\bar{\omega}$ plane, move down and also closer to the imaginary axis,

following an approximately semi-circular path, and eventually collide on the imaginary axis to form two purely imaginary modes, as shown in fig. 3.4. The purely imaginary mode farther from the origin is short-lived, and does not contribute significantly to the low-energy physics of the system. The purely imaginary mode closer to the origin is the hydrodynamic charge diffusion mode, with dispersion relation [146, 147, 148]

$$\bar{\omega} = -i\left(\frac{1}{2}\bar{T}\sqrt{1+\bar{T}^4}\,{}_2F_1\left[-\frac{3}{4},\frac{1}{2};\frac{1}{4};-\frac{1}{\bar{T}^4}\right]-\frac{1}{2}\bar{T}^3\right)\bar{k}^2+O\left(\bar{k}^3\right), \tag{3.32}$$

as shown in fig. 3.4. The decay rate $-\mathrm{Im}\,\bar{\omega}(\bar{k})$ of this hydrodynamic mode decreases as $\bar{T}$ increases. This is analogous to the hydrodynamic regime of an LFL.

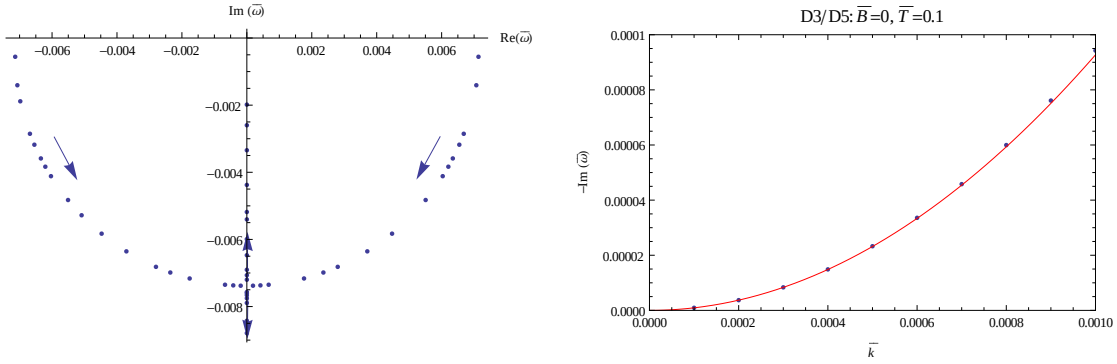

Fig. 3.4: *Left:* The complex $\bar{\omega}$ plane, where the dots are our numerical results for the dominant poles of $G^R_{tt}(\omega,k)$ in the D3/D5 system at $B=0$ and $\bar{k}=0.01$ as $\bar{T}$ changes: the arrows point in the direction of increasing $\bar{T}$. The two complex poles are due to holographic zero sound and the purely imaginary pole closest to the origin is due to charge diffusion. We define the location of the collisionless/hydrodynamic crossover as the value of $\bar{T}$ where the holographic zero sound poles collide on the imaginary axis. *Right:* $-\mathrm{Im}\,\bar{\omega}(\bar{k})$ versus $\bar{k}$ for the charge diffusion mode at $\bar{T}=0.1$, in the regime $\bar{k}\ll\bar{T}^2$. The dots are our numerical results and the red line is the dispersion relation in (3.32).

These results for the D3/D5 system are qualitatively similar to those for the D3/D7 system [94]. In both systems we define the location of the collisionless/hydrodynamic crossover as the value of $\bar{T}$ where the holographic zero sound poles collide on the imaginary axis to form the purely imaginary poles. In both of the D3/Dp systems, we find that the crossover occurs when $|\bar{\omega}|\propto\bar{T}^2$ and $\bar{k}\propto\bar{T}^2$: for the D3/D5 system we show this in fig. 3.5. To find the exact proportionality constant in $|\bar{\omega}|\propto\bar{T}^2$, we performed numerical fits to the data: we find that the crossover occurs when

$$|\bar{\omega}|\approx\begin{cases}0.30\,\bar{T}^2 & \text{for D3/D5,}\\ 0.45\,\bar{T}^2 & \text{for D3/D7.}\end{cases} \tag{3.33}$$

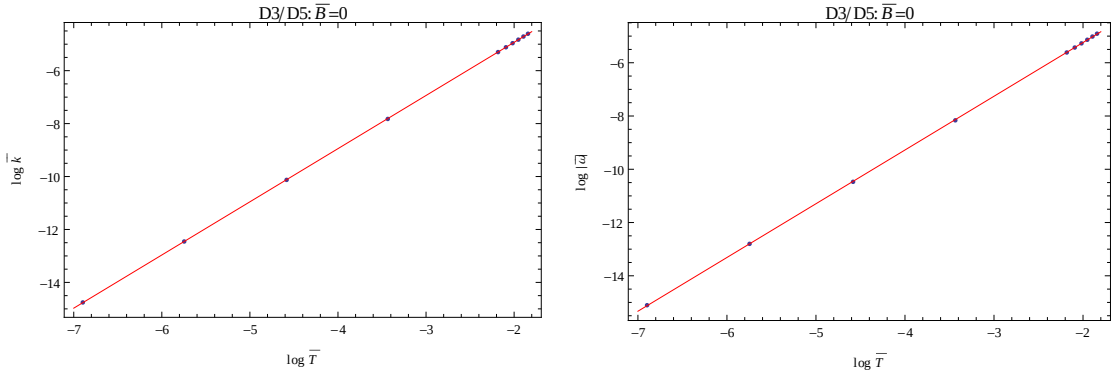

Fig. 3.5: *Left:* $\log \bar{k}$ versus $\log \bar{T}$ and *Right:* $\log |\bar{\omega}|$ versus $\log \bar{T}$ at the location of the collisionless/hydrodynamic crossover for the D3/D5 system at $B = 0$. In both figures the dots are our numerical results and the solid red best-fit line has gradient 2, indicating that $|\bar{\omega}| \propto \bar{T}^2$ and $\bar{k} \propto \bar{T}^2$ at the crossover.

The crossover is also visible in the charge density spectral function $\bar{\chi}_{tt}\left(\bar{\omega}, \bar{k}\right)$. In fig. 3.6 we plot $\bar{\chi}_{tt}\left(\bar{\omega}\right)$ in the D3/D5 system at a fixed $\bar{k}$ as a function of $\bar{\omega}$, for various $\bar{T}$. For small $\bar{T}$, $\bar{\chi}_{tt}\left(\bar{\omega}\right)$ is dominated by a narrow peak due to the holographic zero sound mode. As $\bar{T}$ increases, the peak due to the holographic zero sound mode becomes wider as its decay rate $-\mathrm{Im}\,\bar{\omega}(\bar{k})$ increases: in fig. 3.4, the holographic zero sound poles move down into the complex ω plane. Near the collisionless/hydrodynamic crossover, the peak moves towards the origin, which reflects the location of the corresponding poles of $G^R_{tt}(\omega, k)$ in the complex $\bar{\omega}$ plane. As $\bar{T}$ increases further and the system enters the hydrodynamic regime, the peak near the origin becomes narrower due to the decreasing decay rate $-\mathrm{Im}\,\bar{\omega}(\bar{k})$ of the hydrodynamic charge diffusion mode. Again, these results for $\bar{\chi}_{tt}\left(\bar{\omega}, \bar{k}\right)$ in the D3/D5 system are qualitatively similar to those of the D3/D7 system.

In summary, in the D3/Dp systems, the three regimes of behaviour in response to density perturbations are very similar to those of an LFL. In particular, the decay rate $-\mathrm{Im}\,\bar{\omega}(\bar{k})$ of the holographic zero sound mode has the same form as that of the LFL zero sound mode in both the collisionless quantum and collisionless thermal regimes. Additionally, the boundaries between the regimes are at $\bar{k} \simeq \bar{T}$ and $\bar{k} \simeq \bar{T}^2$, so since $|\bar{\omega}| \simeq \bar{k}$ for the holographic zero sound mode (the poles in the complex $\bar{\omega}$ plane in fig. 3.4 follow an approximately semi-circular path), the boundaries are located at $\bar{\omega} \simeq \bar{T}$ and $\bar{\omega} \simeq \bar{T}^2$, as in an LFL. These similarities between the D3/Dp systems and LFLs are surprising because, as mentioned in sections 1.2 and 3.1, the D3/Dp systems are *not* LFLs. Indeed, no evidence has been found of a Fermi surface in the D3/Dp systems, and in fact the low-energy dynamics may be governed by a (0+1)-dimensional CFT [64, 92, 93, 144].

In both of the D3/Dp systems, J^y's retarded Green's function, $G^R_{yy}(\omega, k)$, also exhibits

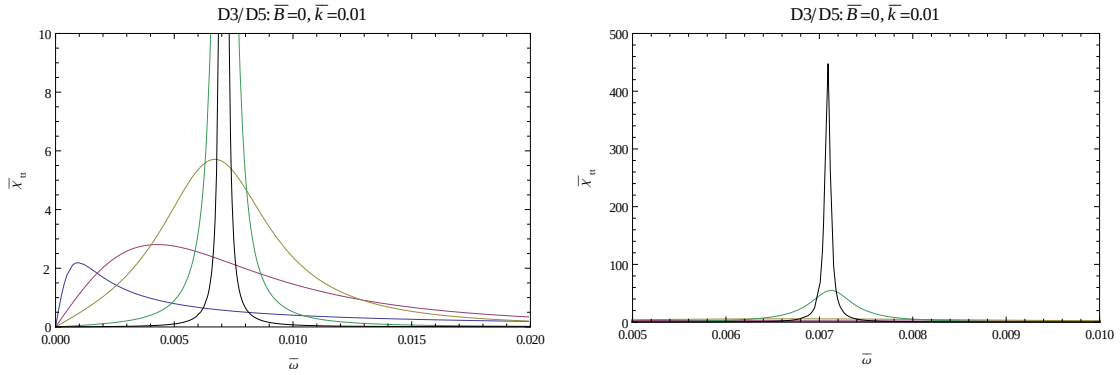

Fig. 3.6: The charge density spectral function $\bar{\chi}_{tt}(\bar{\omega})$ in the D3/D5 system at $B = 0$ as a function of $\bar{\omega}$ and at fixed $\bar{k} = 0.01$. Moving from the tallest peak to the shortest peak corresponds to raising the temperature: $\bar{T} = 0.01$ (black), $\bar{T} = 0.032$ (green), $\bar{T} = 0.1$ (yellow), $\bar{T} = 0.16$ (magenta), $\bar{T} = 0.32$ (blue). The right-hand plot shows the tallest peak in full.

poles in the complex $\bar{\omega}$ plane. As discussed in section 3.2, when B is non-zero and parity is broken, these poles will mix with those of $G^R_{tt}(\omega, k)$, and hence will affect the crossover. As preparation for the non-zero-B case, let us now discuss the poles in $G^R_{yy}(\omega, k)$ when $B = 0$. When $B = 0$, in both of the D3/Dp systems $G^R_{yy}(\omega, k)$ has no poles corresponding to long-lived modes, by which we mean poles satisfying $\bar{\omega} \to 0$ as $\bar{k} \to 0$. The pole in $G^R_{yy}(\omega, k)$ closest to the origin of the complex $\bar{\omega}$ plane is purely imaginary, but is not diffusive: for this mode $\bar{\omega}\left(\bar{k}\right)$ is approximately independent of $\bar{k}$. At low temperatures, for this mode $\mathrm{Im}\,\bar{\omega}(\bar{k}) \propto \bar{T}^2$, as shown in fig. 3.7.

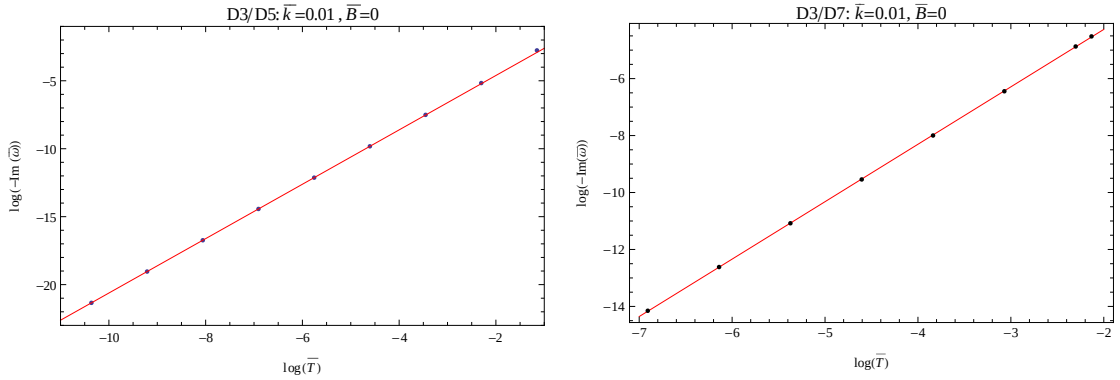

Fig. 3.7: *Left:* $\log\left(-\mathrm{Im}\,\bar{\omega}(\bar{k})\right)$ as a function of $\log \bar{T}$ for the pole in $G^R_{yy}(\omega, k)$ closest to the origin of the complex $\bar{\omega}$ plane in the D3/D5 system at $B = 0$, with $\bar{k} = 0.01$, within the collisionless regime $\bar{k} \gg \bar{T}^2$. *Right:* The same as in the left figure, but in the D3/D7 system. In both figures the dots are our numerical results and the red best-fit lines have gradient 2, indicating that in both cases $\mathrm{Im}\,\bar{\omega}(\bar{k}) \propto \bar{T}^2$.

Following the convention of [89, 90, 92, 93, 94], we described the poles in $G^R_{tt}(\omega, k)$

using complex frequency $\bar{\omega}(\bar{k})$ with real momentum $\bar{k}$. We could then define the crossover by a collision of poles in the complex $\bar{\omega}$ plane, and could identify three distinct regimes of response to density perturbations, dependening upon the relative magnitudes of $\bar{k}$, $\bar{T}$ and $\bar{T}^2$. For the holographic zero sound mode $|\bar{\omega}| \propto \bar{k}$, so we could equivalently characterise the three regimes by the relative magnitudes of $\bar{\omega}$, $\bar{T}$ and $\bar{T}^2$. Crucially, when B is non-zero such a simple translation from real $\bar{k}$ to real $\bar{\omega}$ will in general *not* be possible, as we will see in the next section.

3.4 Crossover at non-zero magnetic field

In this section we study the collisionless/hydrodynamic crossover in both of the D3/Dp systems, with non-zero B. We will normalise B by the appropriate power of ρ to be dimensionless:

$$\bar{B} \equiv \frac{B}{\rho^{2/n}}. \tag{3.34}$$

We will always work with a large, fixed density, such that $\bar{B}, \bar{T}, \bar{\omega}, \bar{k} \ll 1$. In particular, we will always work with values of B below any known phase transitions. In general, the critical value of B for the known transitions is a complicated function of T, but at any given T the critical value of B is bounded from below by the $T = 0$ values given in section 3.1. We will work with $\bar{T} \geq 10^{-3}$ and values of $\bar{B}/\bar{T}^2$ up to 10^4 for the D3/D5 system and up to 10^5 for the D3/D7 system, well below the known transitions.

In our systems, a non-zero B has two major effects on the spectrum of collective excitations at low temperatures. First, a non-zero B breaks parity, and so operators can mix that could not mix when $B = 0$. In particular, we find that when B is non-zero the poles in $G^R_{tt}(\omega, k)$ mix with those of J^y's retarded Green's function, $G^R_{yy}(\omega, k)$. Due to the mixing of poles, for small T the holographic zero sound poles are no longer the only poles near the origin of the complex ω plane: a purely imaginary pole also appears. As a result, the spectral function of J^t, as a function of ω, can exhibit *two* large peaks, one from holographic zero sound and one from the purely imaginary mode.

Second, when $T = 0$, a non-zero B produces a gap in the holographic zero sound dispersion relation $\propto B/\mu$ [144, 149]. Such a gap is consistent with Kohn's theorem [150], which states that for non-relativistic particles with pair-wise interactions of any strength, in an external magnetic field the center-of-mass motion decouples from the relative motion of the particles and behaves as a free particle in a magnetic field. This guarantees a $k = 0$ resonance at the cyclotron frequency, which is $\propto B$.

In section 3.4.1 we determine the dispersion relations of the holographic zero sound mode in our systems for $T = 0$ and non-zero B analytically (without numerics), following [144, 149]. In section 3.4.2 we determine the dispersion relation of the charge diffusion mode at non-zero B, following [147, 148]. In section 3.4.3 we repeat the analysis of section 3.3 but with non-zero B; that is, we study the poles of $G^R_{tt}(\omega, k)$ in the complex ω plane with non-zero B. For sufficiently small B we will show that a collision of poles occurs as we increase T, similar to the $B = 0$ case, but that such a collision does not occur for sufficiently high B. We thus turn to the spectral function $\bar{\chi}_{tt}\left(\bar{\omega}, \bar{k}\right)$ in section 3.4.4, which will show a clear crossover from holographic zero sound to charge diffusion as T increases with respect to ω. The crossover is simplest to understand by studying the poles of $G^R_{tt}(\omega, k)$ in the complex *momentum* plane, as we discuss in section 3.4.5. We summarise our results in section 3.4.6.

3.4.1 Holographic zero sound at non-zero magnetic field

In this subsection we derive the dispersion relation of the holographic zero sound mode when $T = 0$ and with B non-zero. For the D3/D5 system we reproduce the results of [144], while for the D3/D7 system our results are novel. We will also show, using our numerical solutions, that the $T = 0$ dispersion relation is a very good approximation to the low-temperature dispersion relation, as was the case when $B = 0$ (see fig. 3.2).

To determine the dispersion relation without numerics, we follow the procedure of [89, 144]: we solve the equations of motion, (3.18), in two different limits and then match the two solutions in a regime where the limits overlap. More specifically, we take a near-horizon limit of the equations of motion, meaning $r \to 0$, solve the resulting equations, and then take a low-frequency limit of the solution. We then repeat these operations in opposite order: we take a low-frequency limit of the equations of motion, solve the resulting equations, and then take a near-horizon limit of the solution.

We begin by setting $T = 0$, or equivalently $r_+ = 0$, in (3.18), in which case $|g_{tt}| = g_{rr}^{-1} = g_{xx} = r^2$. Our near-horizon $r \to 0$ limit consists of taking $r/\rho^{1/n} \ll 1$ with $r/\sqrt{B} \approx O(1)$, so that

$$g_{xx}^{n-2}\left(g_{xx}^2 + B^2\right) + \rho^2 \to \rho^2, \qquad \omega^2 - u(r)^2 k^2 \to \omega^2. \tag{3.35}$$

The resulting equations have solutions

$$\vec{V}(r,\omega,k) = e^{i\omega/r} \begin{pmatrix} r & \left(1-\frac{i\omega}{r}\right)\frac{B}{\omega} \\ \frac{i}{\omega}\left(1-\frac{i\omega}{r}\right)\frac{B}{\omega} & \frac{i}{\omega}\,r \end{pmatrix} \vec{c}, \tag{3.36}$$

with constant normalisation vector $\vec{c}$, which is the $T=0$ analogue of the $\vec{V}_{\rm nh}$ defined for non-zero T in (3.20). On the right-hand-side of (3.36) the $e^{i\omega/r}$ factor describes an ingoing wave as $r \to 0$, as we discussed in section 3.2.

We now want to take the low-frequency limit of the solution in (3.36), which means $\omega/r \ll 1$ [89]. As emphasised in [144], however, Kohn's theorem suggests that the holographic zero sound dispersion may exhibit a gap when B is non-zero, so if we wish to obtain a non-trivial result we must be careful not to take ω small with fixed B. Instead, we should take ω small with B/ω fixed, *i.e.* we should scale the gap with ω as we make ω small. In this limit the solution of (3.36) becomes

$$\vec{V}(r,\omega,k) = \begin{pmatrix} r+i\omega & \frac{B}{\omega} \\ \frac{iB}{\omega^2} & \frac{i}{\omega}\left(r+i\omega\right) \end{pmatrix} \vec{c}. \tag{3.37}$$

We now need to perform the same operations in the opposite order. First, we take the low-frequency limit of (3.18), meaning $\omega/r \ll 1$ and $k/r \ll 1$ keeping ω/k fixed. As above, when we take ω to be small we also take B to be small, in the sense that we keep B/ω fixed. In these limits, in (3.18) we drop all terms not involving derivatives of E or a_y, as these are sub-leading, and moreover in the remaining terms we drop all factors of B. The resulting equations have solutions

$$\begin{aligned} E(r,\omega,k) &= E_{(0)} + c_E\, r^{1-n}\left[\frac{k^2}{n\sqrt{1+\rho^2/r^{2n}}} + \frac{k^2-n\omega^2}{n(n-1)}\,{}_2F_1\left(\frac{1}{2},\frac{1}{2}-\frac{1}{2n},\frac{3}{2}-\frac{1}{2n},-\frac{\rho^2}{r^{2n}}\right)\right], \\ a_y(r,\omega,k) &= a_{y(0)} + c_y\,\frac{r^{1-n}}{1-n}\,{}_2F_1\left(\frac{1}{2},\frac{1}{2}-\frac{1}{2n},\frac{3}{2}-\frac{1}{2n},-\frac{\rho^2}{r^{2n}}\right), \end{aligned} \tag{3.38}$$

where $E_{(0)}$, c_E, $a_{y(0)}$, and c_y are independent of r but can depend on ω and k. Now we take the near-horizon limit, $r/\rho^{1/n} \ll 1$:

$$\begin{aligned} E(r,\omega,k) &= E_{(0)} + c_E\,\frac{\mu_0}{\rho}\left(\frac{1}{n}\,k^2-\omega^2\right) + c_E\,\frac{\omega^2}{\rho}\,r + O\left(r^{n+1}/\rho^{1+1/n}\right), \\ a_y(r,\omega,k) &= a_{y(0)} - c_y\,\frac{\mu_0}{\rho} + c_y\,\rho^{-1}r + O\left(r^{n+1}/\rho^{1+1/n}\right). \end{aligned} \tag{3.39}$$

We can now match solutions in the regimes where the two limits overlap. Specifically,

we match the terms constant in r and the terms linear in r in (3.37) and (3.39). That gives us four equations involving the two components of $\vec{c}$ as well as $E_{(0)}$, c_E, $a_{y(0)}$, and c_y. We can use two of those equations to eliminate the two components of $\vec{c}$, leaving us with two equations that we can express in matrix form:

$$\begin{pmatrix} E_{(0)} \\ a_{y(0)} \end{pmatrix} = \begin{pmatrix} i\frac{\omega^3}{\rho} + \frac{\mu_0}{\rho}\left(\omega^2 - \frac{k^2}{n}\right) & -\frac{i\,B}{\rho} \\ \frac{i\,B}{\rho} & \left(\frac{i\,\omega}{\rho} + \frac{\mu_0}{\rho}\right) \end{pmatrix} \begin{pmatrix} c_E \\ c_y \end{pmatrix}. \tag{3.40}$$

As discussed in section 3.2, for a quasinormal mode the sources $E_{(0)} = 0$ and $a_{y(0)} = 0$. We can then obtain a non-trivial solution for $\vec{V}(r, \omega, k)$ only if the matrix on the right-hand-side of (3.40) has vanishing determinant.

When $B = 0$, the matrix on the right-hand-side of (3.40) becomes diagonal, *i.e.* E and a_y decouple. In that case the determinant of the matrix will vanish when either diagonal entry vanishes. Setting the upper-left entry to zero gives us the holographic zero sound dispersion relation at $B = 0$, (3.31). Setting the lower-right entry to zero gives us a quasinormal mode with dispersion $\omega = -i\mu_0$, dual to a pole in $G^R_{yy}(\omega, k)$. This purely-imaginary, k-independent mode is distinct from the purely-imaginary, k-independent mode in $G^R_{yy}(\omega, k)$ discussed near the end of section 3.3.2, which had $\mathrm{Im}\,\bar{\omega}(\bar{k}) \propto \bar{T}^2$ (recall fig. 3.7), and hence $\mathrm{Im}\,\bar{\omega}(\bar{k}) \to 0$ as $\bar{T} \to 0$.

When B is non-zero, E and a_y couple, and so the poles are shared by the correlators that mix. Demanding that the determinant of the matrix on the right-hand-side of (3.40) vanishes when B is non-zero gives us

$$\bar{\omega}^4 - 2i\frac{\mu_0}{\rho^{1/n}}\bar{\omega}^3 - \frac{\mu_0^2}{\rho^{2/n}}\bar{\omega}^2 + i\frac{\mu_0}{\rho^{1/n}}\frac{\bar{k}^2}{n}\bar{\omega} + \frac{\mu_0^2}{\rho^{2/n}}\frac{\bar{k}^2}{n} + \bar{B}^2 = 0, \tag{3.41}$$

which determines the dispersion relation of the holographic zero sound: expressed as $\bar{\omega}(\bar{k})$, when both $\bar{B}$ and $\bar{k}$ are non-zero and small, but of the same order, we find

$$\bar{\omega}(\bar{k}) = \pm\sqrt{\frac{1}{n}\bar{k}^2 + \frac{\rho^{2/n}}{\mu_0^2}\bar{B}^2} - i\frac{\rho^{1/n}}{\mu_0}\left[\frac{1}{2n}\bar{k}^2 + \frac{\rho^{2/n}}{\mu_0^2}\bar{B}^2\right] + O\left(\bar{k}^3\right). \tag{3.42}$$

When $B = 0$ we recover the result of [89], namely (3.31), and when B is non-zero, for $n = 2$ we recover the result of [144]. In particular, we have found that the holographic zero sound dispersion relation is gapped: defining $\bar{\omega}_{\mathrm{gap}} \equiv \lim_{\bar{k}\to 0} \mathrm{Re}\,\bar{\omega}(\bar{k})$, we have

$$\bar{\omega}_{\mathrm{gap}} = \frac{\rho^{1/n}}{\mu_0}\bar{B}. \tag{3.43}$$

We can alternatively express the holographic zero sound dispersion relation as

$$\bar{k}(\bar{\omega})^2 = n\left(\bar{\omega}^2 - \frac{\rho^{2/n}}{\mu_0^2}\bar{B}^2\right) + in\,\bar{\omega}\,\frac{\rho^{1/n}}{\mu_0}\left(\bar{\omega}^2 + \frac{\rho^{2/n}}{\mu_0^2}\bar{B}^2\right). \tag{3.44}$$

In fig. 3.8 we present our numerical results for the dispersion relation of the holographic zero sound in both D3/Dp systems with non-zero B, at low temperatures. We find that the $T = 0$ dispersion relation, (3.42), is a very good approximation to the low-temperature dispersion relation, as occured when $B = 0$ (recall fig. 3.2).

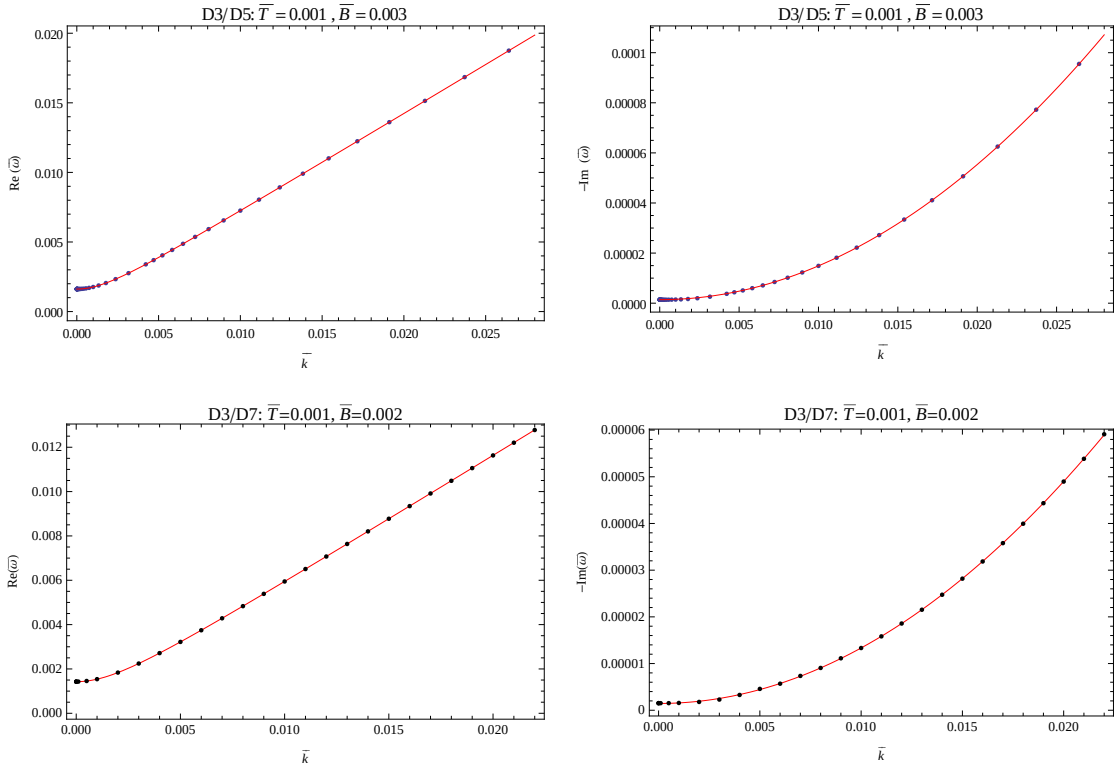

Fig. 3.8: *Top:* $\mathrm{Re}\,\bar{\omega}(\bar{k})$ (left) and $-\mathrm{Im}\,\bar{\omega}(\bar{k})$ (right) versus $\bar{k}$ for the holographic zero sound mode in the D3/D5 system with $\bar{B} = 0.003$ and $\bar{T} = 0.001$, in the range $\bar{k} \gg \bar{T}$. *Bottom:* $\mathrm{Re}\,\bar{\omega}(\bar{k})$ (left) and $-\mathrm{Im}\,\bar{\omega}(\bar{k})$ (right) versus $\bar{k}$ for the holographic zero sound mode in the D3/D7 system with $\bar{B} = 0.002$ and $\bar{T} = 0.001$, in the range $\bar{k} \gg \bar{T}$. In all four plots the dots are our numerical results and the solid red lines come from the $T = 0$ dispersion relation, (3.42). Clearly the $T = 0$ result (3.42) is a very good approximation to the low-temperature dispersion relation, as was the case when $B = 0$ (recall fig. 3.2).

3.4.2 Charge diffusion at non-zero magnetic field

As discussed in section 3.3.2, when $B = 0$ a charge diffusion pole appears in $G^R_{tt}(\omega, k)$ in the hydrodynamic regime $\bar{k}, \bar{\omega} \ll \bar{T}^2$. In this subsection, we will determine the dispersion relation of the longest-lived collective excitation in this hydrodynamic regime when B is non-zero. We will find that the longest-lived mode is that of charge diffusion.

Notice that previous holographic studies of hydrodynamics with a non-zero magnetic field, such as those of [151, 152, 153, 154, 155, 156, 157], employed the typical 'hydrodynamic' limit, in which T is larger than all other scales. In contrast, as mentioned at the beginning of this section, we work in a limit where the charge density is the largest scale.

As in the previous subsection, to determine the dispersion relation of the charge diffusion mode without using numerics, we will solve the equations of motion, (3.18), in two different limits, the near-horizon and low-frequency limits, and then match the two solutions in a regime where the limits overlap.

We begin with the near-horizon limit: we expand the equations of motion, (3.18), in $(r - r_+)$ up to order $(r - r_+)$. We then solve the resulting equations, and take the limits of low frequency and low momentum, ω/T, $k/T \ll 1$, assuming $|\omega| \propto |k^2|$. In these limits we discard a_y's contribution to E's equation of motion, it being sub-leading. To find a quasinormal mode, then, we only need the solution for E in these limits:

$$E(r, \omega, k) = \left(1 + i\,\frac{k^2}{\omega}\left[\lim_{r\to r_+} \frac{(u(r)^2)'}{\sqrt{|g'_{tt}(r)|\,(g_{rr}^{-1}(r))'}}\right](r - r_+)\right) E_{\rm nh}, \tag{3.45}$$

where $E_{\rm nh}$ is the upper component of $\vec{V}_{\rm nh}$. Notice that here, unlike the previous subsection, we do not keep B/ω fixed when we take the low-frequency limit.

We now perform the same operations in the opposite order. First, in the equations of motion (3.18) we take the low-frequency and low-momentum limits, ω/T, $k/T \ll 1$, assuming $|\omega| \propto |k^2|$. In those limits, in the equation of motion for E, (3.18a), we discard the terms without derivatives on E or a_y, as these are sub-leading, and moreover we take

$$\omega^2 - u(r)^2 k^2 \to -u(r)^2 k^2, \tag{3.46}$$

since we assume $|\omega^2| \propto |k^4|$, which is suppressed relative to k^2 in our limits. The solution

for E in these limits is then

$$E(r,\omega,k) = E_{(0)} + C\int_r^\infty d\hat{r}\, Z(\hat{r}), \quad \text{with} \quad Z(\hat{r}) \equiv \frac{u(\hat{r})^3\left(g_{xx}^2(\hat{r})+B^2\right)}{g_{xx}^{(n+1)/2}(\hat{r})|g_{tt}(\hat{r})|g_{rr}^{-1/2}(\hat{r})}, \tag{3.47}$$

where $E_{(0)}$ and C are independent of r but can depend on ω and k. Next we perform the near-horizon limit, expanding the solution in (3.47) in $(r-r_+)$ up to order $(r-r_+)$. We then match the constant term and the term linear in $(r-r_+)$ to the corresponding terms in (3.45). The matching gives us two equation for $E_{(0)}$ and C. Using one of those equations to eliminate C, and using the fact that each of $g_{tt}(r)$, $g_{rr}^{-1}(r)$, and $u(r)^2$ has a simple zero ar $r=r_+$, we find

$$E_{(0)} = E_{\rm nh}\left(1+\frac{ik^2}{\omega}\left[\lim_{r\to r_+}\frac{(u(r)^2)'}{\sqrt{|g_{tt}'(r)|\,(g_{rr}^{-1}(r))'}}\right]\frac{1}{\lim_{r\to r_+}Z(r)}\int_{r_+}^\infty dr\, Z(r)\right). \tag{3.48}$$

Imposing the condition $E_{(0)}=0$ we thus find the dispersion relation of a charge diffusion mode:

$$\omega(k) = -i\left(\left[\lim_{r\to r_+}\frac{(u(r)^2)'}{\sqrt{|g_{tt}'(r)|\,(g_{rr}^{-1}(r))'}}\right]\frac{1}{\lim_{r\to r_+}Z(r)}\int_{r_+}^\infty dr\, Z(r)\right)k^2 + O\left(k^3\right). \tag{3.49}$$

In the D3/D5 system we can perform the integral in (3.49), giving us

$$\begin{aligned}\bar{\omega}(\bar{k}) = -i\bar{T}^2\frac{\sqrt{1+\bar{B}^2+\bar{T}^4}}{\bar{T}^4+\bar{B}^2}\Bigg(&-\frac{\bar{T}}{2}\frac{2\bar{B}^4+\bar{T}^4+2\bar{B}^2\left(1+\bar{T}^4\right)}{\left(1+\bar{B}^2\right)^2\sqrt{1+\bar{B}^2+\bar{T}^4}}\\ &+\frac{\bar{T}^3}{2}\frac{1+2\bar{B}^2}{\left(1+\bar{B}^2\right)^2}\,{}_2F_1\left[-\frac{3}{4},\frac{1}{2},\frac{1}{4};-\left(\frac{1+\bar{B}^2}{\bar{T}^4}\right)\right]\Bigg)\bar{k}^2+O\left(\bar{k}^3\right).\end{aligned} \tag{3.50}$$

When $\bar{B}=0$ we thus recover the result of (3.32), and when $\bar{B}$ is non-zero we recover the result of [147, 148]. In the D3/D7 system we have been unable to evaluate the integral in (3.49) in closed form:

$$\bar{\omega} = -i\bar{T}^2\frac{\sqrt{1+\bar{B}^2\bar{T}^2+\bar{T}^6}}{\bar{T}^4+\bar{B}^2}\left(\int_{\bar{T}}^\infty dx\,\frac{x^2\left(x^4+\bar{B}^2\right)}{\left(1+\bar{B}^2x^2+x^6\right)^{\frac{3}{2}}}\right)\bar{k}^2+O\left(\bar{k}^3\right). \tag{3.51}$$

When $B=0$ we recover the result of [158, 159], while to our knowledge our result with non-zero $\bar{B}$ is novel.

While we have expressed the dispersion relations for the diffusive modes as $\omega(k)$, the expression for $k(\omega)$ is trivial to obtain by inverting (3.50) and (3.51). Notice that,

when expressed as $k(\omega)$, the dispersion relation of the charge diffusion mode will have a non-zero real part.

In fig. 3.9 we present our numerical results for the dispersion relation of the charge diffusion mode in both D3/Dp systems with non-zero B in the regime $\bar{k} \ll \bar{T}^2$, which are extremely good approximations to the dispersion relations in (3.50) and (3.51), as was the case when $B = 0$ (recall fig. 3.4).

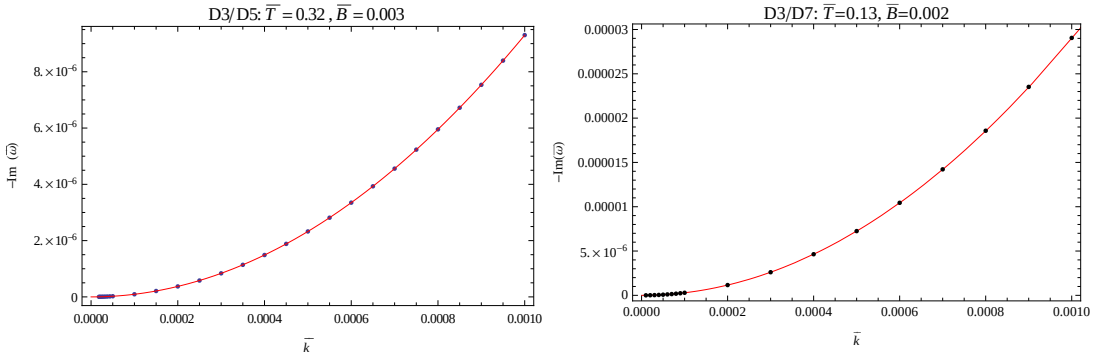

Fig. 3.9: *Left:* $-\mathrm{Im}\,\bar{\omega}$ versus $\bar{k}$ for the charge diffusion mode in the D3/D5 system with $\bar{B} = 0.003$ and $\bar{T} = 0.32$, within the range $\bar{k} \ll \bar{T}^2$. *Right:* The same for the D3/D7 system, with $\bar{B} = 0.002$ and $\bar{T} = 0.13$. For both modes, $\mathrm{Re}\,(\bar{\omega}) = 0$. In both plots the dots are our numerical results and the solid red lines are the dispersion relation in (3.49).

3.4.3 Poles in the complex frequency plane

Having found the dispersion relations of the long-lived excitations in both the $T = 0$ limit and the hydrodynamic limit, we will now numerically investigate the collisionless/hydrodynamic crossover between these two limits. In this subsection we repeat the analysis of section 3.3.2, studying the motion of the poles in $G^R_{tt}(\omega, k)$ in the complex $\bar{\omega}$ plane as we increase $\bar{T}$.

Recall from section 3.3.2 that in both D3/Dp systems, when $B = 0$ a collision of $G^R_{tt}(\omega, k)$'s poles occurs in the complex $\bar{\omega}$ plane: as we increase $\bar{T}$ at fixed $\bar{k}$, the holographic zero sound poles move (approximately) along semi-circles before colliding on the imaginary $\bar{\omega}$ axis to form two purely imaginary poles. The purely imaginary pole closest to the origin is the charge diffusion mode. Indeed, as $\bar{T}$ continues to increase, the charge diffusion pole approaches the origin, *i.e.* becomes more stable, while the other purely imaginary pole moves away from the origin, becoming less stable. We summarise these $B = 0$ results, for both D3/Dp systems, in fig. 3.10.

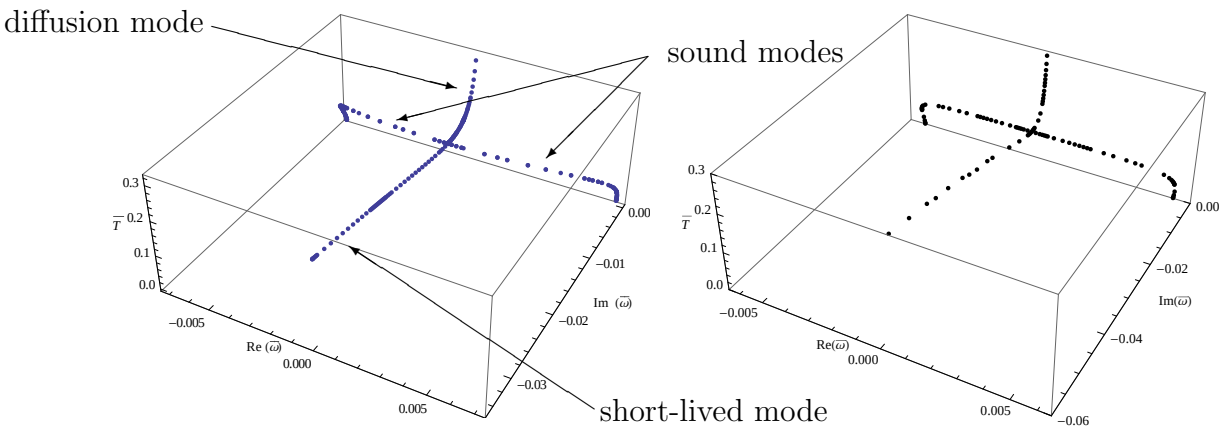

Fig. 3.10: *Left:* The space $(\mathrm{Re}\,\bar{\omega}, \mathrm{Im}\,\bar{\omega}, \bar{T})$, with blue dots indicating our numerical results for the dominant poles in $G^R_{tt}(\omega, k)$ for the D3/D5 system with $\bar{B} = 0$ and $\bar{k} = 0.01$. This plot is a three-dimensional representation of the left plot in fig. 3.4. *Right:* The same as the left plot, but for the D3/D7 system with $\bar{B} = 0$ and $\bar{k} = 0.01$, and with black dots indicating our numerical results. In both cases we see that as we increase $\bar{T}$ (moving vertically in the plot) the two holographic zero sound poles move along (approximate) semi-circles and eventually collide on the imaginary $\bar{\omega}$ axis, producing two purely imaginary poles. The purely imaginary pole closest to the origin is that of charge diffusion, while the other purely imaginary pole is short-lived.

When $\bar{B}$ is non-zero, the poles of $G^R_{yy}(\omega, k)$ mix with those of $G^R_{tt}(\omega, k)$, and thus the latter has an 'extra' purely imaginary pole near the origin, which we henceforth call the 'transverse pole'. For sufficiently small $\bar{B}$ a collision of poles still occurs, however. At very low $\bar{T}$, the three poles of $G^R_{tt}(\omega, k)$ closest to the origin are the two holographic zero sound poles and the transverse pole. As we increase $\bar{T}$, the transverse pole moves down the $\mathrm{Im}\,\bar{\omega}$ axis, whereas the holographic zero sound poles again collide on the $\mathrm{Im}\,\bar{\omega}$ axis and produce two purely imaginary poles at a point closer to the origin than the transverse pole. One of these purely imaginary poles is the charge diffusion mode, which becomes more stable, moving up the $\mathrm{Im}\,\bar{\omega}$ axis, as we increase $\bar{T}$ further. The second purely imaginary mode becomes less stable as we increase $\bar{T}$, and eventually collides with the transverse pole to form two propagating modes, *i.e.* two poles with nonzero real parts. Increasing $\bar{T}$ even more, these propagating modes move down into the complex $\bar{\omega}$ plane, becoming very short-lived, with decay rates $-\mathrm{Im}\,\bar{\omega}(\bar{k})$ increasing as $\bar{T}$ increases. We present some small-$\bar{B}$ results in fig. 3.11, where we depict the motion of poles in the complex $\bar{\omega}$ plane with $\bar{B} = 0.003$ for the D3/D5 system and $\bar{B} = 0.002$ for the D3/D7 system.

We emphasise that at a fixed value of $\bar{T}$, *i.e.* on a horizontal slice of fig. 3.11, two kinds of pole appear near the origin of the complex $\bar{\omega}$ plane. At low temperatures, these are the transverse pole and the poles of the holographic zero sound modes. At

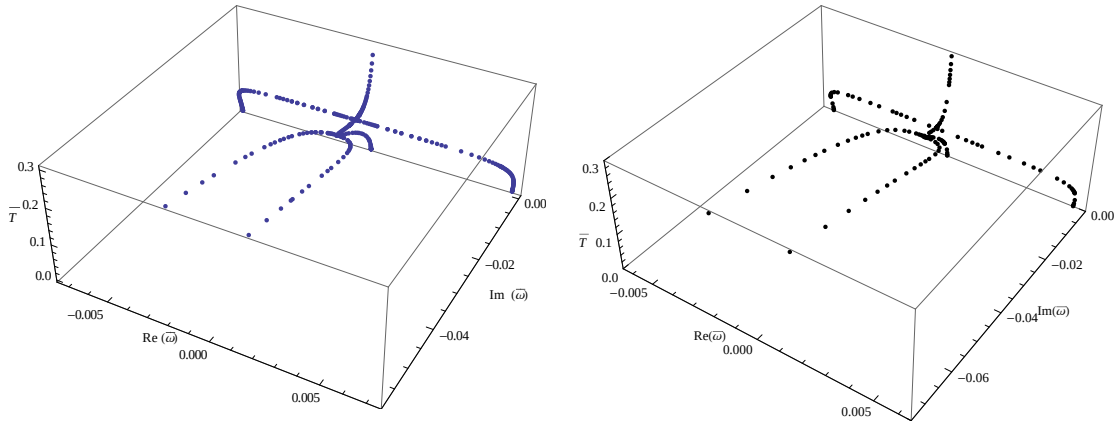

Fig. 3.11: *Left:* The space $(\mathrm{Re}\,\bar{\omega}, \mathrm{Im}\,\bar{\omega}, \bar{T})$, with blue dots indicating our numerical results for the dominant poles in $G^R_{tt}(\omega, k)$ for the D3/D5 system with $\bar{B} = 0.003$ and $\bar{k} = 0.01$. *Right:* The same as the left plot, but for the D3/D7 theory with $\bar{B} = 0.002$ and $\bar{k} = 0.01$, and with black dots indicating our numerical results. In both plots, as we increase $\bar{T}$ (moving vertically in the plot), the purely imaginary transverse pole moves down the $\mathrm{Im}\,\bar{\omega}$ axis, while the holographic zero sound poles eventually collide on the $\mathrm{Im}\,\bar{\omega}$ axis, above the transverse pole, producing two purely imaginary poles. One of these, corresponding to charge diffusion, moves up the $\mathrm{Im}\,\bar{\omega}$ axis, while the other moves down, eventually intersecting the transverse pole and producing two propagating but short-lived modes (the 'horseshoe' in the plot).

high temperatures, the three poles are the charge diffusion mode and the short-lived propagating modes.

For small $\bar{B}$ we can define the location of the collisionless/hydrodynamic crossover by the collision of poles in the complex $\bar{\omega}$ plane, as in the $\bar{B} = 0$ case, however the story is not so simple for larger $\bar{B}$. For sufficiently large $\bar{B}$, as we increase $\bar{T}$ the holographic zero sound poles begin to move towards the $\mathrm{Im}\,\bar{\omega}$ axis before turning around and remaining as propagating modes at higher $\bar{T}$. Most importantly, the holographic zero sound poles never intersect the $\mathrm{Im}\,\bar{\omega}$ axis, *i.e.* no collision of poles occurs. As we increase $\bar{T}$, the transverse pole moves down the $\mathrm{Im}\,\bar{\omega}$ axis, reaches a minimum, and then moves back up the axis, eventually becoming the charge diffusion pole. We present some large-$\bar{B}$ results in fig. 3.12, where we depict the motion of poles in the complex $\bar{\omega}$ plane with $\bar{B} = 0.005$ for the D3/D5 system and $\bar{B} = 0.003$ for the D3/D7 system.

At even higher values of $\bar{B}$ than discussed above, the holographic zero sound poles do not appear to approach the $\mathrm{Im}\,\bar{\omega}$ axis at all, but rather seem to move directly away from it as $\bar{T}$ increases. The transverse pole's behavior is similar to that in fig. 3.12, *i.e.* as $\bar{T}$ increases the transverse pole moves down the $\mathrm{Im}\,\bar{\omega}$ axis, reaches a minimum, and then moves back up the axis, eventually becoming the charge diffusion mode.[5]

[5]We have presented numerical results for poles of $G^R_{tt}(\omega, k)$ in the complex $\bar{\omega}$ plane with fixed mo-

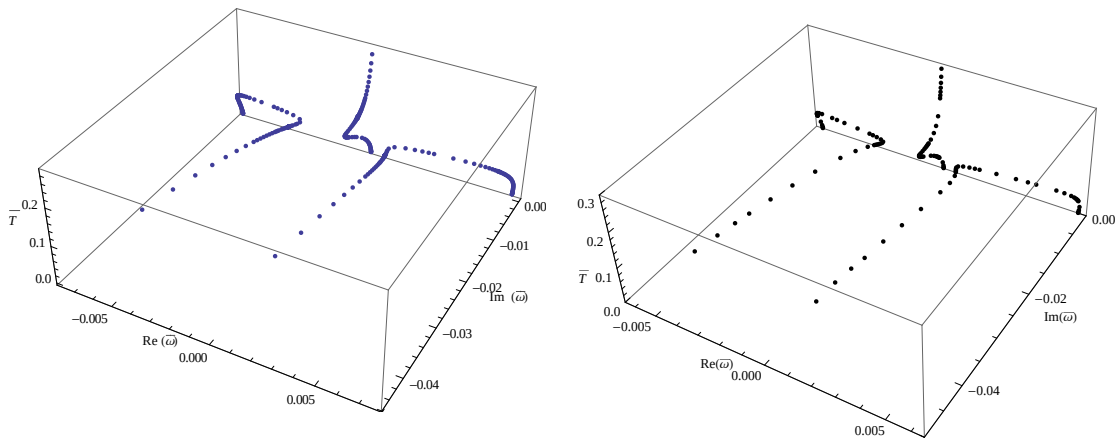

Fig. 3.12: *Left:* The space $(\mathrm{Re}\,\bar{\omega}, \mathrm{Im}\,\bar{\omega}, \bar{T})$, with blue dots indicating our numerical results for the dominant poles in $G^R_{tt}(\omega, k)$ for the D3/D5 system with $\bar{B} = 0.005$ and $\bar{k} = 0.01$. *Right:* The same as the left plot, but for the D3/D7 theory with $\bar{B} = 0.003$ and $\bar{k} = 0.01$, and with black dots indicating our numerical results. In both plots, as we increase $\bar{T}$ (moving vertically in the plot), the holographic zero sound poles move towards the $\mathrm{Im}\,\bar{\omega}$ axis, reach a minimum value of $\mathrm{Re}\,\bar{\omega}$, and then move away from the $\mathrm{Im}\,\bar{\omega}$ axis, remaining as propagating modes at higher values of $\bar{T}$. The purely imaginary transverse pole moves down the $\mathrm{Im}\,\bar{\omega}$ axis, reaching a minimum value, and then moves back up the axis, eventually becoming the charge diffusion pole.

As at smaller $\bar{B}$, at a fixed temperature $\bar{T}$ in the large-$\bar{B}$ regime, *i.e.* on a horizontal slice of fig. 3.12, two kinds of mode are always present, one purely imaginary and the other propagating. However, unlike the small-$\bar{B}$ regime, here we can show that the purely imaginary mode is charge diffusion and the propagating modes are holographic zero sound. Consider for example the temperature range $\bar{k} \gg \bar{T}$ where, when $\bar{B} = 0$, the holographic zero sound mode is present, with a dispersion relation that approximately obeys the $T = 0$ dispersion relation (3.31), as shown in fig. 3.2. In fig. 3.13 we present our numerical results for the dispersion relation of the holographic zero sound as a function of $\bar{B}$ in both D3/Dp systems. We find that our numerical results are very well approximated by the $\bar{T} = 0$ result, (3.42), for all $\bar{B}$. In fig. 3.14, we present our numerical results for the dispersion relation of the longest-lived purely imaginary pole as a function of $\bar{B}$ in the temperature range $\bar{k} \gg \bar{T}$. We find that for large enough $\bar{B}$, this purely imaginary pole is simply the charge diffusion mode. In short, we find that for a fixed $\bar{k} \gg \bar{T}$, both the holographic zero sound and charge diffusion modes coexist at sufficiently high $\bar{B}$.

mentum $\bar{k}$ and increasing $\bar{T}$. If we instead fix $\bar{T}$ and increase $\bar{k}$, then we find results similar to those of the compressible states studied, using holography, in [160], namely $\mathcal{N} = 4$ SYM coupled to (2+1)-dimensional flavour fermions alone, rather than a hypermultiplet, with non-zero $U(1)$ charge density. In that case, the holographic dual was a probe D-brane with non-zero worldvolume electric and magnetic fluxes, including magnetic fluxes along directions of the internal space wrapped by the D-brane.

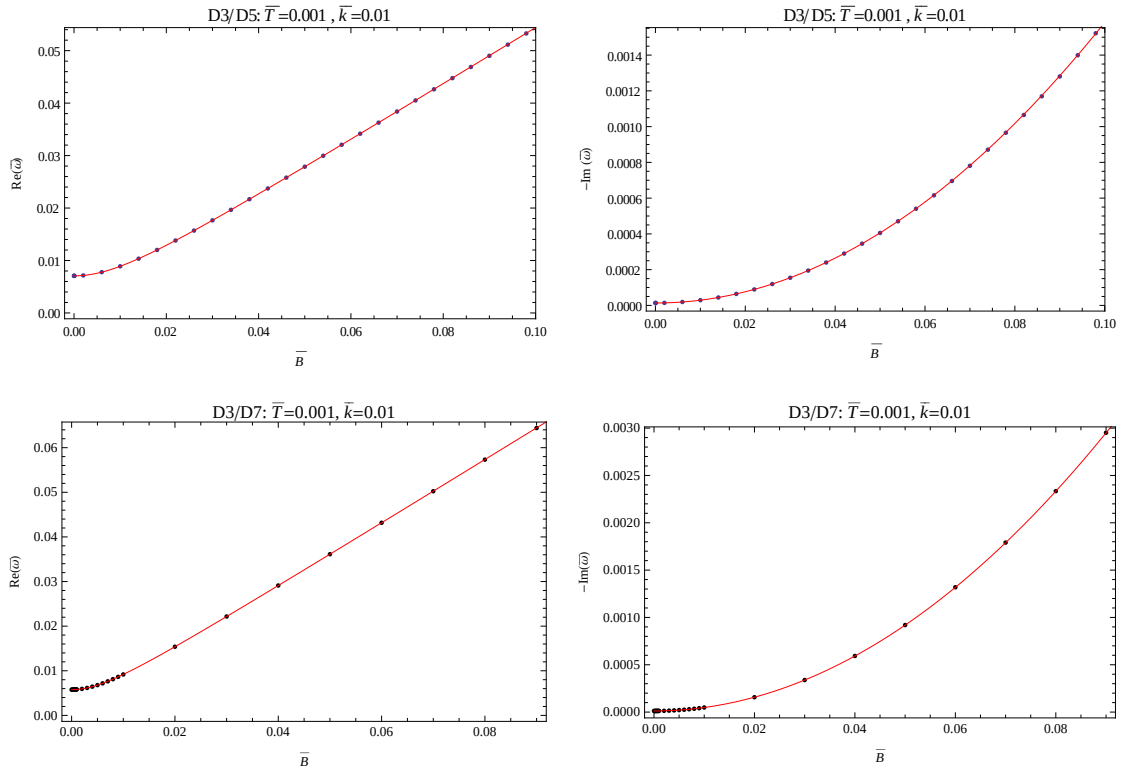

Fig. 3.13: *Top:* $\mathrm{Re}\,\bar{\omega}$ (left) and $-\mathrm{Im}\,\bar{\omega}$ (right) as functions of $\bar{B}$ for the holographic zero sound poles of the D3/D5 system with $\bar{k} = 0.01$ and $\bar{T} = 0.001$, within the range $\bar{k} \gg \bar{T}$. *Bottom:* The same as the top plots, but for the D3/D7 system. In all plots the dots are our numerical results and the solid red lines come from the $\bar{T} = 0$ dispersion relation in (3.42). Clearly (3.42) provides a very good approximation to the numerical results.

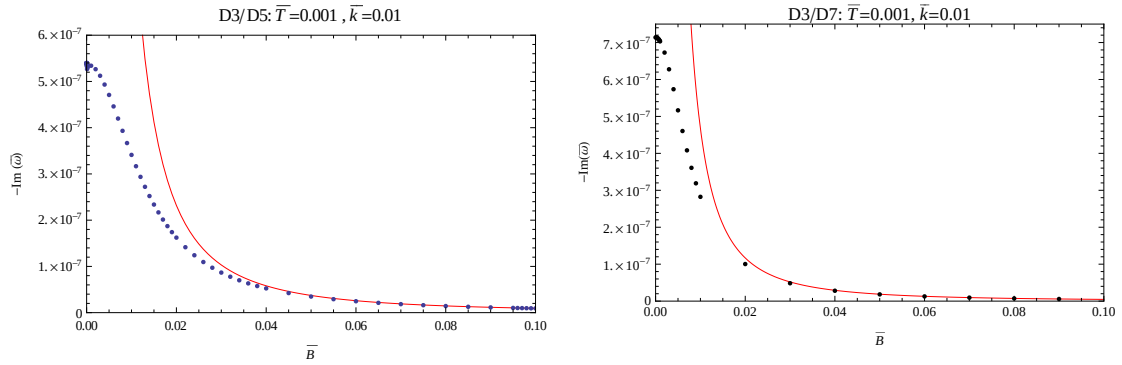

Fig. 3.14: *Left:* $-\mathrm{Im}\,\bar{\omega}$ as a function of $\bar{B}$ for the longest-lived purely imaginary pole of the D3/D5 system with $\bar{k} = 0.01$ and $\bar{T} = 0.001$, within the range $\bar{k} \gg \bar{T}$. *Right:* The same as the left plot, but for the D3/D7 system. In each plot the dots are our numerical results and the solid red line comes from the dispersion relations in (3.50) or (3.51). For sufficiently large $\bar{B}$, we see that the purely imaginary pole becomes that of charge diffusion.

In physical terms, we have learned that if we perturb these systems at a fixed momentum $\bar{k}$, then for sufficiently large $\bar{B}$ we will see both holographic zero sound and charge diffusion, hence for large $\bar{B}$ we cannot characterise the reponse of the system as either collisionless or hydrodynamic. We then seem to have no way of defining a collisionless/hydrodynamic crossover. The story will be very different if we perturb these systems with fixed real frequency $\bar{\omega}$, as we will now show.

3.4.4 Charge density spectral functions

The poles of $G^R_{tt}(\omega, k)$ in the complex $\bar{\omega}$ plane are not directly observable. To gain perspective, we thus turn to a quantity that is directly observable (in principle): the charge density spectral function $\bar{\chi}_{tt}\left(\bar{\omega}, \bar{k}\right)$.

We have so far considered perturbations with fixed real momentum $\bar{k}$. In such cases, the charge density spectral function $\bar{\chi}_{tt}\left(\bar{\omega}, \bar{k}\right)$, as a function of $\bar{\omega}$, will exhibit peaks at frequencies $\bar{\omega}$ determined by the positions (and residues) of the poles in the complex $\bar{\omega}$ plane. For example, when $\bar{B} = 0$, as we increase $\bar{T}$, the spectral function always exhibits only a single dominant peak that moves towards the origin, reflecting the movement of the corresponding pole in the complex $\bar{\omega}$ plane towards the $\mathrm{Im}\,\bar{\omega}$ axis, as we saw in fig. 3.6.

In fig. 3.15 we present our results for $\log \bar{\chi}_{tt}\left(\bar{\omega}, \bar{k}\right)$ in the $\left(\log \bar{\omega}/\bar{T}^2, \log \bar{k}/\bar{T}^2\right)$ plane for both D3/Dp systems at two different values of $\bar{B}/\bar{T}^2$. Here we choose to normalise $\bar{\omega}$ and $\bar{k}$ by $\bar{T}^2$ because in the $B = 0$ case $\bar{\omega}/\bar{T}^2$ and $\bar{k}/\bar{T}^2$ are order one at the crossover. Given these normalisations and the fact that the gap in the $T = 0$ holographic zero sound dispersion relation goes like $\bar{\omega}_{\mathrm{gap}} \propto \bar{B}$, the natural normalisation for $\bar{B}$ is then $\bar{B}/\bar{T}^2$. To make the relationship between poles of $G^R_{tt}(\omega, k)$ and peaks in $\bar{\chi}_{tt}\left(\bar{\omega}, \bar{k}\right)$ explicit, in fig. 3.15 we have also superimposed on the plots our numerical results for the locations of poles of $G^R_{tt}(\omega, k)$ in the complex $\bar{\omega}$ plane (the red dots and blue crosses) as well as the absolute values of the dispersion relations of the long-lived modes, *i.e.* we plot the value of $\left|\bar{\omega}\left(\bar{k}\right)\right|$ for the holographic zero sound dispersion relation in (3.42) and the charge diffusion dispersion relations in (3.50) and (3.51).[6]

Consider first the plots of $\log \bar{\chi}_{tt}\left(\bar{\omega}, \bar{k}\right)$ with $\bar{B}/\bar{T}^2 \ll 1$, figs. 3.15 (a) and (c). For a

[6] In general, the precise location of the peak in $\bar{\chi}_{tt}\left(\bar{\omega}, \bar{k}\right)$ actually depends on the location and residue of the pole in $G^R_{tt}(\omega, k)$ in a complicated way. The results depicted in fig. 3.15 show that for our systems $\left|\bar{\omega}\left(\bar{k}\right)\right|$ gives a very good approximation to the location of the peak. Notice that for a long-lived, propagating mode, this agrees with the usual expectation that the peak is located at the propagating frequency.

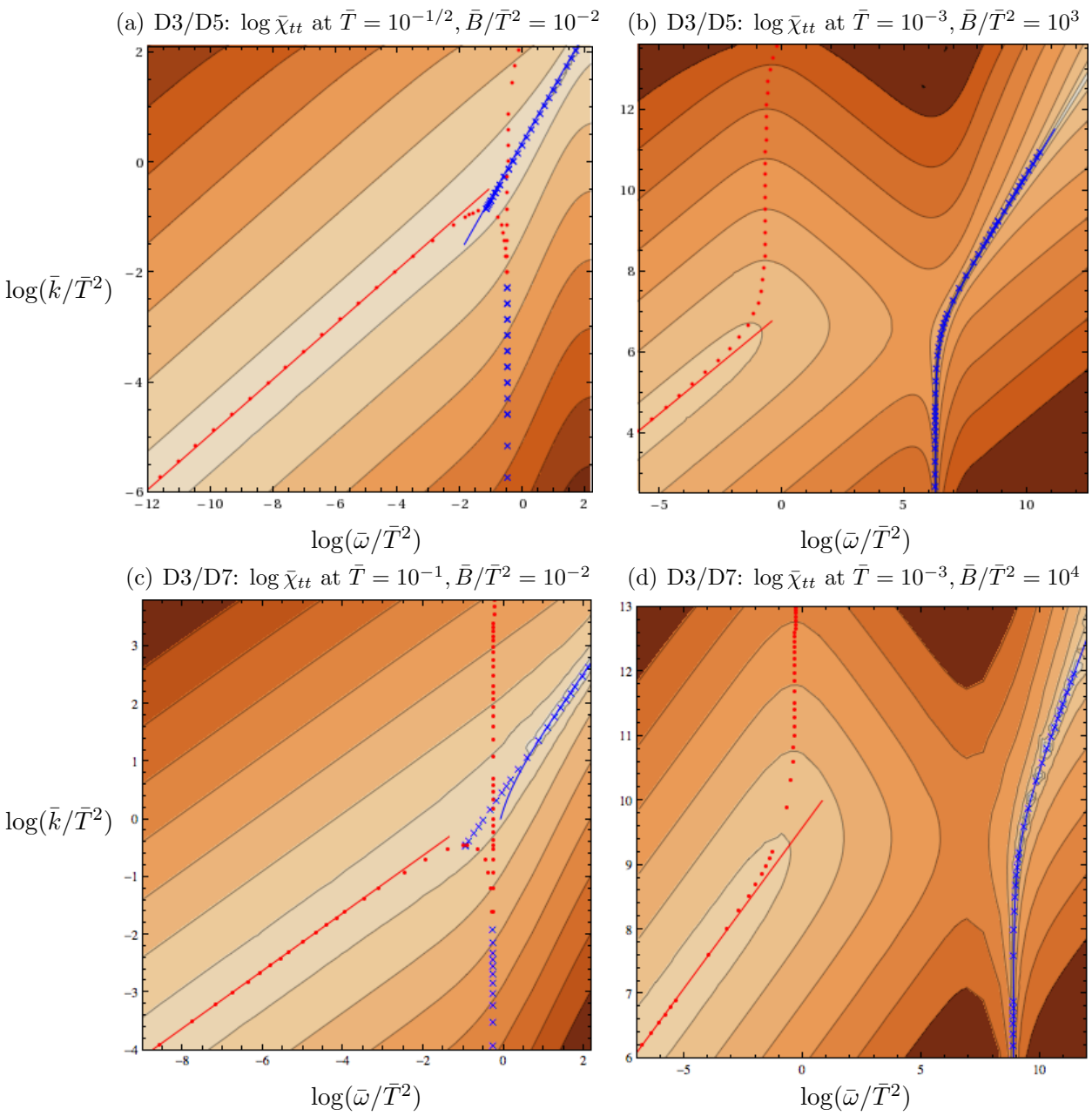

Fig. 3.15: (a) Contour plot of our numerical results for $\log \bar{\chi}_{tt}(\bar{\omega}, \bar{k})$ over the $\left(\log \bar{\omega}/\bar{T}^2, \log \bar{k}/\bar{T}^2\right)$ plane in the D3/D5 system with $\bar{T} = 10^{-1/2}$ and $\bar{B}/\bar{T}^2 = 10^{-2}$. Lighter colours represent larger values of the spectral function, with $\log \bar{\chi}_{tt} = -15, -12.5, -10, \ldots, 2.5$ from darkest to lightest. The red dots and blue crosses are our numerical results for the locations of purely imaginary and propagating poles in $G^R_{tt}(\omega, k)$, respectively. The solid red and blue lines are the values of $\left|\bar{\omega}(\bar{k})\right|$ for the dispersion relations of the charge diffusion, (3.49), and holographic zero sound, (3.42), respectively. (b) The same as (a), but with $\bar{T} = 10^{-3}$ and $\bar{B}/\bar{T}^2 = 10^{3}$. (c) The same as (a) and (b), but for the D3/D7 system with $\bar{T} = 10^{-1}$ and $\bar{B}/\bar{T}^2 = 10^{-2}$ and with $\log \bar{\chi}_{tt} = -10, -8, -6, \ldots, 2$ from darkest to lightest. (d) The same as (c), but with $\bar{T} = 10^{-3}$ and $\bar{B}/\bar{T}^2 = 10^{4}$.

fixed value of the momentum $\bar{k}$, *i.e.* along a horizontal line across the contour plot, the spectral function exhibits only a single peak, which for $\bar{k} \gg \bar{T}^2$, near the top of each plot, is due to the holographic zero sound pole, as indicated by the blue crosses and solid blue line, and for $\bar{k} \ll \bar{T}^2$, near the bottom of each plot, is due to the charge diffusion mode, as indicated by the red dots and solid red line. When $\bar{k} \simeq \bar{T}^2$, these two peaks join, reflecting the collision of the corresponding poles of $G^R_{tt}(\omega, k)$ in the complex $\bar{\omega}$ plane. The 'extra' poles due to mixing with $G^R_{yy}(\omega, k)$ do not produce any significant peaks in the spectral function at these low values of $\bar{B}/\bar{T}^2$. These plots provide additional evidence that at low $\bar{B}$ and with fixed $\bar{k}$, a crossover occurs similar to the crossover at $\bar{B} = 0$.

Now consider the plots of $\log \bar{\chi}_{tt}\left(\bar{\omega}, \bar{k}\right)$ with $\bar{B}/\bar{T}^2 \gg 1$, figs. 3.15 (b) and (d). These are qualitatively different from the $\bar{B}/\bar{T}^2 \ll 1$ plots: now, at a fixed value of $\bar{k}$ (a horizontal line across fig. 3.15 (b) or (d)), the spectral function exhibits *two* peaks, not one peak. At very high $\bar{k}/\bar{T}^2$, near the top of each plot, the holographic zero sound peak is dominant, and at very low $\bar{k}/\bar{T}^2$, near the bottom of each plot, the charge diffusion peak is dominant. In the intermediate region, however, the holographic zero sound and charge diffusion peaks coexist with roughly equal spectral weight. These results agree with what we found by studying poles in the complex frequency plane in the last subsection. In particular, in figs. 3.15 (b) and (d) the holographic zero sound and charge diffusion peaks are no longer joined: as we saw in the previous subsection, the corresponding poles in the $\bar{\omega}$ plane do not collide.

We have so far merely confirmed the analysis of the previous subsection. Now, however, let us consider $\bar{\chi}_{tt}(\bar{\omega}, \bar{k})$ as a function of $\bar{k}$ at a fixed frequency $\bar{\omega}$, *i.e.* a *vertical* line in any of the plots of fig. 3.15. With fixed $\bar{\omega}$, we find that for any $\bar{B}$ and any $\bar{\omega}$ the spectral function exhibits *only one peak*, which at low $\bar{\omega}/\bar{T}^2$, near the left in each plot, is due to charge diffusion, and at high $\bar{\omega}/\bar{T}^2$, near the right in each plot, is due to holographic zero sound. We also find that for larger $\bar{B}$, figs. 3.15 (b) and (d), at intermediate frequencies the spectral function is suppressed by orders of magnitude relative to the holographic zero sound and charge diffusion peaks. That suppression is due to the gap in the holographic zero sound dispersion, as we discuss in more detail in the next subsection. At smaller $\bar{B}$, such as figs. 3.15 (a) and (c), our numerical results indicate that if some suppression of spectral weight occurs in some non-zero range of frequencies at small $\bar{B}$, then either the suppression is very small or the range of frequencies is very narrow.

By studying the spectral function $\bar{\chi}_{tt}(\omega, k)$, we have learned that the response of the

system is simplest to understand using perturbations with fixed frequency $\bar{\omega}$ rather than fixed $\bar{k}$: with fixed $\bar{\omega}$ the spectral function always exhibits only a single peak for any $\bar{B}$, in which case we should be able to characterise the response of the system as either collisionless or hydrodynamic. We are thus able to define a collisionless/hydrodynamic crossover, as we show in the next subsection.

3.4.5 Poles in the complex momentum plane

We saw in the previous subsection that the spectral function $\bar{\chi}_{tt}(\omega, k)$, as a function of momentum $\bar{k}$ at a fixed frequency $\bar{\omega}$, exhibits only a single peak, which in physical terms means the response of the system to an external perturbation with frequency $\bar{\omega}$ is dominated by a single excitation. To study that excitation, we will determine the poles of $G^R_{tt}(\omega, k)$ in the complex $\bar{k}$ plane. We will look for poles with $\mathrm{Re}\,\bar{k} > 0$ and $\mathrm{Im}\,\bar{k} > 0$, and will focus on the poles closest to the origin of the complex $\bar{k}$ plane, corresponding to the modes with the smallest propagating momentum $\mathrm{Re}\,\bar{k}$ and attenuation $\mathrm{Im}\,\bar{k}$.

First, let us revisit the known collisionless/hydrodynamic crossover at $B = 0$, now studying the behavior of poles in the complex $\bar{k}$ plane. In fig. 3.16 we have plotted $\log\left(\mathrm{Re}\,\bar{k}\,(\bar{\omega})\,/\bar{T}^2\right)$ and $\log\left(\mathrm{Im}\,\bar{k}\,(\bar{\omega})\,/\bar{T}^2\right)$ of the pole closest to the origin as functions of $\log\left(\bar{\omega}/\bar{T}^2\right)$, for both D3/D$p$ systems with $\bar{B} = 0$ and $\bar{T} = 0.001$. In fig. 3.16 we also plot the dispersion relations of the holographic zero sound mode at $\bar{T} = 0$, eq (3.44), and of the charge diffusion poles in the complex $\bar{k}$ plane, obtained by inverting (3.50) and (3.51), as well as the location of the collisionless/hydrodynamic crossover extracted from the collision of poles in the complex $\bar{\omega}$ plane, (3.33). We see that at the crossover, no collision of poles occurs in the complex $\bar{k}$ plane. Instead, we see a single pole whose dispersion relation $\bar{k}(\bar{\omega})$ changes at the crossover. For example, we can see from the left plots of fig. 3.16 that $\mathrm{Re}\,\bar{k}(\bar{\omega})$ exhibits a 'kink' at the crossover in both D3/Dp systems.

When $\bar{B}$ is non-zero, we again find no collision of poles in the complex $\bar{k}$ plane. In fact, when $\bar{B} \ll \bar{T}^2$, the behavior of the poles is very similar to the $\bar{B} = 0$ case, as we show in fig. 3.17, which is the same as fig. 3.16, but now with $\bar{B}/\bar{T}^2 = 10^{-2}$. In particular, we still see a kink in $\mathrm{Re}\,\bar{k}(\bar{\omega})$ at approximately the same value of $\bar{\omega}/\bar{T}^2$ as at $\bar{B} = 0$.

When $\bar{B}$ is non-zero and large, $\bar{B} \gg \bar{T}^2$, we find a qualitative difference from the $\bar{B} \ll \bar{T}^2$ case: at low $\bar{\omega}/\bar{T}^2$ the mode is that of charge diffusion until a local *maximum* in $\mathrm{Re}\,\bar{k}(\bar{\omega})$ at some $\bar{\omega}$. For larger $\bar{\omega}$, the mode is no longer that of charge diffusion. We show this in fig. 3.18, which is the same as figs. 3.16 and 3.17, but now with $\bar{B}/\bar{T}^2 = 10^3$

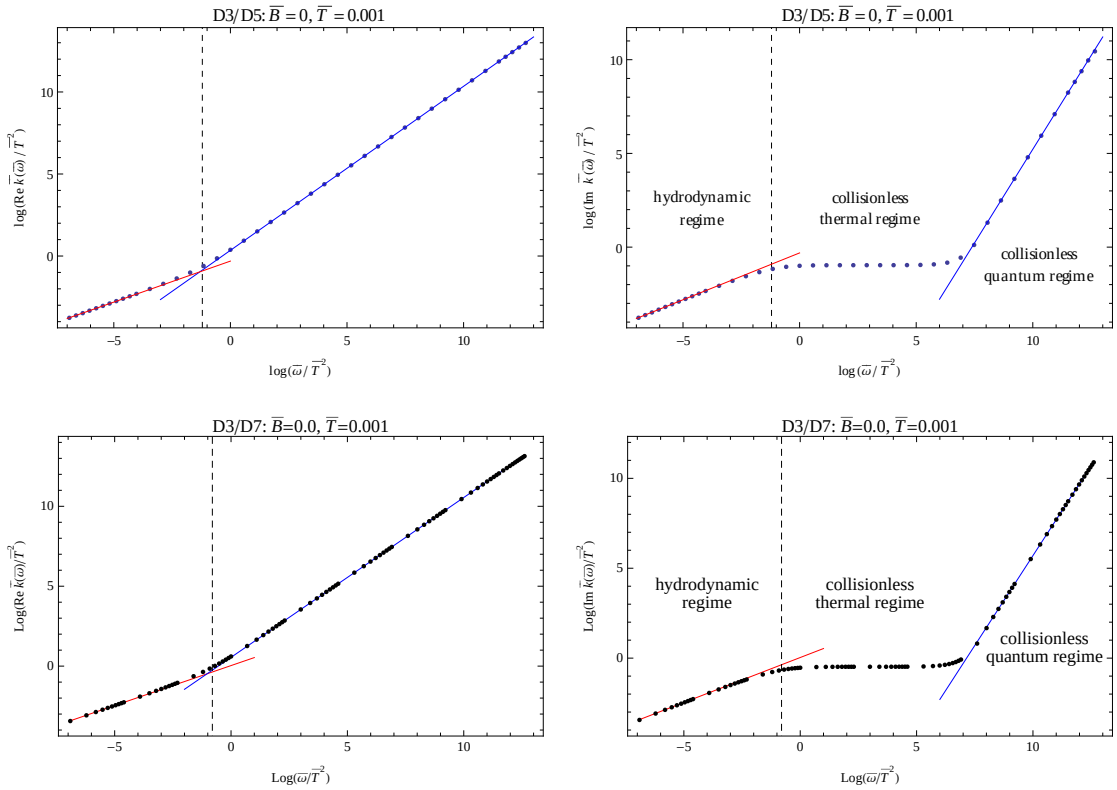

Fig. 3.16: *Top:* $\log\left(\mathrm{Re}\,\bar{k}\left(\bar{\omega}\right)/\bar{T}^2\right)$ (left) and $\log\left(\mathrm{Im}\,\bar{k}\left(\bar{\omega}\right)/\bar{T}^2\right)$ (right) as functions of $\log\left(\bar{\omega}/\bar{T}^2\right)$ for the pole in $G^R_{tt}(\omega,k)$ closest to the origin of the complex $\bar{k}$ plane in the D3/D5 system with $\bar{B}=0$ and $\bar{T}=0.001$. The dots are our numerical results. The solid red lines, beginning on the left of each plot, come from the dispersion relation of the charge diffusion mode obtained by inverting (3.49) and the solid blue lines, beginning on the right of each plot, come from the holographic zero sound dispersion relation at $\bar{T}=0$, (3.44), and the vertical dashed line is the location of the collisionless/hydrodynamic crossover, as defined by a collision of poles in the complex $\bar{\omega}$ plane, (3.33). *Bottom:* The same as the top plots, but for the D3/D7 system. On the right plots we also indicate the hydrodynamic, collisionless thermal, and collisionless quantum regimes, as defined in section 3.3.2.

for the D3/D5 system and $\bar{B}/\bar{T}^2=10^4$ for the D3/D7 system. Remarkably, the local maximum in $\mathrm{Re}\,\bar{k}(\bar{\omega})$ occurs at approximately the same value of $\bar{\omega}/\bar{T}^2$ as the kink in $\mathrm{Re}\,\bar{k}(\bar{\omega})$ at $\bar{B}=0$ (the vertical dashed line in the left plots of fig. 3.18).

In the intermediate regime $\bar{B}\simeq\bar{T}^2$, at low $\bar{\omega}/\bar{T}^2$ the mode is still that of charge diffusion while at high $\bar{\omega}/\bar{T}^2$ the mode is still that of holographic zero sound, and the transition between the two still occurs at approximately the same value of $\bar{\omega}/\bar{T}^2$ as the kink in $\mathrm{Re}\,\bar{k}(\bar{\omega})$ at $\bar{B}=0$, however at the transition neither a sharp kink nor a clear maximum in $\mathrm{Re}\,\bar{k}(\bar{\omega})$ were visible to us. The spectral function, at fixed $\bar{\omega}$, as a function of $\bar{k}$, still exhibits only a single peak, which is due to charge diffusion for small $\bar{\omega}/\bar{T}^2$ and to holographic zero sound for large $\bar{\omega}/\bar{T}^2$.

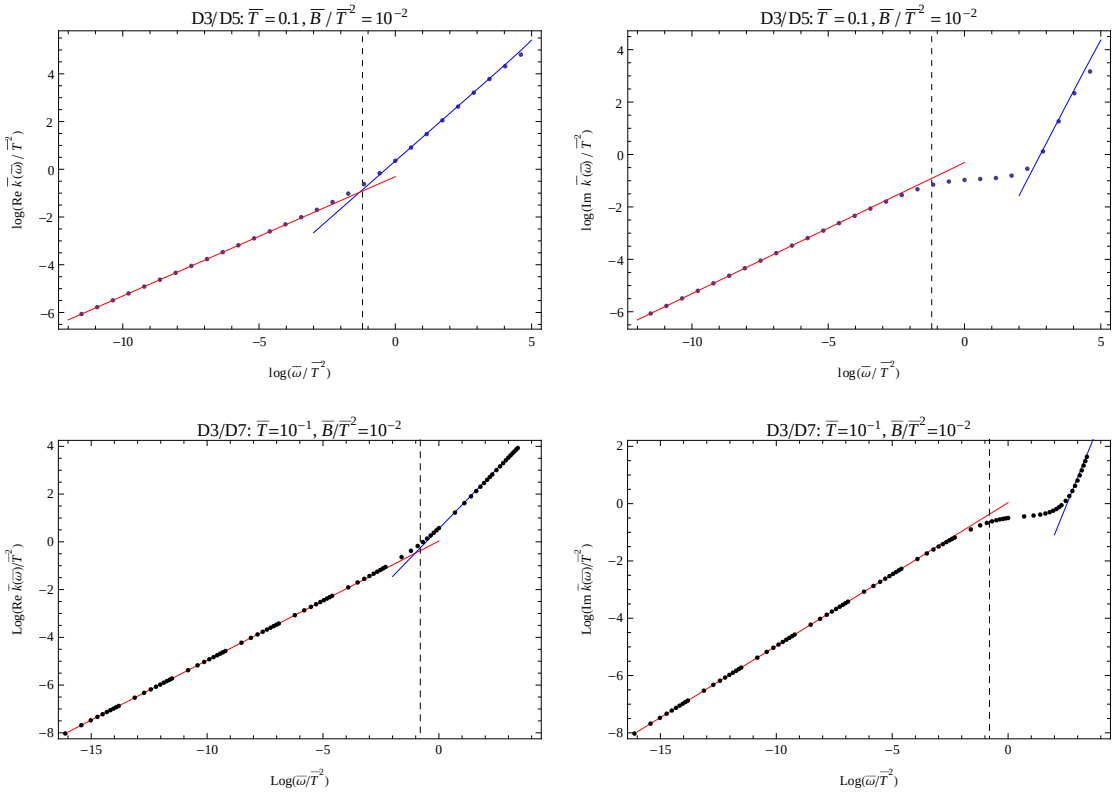

Fig. 3.17: As fig. 3.16 but with $\bar{T}=0.1$ and $\bar{B}/\bar{T}^2=10^{-2}$, within the regime $\bar{B}/\bar{T}^2 \ll 1$. Again the vertical dashed line is the location of the collisionless/hydrodynamic crossover, as defined by a collision of poles in the complex $\bar{\omega}$ plane at $\bar{B}=0$.

We have found that as we increase $\bar{\omega}$ the pole in $G^R_{tt}(\omega,k)$ in the complex $\bar{k}$ plane ceases to be that of charge diffusion approximately at the location of the crossover in the $\bar{B}=0$ case, (3.33), *for any value of* $\bar{B}$. In other words, for any value of $\bar{B}$, the response of the system to a density perturbation with fixed $\bar{\omega}$ below this value is dominated by charge diffusion, while the response to a perturbation with larger $\bar{\omega}$ is not. We have thus identified a clean boundary to the regime of hydrodynamic reponse that is approximately $\bar{B}$-independent. We therefore define the location of the crossover from the hydrodynamic to the collisionless regime as occuring at this value of $\bar{\omega}/\bar{T}^2$, (3.33): for the D3/D5 system $\bar{\omega}\approx 0.30\bar{T}^2$ and for the D3/D7 system $\bar{\omega}\approx 0.45\bar{T}^2$.

Let us now discuss in detail the region of suppressed spectral weight that we mentioned at the end of section 3.4.4, in the regime of large magnetic field, $\bar{B}\gg\bar{T}^2$. In fig. 3.19 we reproduce fig. 3.15, the contour plots of $\log\bar{\chi}_{tt}(\bar{\omega},\bar{k})$ in the plane of $\left(\log\bar{\omega}/\bar{T}^2, \log\bar{k}/\bar{T}^2\right)$, but now with two differences: first, instead of a contour plot of $\log\bar{\chi}_{tt}(\bar{\omega},\bar{k})$ we present a density plot of $\bar{\chi}_{tt}(\bar{\omega},\bar{k})$, and second we superimpose on the density plots our numerical results for the locations of the pole of $G^R_{tt}(\omega,k)$ closest to the

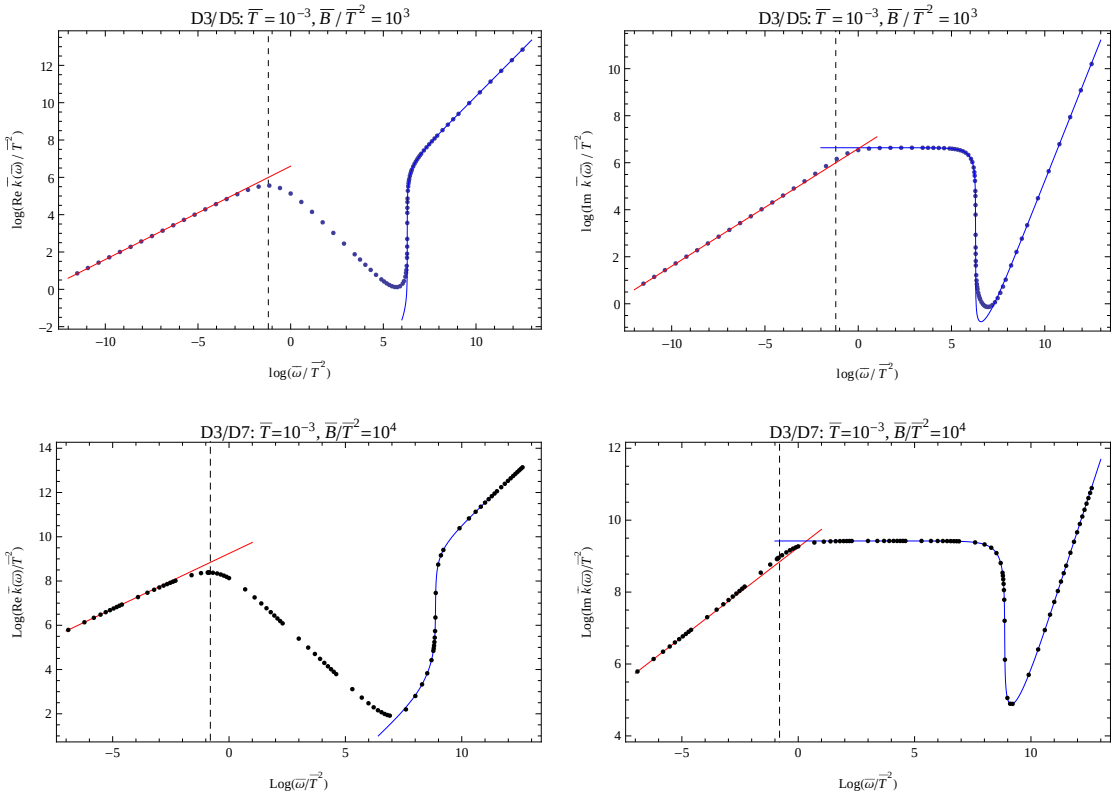

Fig. 3.18: As fig. 3.17 but with $\bar{T} = 10^{-3}$ and $\bar{B}/\bar{T}^2 = 10^3$ for the D3/D5 system and $\bar{B}/\bar{T}^2 = 10^4$ for the D3/D7 system, within the regime $\bar{B}/\bar{T}^2 \gg 1$.

origin in the complex $\bar{k}$ plane as well as the values of $|\bar{k}(\bar{\omega})|$ for the $T = 0$ holographic zero sound dispersion relation, (3.44), and for the charge diffusion, obtained by inverting (3.49). In fig. 3.19 we see clearly that at a fixed frequency $\bar{\omega}$ the peak in the spectral function $\bar{\chi}_{tt}\left(\bar{\omega}, \bar{k}\right)$ is given to good approximation by these values of $\left|\bar{k}\left(\bar{\omega}\right)\right|$.

In the regime $\bar{B}/\bar{T}^2 \gg 1$, as shown in figs. 3.19 (b) and (d), suppose we start with small $\bar{\omega}/\bar{T}^2$, that is, we consider a vertical line near the left of each plot, where the spectral function exhibits a single peak due to charge diffusion. As we increase $\bar{\omega}/\bar{T}^2$, moving to the right in each plot, we encounter the collisionless/hydrodynamic crossover, where the peak is no longer due to charge diffusion. For larger $\bar{\omega}/\bar{T}^2$, a peak is still present in the spectral function, but is smaller by orders of magnitude compared to the charge diffusion peak. Only at sufficiently large $\bar{\omega}/\bar{T}^2$ does the peak grow again by orders of magnitude, now being the peak due to holographic zero sound. In other words, for an intermediate range of frequencies $\bar{\omega}/\bar{T}^2$, the spectral weight is suppressed. The high-frequency end of that intermediate region (on the right in the plots), is marked by a minimum in the value of $\left|\bar{k}\left(\bar{\omega}\right)\right|$ of the corresponding pole: in each of figs. 3.19 (b) and

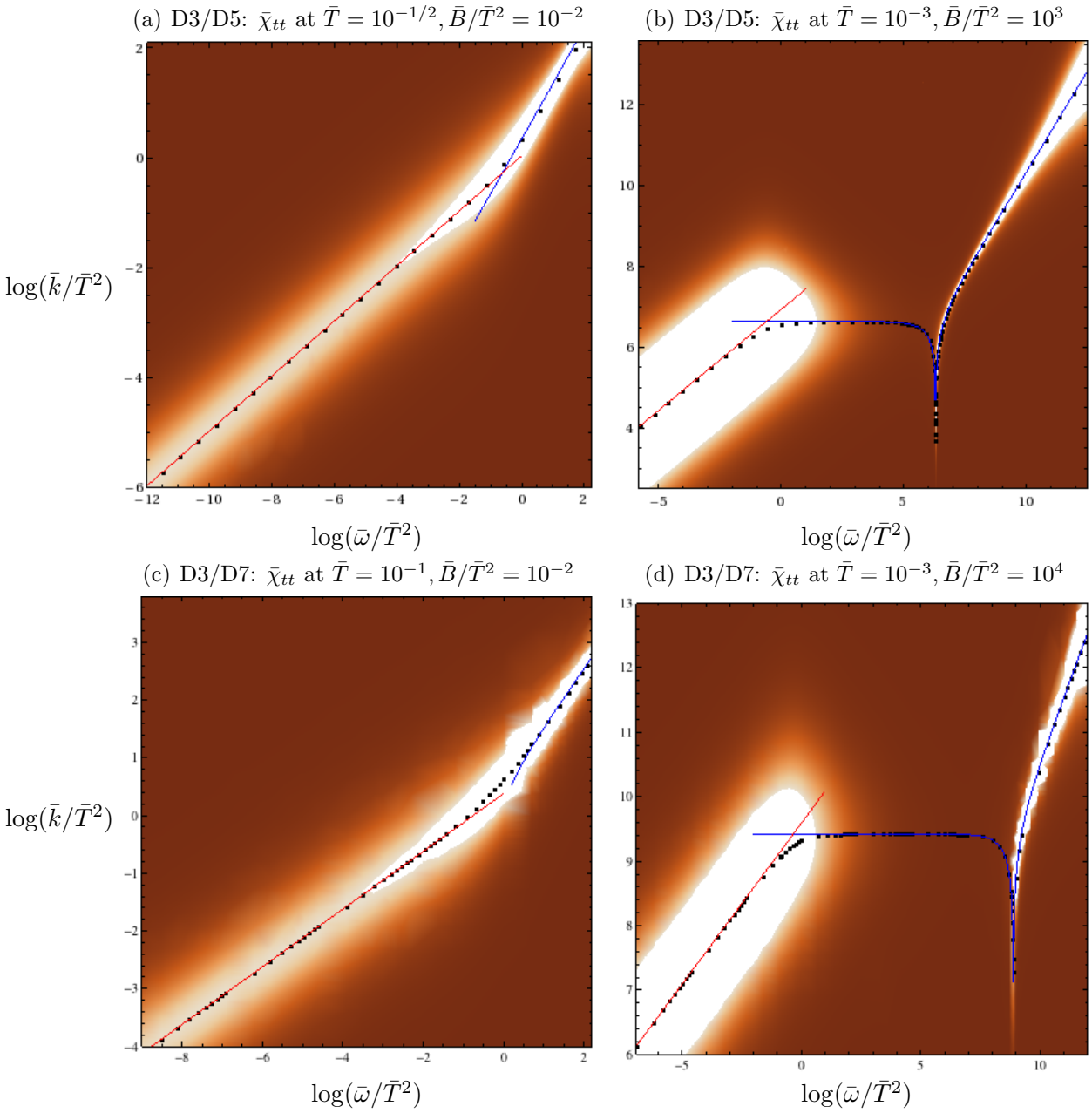

Fig. 3.19: (a) Density plot of our numerical results for $\bar{\chi}_{tt}(\bar{\omega}, \bar{k})$ over the $\left(\log \bar{\omega}/\bar{T}^2, \log \bar{k}/\bar{T}^2\right)$ plane in the D3/D5 system with $\bar{T} = 10^{-1/2}$ and $\bar{B}/\bar{T}^2 = 10^{-2}$. (This plot uses the same data as that used to make fig. 3.15.) Lighter colours represent larger values of the spectral function, as in fig. 3.15. The black dots are our numerical results for the location of the pole in $G^R_{tt}(\omega, k)$ closest to the origin in the complex $\bar{k}$ plane. The solid red line starting at the bottom left of the plot is the value of $\left|\bar{k}\left(\bar{\omega}\right)\right|$ for the charge diffusion mode obtained by inverting the dispersion relation in (3.49), and the solid blue line starting at the top right of the plot is the value of $\left|\bar{k}\left(\bar{\omega}\right)\right|$ for the holographic zero sound mode, (3.44). (b) The same as (a), but with $\bar{T} = 10^{-3}$ and $\bar{B}/\bar{T}^2 = 10^3$. (c) The same as (a) and (b), but for the D3/D7 system with $\bar{T} = 10^{-1}$ and $\bar{B}/\bar{T}^2 = 10^{-2}$. (d) The same as (c), but with $\bar{T} = 10^{-3}$ and $\bar{B}/\bar{T}^2 = 10^4$.

(d), the solid blue line on the right has a cusp with a distinct minimum. The value of $\bar{\omega}$ at that minimum, $\bar{\omega}_{\rm min}$, is fixed by the gap in the holographic zero sound dispersion relation, $\bar{\omega}_{\rm gap}$ in (3.43): in fig. 3.20 we plot $\log\left(\bar{B}/\bar{T}^2\right)$ versus the value of $\log\left(\bar{\omega}_{\rm min}/\bar{T}^2\right)$, and find very good agreement with the value of $\bar{\omega}_{\rm gap}$. Notice that such a minimum does not occur for $\bar{B}/\bar{T}^2 \ll 1$, *i.e.* the solid blue line in figs. 3.19 (a) and (c) has no minimum like that in figs. 3.19 (b) and (d).

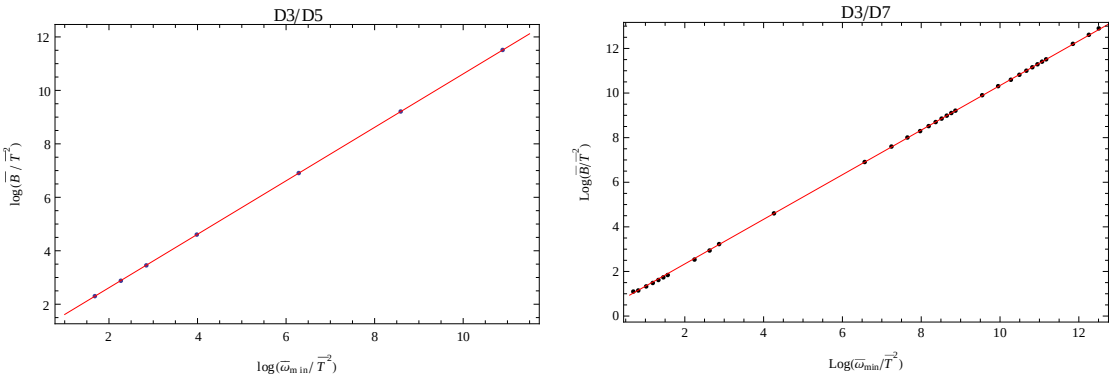

Fig. 3.20: *Left:* $\log\left(\bar{B}/\bar{T}^2\right)$ versus $\log\left(\omega_{\rm min}/\bar{T}^2\right)$ for the D3/D5 system, where $\bar{\omega}_{\rm min}$ is the high-frequency end of the region of suppressed spectral weight, *i.e.* the cusp in the solid blue lines in figs. 3.19 (b) and (d). The dots are our numerical results and the solid red line is derived from the gap in the $\bar{T}=0$ holographic zero sound dispersion relation, the $\bar{\omega}_{\rm gap}$ in (3.43). Clearly (3.43) is a very good approximation to the numerical result for $\bar{\omega}_{\rm min}$. *Right:* The same as the left figure, but for the D3/D7 system.

3.4.6 Overview of the collisionless/hydrodynamic crossover

We can now give an overview of the collisionless/hydrodynamic crossover in our systems at non-zero $\bar{B}$. When $\bar{B} \ll \bar{T}^2$, if we fix a real $\bar{k}$ and study poles in $G^R_{tt}(\omega,k)$ in the complex $\bar{\omega}$ plane, then we find that as we increase $\bar{T}$ a collision of poles occurs, allowing us to define the crossover in a fashion similar to the $\bar{B}=0$ case. When $\bar{B} \gg \bar{T}^2$, no such collision of poles occurs in the complex $\bar{\omega}$ plane. Indeed, in this regime of large $\bar{B}$, the spectral function, for fixed $\bar{k}$ as a function of $\bar{\omega}$, generically exhibits two peaks, one for holographic zero sound and one for charge diffusion, preventing us from identifying this regime as either collisionless or hydrodynamic. We found that for any $\bar{B}$, if we instead fix real $\bar{\omega}$ and study poles in $G^R_{tt}(\omega,k)$ in the complex $\bar{k}$ plane, then we find a single pole, and in the spectral function we find a single peak. As we increase $\bar{T}$, we could then define the crossover as the value of $\bar{T}$ where the single pole becomes that of charge diffusion, and hence the system enters the hydrodynamic regime.

Remarkably, we found that the value of $\bar{T}$ where that crossover occurs is approximately $\bar{B}$-independent, being given by the $\bar{B} = 0$ value, (3.33): $|\bar{\omega}| \approx 0.30\,\bar{T}^2$ for the D3/D5 system and $|\bar{\omega}| \approx 0.45\,\bar{T}^2$ for the D3/D7 system. In the language of LFL theory, this would indicate that the collision frequency of the quasiparticles is independent of $\bar{B}$. We summarise our results in fig. 3.21.

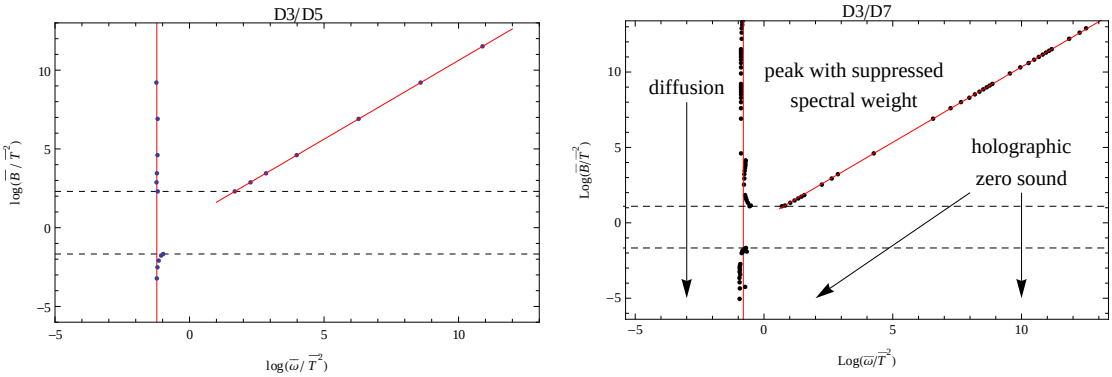

Fig. 3.21: An overview of our main results: $\log\left(\bar{B}/\bar{T}^2\right)$ versus $\log\left(\omega/\bar{T}^2\right)$ for the D3/D5 system (left) and the D3/D7 system (right). The lines and dots have the same meanings in the two plots. The solid red vertical line denotes the collisionless/hydrodynamic crossover, defined for increasing $\bar{T}$ with fixed $\bar{\omega}$ as the value of $\bar{T}$ where the pole of $G^R_{tt}(\omega, k)$ closest to the origin of the complex $\bar{k}$ plane becomes that of charge diffusion. That value of $\bar{T}$ is approximately the same as the $\bar{B} = 0$ value in (3.33). The dots on the solid red vertical line above the dashed lines are extracted from poles in the complex $\bar{k}$ plane, as discussed in section 3.4.5, while those below the dashed lines are extracted from a collision of poles in the complex $\bar{\omega}$ plane, as discussed in sections 3.3.2 and 3.4.3. In the region between the horizontal dashed lines we had difficulty extracting a precise location of the crossover from our numerics. The solid red diagonal line is the value of the gap in the $T = 0$ dispersion relation for holographic zero sound, (3.43). The dots on the solid red diagonal line are our numerical results for $\bar{\omega}_{\rm min}$, reproduced from fig. 3.20. On the right figure we have indicated the nature of the dominant peak in the spectral function with fixed $\bar{\omega}$ as a function of $\bar{k}$.

We can actually provide a quantitative estimate of the $O(1)$ value of $\bar{B}/\bar{T}^2$ at which, as $\bar{B}$ increases in the collisionless regime, the gap in the holographic zero sound dispersion relation produces suppression of spectral weight. In fig. 3.21, the diagonal red line represents the value of the gap $\bar{\omega}_{\rm gap}$ in the $\bar{T} = 0$ dispersion relation of the holographic zero sound, (3.43), while the vertical red line represents the location of the crossover, *i.e.* the value of $\bar{\omega}$ in (3.33). By extending the diagonal red line down to the intersection with the vertical red line, we can estimate the $O(1)$ value of $\bar{B}/\bar{T}^2$ that we want: we simply equate the $\bar{\omega}_{\rm gap} \propto \bar{B}$ in (3.43) with the $\bar{\omega} \propto \bar{T}^2$ in (3.33) and solve for $\bar{B}/\bar{T}^2$,

$$\bar{B}/\bar{T}^2 \approx \begin{cases} 0.56 & \text{for D3/D5,} \\ 0.63 & \text{for D3/D7.} \end{cases} \tag{3.52}$$

For a holographic quantum liquid in which the $U(1)$ density is produced by fermions alone, a result of [160] is that the holographic zero sound's dispersion relation becomes gapped when $\bar{B}/\bar{T}^2 \gtrsim 0.18$. The relationship between that value of $\bar{B}/\bar{T}^2$ and the value above which the spectral weight of the holographic zero sound is suppressed would be interesting to study.

Chapter 4

A soliton menagerie in AdS

In this chapter, based on [161], we study charged scalar solitons in asymptotically global AdS_4 spacetimes.

We focus on three specific bulk theories: (i) a phenomenological Abelian-Higgs model with a massive charged scalar, (ii) the consistent truncation of [46] and (iii) a consistent truncation of eleven-dimensional supergravity originally studied in [104] (and more recently in [116]). In the following section we describe these theories and discuss the general features common to all examples.

We then move on to explore the behaviour of charged scalar solitons in these theories in the following three sections. For given Lagrangian parameters we encounter multiple branches of solitons: some which are perturbatively connected to the AdS vacuum and surprisingly, some which are not. We explore the phase space of solutions by tuning the charge of the scalar field and changing scalar boundary conditions at AdS asymptopia, finding intriguing critical behaviour as a function of these parameters. In particular, we demonstrate that global solitons can generically become large relative to the AdS length scale and furthermore, in the planar limit they smoothly connect up with the zero temperature limit of planar scalar hair black holes.

4.1 Generalities

First we set the stage for our discussion of solitons. We describe the bulk theories and the ansatz we work with, along with details of the choice of boundary conditions at our disposal. After a brief summary of known analytical solutions, we quickly review the

planar limit of global solitons, which forms a crucial component of our considerations in later sections.

4.1.1 Theories, Ansätze and boundary conditions

We begin our exploration of gravitating global solitons in the familiar territory of phenomenological models for superfluid instabilities [31]. This family of theories contains all the ingredients we require to build global soliton solutions, whilst providing some useful dials with which we can navigate the space of solutions. In detail, this family is parametrised by the mass m_ψ and charge q of the scalar field and we write the action as

$$S = \frac{1}{16\pi G_4}\int d^4x\sqrt{-g}\left(R + \frac{6}{\ell^2} - \frac{1}{4}\hat{F}^2 - \left|d\psi - iq\hat{A}\ell^{-1}\psi\right|^2 - m_\psi^2|\psi|^2\right) \tag{4.1}$$

supplemented by appropriate boundary terms, where $\hat{F} = d\hat{A}$ is the Maxwell field strength and ℓ is the AdS length.[1] We will find it convenient to work with manifestly real and gauge invariant quantities, which can be achieved at the level of the action by absorbing the phase α of the scalar $\psi = \phi\, e^{i\alpha}$ into the gauge field, $A \equiv \hat{A} - q^{-1}\ell d\alpha$:

$$S = \frac{1}{16\pi G_4}\int d^4x\sqrt{-g}\left(R - \frac{1}{4}F^2 - (\partial\phi)^2 - \frac{1}{\ell^2}q^2\phi^2A^2 - \frac{1}{\ell^2}\left(-6 + m_\phi^2\ell^2\,\phi^2\right)\right), \tag{4.2}$$

where ϕ is real and $m_\phi \equiv m_\psi$. The equations of motion of this new action are the same as those arising from (4.1).[2] As we will see momentarily, the advantage of this form is that the action may be more readily compared with consistent truncations.

Working with phenomenological models is instructive, but has a number of drawbacks. One concern is that any interesting features might be artefacts of the chosen action. Indeed, one could consider infinitely many alterations of the action (4.2). In a phenomenological context it is also more difficult to discuss consequences for any CFT dual. For these reasons we also adopt two consistent truncations of 11D supergravity with the same field content. In previous work [106], global soliton solutions were constructed within a truncation of $\mathcal{N} = 8$ $SO(6)$ gauged supergravity in (4+1) dimensions, where equal charges were turned on in $U(1)^3 \subset SO(6)$. Here we will be interested in a lower dimensional analogue, employing truncations of (3+1)-dimensional $\mathcal{N} = 8$ $SO(8)$

[1] Note that we have changed conventions slightly with respect to (2.1) such that the rescaled gauge field is now dimensionless.

[2] The equation of motion for the phase $\nabla_a\left(A^a\phi^2\right) = 0$ follows from the Maxwell equations, and is a consequence of conservation of the global $U(1)$ current, $J^a \propto \phi^2A^a$. Recall that α is contained in A in a gauge invariant manner.

gauged supergravity. Superfluid black branes for various truncations of this $SO(8)$ theory were considered in [116]. We will consider the equally charged truncation $U(1)^4 \subset SO(8)$ [116] and we will consider also a single field truncation first studied in [46] (the M-theory superconductor construction). Whilst this latter single field truncation admits a $SU(4)$ invariance, it is part of a larger $SU(3) \subset SO(8)$ truncation [162] explored in [116], as such we shall refer to this as the $SU(3)$ truncation.

Moving forward we employ a bulk action that is sufficiently general to encompass each of these theories:

$$S_{\text{bulk}} = \frac{1}{16\pi G_4}\int d^4x\sqrt{-g}\left(R - \frac{1}{4}F^2 - (\partial\phi)^2 - \frac{1}{\ell^2}Q(\phi)A^2 - \frac{1}{\ell^2}V(\phi)\right). \tag{4.3}$$

The equations of motion from this action and the required boundary terms are presented in appendix 4.A. The specific cases of the charge coupling $Q(\phi)$ and potential $V(\phi)$ for the theories of interest are summarised in table 4.1. For the rest of this chapter, we will

Theory	$Q(\phi)$	$V(\phi)$	$\text{mass}^2\,\ell^2$	charge
Phenomenological [31]	$q^2\phi^2$	$-6 + m_\phi^2\ell^2\,\phi^2$	$m_\phi^2\ell^2$	q
$SU(3)$ [46]	$\frac{1}{2}\sinh^2\sqrt{2}\phi$	$\cosh^2\frac{\phi}{\sqrt{2}}\left(-7+\cosh\sqrt{2}\phi\right)$	-2	1
$U(1)^4$ [116]	$\frac{1}{2}\sinh^2\frac{\phi}{\sqrt{2}}$	$-2\left(2+\cosh\sqrt{2}\phi\right)$	-2	$\frac{1}{2}$

Table 4.1: Components of the action (4.3) for the theories under consideration, together with the mass and charge for the scalar field fluctuations about the $\phi = 0$ extremum of $V(\phi)$.

specialise to the case $m_\phi^2\,\ell^2 = -2$ when discussing the phenomenological theory.[3] For orientation we show the scalar potentials for the three cases in fig. 4.1; some of their features will play a role in our analysis later. We will set the AdS length scale $\ell = 1$ in what follows.

Ansatz for global solitons

Throughout this chapter we will employ the following metric ansatz (preserving $\mathbb{R}_t \times SO(3)$) for spherically symmetric, static global solutions:

$$ds^2 = -g(r)e^{-\beta(r)}dt^2 + \frac{dr^2}{g(r)} + r^2 d\Omega_2^2 \tag{4.4}$$

[3] Many of the features we encounter generalise to other values of $m_\phi^2\,\ell^2$. Heuristically we expect the properties of the solutions we consider to depend on the charge to mass ratio of the scalar field, which after all controls the balance of Maxwell repulsion versus gravitational attraction.

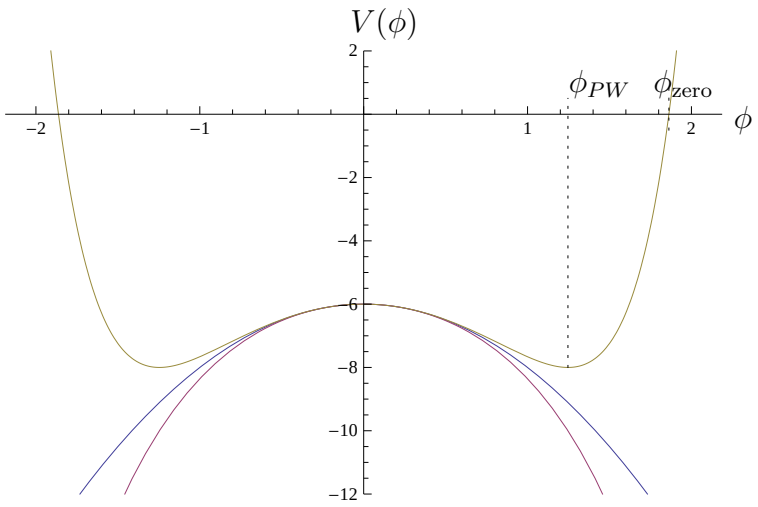

Fig. 4.1: The scalar potentials for the three models we consider. The $SU(3)$ truncation has the potential with a global minimum at ϕ_{PW} and a zero at ϕ_{zero}. The Abelian-Higgs potential and the $U(1)^4$ truncation have potentials that are unbounded from below, with the latter being exponential (thus steeper) while the former is quadratic.

where $d\Omega_2^2$ is the line element for a unit S^2. For the vector and scalar field we take $A = A_t(r)dt$ and $\phi = \phi(r)$. Thus for the solutions of interest $\xi = \partial_t$ is a timelike Killing vector field and since $\mathcal{L}_\xi \phi = \mathcal{L}_\xi A = 0$ our solutions are globally static solitons.

With this ansatz, the boundary of global AdS is located at $r \to \infty$, where the fields admit the asymptotic expansions

$$A_t(r) = \mu - \frac{\rho}{r} + \dots \tag{4.5a}$$

$$\phi(r) = \frac{\phi_1}{r} + \frac{\phi_2}{r^2} + \dots \tag{4.5b}$$

$$\beta(r) = \beta_\infty + \dots \tag{4.5c}$$

$$g(r) = r^2 + 1 + \frac{\phi_1^2}{2} - \frac{g_1}{r} + \dots \tag{4.5d}$$

for each of the theories listed in table 4.1. We will use coordinate freedom in t to set $\beta_\infty = 0$. We will require in most cases that the solutions are regular at the origin in the IR, which determines the following small r expansion near $r = 0$:

$$A_t(r) = A_c + \dots \tag{4.6a}$$

$$\phi(r) = \phi_c + \dots \tag{4.6b}$$

$$\beta(r) = \beta_c + \dots \tag{4.6c}$$

$$g(r) = 1 + \dots \tag{4.6d}$$

In this expansion $g(r)$ is completely determined and the expansion proceeds in powers of r^2 as required.

Boundary conditions for the scalar

Since the scalar field ϕ has mass $m_\phi^2 = -2$, which is the conformal mass term in AdS_4, we have a choice of boundary conditions as mentioned at the end of section 1.1.1. We can impose the standard (ϕ_1 fixed) or alternate (ϕ_2 fixed) boundary conditions, or we can also consider more general multi-trace boundary conditions. For the standard and alternate boundary conditions we denote the CFT operator dual to ϕ as $\mathcal{O}_{\phi_1}$ or $\mathcal{O}_{\phi_2}$, with dimensions $\Delta = 2$ or $\Delta = 1$, respectively. Note that as a result we have $\langle \mathcal{O}_{\phi_1} \rangle = \phi_2$ *etc.*. In the $U(1)^4$ truncation, turning on the $\Delta = 1$ operator is a supersymmetric deformation of the CFT [104]. As described in [99, 100] the multi-trace boundary conditions are in general given by picking a local functional $\phi_2(\phi_1)$. Of particular interest to us will be the relevant double-trace operator $\mathcal{O}_{\phi_2}^2$ that we will turn on to deform the CFT:

$$\delta S_{\text{CFT}} \propto \int d^3x \, \varkappa \, \mathcal{O}_{\phi_2}^2. \tag{4.7}$$

This is achieved by choosing

$$\phi_2(\phi_1) = \varkappa \, \phi_1. \tag{4.8}$$

Such a deformation will be useful for exploring the structure of solutions arising in consistent truncations. Previous work involving the use of double-trace deformations in the context of holographic superfluids can be found in [119].

Conserved charges from asymptotics

Once we have fixed our boundary conditions, we can immediately read off the conserved charges. From the fall-off of the scalar field we learn that for standard and alternate boundary conditions, the vacuum expectation value (vev) of the dual CFT operator is

$$\langle \mathcal{O}_{\phi_1} \rangle = \phi_2 \;\; (\Delta = 2, \varkappa \to \infty) \, , \qquad \langle \mathcal{O}_{\phi_2} \rangle = \phi_1 \;\; (\Delta = 1, \varkappa = 0), \tag{4.9}$$

while for double-trace deformations we have

$$\langle \mathcal{O}_{\phi_2} \rangle = \phi_1 \;\; (\varkappa \neq 0). \tag{4.10}$$

The fall-off of the gauge field tells us that the boundary chemical potential is set by μ, while ρ gives the charge density. The ADM mass density of our solution is obtained from the fall-off of the metric and the scalar field (see appendix 4.A); for double-trace boundary conditions (4.8) we have

$$m = g_1 + \frac{3}{2}\varkappa\phi_1^2\,, \tag{4.11}$$

while for solutions with vevs for single-trace operators (*i.e.* either $\phi_1 \neq 0$ or $\phi_2 \neq 0$),

$$m = g_1\,. \tag{4.12}$$

For brevity we will often denote the CFT quantities characterising the bulk gravitational solution (parametrised by the core value of the scalar ϕ_c) collectively via $\mathcal{X} = \{m, \rho, \langle\mathcal{O}\rangle\}$. These data correspond to the one-point function of conserved operators ($T_{\mu\nu}$ and J_μ) and of $\mathcal{O}$ and serve to characterise the CFT state.

4.1.2 Exact solutions

For each of the theories in table 4.1 we have simple solutions at $\phi = 0$, where $V'(0) = Q'(0) = Q(0) = 0$. At this point in moduli space we have a family of exact solutions, the Reissner-Nordström-AdS$_4$ (henceforth RN-AdS$_4$) black hole:

$$g(r) = r^2 + 1 - \frac{m}{r} + \frac{\rho^2}{4r^2}, \quad \beta(r) = 0, \quad A_t(r) = \mu - \frac{\rho}{r} \quad \text{at} \quad \phi(r) = 0, \tag{4.13}$$

which for $m = \rho = 0$ is global AdS$_4$ with radius of curvature ℓ (here set to 1). Fluctuations of the scalar field about this point have masses and charges given by the last two columns in table 4.1.

Other vacua in $SU(3)$

For the phenomenological theory and the $U(1)^4$ equal charged truncation, $\phi = 0$ is the only extremum of $V(\phi)$. However, for the single scalar truncation of $SU(3)$ there are two more located at $\phi = \phi_{PW} = \pm\sqrt{2}\,\mathrm{arccosh}\,\sqrt{2}$.[4] At this point we have another

[4]This vacuum was shown to be perturbatively unstable in [162]. We anticipate that the properties of the solutions constructed and conclusions drawn in this chapter will not depend on this fact. One could instead study a perturbatively stable alternative, for example the single field truncation of [163]. The auther wishes to thank Nikolay Bobev for pointing this out.

one-parameter family of exact solutions:

$$g(r) = \frac{4}{3}r^2 + 1 - \frac{m}{r}, \quad \beta(r) = 0, \quad A_t(r) = 0 \qquad \text{at} \quad \phi(r) = \pm\sqrt{2}\,\text{arccosh}\,\sqrt{2}, \quad (4.14)$$

which for $m = 0$ is global AdS_4 with radius of curvature $\frac{\sqrt{3}}{2}$.

Singular neutral solitons in $U(1)^4$

We also find the following one-parameter family of singular solutions in the $U(1)^4$ truncation, parametrised by the $\Delta = 1$ scalar fall off, ϕ_1:

$$\begin{gathered} g(r) = r^2 + 1 + \frac{\phi_1^2}{2} + \frac{\phi_1^2}{2r^2}, \quad e^{-\beta(r)}g(r) = r^2 + 1, \\ A_t(r) = 0, \quad \phi(r) = \sqrt{2}\,\text{arcsinh}\,\frac{\phi_1}{\sqrt{2}r}. \end{gathered} \tag{4.15}$$

This solution corresponds to a neutral soliton with no conserved charges, but has a non-trivial vev $\langle \mathcal{O}_{\phi_2} \rangle$. From the asymptotic scalar fall-off it is clear that there is no deformation in the dual CFT. The solution above corresponds to a designer gravity soliton where the $\Delta = 1$ operator $\mathcal{O}_{\phi_2}$ of the CFT spontaneously acquires an expectation value that breaks the $U(1)$ global symmetry on the boundary. The planar limit of this singular global solution, to be discussed later, will play an important role in the supersymmetric solutions of this theory.

4.1.3 The planar limit of global AdS solutions

In this chapter we will be faced with families of global solutions; indeed, we have already encountered some examples in section 4.1.2. We will be able to construct planar solutions by taking a limit of these global families of solutions, if the appropriate limit exists. This will allow us to make comparisons with solutions in planar AdS, many of which have already been constructed.

Heuristically, the planar limit can be visualised as arising when the object of interest (say the soliton) becomes parametrically larger in size when compared with the AdS scale ℓ (here set to 1). In a sense, the object is reaching out towards the AdS boundary and hence one can zoom into a local patch. As we do so, the effects of curvature become less significant and the boundary begins to look planar. Of course, in the process of zooming we must ensure that masses, charges or expectation values can be made sufficiently large,

sufficiently quickly in order that we do not end up in vacuum Poincaré AdS. The goal of this section is to quantify this scaling limit.

Consider the simple example of the global Schwarzschild-AdS$_4$ solution, the $\rho = 0$ case of (4.13):

$$ds^2 = -r^2\left(1+\frac{1}{r^2}-\frac{m}{r^3}\right)dt^2 + \frac{dr^2}{r^2\left(1+\frac{1}{r^2}-\frac{m}{r^3}\right)} + r^2 d\Omega_2^2 \tag{4.16}$$

This is a one-parameter family of solutions; a physical measure of the mass can be constructed by taking an appropriate ratio with the curvature scale of the boundary, for example. For a fixed solution on this branch, there is no analogue of the Poincaré AdS scaling symmetry, which applied as a coordinate scaling

$$r \to \xi\, r, \qquad t \to \xi^{-1} t \tag{4.17}$$

alters the metric in the following way

$$ds^2 = -r^2\left(1+\frac{1}{\xi^2 r^2}-\frac{m}{\xi^3 r^3}\right)dt^2 + \frac{dr^2}{r^2\left(1+\frac{1}{\xi^2 r^2}-\frac{m}{\xi^3 r^3}\right)} + r^2\xi^2 d\Omega_2^2. \tag{4.18}$$

Taking ξ finite does not change the boundary curvature; after all, we are only making a change of coordinates. However, if we take the singular limit $\xi \to \infty$ of this coordinate transformation, then the boundary curvature becomes zero. In this limit, curvature and mass terms disappear and we are left with Poincaré AdS. If however, we simultaneously move along the branch of solutions,

$$r \to \xi\, r, \qquad t \to \xi^{-1} t, \qquad m \to \xi^3\, m, \qquad \xi^2\, d\Omega_2^2 \to d\vec{x}_2^2, \tag{4.19}$$

then in the $\xi \to \infty$ limit a mass term survives:

$$ds^2 = -r^2\left(1-\frac{m}{r^3}\right)dt^2 + \frac{dr^2}{r^2\left(1-\frac{m}{r^3}\right)} + r^2\, d\vec{x}_2^2; \tag{4.20}$$

namely, we have recovered planar Schwarzschild-AdS$_4$. Note that each choice of m in (4.20) is equivalent up to coordinate transformations, so it is a zero-parameter family. Another way of saying this is that m has scaling dimension 3, and without another parameter we cannot construct a quantity invariant under the scaling symmetry (where we now must include x^i rescaling). It is important to emphasise that in order to obtain a non-trivial solution in the planar limit it was necessary to have a branch of solutions with

an unbounded asymptotic coefficient. In doing so we have moved from a one-parameter family of global solutions to a single planar solution. Similarly, we may obtain planar solutions by applying this procedure to the global solutions (4.14) and (4.15).

More generally we can consider a family of global solutions characterised by their asymptotic expansion (4.5). For concreteness we focus on a one-parameter family of solutions, with parameter v. The asymptotic coefficients of these solutions will be functions of v, and in general we will have five of them:

$$m(v), \quad \mu(v), \quad \rho(v), \quad \phi_1(v), \quad \phi_2(v). \tag{4.21}$$

with scaling dimensions $3, 1, 2, 1, 2$ respectively. If any one of these is unbounded from above, it is easy to show that a planar solution exists with a non-trivial asymptotic expansion. The global Schwarzschild-AdS$_4$ solution considered above is one example.

The number of asymptotic charges that survive in the planar limit depends not only on whether that parameter is unbounded, but also on how fast it grows along the branch compared with other coefficients. Let us work with quantities of unit scaling dimension:

$$\tilde{c}_I(v) \equiv c_I(v)^{\frac{1}{\Delta[c_I]}}, \tag{4.22}$$

where $\Delta[c_I]$ denotes the scaling dimension of c_I. We require at least one coefficient to be unbounded along the branch, and in this regime we may study their growth assuming a power-law v dependence,

$$v\frac{d}{dv}\tilde{c}_I(v) = p_I\,\tilde{c}_I(v). \tag{4.23}$$

In particular we can choose our parameter along the branch, v, to coincide with $\tilde{c}_I$ for the largest p_I. Then, in this new parameterisation, the coefficient $\tilde{c}_I$ will survive the planar limit if it scales as

$$v\frac{d}{dv}\tilde{c}_I(v) = \tilde{c}_I(v). \tag{4.24}$$

as we send $v \to \infty$.

Let us take the example of an unbounded mass, $m^{1/3}$, growing fastest out of all five coefficients. We know at least that m survives the limiting process. In order for the other coefficients to survive in the planar limit, they must grow as

$$c_I(m) \propto m^{\frac{\Delta[c_I]}{3}}. \tag{4.25}$$

For example, the ϕ_1 must be unbounded and grow $\phi_1 \propto m^{\frac{1}{3}}$ at large m, if we are to

have $\langle \mathcal{O}_{\phi_2} \rangle \neq 0$ in the planar theory. If at least two coefficients survive in the planar limit, they can be used to construct the physical parameters of the planar solution. For example, $m\,\phi_1^{-3}$ is a quantity with scaling dimension zero and is therefore a physical parameter on the space of planar solutions.

The above results trivially generalise to higher dimensions: note that m, the mass density, has scaling dimension d in AdS_{d+1}. From this we can infer an important point: for a conserved $U(1)$ charge ρ it is easy to show using the above that $\rho \propto m^{\frac{d-1}{d}}$ in AdS_{d+1}. On the other hand the BPS equations for supersymmetric solutions (relevant in particular for $d \leq 6$) imply that $m \propto \rho$. Thus if we had a global AdS_{d+1} supersymmetric solution and consider scaling it to the planar limit, we will necessary end up with an $m = 0$ planar solution. Note that this general argument, based on scalings alone, does not exclude the possibility that a supersymmetric global solution can connect with a planar solution with $m = 0$ and $\rho \neq 0$ and in fact we will see an example of this in section 4.4.2. Of course, with such scalings there is a danger that the resulting solution with planar symmetry can be horribly unphysical: a case in point is the scaling limit of the $m = \rho$ RN-AdS_4 solution which leads to a zero mass, but non-zero charge planar singular solution.

In the following sections we will see examples of branches of solutions where all asymptotic coefficients are bounded, and therefore do not connect with the planar limit. We will also see cases where all coefficients grow in exactly the right way to survive taking the planar limit and an example where only $\langle \mathcal{O}_{\phi_2} \rangle$, *i.e.* ϕ_1, survives. The latter example will actually correspond to a supersymmetric solution scaled up to the planar limit consistent with the observation above.

4.2 Phenomenological Abelian-Higgs models

The simplest bulk Lagrangian we consider is the Abelian-Higgs model coupled to gravity (4.2). We fix the mass of the scalar field $m_\phi^2 = -2$ and study the space of solutions as a function of q. As discussed we will work in the ansatz outlined in section 4.1.1, whose large r behaviour is given by (4.5). The behaviour of the fields in the IR ($r \to 0$) will depend on the specific solution considered.

4.2.1 Global solitons

First we construct horizon-free regular global soliton solutions whose IR boundary conditions are given by the core expansion (4.6). We pick a theory by fixing q. The near core expansion contains three undetermined coefficients, whilst the asymptotic expansion contains four once we specify a boundary condition for the scalar, discussed previously. The total differential order of the equations of motion is six so we therefore expect to find one-parameter branches of solutions within a given theory. In this subsection we illustrate our findings for the choice $\phi_1 = 0$, corresponding to an expectation value for an operator $\mathcal{O}_{\phi_1}$ with $\Delta = 2$.

Condensates of the $\Delta = 2$ operator $\mathcal{O}_{\phi_1}$

Let us begin by considering solutions that are accessible within perturbation theory about the vacuum global AdS_4 solution (the $m = \rho = 0$ case of (4.13)). We demonstrate how these can be constructed analytically in appendix 4.B; here we present the results of direct numerical integration of the equations of motion.

For any value of $q \neq 0$, we find a branch of smooth solitons that is continuously connected to the global AdS_4 vacuum, parametrised by the core value of the scalar ϕ_c. From the results of the perturbative construction, we learn that for small solitons $m = \rho/q$, while small extremal RN-AdS_4 black holes have $m = \rho$. This implies that for $q < q_{\rm ERN} \equiv 1$, the solitons we construct will be heavier than RN-AdS_4 black holes in a fixed charge sector [105]. We focus on the regime $q > q_{\rm ERN}$ to illustrate some of the new features in the space of soliton solutions.

For orientation in fig. 4.2 we present the radial profile of ϕ for a representative global soliton in this regime. To obtain this solution we picked a theory by fixing q, then picked a value for ϕ_c to specify a position along the one-parameter family of solutions.

The solution constructed in fig. 4.2 has no nodes in the scalar profile, since we have tried to macroscopically populate the single particle ground state of the scalar field. As explained in section 1.3, the linear scalar wave equation in global AdS has a discrete spectrum of eigenstates with energies $\omega = \Delta + 2\,n$ (setting $l = 0$ for spherically symmetric configurations). We are going to focus on solitons that have $n = 0$; there are other solutions at the same value of q and ϕ_c with higher numbers of nodes in the radial profile, corresponding to populating the excited oscillator states. Such solutions have lower masses and can also be constructed perturbatively (cf. [105]). We will not study

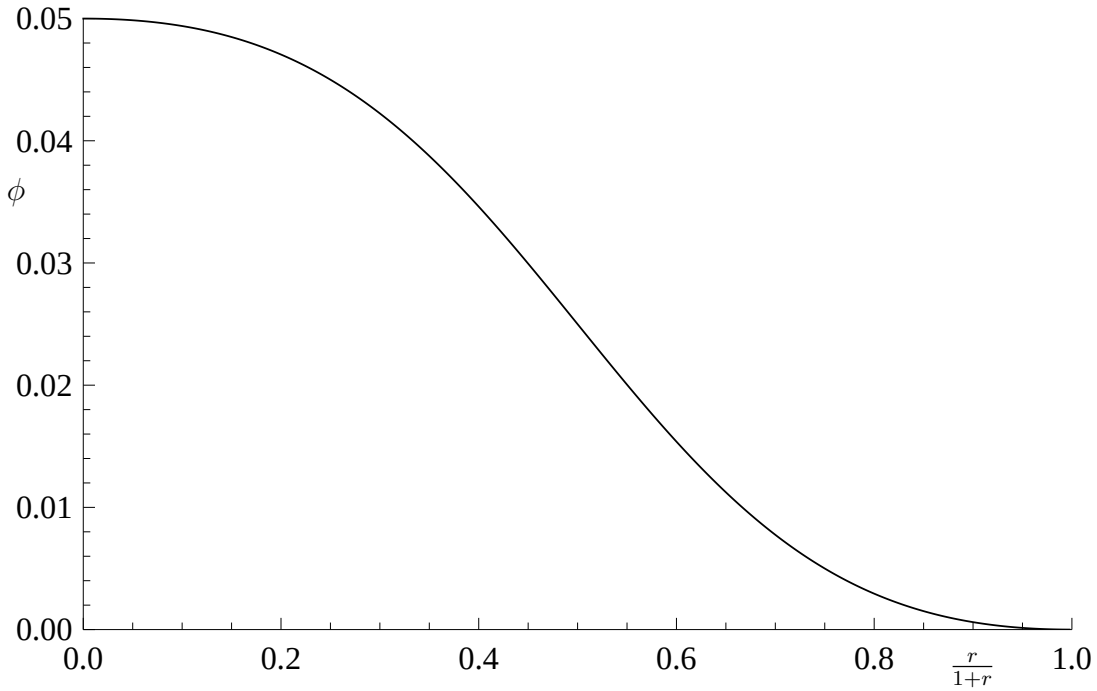

Fig. 4.2: $\phi(r)$ for a representative low mass global soliton with $\Delta = 2$ boundary condition. For this solution we have chosen $q^2 = 1.2$ and fixed the point along the branch by fixing $\phi_c = 0.05$. At this point we find asymptotic data: $q\mu = 2.001(4), \rho = 0.002(1), m = 0.001(9), q\phi_2 = 0.053(6)$ and other near core data: $qA_c = 1.998(4), \beta_c = 0.002(5)$.

such solutions here.[5]

Starting with the zero node solutions we can consider moving along the branch to larger ϕ_c values within a fixed theory (fixed q). As we do we leave the realm of solutions which may be approximated by perturbation theory. Outside the perturbative regime we find that the solutions strongly depend on the charge parameter q. This is illustrated by mass, m, along the branch and is shown in fig. 4.3. We find that m is either bounded or unbounded depending on the value of q, and that there is a critical value $q = q_c$ at which there is a transition between the two behaviours. Numerically we find

$$q_c^2 \simeq 1.259 \ , \qquad \phi_1 = 0 \ \ \text{(equivalently } \Delta = 2). \tag{4.26}$$

The nature of the transition is not clear from considering only these branches of solutions and we will address this momentarily.

For $q < q_c$ all asymptotic charges $\mathcal{X} = \{m, \rho, \phi_2\}$ and μ are bounded, non-monotone functions of ϕ_c. We know from the discussion of section 4.1.3 that this branch of solutions therefore does not connect with a non-vacuum solution in the planar limit; implementing

[5] At fixed ϕ_c, higher node solutions have lower masses; however, holding ρ fixed leads to these being heavier than the zero node solutions.

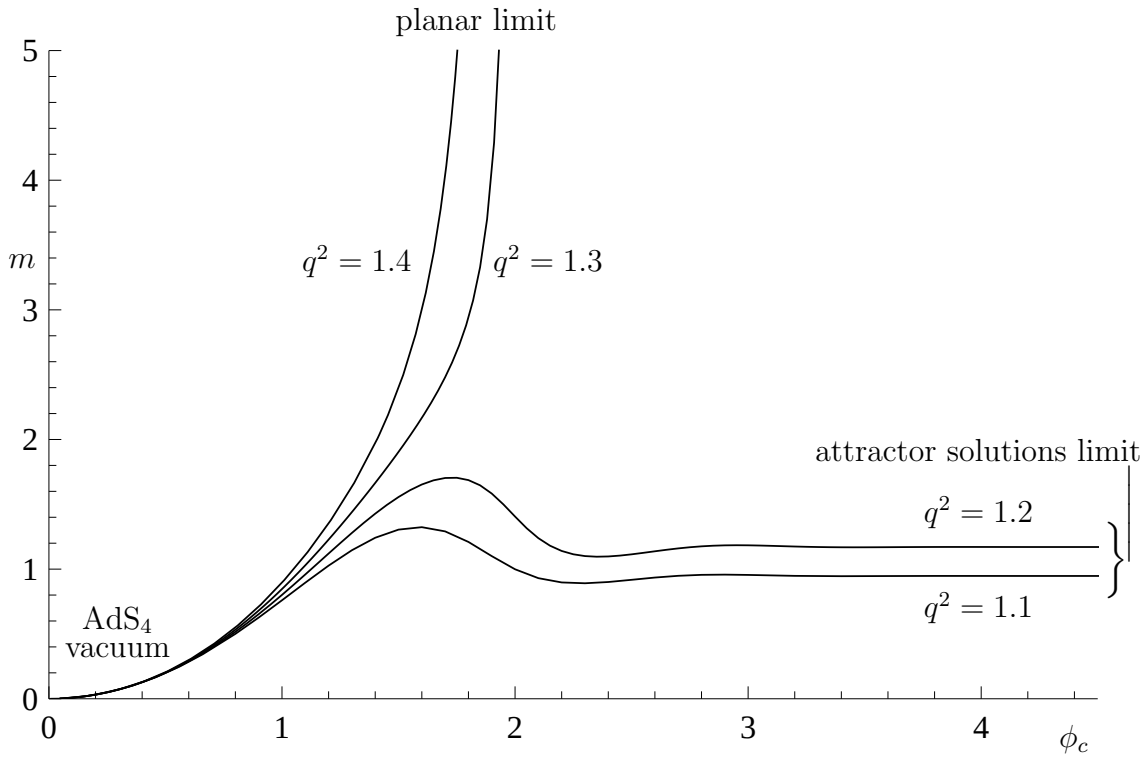

Fig. 4.3: $m(\phi_c)$ for branches which are accessible in perturbation theory about the vacuum solutions, for fixed values of q, as labelled. The mass is either bounded or unbounded depending on whether q^2 is greater or less than the critical value, $q_c^2 \simeq 1.259$. The two limits are discussed in the main text.

the scaling lands us exactly at Poincaré AdS_4. One can also show numerically that the solutions attain a maximal conserved charge at some finite value of ϕ_c, which we label as $\mathcal{X}^{(1)}_{\text{max}}$.

Moreover, at large ϕ_c they exhibit decaying oscillations about an asymptotic value of the charge, $\mathcal{X}^{(1)}_{\infty}$. This is similar to the behaviour seen for stars in AdS [108, 109, 112, 113] and also for charged solutions in AdS_5 [106]. In the context of radiation stars, the solutions are damped to a singular solution with infinite core density, which exhibits an invariance under a scaling symmetry [164, 113, 165]. In this sense we say that the large ϕ_c solutions are controlled by an attractive fixed-point under the action of a scaling, or for brevity, *attractor solutions*.[6]

For theories with $q > q_c$ all asymptotic coefficients are unbounded; the branch of solutions then connects with a non-vacuum solution in the planar limit. One natural candidate planar solution is the zero-temperature limit of a planar black hole with

[6] We emphasise that we have not investigated the scaling characteristics at large ϕ_c of the solutions presented, though we will study another scaling limit, the planar limit introduced in section 4.1.3, extensively.

$\langle \mathcal{O}_{\phi_1} \rangle = \phi_2 \neq 0$. Parametrising the branch by μ, if all coefficients are to survive the planar limit we must have that each of the following dimensionless quantities

$$m\mu^{-3}, \qquad \rho\mu^{-2}, \qquad \phi_2\mu^{-2} \tag{4.27}$$

become constant at large μ. These quantities are plotted along the unbounded branch in fig. 4.4; they indeed asymptote to constant values at large μ. Furthermore, comparison with the corresponding quantities for planar hairy black holes at low temperature in the same theory reveals good agreement between the large μ global solutions and the low T/μ planar hairy black holes. We will henceforth refer to these solutions as *planar solitons*.

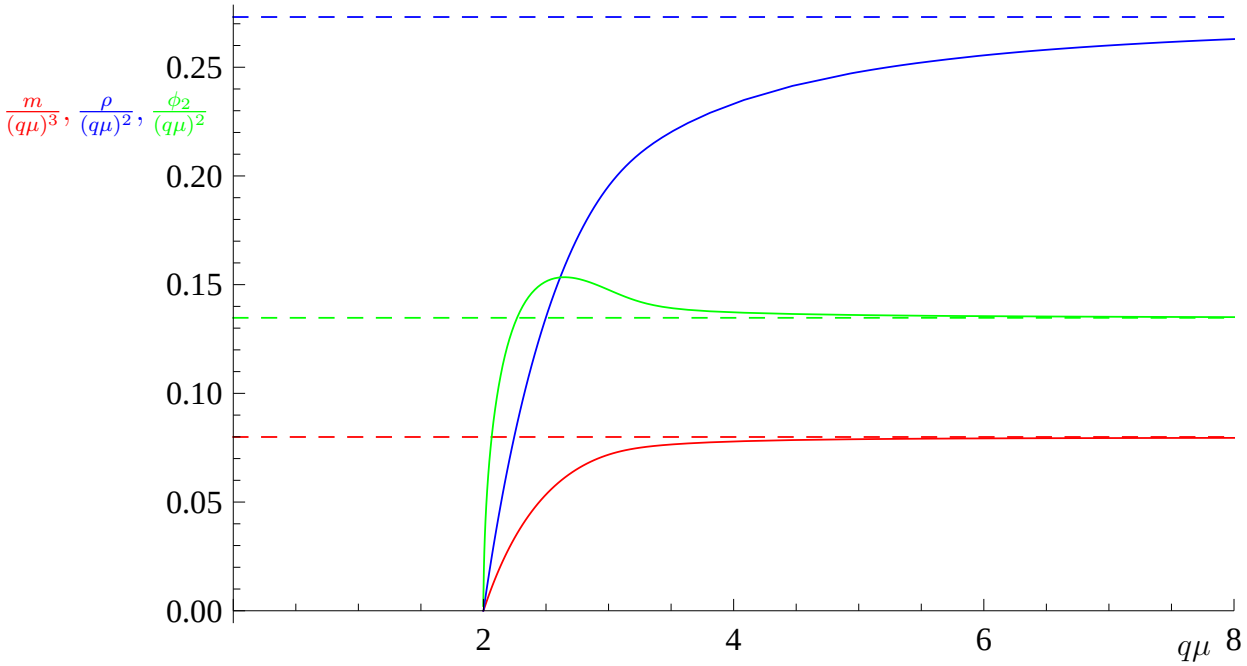

Fig. 4.4: The scaling invariants (4.27) for the branch connected to global AdS_4 in theories where $q > q_c$. Here as a representative example we have chosen $q^2 = 1.3$. Red is the m invariant, green is the ϕ_2 invariant and blue is the ρ invariant. The dashed lines indicate these quantities for planar hairy black hole solutions at low temperature.

One might expect that something happens to the family of planar hairy black hole solutions as one lowers q below q_c given the qualitative changes observed in the global solitons constructed so far. However, the planar hairy black hole solutions do continue to exist for $q < q_c$ with no obvious qualitative change. This suggests there are other global soliton branches that we have so far not constructed; *i.e.* branches that are not perturbatively connected to the global AdS_4 vacuum. *A priori* these could be singular, which would be a bit disappointing; one can always construct singular solitons by simply

integrating in the boundary data.

However, we find that there are smooth global solitons that become planar even for $q < q_c$. We now present a more complete picture of the regular global soliton solutions at fixed q, including branches of solutions that cannot be constructured in perturbation theory around vacuum global AdS_4.

In fig. 4.5 we present all branches of zero node solutions found for a range of fixed q values. At low $q < q_c$, we find a new branch of solutions that is not connected to the

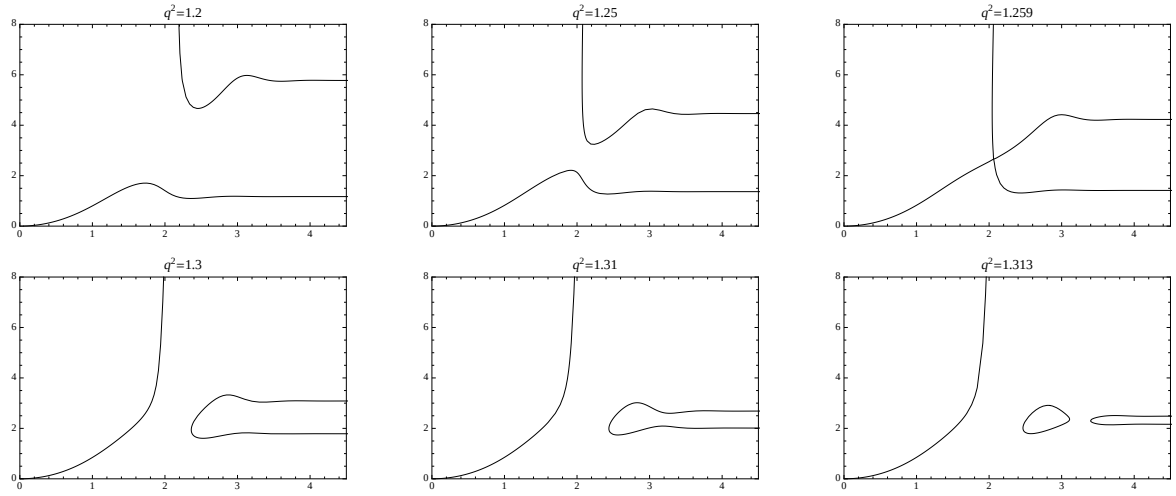

Fig. 4.5: $m(\phi_c)$, for a range of fixed q illustrating the existence of a planar limit even when there is a branch with a mass bounded from above. Each maximum of the bottom branch connects with the corresponding minimum of the top branch as q is increased.

vacuum solution, exhibiting a minimum m for the branch. There is now a new attractor solution, labelled by conserved charges $\mathcal{X}^{(2)}_{\infty}$, which controls the behaviour of this branch at large ϕ_c. The minimal charge solution along this branch is denoted by $\mathcal{X}^{(2)}_{\text{min}}$. We also note that the scalar field at the core is bounded from below along this new branch of solutions.

The presence of this second attractor solution has interesting implications for the phase space of solutions. As q is increased we note that the attractor values of the charges start to move closer to each other. Moreover, the first maximum of the lower branch and the first minimum of the upper branch (*i.e.* the extrema occurring at the smallest ϕ_c on the corresponding branches) move together. We define the critical parameter q_c as the value at which the two branches meet, *i.e.* $\mathcal{X}^{(1)}_{\text{max}}(q_c) = \mathcal{X}^{(2)}_{\text{min}}(q_c)$. At this point an unbounded branch of solutions connected to the global AdS_4 vacuum is born.

For $q > q_c$ we can find multiple solution branches, depending sensitively on the precise value of q. In addition to the branch connecting the AdS_4 vacuum to planar

solitons, for $q \gtrsim q_c$ we find a second branch that is not well parametrised by ϕ_c: for some values of ϕ_c there are at least two solutions with different asymptotic charges. In this regime, the curve $\mathcal{X}(\phi_c)$ appears to connect the two large core scalar values $\mathcal{X}_\infty^{(1)}$ and $\mathcal{X}_\infty^{(2)}$ respectively.

Increasing q further, we find that there is a succession of mergers and splits in the family of solutions. At critical values q_i (where $q_{i+1} > q_i$ with $q_1 \equiv q_c$), the i^{th} maximum of the bottom branch connects with the i^{th} minimum of the top branch, leaving closed branches (bubbles) in parameter space as illustrated in fig. 4.5. We have checked this behaviour up to q_2. Since the solutions for large ϕ_c are governed by the damped oscillations about the attractors, we might expect an asymptotic sequence of bubble creations in solution space. However, the two attractor solutions that control the asymptotic behaviour merge together and move off (into the complex domain) above $q_\infty^2 \simeq 1.313(8)$. This behaviour is illustrated in fig. 4.6. For $q > q_\infty$ there is a single branch of solutions; this is continuously connected to the global AdS_4 vacuum and has unbounded conserved charges.

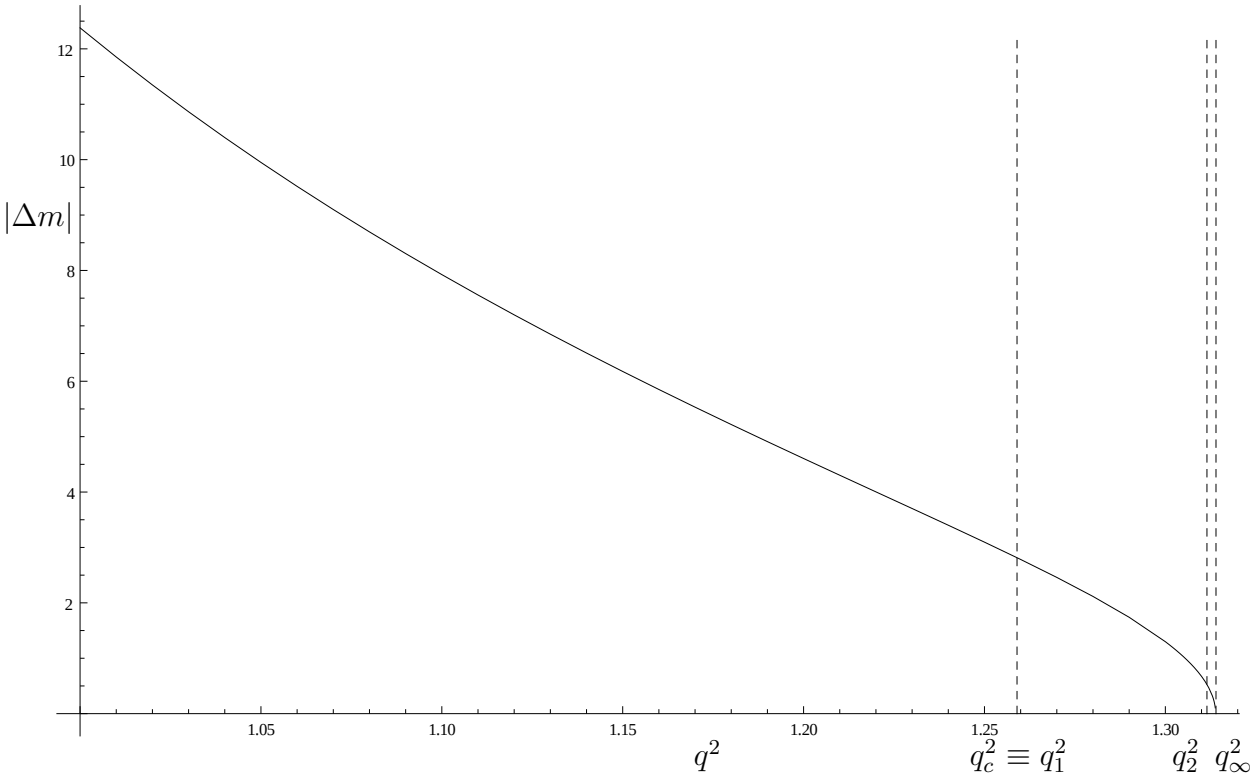

Fig. 4.6: Difference in mass for the two large ϕ_c solutions as a function of q^2. At q_1^2 the two branches of solution meet, as demonstrated in the third pane of fig. 4.5. Above q_∞^2 the large ϕ_c solutions cease to exist. We expect to see an infinite sequence of q_i values between q_2^2 and q_∞^2, corresponding to the nucleation of closed solution branches.

Let us pause and take stock of our findings so far. It is useful to plot these branches of solutions at various fixed values of q as contour lines of a function $q(m, \phi_c)$, as in fig. 4.7. We have now constructed unbounded global soliton solutions for all values of

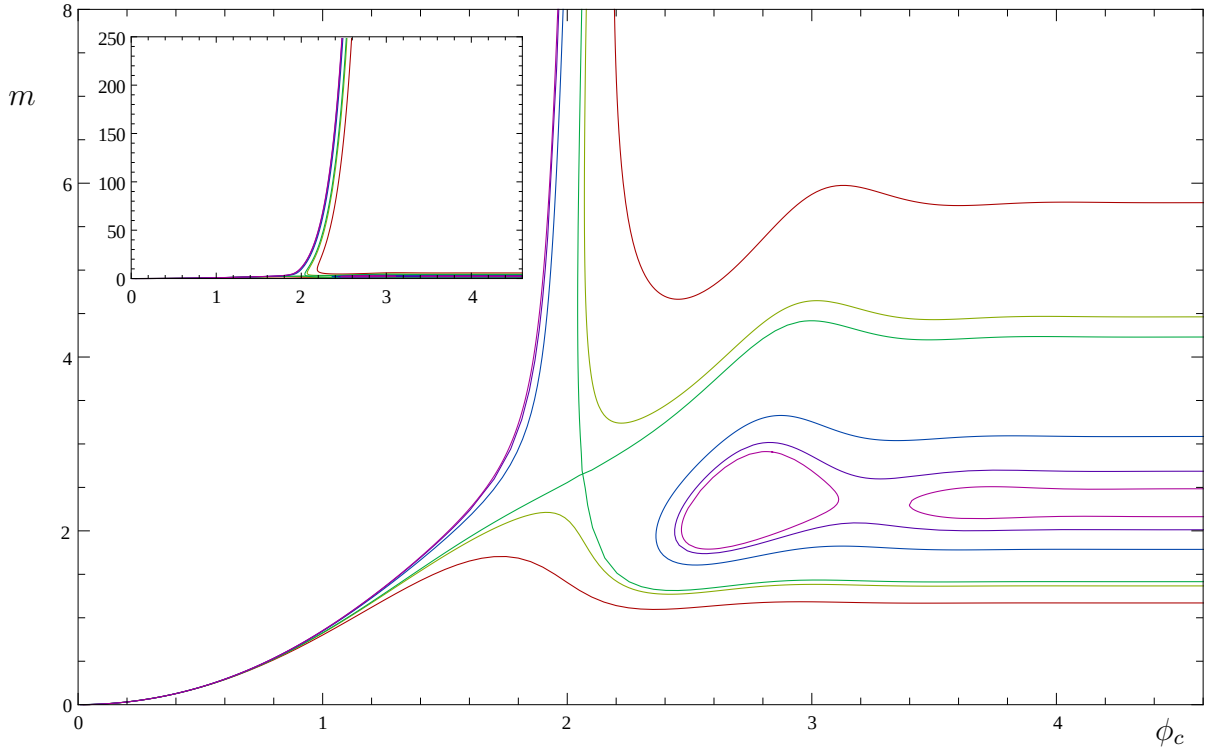

Fig. 4.7: Contours of the function $q(m, \phi_c)$. Colour represents the value of q, distinguishing each theory shown individually in fig. 4.5. Inset is the behaviour over a large range of m.

q. While for $q < q_c$ the unbounded branch is disconnected from global AdS_4, we saw that there was a single connected branch when $q > q_c$. Moreover, as in the cases $q > q_c$ where we encountered planar solitons, the unbounded $q < q_c$ solutions match on to the hairy planar black hole solutions at low T/μ, *i.e.* we have planar solitons for all values of q. This is illustrated in fig. 4.8. From fig. 4.8 it is clear that the conserved charges (normalised by μ to account for scaling) spiral into the attractor curves; this is of course expected given the presence of damped oscillations about the attractor solutions.

Another feature clearly visible is the presence of bubbles in the solution space: all solution branches occupy a finite volume of μ-normalised parameter space and $m(\phi_c)$ bubbles are closed curves in this space. We will soon see that the latter are subdominant in the microcanonical ensemble, but their presence is a testament to the non-linearities inherent in the theory. It is also reassuring that the asymptotic values of the rescaled parameters smoothly merge onto those of the planar hairy black holes irrespective of whether $q < q_c$ or $q > q_c$.

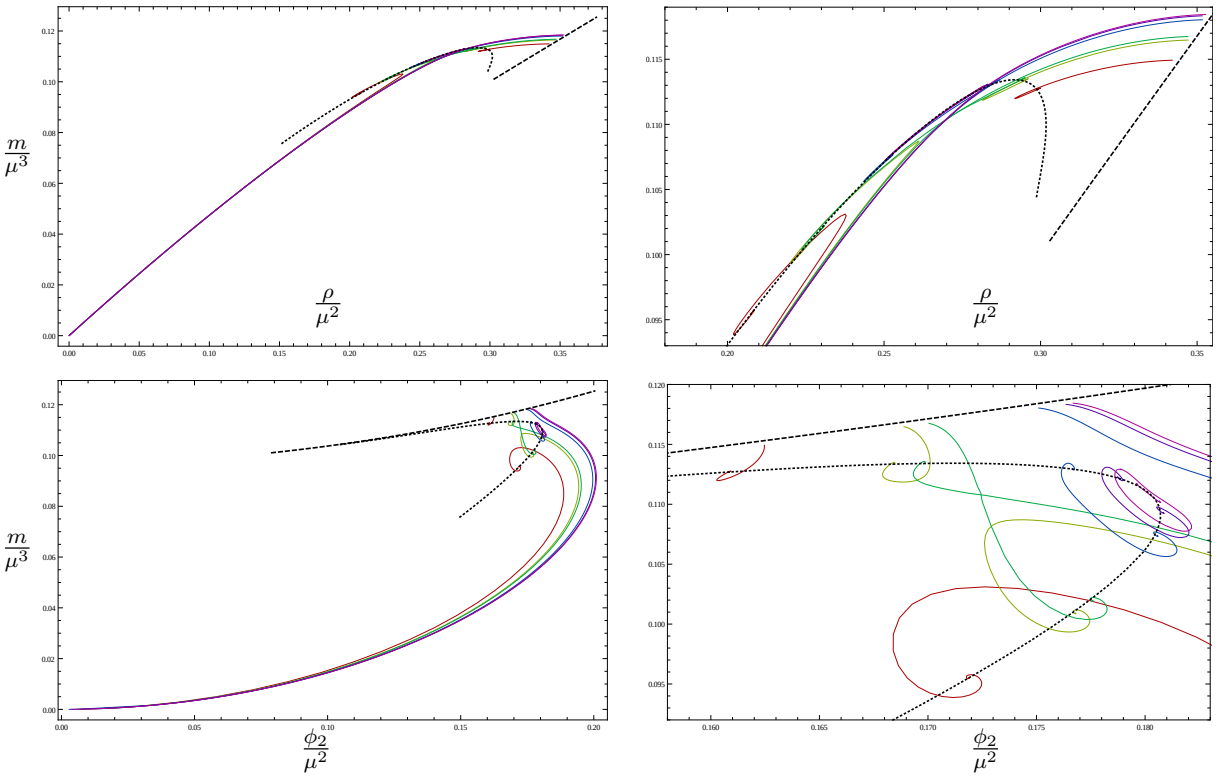

Fig. 4.8: Scaling invariants illustrating convergence to the planar solutions, for the values of q shown in fig. 4.5 and fig. 4.7. The black dotted line represents the attractor solutions at large ϕ_c plotted for an interval of q. The black dashed line represents the low temperature planar hairy black holes plotted for an interval of q. The scaled conserved charges spiral into the attractor lines but smoothly asymptote to the line of planar solitons for large charges. The right panels zoom into the interesting region to illustrate these features.

We will now discuss some of the qualitative features of the solutions themselves, and how the various branches are distinguished. Many of these branches will exhibit behaviour different from the perturbative solitons, with the latter exemplified by the radial profile fig. 4.2. For this purpose it will be useful to illustrate how the solutions probe the potential $V(\phi)$; this is illustrated in fig. 4.9 for the two branches of solution at $q^2 = 1.2 < q_c^2$ and in fig. 4.10 for the two branches of solution at $q^2 = 1.3 > q_c^2$.

Each solution shown in fig. 4.9 and fig. 4.10 begins at $\phi = \phi_c$ in the IR (by construction) and monotonically in r traces out a path to the $\phi = 0$ maximum of $V(\phi)$ in the UV (as enforced by our boundary conditions). Those solution branches that are connected to the AdS_4 vacuum explore the full domain $\phi_c \in [0, \infty)$ at the core. Along this branch solutions either tend to the planar limit as $\phi_c \to \infty$ if $q > q_c$ or to the attractor $\mathcal{X}_\infty^{(1)}$ if $q < q_c$. On the other hand, the branches of solutions that are not connected to the vacuum are restricted to a bounded domain $[\phi_{\min}(q), \infty)$ at the core with the precise nature depending on q.

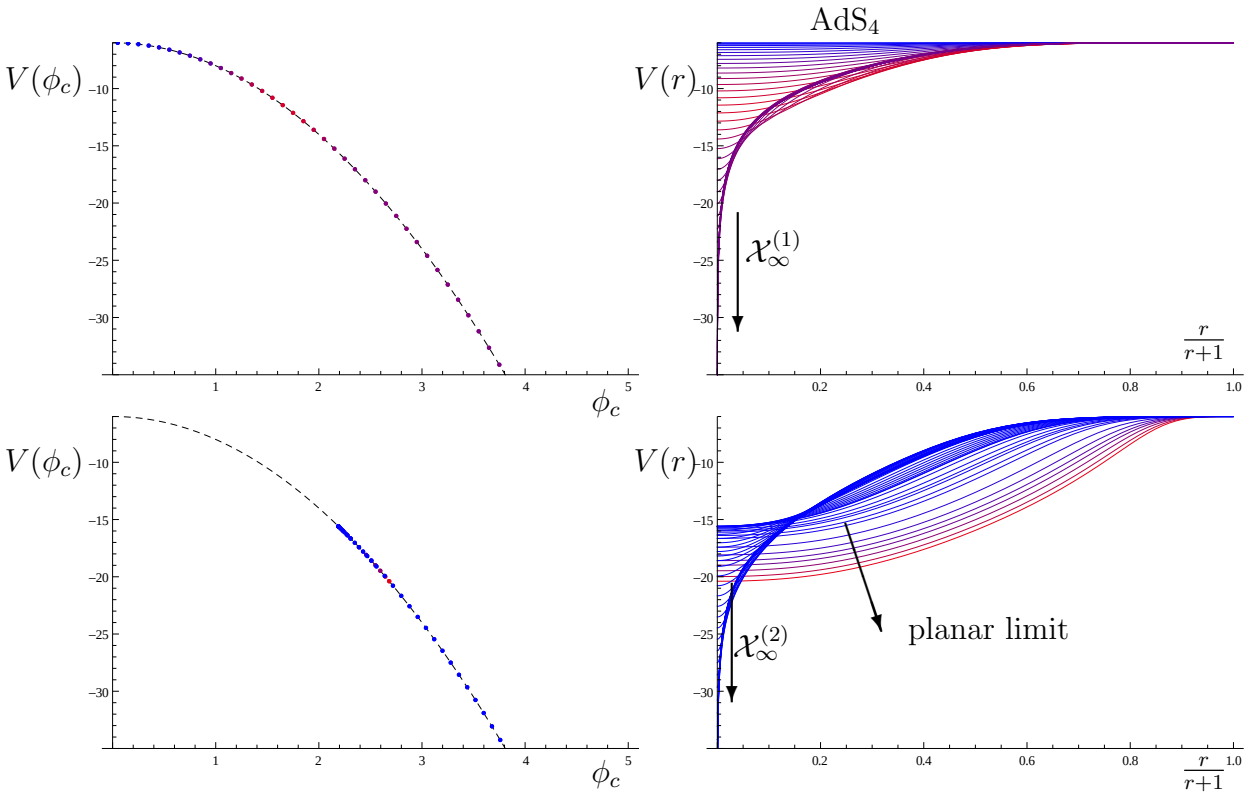

Fig. 4.9: *Left column*: $V(\phi)$ with each dot corresponding to the value of ϕ_c for solutions shown in the *Right column*: radial plots of the potential $V(\phi(r))$ evaluated on solutions belonging to the two branches at $q^2 = 1.2 < q_c^2$ (as illustrated in fig. 4.5). *Top row*: Solutions belonging to the branch with a maximum mass. *Bottom row*: Solutions belonging to the branch not connected to the vacuum; solutions are only shown up to a finite mass. Colour indicates the mass, with red corresponding to higher values.

For $q < q_c$ we have two distinguished end-point solutions: one that becomes planar as $\phi \to \phi_{\rm min}(q)$ and the other that goes to the attractor $\mathcal{X}_\infty^{(2)}$ as $\phi_c \to \infty$. For $q_c < q < q_\infty$ the solution curve that is double-branched asymptotes to the attractors $\mathcal{X}_\infty^{(1)}$ and $\mathcal{X}_\infty^{(2)}$ for large ϕ_c. The behaviour around $\phi_{\rm min}(q)$ is complex, owing to the bubbles, and we restrict attention to the part of the branch connecting the two attractors in fig. 4.10.

In short, the non-vacuum 'ends' of all branches shown are governed by the behaviour of $V(\phi)$ at large ϕ. This is clearly illustrated by the asymptotic growth of the charges $\mathcal{X}$ as a function of ϕ_c, as illustrated in the left panel of fig. 4.7. Since there is a non-trivial behaviour of the region of field space explored for different values of q, we may thus anticipate rather different behaviour for the consistent truncations of later sections, at least for large values of ϕ. In particular, as we alter the potential we anticipate qualitatively different growth of the $\mathcal{X}$ with ϕ_c.

Finally, let us consider the planar limit of the solutions for all q. The fact that we

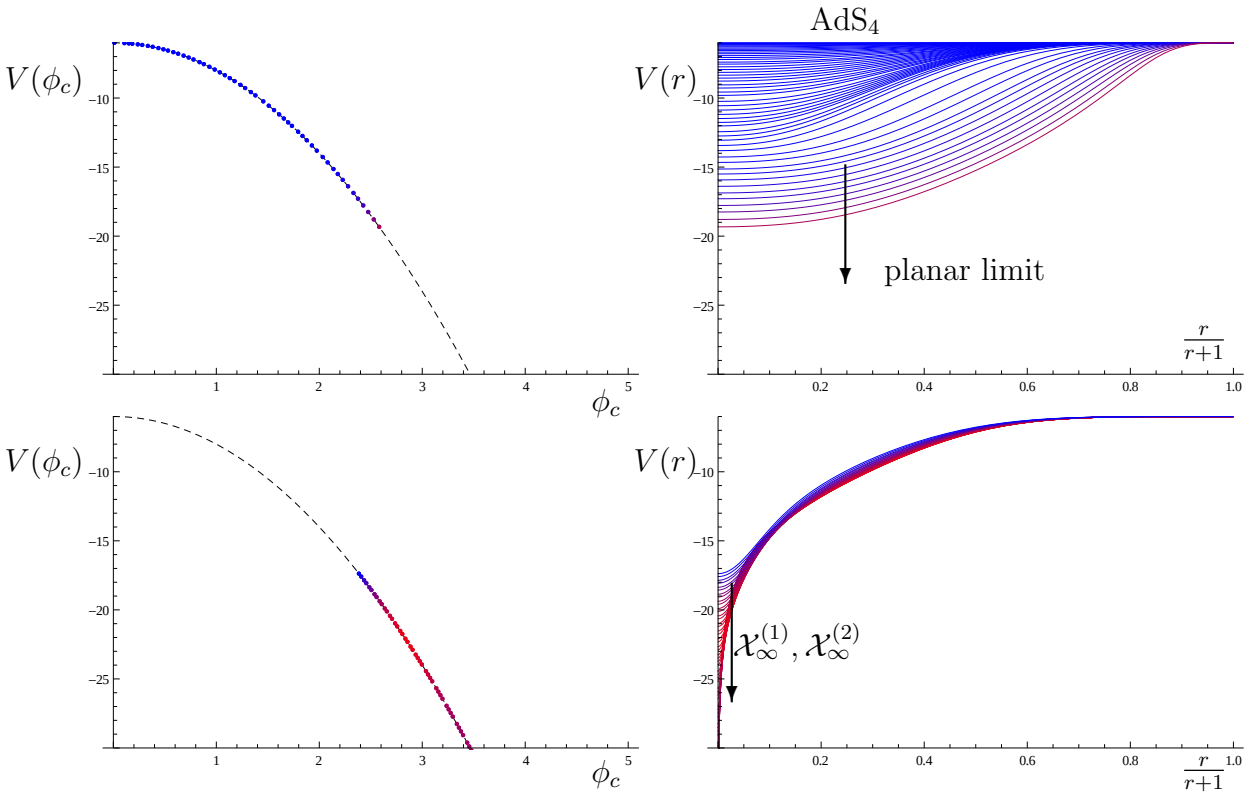

Fig. 4.10: As fig. 4.9 but for the two branches at $q^2 = 1.3 > q_c^2$. *Top row*: Solutions belonging to the branch connecting the vacuum to the planar limit; solutions are only shown up to a finite mass. *Bottom row*: Solutions belonging to the branch connecting the two attractor solutions.

attain the planar solitons in the scaling regime indicates that the profiles of the scalar field, gauge potential and the metric should go over to the zero-temperature planar superfluid solutions constructed in [115]. It is curious that in all cases this limit is attained with the scalar field pinned at some point down the potential away from the origin. It would be interesting to understand how this can be related to the non-trivial near-horizon behaviour seen for the zero-temperature solutions in [115].

Microcanonical phase diagram for states with $\langle \mathcal{O}_{\phi_1} \rangle \neq 0$

So far we have focused on exploring the rich structure of global solitons and their connection with the planar limit. It is also interesting to consider the implications of these solutions for the microcanonical phase diagram, *i.e.* examine the behaviour of the conserved charges $m(\rho)$. We will now sketch the features of this phase digram in brief and discuss the location of solitonic solutions with respect to the phase boundary in the microcanonical ensemble.

Behaviour for $q < q_c$: For values of $q < q_c$ we know from the construction of solitons we only have solutions with mass in the range $[0, m^{(1)}_{\rm max}] \cup [m^{(2)}_{\rm min}, \infty)$, while the charge lies in the range $[0, \rho^{(1)}_{\rm max}] \cup [\rho^{(2)}_{\rm min}, \infty)$. Recall that our notation here is tied to the attractor solutions that have conserved charges $\mathcal{X}^{(1)}_\infty$ and $\mathcal{X}^{(2)}_\infty$: $\mathcal{X}^{(1)}_{\rm max}$ and $\mathcal{X}^{(2)}_{\rm min}$ are the extremal values along the branch connected to a particular attractor.

This implies that we have a gap in the microcanonical phase diagram: no smooth solitonic solutions exist for $m \in (m^{(1)}_{\rm max}, m^{(2)}_{\rm min})$ and $\rho \in (\rho^{(1)}_{\rm max}, \rho^{(2)}_{\rm min})$. The gap in the mass spectrum is clear for example from fig. 4.7. We believe that the spectrum of smooth solitonic solutions is exhausted by the solutions we have presented hitherto in section 4.2.1. In particular, we conjecture that the gap in the microcanonical phase diagram is a physical feature. This is illustrated clearly in the phase curves shown in fig. 4.11.

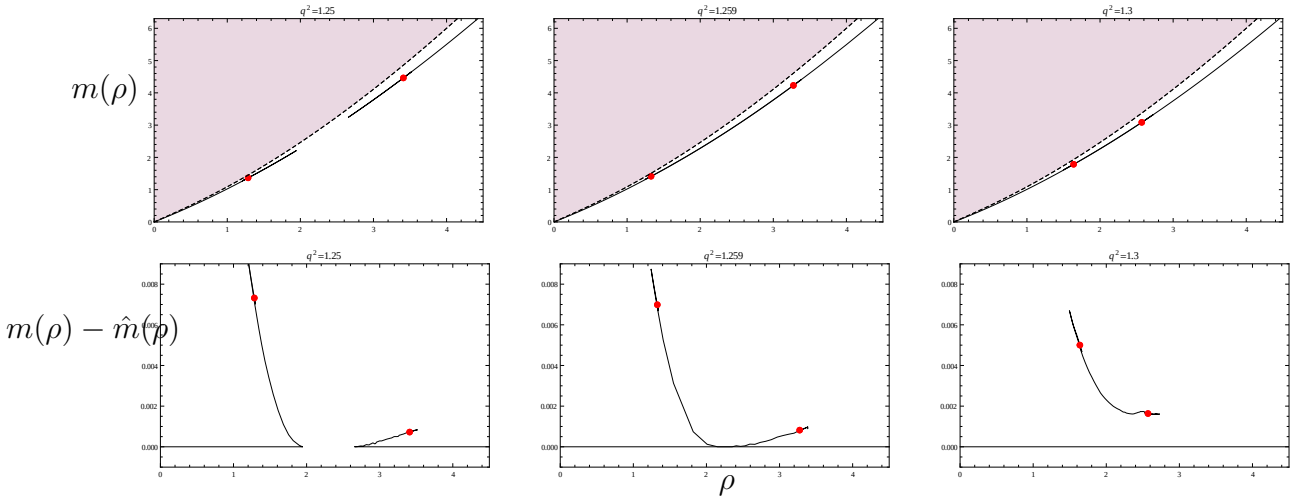

Fig. 4.11: Soliton branches in the microcanonical phase diagram for $q < q_c$, $q \simeq q_c$ and $q > q_c$. Top: $m(\rho)$, bottom: $m(\rho)$ with phase boundary function $\hat{m}(\rho)$ (4.28) to illustrate the disfavoured branches. Red dots illustrate the positions of the singular attractor solutions. The black dashed line is the one parameter family of extremal RN-AdS black holes demarcating the region of hair-free black holes.

The end-points of the phase lines, *i.e.* $(\rho^{(1)}_{\rm max}, m^{(1)}_{\rm max})$ and $(\rho^{(2)}_{\rm min}, m^{(2)}_{\rm min})$ in the (ρ, m) plane, are *indirectly* controlled by our attractor solutions $\mathcal{X}^{(1)}_\infty$ and $\mathcal{X}^{(2)}_\infty$, respectively. This is to be expected; a dynamical systems attractor typically controls the region of the phase plot within its basin of attraction. We know from our numerics that for $q < q_c$ the solutions that stay connected to the global AdS_4 vacuum are within the basin of attraction of $\mathcal{X}^{(1)}_\infty$ and those that are connected to the planar zero temperature hairy black hole are within the basin of attraction of $\mathcal{X}^{(2)}_\infty$. However, the charges at these end-points points are set by the extremal values of mass and charge obtained along each

solution branch. In particular, it is important to note that the solution relevant for these end-points is not the attractor solution; we shall see where the latter lie momentarily.

Let us first define the 'phase boundary' curve $\hat{m}(\rho)$ as:

$$\hat{m}(\rho) = \{m(\rho) : (0,0) \to (\rho^{(1)}_{\rm max}, m^{(1)}_{\rm max})\} \cup \{m(\rho) : (\rho^{(2)}_{\rm min}, m^{(2)}_{\rm min}) \to (\infty, \infty)\}. \tag{4.28}$$

The presence of oscillations around the attractor solutions implies that the phase curve $m(\rho)$ as such is a multi-branched zig-zag starting at the extremum mass and charge points $(\rho^{(1)}_{\rm max}, m^{(1)}_{\rm max})$ and $(\rho^{(2)}_{\rm min}, m^{(2)}_{\rm min})$ in the (ρ, m) plane.[7] In defining $\hat{m}(\rho)$ we have simply removed these zig-zags. The attractor solutions mark the terminus of the zig-zags; we have indicated this explicitly in fig. 4.11 and they lie in the region above the phase boundary.

The zig-zag portion of the curve $m(\rho)$ that connects the extremal value of the mass/charge and the attractor points are subdominant in the microcanonical ensemble. We will see in section 4.2.2 that the region above the $\hat{m}(\rho)$ curve is populated with global hairy black holes with non-zero horizon area. Since black holes carry entropy, it immediately follows that these solutions dominate the microcanonical ensemble (where the entropy or the density of states is to be maximised). The solitonic solutions have no entropy and thus correspond to subdominant saddle point configurations of the corresponding field theory.[8]

A natural question is what happens in the gap between the extrema, *i.e.* between the points $(\rho^{(1)}_{\rm max}, m^{(1)}_{\rm max})$ and $(\rho^{(2)}_{\rm min}, m^{(2)}_{\rm min})$. Let us first note that global hairy black holes are untouched by this gap in the spectrum; they continue to exist for $m \in (m^{(1)}_{\rm max}, m^{(2)}_{\rm min})$ and $\rho \in (\rho^{(1)}_{\rm max}, \rho^{(2)}_{\rm min})$. However, as we lower the mass of the black holes for fixed charge in the domain $(\rho^{(1)}_{\rm max}, \rho^{(2)}_{\rm min})$, we expect at some point to hit a minimal mass solution. This solution should have vanishing horizon area and thus be horizon-free.

It is tempting to conjecture that the curve given by $\hat{m}(\rho)$ is the true microcanonical phase boundary of the theory and furthermore argue that the black holes that exist in the soliton gap region terminate on a singular soliton solution. It would be interesting to flesh this out more concretely, but we will refrain from doing so for this phenomenological model. A detailed analysis of hairy black holes can be found in [120] addressing these issues. The other models we study have string theory embeddings (or even known dual

[7] The asymptotic behaviour of this zig-zag, which zeroes in onto the attractor solutions, can be inferred directly from the approach to the attractor solutions.

[8] In the standard parlance of holography, the black holes have $O(N_c^2)$ entropy, as in (1.20), whereas that of the solitons is subleading in the large N_c expansion.

field theories) and so will accord much better control for us to address such issues. We should note that for sufficiently large masses at fixed charge the microcanoical phase diagram is dominated by the RN-AdS$_4$ black holes, which maximise the entropy for given charge.

Behaviour for $q \geq q_c$: The behaviour of the microcanonical phase diagram for $q = q_c$ is quite interesting. By definition at q_c the two branches of solutions cross. As noted earlier the extremal mass/charge solution of the two branches merge at this value of the scalar charge, implying that we should expect that the gap in the microcanonical phase diagram closes off at this point. Indeed this is exactly what we observe. The plot of $m(\rho)$ for the two branches cross and one can smoothly pass between the two branches.

At q_c we in addition expect to see a kink in the phase curve due to the crossing. This arises because of the zig-zags between the extremal mass/charge solutions on each branch and the corresponding attractor. This behaviour is also clearly visible in the middle panel of the triptych fig. 4.11.

The minimal mass solution for a given charge, *i.e.* the phase boundary $\hat{m}(\rho)$, now always corresponds to a smooth soliton; one simply jumps from the solution that is connected to the global AdS$_4$ vacuum to one that is connected to the planar hairy black holes.

For $q_c < q < q_\infty$ we still have the two attractor solutions $\mathcal{X}_\infty^{(1)}$ and $\mathcal{X}_\infty^{(2)}$. Now however that they have larger mass for a given charge than the solution on the branch of solutions that connects the global AdS$_4$ vacuum to the planar solutions. Moreover, the kink in the phase curve that occurs for $q = q_c$ is now smoothed out and the attractor solutions control a region above this curve. However, as before everywhere above the $\hat{m}(\rho)$ curve we expect to see global hairy black holes. The latter dominate the ensemble owing to their non-zero entropy; the solitonic solutions that belong to the bubbles or those that stay connected to the attractor solutions are subdominant configurations.

For $q > q_\infty$ we have a simple phase curve; $m(\rho)$ (which now coincides with $\hat{m}(\rho)$) is smooth and characterises the solutions with minimal mass for a given asymptotic charge. We have found no smooth solutions elsewhere in the (ρ, m) plane.

4.2.2 Global hairy black holes

To round off our discussion about the microcanonical phase diagram we need some information about black hole solutions that exist in the theory. We know that the Lagrangian

(4.2) has amongst its solutions RN-AdS$_4$ black holes, which attain extremality along a curve $m(\rho)$. Prior to the seminal work of [30] it was commonly believed that these solutions form the phase boundary of the microcanonical ensemble. We now of course know this to be false: there are scalar hair black holes and charged solitons in the theory. These solutions in fact allow one to attain lower masses. As explained in [106], they allow one to close the gap between the extremality and BPS bound for superconformal field theories with holographic duals. As argued above, they facilitate the delineation of the true phase boundary.

We will now quickly sketch out the behaviour of the global hairy black holes of (4.2). The equations of motion are the same as before, as are the asymptotic boundary conditions. The only change is the IR boundary condition: we require the presence of a non-degenerate Killing horizon. This operationally implies that there is a locus $r = r_+$ where the function $g(r)$ has a simple zero with $g'(r_+)$ being proportional to the surface gravity of the black hole. Regularity of the Euclidean solution determines the period of the thermal circle and hence the temperature to be $T = \frac{1}{4\pi}\, g'(r_+)\, e^{-\frac{1}{2}\beta(r_+)}$.

The rest as before involves numerical integration of the field equations. We still have a system of differential order six and our asymptotic data including the scalar boundary condition leaves four parameters. We impose $A(r_+) = 0$ to ensure that we have a well-defined one-form on the horizon. We then have four undetermined parameters at the horizon: $A'(r_+)$, $\phi(r_+)$, $\beta(r_+)$ and r_+. We therefore expect to see a two-parameter family of black hole solutions. One of these parameters without loss of generality can be taken to be the horizon size r_+, which makes it easy to talk about small/big black holes by comparing the solution relative to the characteristic AdS scale ℓ (here set to 1). Small black holes with $r_+ \ll 1$ can be constructed perturbatively along the lines discussed in [105]. We instead construct black hole solutions directly by numerical integration and the result of our numerics is shown in fig. 4.12.

The main feature we want to illustrate here is that the large global black holes do indeed pass over nicely to the appropriate planar soliton (*i.e.* zero-temperature limit of the planar hairy black holes). This is achieved by scaling up the parameters of the solution, say μ whilst holding r_+ fixed. Alternatively, we could instead consider a scaling where we scale up r_+, resulting in a planar black hole with non-zero horizon size. In both cases the planar solutions correspond in the field theory to superfluid configurations with zero superfluid velocity on $\mathbb{R}^{2,1}$. The global hairy black holes in contrast correspond to superfluid configurations for the same field theory on $\mathbb{R} \times S^2$. Furthermore, by explicit construction we have verified that the microcanonical phase diagram is populated by

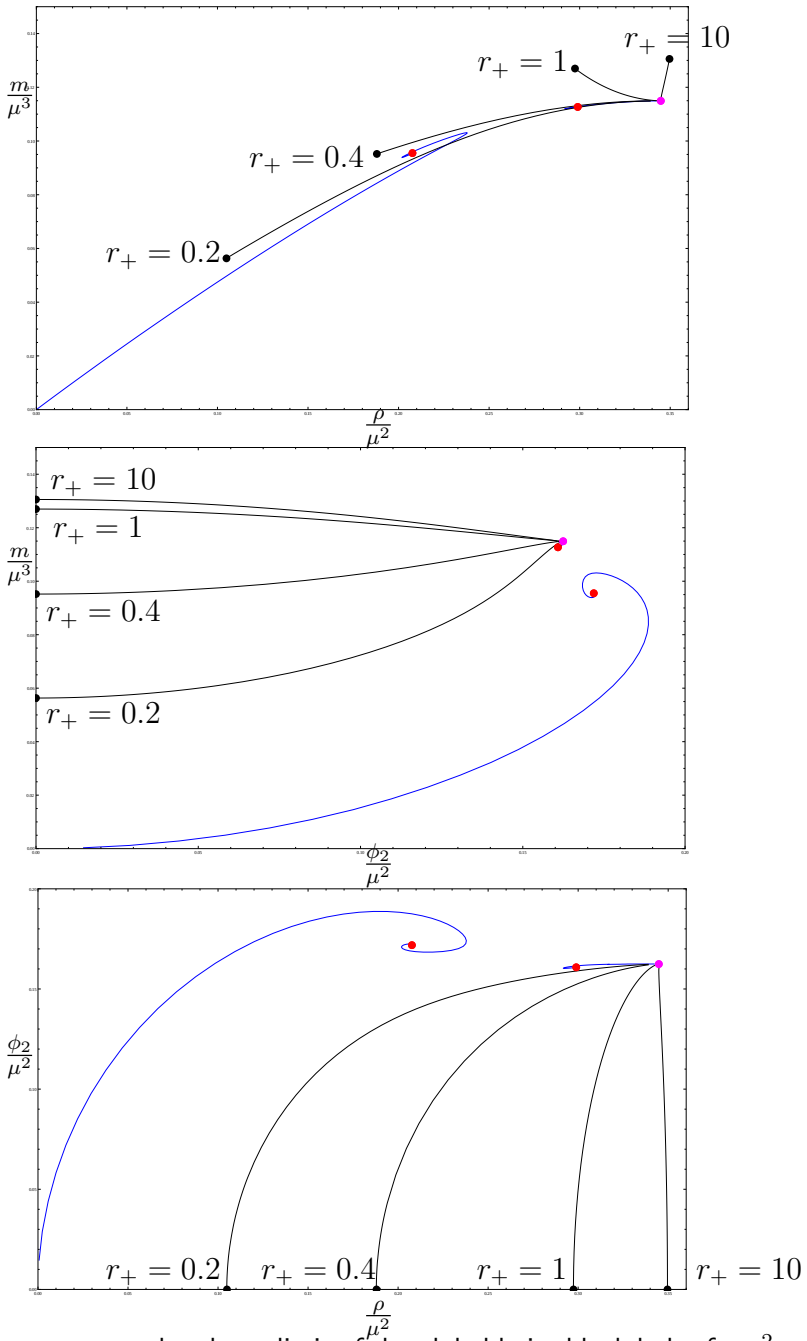

Fig. 4.12: Convergence to the planar limit of the global hairy black holes for $q^2 = 1.2$. The black lines are one parameter families of hairy black holes at fixed horizon size r_+, for $r_+ = 0.2, 0.4, 1, 10$. The blue lines are the soliton solutions discussed in section 4.2.1. The magenta dot indicates the low temperature planar hairy black hole solution. The red dots illustrate the positions of the putative soliton attractor solutions. The black dots indicate the RN-AdS$_4$ black hole as given in (4.13) at the critical temperature for the onset of the scalar hair instability.

hairy black holes above the soliton phase curve discussed in section 4.2.1 at least for the values of r_+ plotted here.[9]

[9]For smaller values of r_+ not shown, there appear to be two branches of solution as in the soliton

4.2.3 Exploring scalar boundary conditions

We have demonstrated that by varying the parameter q we may obtain a rich class of global soliton solutions for the phenomenological Abelian-Higgs models. Later we will concentrate on the theories resulting from consistent truncations where we have no parameters to vary; the Lagrangian has a fixed scalar potential and gauge coupling. However, as advertised the theories we consider have the scalar mass lying in the window where both modes are normalisable. We can use this freedom to explore the behaviour of solitons as a function of scalar boundary conditions.

Of main interest to us will be to allow scalar boundary conditions that deform the dual CFT using double-trace deformations, as described in section 4.1.1. In order to make comparisons between one of these consistent truncations and the phenomenological theories, we now consider such deformations at fixed q. Before turning to this we quickly summarise the situation when we quantise the bulk scalar as a dimension $\Delta = 1$ operator on the boundary. This alternate boundary condition is of course the limiting case of double-trace deformations and we should anticipate that the double-trace deformations fall between the cases where $\langle \mathcal{O}_{\phi_2} \rangle \neq 0$ and $\langle \mathcal{O}_{\phi_1} \rangle \neq 0$.

Condensates of the $\Delta = 1$ operator $\mathcal{O}_{\phi_2}$

The behaviour of global solutions where the scalar field is required to behave as $\phi(r) \to \frac{\phi_1}{r}$ as $r \to \infty$, *i.e.* treating ϕ_2 as the source and setting it to zero, is qualitatively similar to the $\Delta = 2$ case discussed above. We find that there is a critical charge q_c; below q_c the global AdS_4 vacuum is disconnected from the planar hairy solutions, while above q_c the two are connected.

The main feature of interest is the value of q_c itself: we find it numerically to be

$$q_c^2 \simeq 0.57 \ , \qquad \phi_2 = 0 \ \ \text{(equivalently } \Delta = 1\text{)}. \tag{4.29}$$

The fact that q_c is lower for $\Delta = 1$ than for $\Delta = 2$ boundary condition makes physical sense. In the former case, the scalar field decays more slowly, implying that the asymptotic field is being held higher. This effectively implies that there is more charge repulsion in this case, and so one encounters the critical behaviour at a smaller value of

case. One branch connects to the AdS_4 vacuum, and the other connects with the planar limit. We have been unable to determine numerically whether or not these branches join in the vicinity of the soliton gap.

the scalar charge q.[10]

Double-trace deformations

Having seen the behaviour of the charged scalar solitons for both $\Delta = 1$ and $\Delta = 2$ boundary conditions, we now turn to the analysis of mixed boundary conditions $\phi_2(\phi_1)$. Specifically, we consider deforming the field theory by the double-trace operator $\mathcal{O}^2_{\phi_2}$ by employing the boundary condition (4.8).

In the $\Delta = 2$ boundary condition we encounter a critical theory with charge $q_c(\Delta = 2) \simeq 1.259$. Above this value of the scalar charge solutions exist for all masses $m \in [0, \infty)$ while for theories with $q < q_c(\Delta = 2)$ we found a gap in the soliton spectrum. Based on this observation we shall comment on two interesting cases.

First, when the theory under consideration lies within the window $q_c(\Delta = 1) < q < q_c(\Delta = 2)$ there is a gap in the $\Delta = 2$ soliton spectrum but no gap in the $\Delta = 1$ spectrum. In this special window we have the opportunity of studying new critical behaviour as a function of the deformation parameter $\varkappa$ described in section 4.1.1. In particular we can move from an ungapped spectrum ($\varkappa = 0$) via a critical theory at $\varkappa = \varkappa_c(q)$ to a gapped spectrum when $\varkappa > \varkappa_c(q)$. Such phenomena would be interesting to study further.

The second interesting case lies precisely at the critical theory $q_c(\Delta = 2) \simeq 1.259$. This will be of particular interest in the context of the consistent truncation studied in section 4.3, which as we shall show, has qualitatively similar features. At this fixed value of q we can again consider deformations using the parameter $\varkappa$. The results are illustrated in fig. 4.13. In the $\Delta = 1$ case we have only one branch of solutions. Interestingly, we see the emergence of a new branch of solutions not connected with the vacuum at large ϕ_c for deviations away from this case. Specifically for deformations satisfying $\varkappa \gtrsim 10.2\mu$ we see the emergence of many familiar features at large ϕ_c including the closed bubble solutions previously encountered at supercritical values of q. In this sense the relevant deformations appear to be decreasing the effective value of the charge. At larger values of $\varkappa$ both branches converge to the $\Delta = 2$ critical branch configuration, as expected.

There are two important features to note about the double-trace deformed solutions. One is that they seem not amenable to a leading order perturbative construction about the global AdS_4 vacuum (see appendix 4.B for the technical argument). This should be expected; the deformation breaks conformal symmetry and AdS_4 is not necessarily the

[10] Small solitons with $\Delta = 1$ have $m = \frac{\rho}{2q}$, which implies that $q_{\text{ERN}} = 1/2$. Once again we focus on q larger than this so that our solitons are lighter than the corresponding RN-AdS_4 black hole at fixed charge.

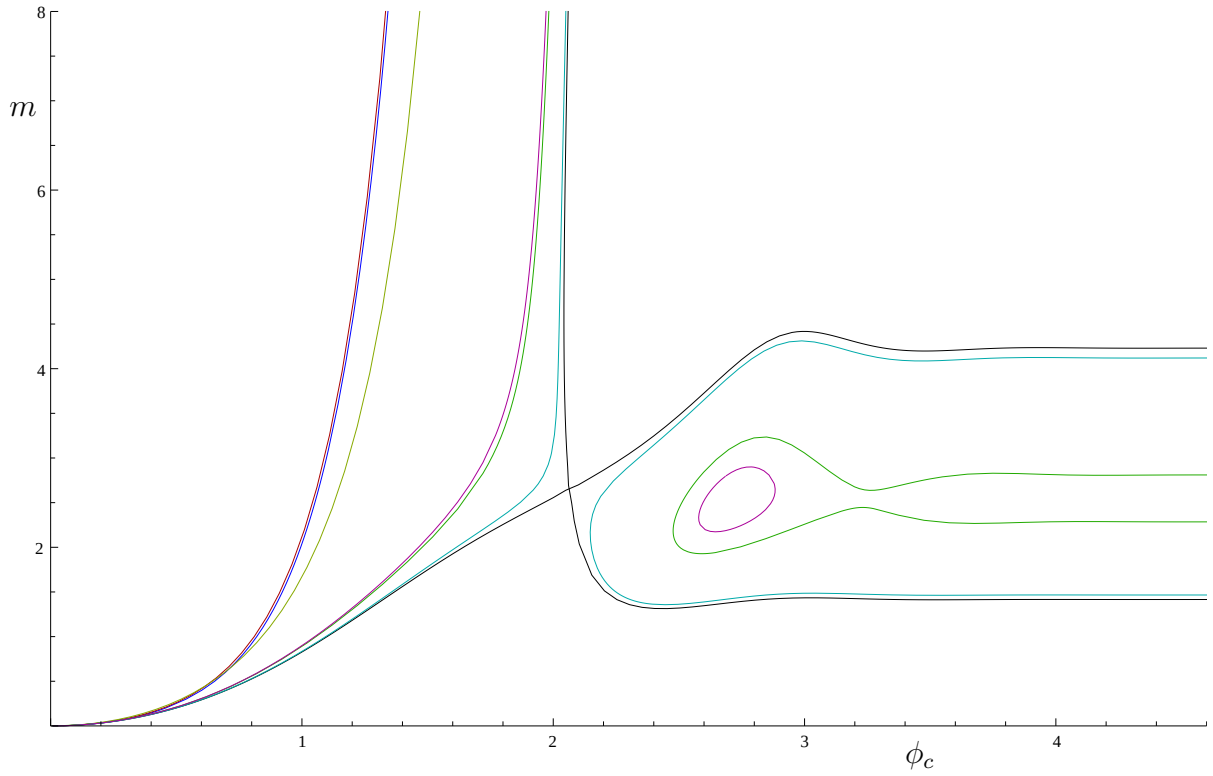

Fig. 4.13: Global solitons in the double-trace deformed Abelian-Higgs model with $q = q_c(\Delta = 2) \simeq 1.259$ with curves shown at fixed $\mu^{-1}\varkappa = 0.1, 1, 10.5, 12, 100$. For $\varkappa = 0$ we have the $\Delta = 1$ boundary condition; the solutions and their deformations here smoothly connect the AdS_4 vacuum to the planar solitons. At large $\mu^{-1}\varkappa$ we encounter the $\Delta = 2$ boundary conditions wherein we see the expected merger between the two solution branches. In addition we see closed branches in parameter space for a finite range of $\mu^{-1}\varkappa$.

true ground state of the system with the double-trace boundary conditions. A second related fact is that the mass density of the bulk solutions also receive contributions from the scalar field; see (4.11). As noted in various places in the designer gravity literature [101, 102, 166] and more recently in [103] the conserved energy for such deformations can indeed be negative (though still bounded from below hence ensuring a positive energy theorem). This in particular does imply that AdS_4 vacuum is not the appropriate background for perturbation theory to construct charged solitons; one should rather use the minimum energy designer gravity soliton for this purpose. Since one mostly can only construct the latter numerically, it is simpler therefore to construct charged solitons directly by numerical integration.

4.3 Charged solitons in the $SU(3)$ truncation

So far we have studied solitons in the phenomenological Abelian-Higgs model. Whilst this system has the luxury of a quadratic scalar potential $V(\phi)$ and Maxwell coupling $Q(\phi)$, it suffers from the drawback of not having a consistent embedding into any known supergravity theory. To determine whether the features described above are artefacts of the modelling then we need to generalise our considerations. As described in section 4.1.1, we can turn to models that arise via consistent truncations of eleven-dimensional 11D supegravity to ascertain whether the features we see are generically accessible in gravitational systems that might have holographic field theory duals. This in addition has the added benefit of allowing us to explore the behaviour of the solutions for different choices of scalar potentials/Maxwell couplings.

4.3.1 Basic facts about the $SU(3)$ truncation

With this motivation in mind, we turn to a very simple model that arises from the consistent truncation of 11D supergravity on a skew-whiffed Sasaki-Einstein manifold [46]. We referred to this as the $SU(3)$ truncation in table 4.1. This was the first model to embed (2+1)-dimensional holographic superfluids into 11D supergravity [46].

Since the Lagrangian (4.3) now has a fixed scalar potential $V(\phi)$ and Maxwell coupling $Q(\phi)$, given by

$$V(\phi) = \cosh^2\frac{\phi}{\sqrt{2}}\left(-7+\cosh\sqrt{2}\phi\right), \quad Q(\phi) = \frac{1}{2}\sinh^2\sqrt{2}\phi \tag{4.30}$$

and hence $m_\phi^2 = -2$ and $q = 1$, we have no free parameters to dial. The only freedom we are left with is the choice of boundary condition, which as discussed in section 4.1.1 we will generically take to be of the double-trace form (4.8), parametrised by $\varkappa$.[11]

Before we proceed with the discussion of solitons, let us first recall that the potential $V(\phi)$ in (4.30) has three extrema as noted previously in section 4.1.2. One is the global AdS_4 vacuum at $\phi = 0$, but we have in addition local minima at scalar values quoted

[11] It can be checked that the theory with the double-trace deformation has a positive energy theorem; the general analysis of [103] applies here and we have explicitly computed the off-shell scalar fake-superpotential to confirm this. We should also note here that the same paper claims to construct neutral designer gravity solitons for the consistent truncation constructed in [46] and obtain the off-shell fake-superpotential. However, they choose as their scalar potential (in our conventions) $V(\phi) = 5 - 12\cosh(\phi/\sqrt{2}) + \cosh(\sqrt{2}\phi)$, which is different from what we obtain. Consequently the cubic term in our fake-superpotential has a slightly different coefficient, *i.e.* $s_c \simeq 0.7$.

in (4.14); see fig. 4.1. The latter solution is the Pope-Warner (PW) [167] vacuum with effective AdS_4 radius $\frac{\sqrt{3}}{2}$. About this vacuum the scalar potential behaves as $V(\phi) \simeq -8 + 8\,(\phi - \phi_{PW})^2$, so that the PW vacuum has an irrelevant operator. The presence of a second extremum to the scalar potential implies that we should anticipate domain wall solutions that interpolate between the two vacua. We will indeed find that such solutions, as well as the distinguished point ϕ_{zero} at which $V(\phi)$ vanishes, play an interesting role.

4.3.2 Global solitons with standard and alternate boundary conditions

First we turn to the standard and alternate quantisations of the scalar field, *i.e.* consider the two special cases $\varkappa = 0$ and $\varkappa \to \infty$, or equivalently the $\Delta = 1, 2$ boundary conditions, respectively. Direct numerical integration of the field equations allows one to show the existence of solitons (small solitons as always can be constructed perturbatively). The results of the numerics are reported in fig. 4.14 where as in section 4.2 we have chosen to plot the conserved mass density of the solution as a function of the scalar value ϕ_c at the origin.

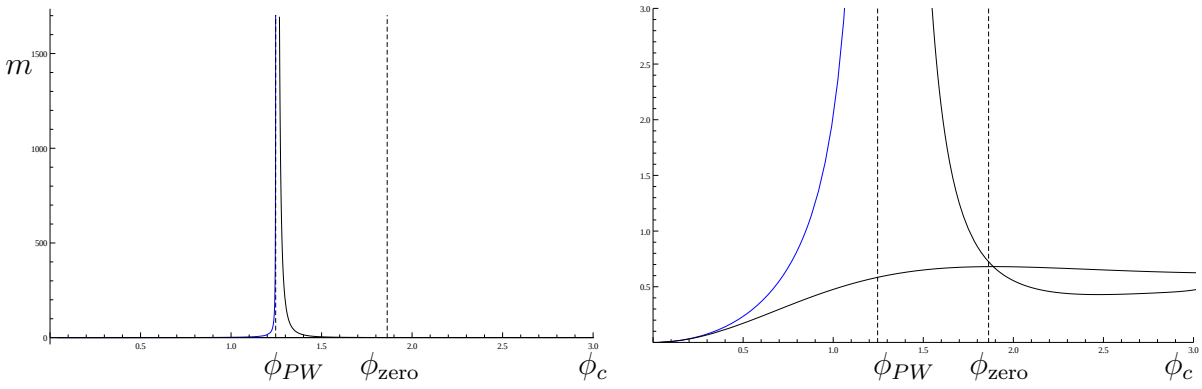

Fig. 4.14: Charged scalar soliton branches for dimension $\Delta = 2$ ($\varkappa \to \infty$) (black) and dimension $\Delta = 1$ ($\varkappa = 0$) (blue) for the $SU(3)$ consistent truncation. The vertical dashed line is the value of the scalar ϕ in the Pope-Warner vacuum. The right plot is the same data as the left illustrating the low mass behaviour.

For the alternate quantisation $\Delta = 1$ we note that we have a single branch of solitonic solutions that remains connected to the vacuum global AdS_4 solution (at $\phi = 0$). The scalar field remains bounded $\phi \in [0, \phi_{PW})$ and we obtain large solitons as $\phi_c \to \phi_{PW}$.

For the standard quantisation $\Delta = 2$ we note that we have two branches of solitonic solutions that cross close to $\phi_c = \phi_{\text{zero}}$. We interpret these solutions in light of this

crossing in the following manner:

1. The branch emanating from vacuum global AdS_4 solution (at $\phi = 0$) is taken to be the one where $\phi_c \in [0, \phi_{\text{zero}})$. Along this branch, we find two solutions for a given value of $\phi_c \in (\phi_{PW}, \phi_{\text{zero}})$, and for one solution with $\phi_c \to \phi_{PW}$ the conserved charges $\mathcal{X}$ diverge. This we will call the favoured branch, since we attain all possible values of the conserved charges. We will see in section 4.3.4 that this branch has the lowest mass at any given charge.

2. The second branch is the set of solutions with $\phi_c > \phi_{\text{zero}}$ with bounded conserved charges. We note that the region for $\phi > \phi_{\text{zero}}$ is governed by an exponentially growing potential, and whilst we see two branches of solution it is unclear that they exhibit damped oscillations as observed in the phenomenological model (where the potential was unbounded from below).[12]

Based on these observations we see that the theory has many features in common with the phenomenological Abelian-Higgs model at the critical charge q_c, at least for solutions with $\phi_c < \phi_{\text{zero}}$.

Given the behaviour of $m(\phi_c)$ for the two choices of boundary conditions, let us examine the scalar profiles; these are plotted in fig. 4.15 using their potential value $V(\phi(r))$ for the three branches of solutions. We note that the branch of solitons that attains a planar limit always has the scalar field approaching the value ϕ_{PW} in the limit. As anticipated, in the dimension $\Delta = 1$ boundary condition the scalar field explores only the region between the global AdS_4 vacuum at the origin and the Pope-Warner vacuum. While for $\Delta = 2$ the scalar field explores all of the field space $\phi \in [0, \infty)$, it gets more and more localised to the region $\phi \in [0, \phi_{PW})$ as we increase the asymptotic charges.

The singling out of the point $\phi = \phi_{PW}$ is quite natural; once the scalar field enters a local minimum it has to pay a gradient price to get out of the potential well. Hence in the asymptotic limit, the field prefers to stay at the PW vacuum and quickly transit into the AdS_4 vacuum at the origin. The geometry in the limit $\mathcal{X} \to \infty$ starts to resemble very closely a thin shell geometry; we have a bubble of the 'true vacuum' which in our consideration is the PW vacuum at $\phi = \phi_{PW}$ inside the 'false vacuum' at $\phi = 0$. Effectively our large scalar solitons are morphing into the domain wall solutions of planar AdS.

[12] This issue is irrelevant for the purposes of the microcanonical phase diagram, since the two branches cross at finite $\phi_c = \phi_{\text{zero}}$.

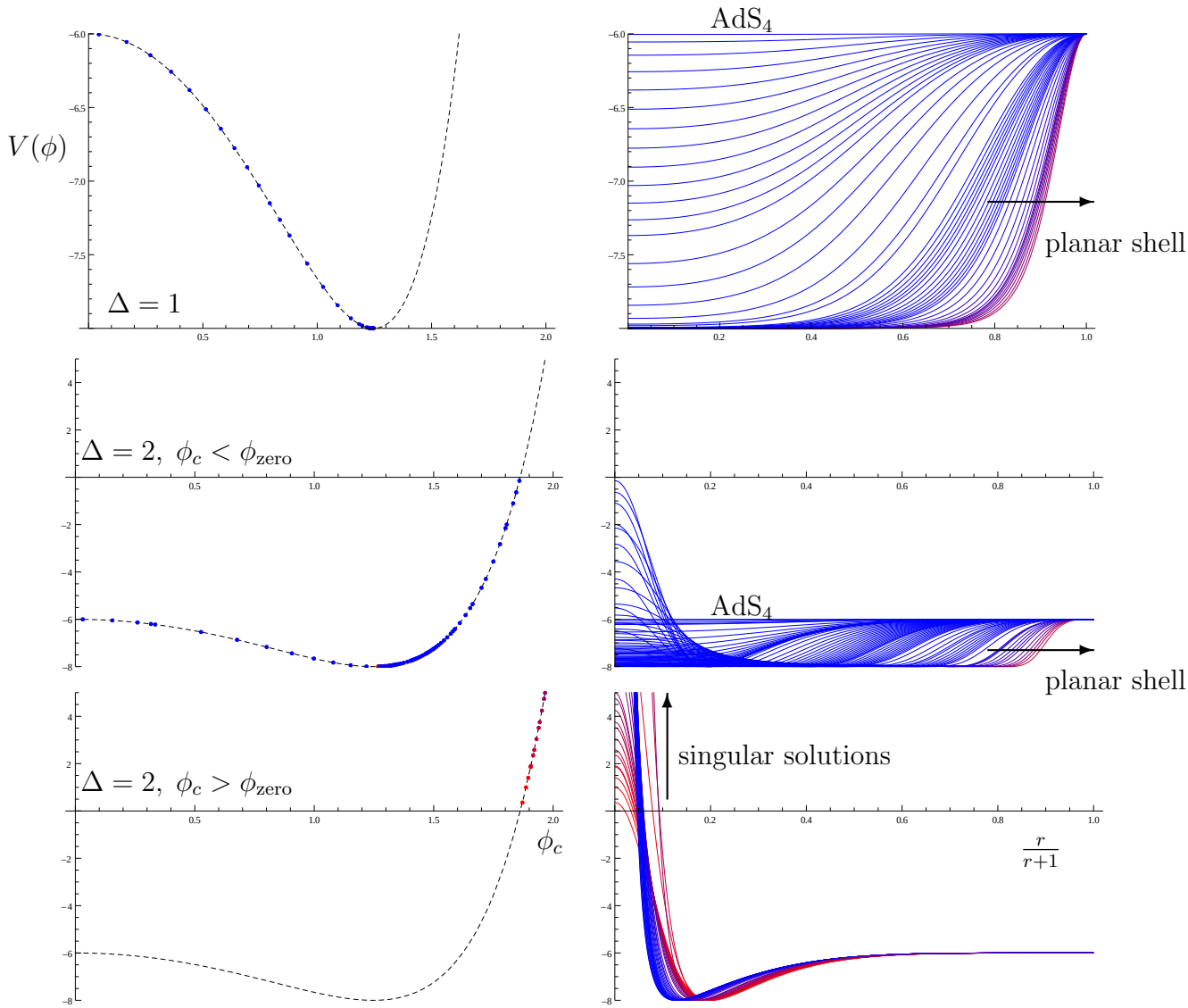

Fig. 4.15: *Left column*: Plot of $V(\phi)$ with each dot corresponding to the value of ϕ_c for solutions shown in the *Right column*: radial plots of the potential $V(\phi(r))$ evaluated on solutions belonging to each of the three branches shown in fig. 4.14). *Top row*: $\Delta = 1$. *Middle row*: $\Delta = 2$ for solutions where $\phi_c < \phi_{\rm zero}$. *Bottom row*: $\Delta = 2$ for solutions where $\phi_c > \phi_{\rm zero}$. Colour indicates the mass, with red corresponding to higher values.

In the standard holographic lore these planar geometries correspond to RG flows driven by vevs. We start in the AdS$_4$ vacuum at the origin of field space and turn on an expectation value for either the $\Delta = 1$ operator $\mathcal{O}_{\phi_2}$ or the $\Delta = 2$ operator $\mathcal{O}_{\phi_1}$. The operators in question, being relevant, drive us away from the fixed point, and in the deep IR we flow to the new conformal fixed point given by the Pope-Warner vacuum. This is

precisely the behaviour expected for multi-extrema scalar potentials as discussed in the planar holographic superfluid context in [114], as was indeed confirmed in the original analysis of the model (4.30) in [46]. The global solitons we have constructed here are the analogues for such RG flows when one considers the field theory on $\mathbb{R} \times S^2$; previously such solutions were studied (for neutral scalars) using fake-supergravity techniques in [168].

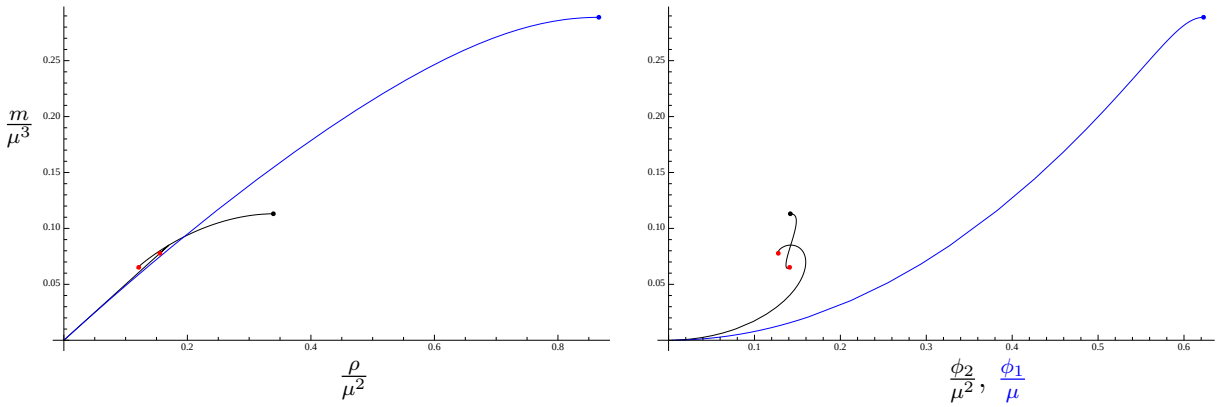

Fig. 4.16: Scaling invariants illustrating convergence to the planar solutions for the branches shown in fig. 4.14. The black dot is the low-temperature planar hairy black hole for $\Delta = 2$ and the blue dot is the corresponding solution for $\Delta = 1$ boundary conditions. The red dots represent the largest ϕ_c solutions obtained numerically.

We can also check for consistency that the large solitons we construct here morph smoothly into the planar hairy black holes. In fig. 4.16 we plot the scaled charges of the theory (in units of μ) to check that as we take $\mu \to \infty$ holding the appropriate dimensionless quantity fixed, the solution becomes a planar soliton. There are again a few distinguished points in this diagram: (i) the global AdS_4 vacuum, (ii) the large soliton asymptoting to the planar hairy black holes, and (iii) two large ϕ_c solutions. This confirms that many features of the picture we had for the case of the Abelian-Higgs model indeed carry through to a model that can be consistently embedded in 11D supergravity.

Aside from the global minimum ϕ_{PW}, we see that the zero of the scalar potential ϕ_{zero} also plays a role in determining the nature of the solutions. This happens only for the $\Delta = 2$ case where $\phi_c > \phi_{PW}$ solutions exist.

For both parts of the favoured branch of solutions, *i.e.* with $\phi_c \in (\phi_{PW}, \phi_{\text{zero}})$, we find that the scalar field attains ϕ_{zero} from below; the field always stays in the region where the potential is negative. It is only for the second disfavoured branch of solutions do we find $\phi_c > \phi_{\text{zero}}$. Thus the (putative) attractor solutions that start out with large values

of core scalar correspond to situations where the scalar field begins on the positive arm of the potential in the IR. Solutions that explore this part of the potential are subdominant in the microcanonical ensemble, as we will see.

4.3.3 Exploring criticality: double-trace deformations

One of the interesting features of the $SU(3)$ truncation under consideration is that it appears to sit at the critical value of the charge q_c for the dimension $\Delta = 2$ quantisation. As noted earlier, the two branches of solutions appear to intersect and it would appear that if one were to detune the charge repulsion then the branches would become disconnected. Note that this interpretation is quite natural despite $q = 1$ being less than the critical value for the phenomenological model. In general we should expect the value of q_c to depend on the details of $V(\phi)$ and $Q(\phi)$, so it is not surprising that there is a smaller value of q_c when we allow non-linearities into the potential.

One way to verify this of course is to tweak the Maxwell coupling so that we can explore the behaviour of $\Delta = 2$ solitons more cleanly. However, this takes us back to the realm of phenomenological models. A more useful strategy then is to explore the behaviour of the system as we tweak the scalar boundary condition, which allows us to stay within the consistent truncation. The result of our numerical exploration is presented in fig. 4.17.

As can be inferred directly from this plot we see that the double-trace boundary condition with $\varkappa \in (0, \infty)$ interpolates between the two cases of $\Delta = 1$ and $\Delta = 2$ quantisations. As we increase $\varkappa$ up from zero, we see that the curves migrate towards the right; the presence of $\phi_2 \neq 0$ clearly manifests itself. What is even more striking is the emergence of new branches of solutions as we increase $\varkappa$. It appears that there are two soliton branches for any $\varkappa \in (0, \infty)$:

1. One branch connects the global AdS_4 vacuum to the planar solitons. The latter are again attained as $\phi_c \to \phi_{PW}$. For $\varkappa$ larger than some critical value $\varkappa_\star$ this branch of solitons becomes multi-valued. This occurs for $\phi_c \in (\phi_{PW}, \phi_{\text{zero}})$. For all finite values of $\varkappa$ along this branch of solitons ϕ_c stays bounded from above by ϕ_{zero}.

2. There are solutions for values of $\phi_c \gtrsim \phi_{\text{zero}}$ as in the case of the $\Delta = 2$ boundary condition with at least two solutions with different conserved charges for given ϕ_c, as previously encountered in the Abelian-Higgs model. Such a double-valued solution branch is observed already for $\varkappa/\mu = 10$. We believe that these branches

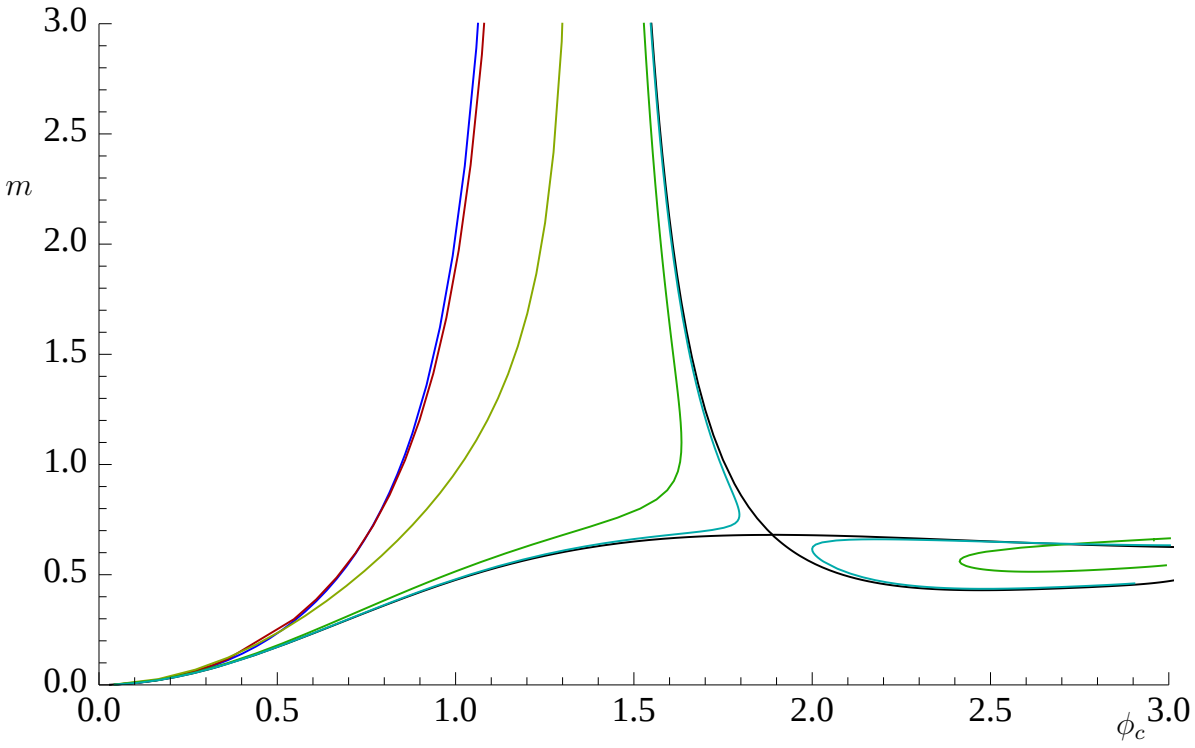

Fig. 4.17: Soliton branches with double-trace deformations at fixed $\mu^{-1}\varkappa = 0.1, 1, 10$ and 100. For reference $\Delta = 1$ is shown in blue and $\Delta = 2$ in black, as in fig. 4.14.

exist all the way down to $\varkappa \to 0$, though at increasingly larger values of ϕ_c, which makes them hard to access numerically.

It is quite reassuring to see that the consistent truncation model incorporates all the crucial physical features encountered in the phenomenological model. A very natural question here is: why is the $\Delta = 2$ boundary condition precisely at the critical point of the theory? We believe this has to do with the full details of the non-linear problem; it would be quite interesting to ascertain the physical reason behind this. We leave this issue for future investigation.

4.3.4 Microcanonical phase diagram

It is interesting to examine the microcanonical phase diagram of the theory characterised by (4.30), presented in fig. 4.18. We will discuss this for the various choices of boundary conditions in turn.

For the $\Delta = 1$ boundary condition, we have a smooth curve $m(\rho)$. These are smooth

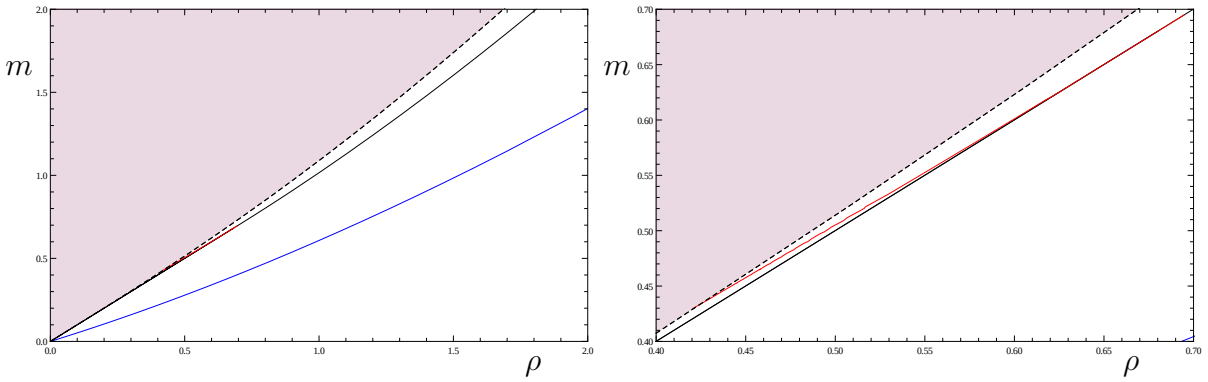

Fig. 4.18: Microcanonical phase diagram for the theory (4.30). $\Delta = 1$ global solitons are shown in blue, $\Delta = 2$ for $\phi_c < \phi_{\text{zero}}$ in black and $\Delta = 2$ for $\phi_c > \phi_{\text{zero}}$ in red. The right-hand panel shows in more detail where the latter solitons lie. The dashed line indicates extremal RN-AdS$_4$ black holes.

solitons that we suspect have the minimal mass in a fixed charge sector.[13] Increasing the mass above this causes one to encounter global scalar hair black holes that dominate the ensemble. For sufficiently high m at fixed ρ, hair-free RN-AdS$_4$ solutions dominate.

The situation is similar for the $\Delta = 2$ boundary condition; the main new element is that the phase boundary has a non-analytic point. This corresponds to the value of m and ρ of the soliton that lies at the intersection of the two solution branches. It is hard to tell from a numerical plot that this is the case. It is also possible that we should encounter some zig-zags in the region above the phase boundary controlled by the attractor solutions, which we however have been unable to verify. The rest of the phase diagram is qualitatively similar to the $\Delta = 1$ case. A curious feature is that second branch of solutions with $\phi_c > \phi_{\text{zero}}$ appears to smoothly merge onto the extremal RN-AdS$_4$ phase line. We thus have two solutions with the same mass for low values of charge; of course the extremal black holes dominate by virtue of their non-vanishing horizon area, but it is curious to see non-uniqueness in the microcanonical phase space at zero temperature.

Double-trace deformations (not shown) reveal smooth solitonic branches for all ρ between the $\Delta = 1$ soliton branch and the $\Delta = 2$ branch. This branch is clearly smooth for $\varkappa \in [0, \varkappa_\star]$. Despite there being some multi-valued behaviour of $\mathcal{X}(\phi_c)$ for $\varkappa > \varkappa_\star$, the phase boundary appears to remain smooth. In addition we have new branches from the region $\phi_c > \phi_{PW}$ that exist for a finite range of ρ. These all lie above the phase boundary and are therefore subdominant in the microcanonical ensemble.

[13] See chapter 6 for a discussion of this point.

4.4 Charged solitons in the M2-brane theory

Our discussion thus far has focused on two models: one phenomenological and another that arises from a consistent truncation of 11D supergravity. In neither case though do we actually know any details regarding the candidate dual field theory. We now turn to an example that has a known dual CFT. We begin with some details of this CFT and the truncation we wish to study, then move on to explore the solutions we have found.

4.4.1 A consistent truncation of the M2-brane theory

Consider the maximally supersymmetric theory with 16 supercharges in (2+1) dimensions, which arises as the low energy limit of the world-volume dynamics of N M2-branes. This theory is superconformal and has $SO(8)$ R-symmetry. One can define this theory in the limit $k \to 1$ of a family of $\mathcal{N} = 6$ superconformal Chern-Simons theories with a gauge group $U(N)_k \times U(N)_{-k}$ (where the subscripts denote the Chern-Simons levels) and a 't Hooft coupling $\lambda \equiv N/k$ [44]. It is believed that in the case of $k = 1, 2$, the supersymmetry should get enhanced to $\mathcal{N} = 8$, *i.e.* 16 supercharges. We will refer to this theory as the M2-brane theory for simplicity. The field theory with $k \to 1$ is dual to M-theory on $\mathrm{AdS}_4 \times S^7$ with $G_4 = 3\,(2N)^{-3/2}$.

The M2-brane theory has bosonic operators that are charged under the $SO(8)$ R-symmetry. Of interest to us will be operators that carry equal charges under $U(1)^4 \subset SO(8)$; in fact, we will be interested in the lightest chiral primary operator of this type. The operator in question has conformal dimension $\Delta = 1$ and since it is a chiral primary has R-charge also equal to unity; we will refer to this operator henceforth as $\mathcal{O}_1$. The conformal dimension immediately implies that we are dealing with a bulk scalar field with mass $m_\phi^2 = -2$.

It turns out that this chiral primary operator, the stress tensor $T_{\mu\nu}$ and the charge current J_μ (where J_μ is the diagonal Cartan generator of $U(1)^4 \subset SO(8)$) form a closed sub-sector of the theory at large N. In particular, for $\mathcal{O}_x$ being any other operator in the spectrum of the M2-brane theory we have

$$\langle T_{\mu_1\nu_1} \cdots T_{\mu_j\nu_j}\, J_{\sigma_1} \cdots J_{\sigma_k}\, \mathcal{O}_1^n\, \mathcal{O}_x \rangle = 0 \tag{4.31}$$

for any $j, k, n \in \mathbb{Z}_+$. This statement, which constrains the field theory OPE in the planar limit, arises from the fact that the corresponding supergravity theory admits a consistent

truncation to a theory of Einstein-Maxwell-charged scalar dynamics in four dimensions. We have been calling this theory the $U(1)^4$ truncation.

The gravitational dynamics of this truncated sector of the M2-brane theory is given by the Lagranagian (4.3) with scalar potential $V(\phi)$ and Maxwell coupling $Q(\phi)$ given by:

$$V(\phi) = -2\left(2 + \cosh\sqrt{2}\phi\right), \quad Q(\phi) = \frac{1}{2}\sinh^2\frac{\phi}{\sqrt{2}}. \tag{4.32}$$

We infer from this Lagrangian that ϕ corresponds to a field of mass $m_\phi^2 = -2$ and $q = \frac{1}{2}$.

This truncation, whose existence was first noted in [104], was recently analysed for holographic superconductivity in [116]. The analysis of [104] will come into play soon. We also note that the corresponding sector of $\mathcal{N} = 4$ SYM in (3+1) dimensions was discussed in the context of charged solitons in [106]; we will have occasion to contrast the behaviour of these two systems during the course of our analysis. In the rest of this section we analyse the behaviour of charged solitons and black holes of this truncation.

Note that the connection to the M2-brane theory is contingent on our quantising the theory (4.3), (4.32) with $\Delta = 1$ boundary conditions for the scalar. We could of course choose to pick $\Delta = 2$ or other boundary conditions as discussed before in section 4.1.1. The former corresponds to some non-supersymmetric CFT in $d = 2+1$, whose spectrum differs from that of the M2-brane theory by one single-trace operator (assuming all other fields are quantised similarly in the two cases). The choice of boundary conditions via $\phi_2(\phi_1)$ can be understood as non-supersymmetric multi-trace deformations of the M2-brane theory.

4.4.2 BPS configurations and supersymmetry equations

One of the advantages of working with a supersymmetric field theory is that we can examine the behaviour of BPS configurations. It turns out that some of the solitonic solutions with the $\Delta = 1$ boundary condition on the scalar can be obtained as solutions to BPS equations. The latter have the distinct advantage of being much simpler than the full set of field equations given in appendix 4.A.

The BPS configurations we are interested in preserve $\frac{1}{8}$ of the original supersymmetries and were written down originally in [104], which we now exploit. Let us first define

a new radial coordinate:[14]

$$r = u\, H(u). \tag{4.33}$$

Consider the following ansatz for the dynamical fields:

$$g(r) = (1 + u^2\, H(u)^4) \left(1 + u\, \frac{H'(u)}{H(u)}\right)^2 \tag{4.34a}$$

$$A_t(r) = \frac{2}{H(u)} \tag{4.34b}$$

$$\phi(r) = \sqrt{2}\, \text{arccosh}\, (H(u) + u\, H'(u)) \tag{4.34c}$$

$$e^{-\beta(r)} = \frac{1}{(H(u) + u\, H'(u))^2} \tag{4.34d}$$

In terms of these new variables, the equations of motion following from (4.3) with (4.32) turn out to be equivalent to a single non-linear second order ODE for $H(u)$ [104]:

$$\left(1 + u^2\, H^4\right) \frac{d^2}{du^2}\, (u\, H) + u\, H^3 \left(\left[\frac{d}{du}\, (u\, H)\right]^2 - 1\right) = 0 \tag{4.35}$$

We note that [104] derives a set of BPS equations that are valid for the M2-brane system with unequal charges in $U(1)^4 \subset SO(8)$; it would be interesting to study the behaviour of solitons in those systems as well, but our current focus will be on the restricted subspace of equal charges.

Asymptopia and conserved charges: The equation (4.35) is straightforward to analyse. First of all we note that the asymptotic solution takes the form:

$$\begin{aligned} &H(u) \to 1 + \frac{h_1}{u} - \frac{h_2}{u^2} + \frac{h_1\, h_2}{u^3} + \cdots\,, \qquad u \to \infty \\ \implies\quad &r = u\, H \simeq u + h_1 - \frac{h_2}{u} + \frac{h_1\, h_2}{u^2} + \cdots \end{aligned} \tag{4.36}$$

It turns out that the large u behaviour of $H(u)$ is precisely such that the solution is normalisable. To check this let us compute the physical fields in the usual radial variable.

[14] Comparison with the results of [104] involves setting their coupling constant $g = \frac{1}{2}$ and rescaling their fields. Specifically, $X_i = 1$, $A^i_{\text{there}} = \frac{1}{\sqrt{2}}\, A$ and $\varphi_i = \frac{\phi}{\sqrt{2}}$ for $i = 1, \cdots, 4$. The X_i are the familiar scalars encountered in four dimensional $U(1)^4$ gauged supergravity and φ_i are the hyperscalars.

We find:

$$\begin{aligned}\phi(r) &= \frac{2\sqrt{h_2}}{r} - \frac{\sqrt{h_2}\,(3+2\,h_2)}{3\,r^3} + \cdots \\ A_t(r) &= 2\left(1 - \frac{h_1}{r} + \cdots\right) \\ g(r) &= r^2 + (1+2\,h_2) - \frac{2\,h_1}{r} + \cdots\end{aligned} \tag{4.37}$$

From this information we have a simple identification between the parameters (h_1, h_2) and those used earlier,

$$g_1 = 2\,h_1\,, \qquad \phi_1 = 2\,\sqrt{h_2}\,, \qquad \mu = 2\,, \qquad \rho = 2\,h_1, \tag{4.38}$$

with which we can check that our solution indeed satisfies the correct boundary conditions (4.5). It is also clear from $q = \frac{1}{2}$ that $\mu\, q = 1$ as required (see appendix 4.B) and the mass density, which for $\Delta = 1$ boundary condition is given by g_1, scales linearly with the charge density: $m = \rho$ along the solution branch.

Regular core analysis: The other piece of data we need is the behaviour at $u = 0$. It is easy to show that there is a smooth solution with series expansion

$$H(u) = h_c + \frac{1}{6}\,h_c^3\,(1-h_c^2)\,u^2 + \frac{1}{40}\,h_c^5\,(1-6\,h_c^2+5\,h_c^4)\,u^4 + \ldots, \tag{4.39}$$

which then implies that

$$\phi_c = \sqrt{2}\,\mathrm{arccosh}(h_c). \tag{4.40}$$

At this point it is clear that we have a one-parameter family of solutions. Since there is no constraint coming from the asymptotic boundary conditions, and given that the core behaviour is controlled by a single parameter, we are free to simply pick h_c or equivalently ϕ_c and integrate (4.35) out. Every such solution is guaranteed to be a smooth soliton. Before discussing the numerical results let us also pause to note some other interesting features of the equation at hand.

Singular core behaviour: We could also ask if it is possible to relax the requirement of a regular core to construct other potential solutions. For the moment, let us call these 'irregular' solitons. The equation (4.35) actually admits a one parameter family of special solutions given by

$$H(u) = 1 + \frac{h_s}{u}. \tag{4.41}$$

This solution is the supersymmetric case of the more general solution presented in (4.13) with $m = \rho = 2h_s$. This solution has lower mass than the extremal solution at the same charge and is singular at the core. These solutions are the AdS_4 analogs of superstars. The fact that static supersymmetric solutions are singular in AdS has been known since the early work of [169]. We can also study the planar limit of this superstar. The only parameter of the solution is h_s, and taking the planar limit by sending $h_s \to \infty$ results in a (zero-parameter) $m = 0$, $\rho \neq 0$ singular planar RN-AdS_4 solution.

Another special solution exists if we simplify the ODE in the approximation of large uH, that is, by replacing the coefficient of the second derivative term by $u^2 H^4$ (*i.e.* dropping the 1), whereby

$$H(u) = \sqrt{1 + \frac{c_1}{u} + \frac{c_2}{u^2}}, \tag{4.42}$$

which indicates the possible presence of a two parameter family of solutions with a $\frac{1}{u}$ core singularity. There is indeed a solution with $H(u) \simeq u^{-1}$ at the origin as one can check by a series expansion. It transpires that there are no other singular core solutions for this system; we will return to this issue once we discuss the results of our numerics.

4.4.3 Global solitons of the $U(1)^4$ truncation

We now turn to the results of numerical studies of solitons of the theory (4.3) and (4.32). We first discuss the behaviour of solitons for the $\Delta = 1$ boundary condition on the scalar, which as we have just seen can be equivalently studied using the supersymmetry equations.

The result of the numerical integration of the field equations is demonstrated in fig. 4.19; here we plot the scalar profile for a rescaled radial variable. The solutions are smooth at the origin, though they start to look more and more 'spiky' as ϕ_c gets large. We have for consistency checked that the results from integrating the full set of field equations produces the same behaviour as the supersymmetric equation (4.35).

It is interesting to ask what happens to the conserved charges $\mathcal{X}$ as we tune the core scalar value. Given the BPS nature of these solutions, the mass and charge scale together $m = \rho$. What is very curious is that the functions $m(\phi_c)$ and $\phi_1(\phi_c) = \langle \mathcal{O}_{\phi_2} \rangle(\phi_c)$ are monotonic in ϕ_c, albeit with very slow growth; see fig. 4.20. The curve fits to a power-law profile: for $\phi_c \gg 1$ we find

$$\phi_1(\phi_c) \simeq 0.8\sqrt{\phi_c} + 0.5\,, \qquad m(\phi_c) \simeq 1.1\sqrt{\phi_c} + 0.5 \tag{4.43}$$

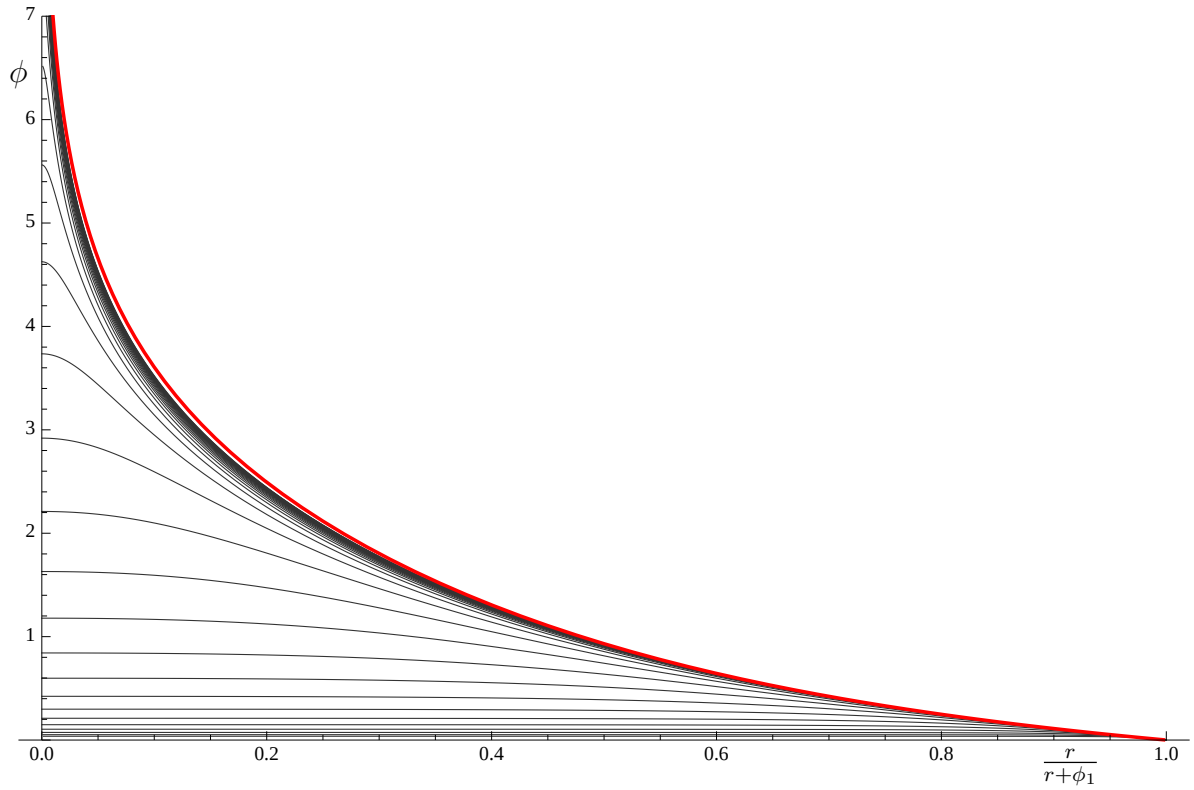

Fig. 4.19: Scalar field ϕ profiles for the supersymmetric $\Delta = 1$ global soliton for various values of ϕ_c. The red line is the analytic planar solution (4.45), which depends only on $\frac{r}{\phi_1}$ and is the reason for our choice of radial variable (see section 4.4.4).

The fact that we have unbounded conserved charges along the soliton branch is not new by now; this behaviour has already been seen, for example in section 4.3, for a similar $\Delta = 1$ boundary condition. What is surprising however, is that this slow growth of asymptotic charges is indicative of critical behaviour, as we now demonstrate.

We can move away from the $\Delta = 1$ BPS solutions by turning on the double-trace coupling (4.8). This allows an admixture of $\frac{1}{r}$ and $\frac{1}{r^2}$ fall-offs, so we can no longer use (4.35) and must instead use the full equations of motion. Our results are shown in fig. 4.20. We note here that increasing $\varkappa$ causes the $m(\phi_c)$ curve to droop down; the $\varkappa = 0$ curve corresponding to the supersymmetric boundary conditions envelopes all solutions with $\varkappa \neq 0$ for large ϕ_c. For small values of $\varkappa$ we encounter a multi-valued curve $m(\phi_c)$; the curve loops back onto itself in a very pronounced manner. At large values of ϕ_c it appears to oscillate down towards an attractor solution, though this is hard to ascertain with a great deal of precision. At the other end of the boundary conditions, *i.e.* as $\varkappa \to \infty$, we see that the loop-back effect has almost disappeared and we encounter a situation akin to $q < q_c$ for the Abelian-Higgs model studied in section 4.2.

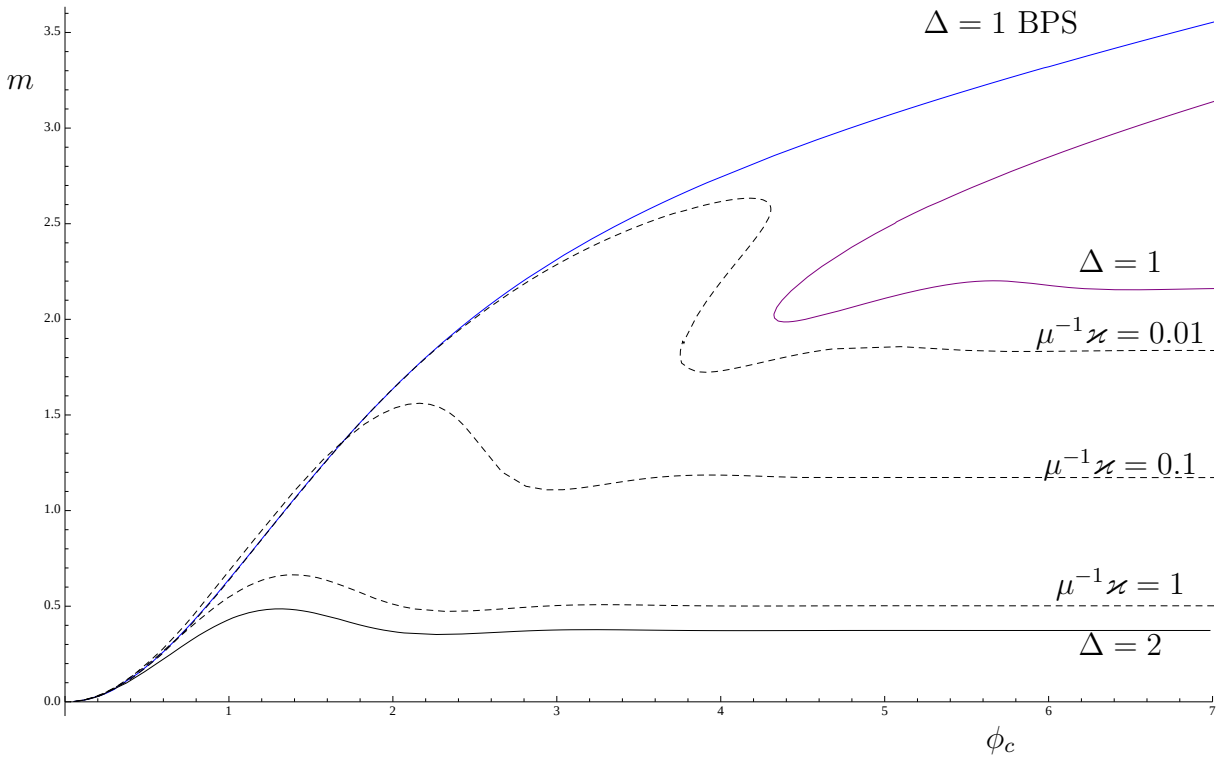

Fig. 4.20: Soliton branches in the theory (4.32). The blue line is the $\Delta = 1$ supersymmetric soliton and appears together with a non-BPS branch of the full set of equations in purple. The dashed lines are branches in the presence of double trace deformations with $\mu^{-1}\varkappa = 0.01, 0.1$ and 1 showing convergence towards the $\Delta = 2$ branch in solid black.

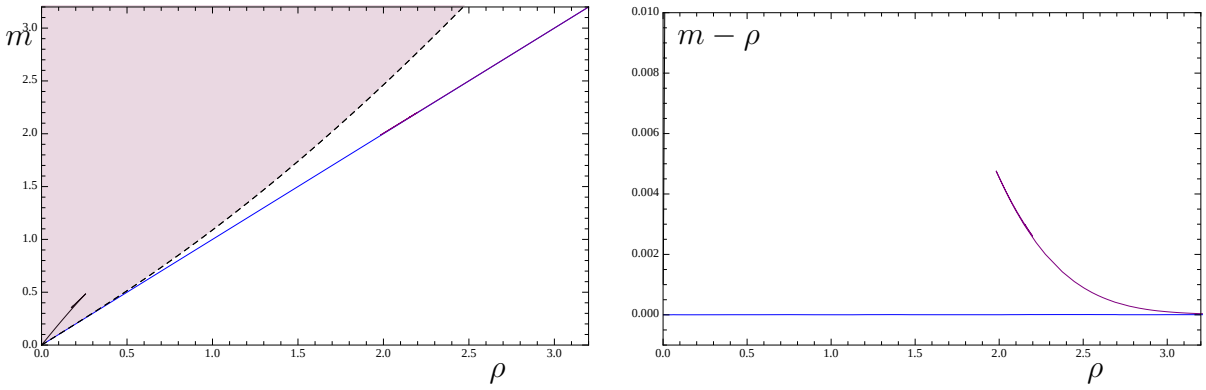

Fig. 4.21: Microcanonical phase diagram for the theory (4.32), showing both the $\Delta = 1$ supersymmetric soliton saturating the BPS bound (blue) and the $\Delta = 1$ non-BPS branch with the same boundary conditions (purple). The $\Delta = 2$ soliton branch is shown in black and lies above the extremal RN-AdS$_4$ line, as expected based on the perturbative results of appendix 4.B.

It is in this sense that the $\Delta = 1$ boundary condition is critical; for small deformations by $\varkappa$ the branch switches from unbounded to bounded. Compare this notion of

criticality, here on the $\Delta = 1$ branch, with that seen in the $SU(3)$ truncation section 4.3. In the latter, critical behaviour was also observed with the two $\Delta = 2$ solution branches intersecting. Here by contrast we now seem to have a single solution branch. Furthermore, along this solution branch the field explores the full domain $\phi \in [0, \infty)$. Whilst in earlier examples, as we have discussed using the scalar profiles, the field preferentially likes to stay in a bounded region, from fig. 4.19 we see that now the scalar field explores the full range of the potential. The main difference of course can simply be attributed to the scalar potential itself; unlike the $SU(3)$ model whose potential given in (4.30) had the Pope-Warner extremum, here we have a monotonic potential function in (4.32). Note also that in contrast to the bottom up models, the potential in the current $U(1)^4$ truncation is exponential and hence a lot steeper.

One fascinating aspect of the double-trace deformations is that it reveals a new solution branch even for the $\Delta = 1$ boundary condition. These solutions are a relic of the folding-back feature noted for $\varkappa \neq 0$: in the limit $\varkappa \to 0$ the fold pinches off and leaves behind this second branch of solutions. This is unprecedented from just the BPS equation (4.35); as we saw in section 4.4.2 one just picks a core value for the scalar and integrates out. However, nothing prevents non-supersymmetric solitons from existing within the $\Delta = 1$ boundary condition. For consistency one anticipates that the mass of solutions along this branch is larger than the BPS value for a given charge ρ. Indeed we find that this is true, as illustrated in the microcanonical phase plot fig. 4.21: they reside above the BPS line and co-exist with global hairy black holes. The solutions encountered along this new branch are therefore subdominant saddles of the microcanonical ensemble. Note that the ability to tune $\varkappa$ was crucial here: by constructing solitons for $\varkappa \neq 0$ and then relaxing back towards $\varkappa \to 0$, we can explore a larger region of the solution space and thus reveal new branches.

4.4.4 Planar theory: analytical neutral soliton and hairy black holes

We have by now a good understanding of the solitonic solutions with various boundary conditions. In the supersymmetric $\varkappa = 0$ case, we learnt that solitons can get arbitrarily large. From our previous experience we would expect the large mass soliton to morph into a zero-temperature planar black hole with scalar hair. The new wrinkle in the story is that no such black hole exists!

The theory under consideration with $\Delta = 1$ boundary conditions was recently studied

in the context of holographic superconductors in [116]. Whilst a probe scalar analysis reveals the possibility of a critical temperature T_c at which planar RN-AdS$_4$ black holes may become unstable towards condensation of the charged scalar field, it transpires that this linear analysis only reveals the presence of a new branch of hairy black hole solutions. These planar hairy black holes start their existence at $T = T_c$, but turn out to be subdominant saddle points. More to the point, they only exist for $T \geq T_c$; there is no solution for lower values of temperature with scalar condensate. The upshot, which we have confirmed numerically, is simply that we have a hairy black hole extending off to large temperatures (see fig. 1 of [116]).

The absence of candidate planar hairy black holes with $T \to 0$ poses a puzzle for our family of supersymmetric solitons: what happens to them in the limit $\phi_c \to \infty$? Could it be that they go over to the planar hairy black hole of arbitrarily large temperature? This bizarre possibility does not come to pass. Rather the solutions go over to a very curious solution: a neutral scalar solution with a singular core.

To understand this, let us recall the exact solution of the field equations presented earlier in (4.15). This is a neutral solution since the gauge field is switched off; it also does not carry any energy density, and so has $m = \rho = 0$. It is however not supersymmetric since the solution does not fall into the BPS ansatz. All the freedom for this family is encoded in a single parameter, which we have chosen to be ϕ_1 for convenience. The core region has $\phi \simeq -\log r$, indicating that this is a not a regular solution. Since $\phi_1(\phi_c) \to \infty$ along the branch of supersymmetric solitons, let us ask what happens to (4.15) as we take it to large field values.

Based on the scalings discussed in section 4.1.3 and accounting for ϕ_1 having dimension one, *i.e.*

$$r \to \xi\, r, \qquad t \to \xi^{-1} t, \qquad \phi_1 \to \xi\, \phi_1, \qquad \xi^2\, d\Omega_2^2 \to d\vec{x}_2^2, \tag{4.44}$$

we find that the solution morphs into the following planar AdS$_4$ geometry:

$$ds^2 = r^2\, \eta_{\mu\nu}\, dx^\mu\, dx^\nu + \frac{dr^2}{\frac{\phi_1^2}{2} + r^2}\,, \qquad \phi(r) = \sqrt{2}\, \text{arcsinh}\, \frac{\phi_1}{\sqrt{2} r}. \tag{4.45}$$

The geometry has a singular horizon at $r = 0$ (the Ricci scalar diverges there), which goes hand in hand with the diverging scalar field. However, this is the desired endpoint of the large supersymmetric solutions. For one, the scalar profile in (4.45) is the limiting behaviour of the large ϕ_1 BPS solitons, as illustrated in fig. 4.19. Furthermore,

by examining the behaviour of $m(\phi_c)$ and $\phi_1(\phi_c)$ along the branch of BPS solutions, we realise that $m \sim \phi_1$ for $\phi_1 \gg 1$. This implies that in the scaling limit the mass and charge of the supersymmetric solutions are rescaled away and we go over to a non-trivial geometry (4.45) supported by the scalar field.

The existence of a non-trivial metric with no mass is a very curious phenomenon, but is not entirely unprecedented. For one the scaling arguments presented in section 4.1.3 imply that global supersymmetric solutions must necessarily go over to $m = 0$ planar solutions. Also as is well-known from the designer gravity constructions, it is possible owing to the presence of non-trivial boundary conditions to attain solutions with zero ADM mass. As mentioned earlier, once one relaxes boundary conditions we are guaranteed a positive energy theorem (under certain assumptions; *c.f.* [103]), but the global minimum of the energy can indeed be negative. In fact, the solution (4.45) is also the limiting behaviour of designer gravity solitons originally studied in [101]. In the designer gravity language one engineers boundary conditions $\phi_2(\phi_1)$ so as to guarantee the existence of solitons. For the theory with potential (4.32) the designer soliton curve $\phi_2(\phi_1) \to$ constant for $\phi_1 \gg 1$. As noted in [103] this is a non-generic case with an exactly determinable fake-superpotential; knowledge of the latter allows us to infer the solution (4.45).

4.A Bulk equations of motion and boundary terms

In this appendix we present the equations of motion for the general action of (4.3), and discuss the required boundary counterterms. The functions $Q(\phi)$ and $V(\phi)$ for the theories of interest are listed in table 4.1. We find

$$\begin{aligned} R_{ab} - \frac{1}{2}g_{ab}R &= \frac{1}{2}\left(F_{ac}F_b{}^c - \frac{1}{4}g_{ab}F^2\right) + \left(\partial_a\phi\partial_b\phi - \frac{1}{2}g_{ab}\left(\partial\phi\right)^2\right) \\ &\quad + \frac{1}{\ell^2}Q(\phi)\left(A_aA_b - \frac{1}{2}g_{ab}A^2\right) - \frac{1}{2\ell^2}g_{ab}V(\phi) \end{aligned} \tag{4.46}$$

$$\nabla_a F^{ab} = \frac{2}{\ell^2}Q(\phi)A^b \tag{4.47}$$

$$\Box\phi = \frac{1}{2}\frac{Q'(\phi)}{\ell^2}A^2 + \frac{1}{2}\frac{V'(\phi)}{\ell^2}. \tag{4.48}$$

We must supplement our bulk action (4.3) with appropriate boundary terms: our total action is

$$S = S_{\rm bulk} + \frac{1}{8\pi G_4}\int d^3x\,\sqrt{-\gamma}\,\mathcal{K} + S_{\rm ext} + S_{\rm ct}, \tag{4.49}$$

where $S_{\rm ext}$ is the collection of scalar and Maxwell boundary terms necessary for a good variational principle (we have explicitly indicated the Gibbons-Hawking term). $S_{\rm ct}$ is an expression covariant in intrinsic boundary quantities designed to render the on-shell action finite.

The boundary terms for Einstein-scalar theories with multi-trace boundary conditions for scalars were originally derived using the covariant phase space formalism in [102] and extended to include Maxwell fields in [119]. By analysing the asymptotic behaviour of various fields it is easy to convince oneself that the counter-terms of interest are independent of $Q(\phi)$ and depend only on the quadratic approximation to $V(\phi)$. Thus, by writing down the counterterms for (4.2), we immediately obtain the results for the more general case. We thus directly borrow the results of these references and quote the final answer without further derivation below.

The main quantity we require is the ADM energy density m, which we use to characterise our solutions. This turns out to be given by [101, 102]:

$$m = g_1 + \phi_1\,\phi_2 + \frac{1}{2}\,\varkappa\,\phi_1^2 \equiv g_1 + \frac{3}{2}\,\varkappa\,\phi_1^2 \tag{4.50}$$

for double-trace boundary conditions. Here g_1 is the coefficient of the $1/r$ term in the asymptotic behaviour of the metric function $g(r)$ as indicated in (4.5d), with ϕ_1 and ϕ_2 the fall-offs of the scalar field (4.5b). Note that in exactly $\Delta = 1$ and $\Delta = 2$ cases we have $g_1 = m$. The total energy of the solutions is $E = \mathrm{Vol}(S^2)\,m$; we prefer to use the energy density since it is more naturally suited to analysing the planar limit. The other conserved charge of interest, the charge density, is simply ρ from the fall-off of the gauge field, given in (4.5a).

4.B Perturbative construction of global solitons

In this appendix we explain the strategy to construct global solitons in a perturbation expansion around the AdS_4 vacuum. The first construction of such solutions was presented in [105] and we will effectively be reviewing the same for our models. The general logic of our construction is independent of the details of the scalar field, though both $V(\phi)$ and $Q(\phi)$ will enter into the details of the perturbation theory.

The starting point for such a construction is the fact that the eigenmodes of the charged scalar field in global AdS_4 have frequencies $\omega = \Delta + 2\,n$ with $n \in \mathbb{Z}_+$ as long as we maintain spherical symmetry. Actually, we will be interested in the ground state soliton,

so we also have the luxury of setting $n = 0$. This ground state is then characterised by the zero-point energy Δ, which is of course determined solely by the scalar mass via the standard formula $\Delta = \frac{3}{2} \pm \sqrt{\frac{9}{4} + m_\phi^2\,\ell^2}$, where we are restricting attention to AdS_4. We will also have need of the scalar wavefunction, which for $m_\phi^2\,\ell^2 = -2$ takes a simple form:[15]

$$\phi_{\rm lin}(r) = \frac{1}{(1+r^2)^{\frac{\Delta}{2}}}. \tag{4.51}$$

This wavefunction is clearly regular at the origin and satisfies $\phi_{\rm lin}(r) \to r^{-\Delta}$ as $r \to \infty$. Since we noted that the scalar field here has a nontrivial ground state energy, a neutral scalar field will also have a temporal oscillation with frequency $\omega = \Delta$ that is a pure phase. For a charged scalar field this phase can be absorbed into a background gauge field (by the same trick we used in writing the Lagrangian in section 4.1.1). Essentially all we need to do is turn on a constant background gauge field tuned such that we mock up the phase. The upshot of this discussion is that there is a static perturbation around the global AdS_4 geometry (4.13) (with $m = \rho = 0$) where

$$\phi_{\rm lin}(r) = \frac{1}{(1+r^2)^{\frac{\Delta}{2}}}\,, \qquad \mu = \frac{\Delta}{q}, \tag{4.52}$$

assuming that for small ϕ, $Q(\phi) \simeq q^2\,\phi^2$. This is all the data we need to set up the perturbation expansion.

We denote by ϵ the expectation of the dual operator in the field theory; *i.e.* $\epsilon = \langle \mathcal{O}_\Delta \rangle$. This will be the small parameter we use in our perturbation theory. Treating both $\Delta = 1$ and $\Delta = 2$ together, the perturbative solution ansatz can be written as

$$\begin{aligned}
\phi(r) &= \frac{\epsilon}{(1+r^2)^{\frac{\Delta}{2}}} + \sum_{k=1}^{\infty} \epsilon^{2k+1}\,\phi_{(2k+1)}(r) \\
A_t(r) &= \frac{\Delta}{q} + \sum_{k=1}^{\infty} \epsilon^{2k}\,A_{(2k)}(r) \\
g(r) &= 1 + r^2 + \sum_{k=1}^{\infty} \epsilon^{2k}\,g_{(2k)}(r) \\
f(r) &= 1 + r^2 + \sum_{k=1}^{\infty} \epsilon^{2k}\,f_{(2k)}(r),
\end{aligned} \tag{4.53}$$

where for brevity we define $f(r) \equiv g(r)\,e^{-\beta(r)}$.

[15] For generic Δ, the scalar profiles that solve the linearised wave equation are hypergeometric functions.

Next we solve for the corrections $\phi_{(2k+1)}(r)$, $A_{(2k)}(r)$, $g_{(2k)}(r)$, $f_{(2k)}(r)$ by recursively solving the equations order by order in powers of ϵ. Most of the analysis is in fact analytical, because the linearised equations admit closed-form solutions. The integration constants are all fixed by the choice of boundary conditions: regularity at the origin and normalisability at AdS asymptopia (which we take to also include the scalar boundary condition provided in terms of the fall-off condition).

We now simply quote the results of such a construction for the Abelian-Higgs model discussed in section 4.2. The physical parameters characterising the solution are all expressed as functions of $\langle \mathcal{O}_\Delta \rangle$. For the $\Delta = 2$ boundary condition we find

$$\begin{aligned}
\epsilon &= \langle \mathcal{O}_{\phi_1} \rangle \\
\mu &= \frac{2}{q} + \frac{5q^2-2}{8q}\epsilon^2 + \frac{(52\pi^2-615)\,q^4 + (1322-114\pi^2)\,q^2 + 74\pi^2 - 821}{384q}\epsilon^4 + \mathcal{O}(\epsilon^6) \\
\rho &= \frac{\pi}{4}q\epsilon^2 - \frac{\pi}{192}q\left(\left(4\pi^2-25\right)q^2 + 58 - 8\pi^2\right)\epsilon^4 + \mathcal{O}(\epsilon^6) \\
m &= \frac{\pi}{4}\epsilon^2 - \frac{\pi}{384}\left(\left(8\pi^2-65\right)q^2 + 122 - 16\pi^2\right)\epsilon^4 + \mathcal{O}(\epsilon^6) \\
\phi_c &= \epsilon + \frac{1}{48}\left(\left(16-3\pi^2\right)q^2 + 6\pi^2 - 40\right)\epsilon^3 + \mathcal{O}(\epsilon^5)
\end{aligned} \tag{4.54}$$

while the $\Delta = 1$ boundary condition leads to

$$\begin{aligned}
\epsilon &= \langle \mathcal{O}_{\phi_2} \rangle \\
\mu &= \frac{1}{q} + \frac{2q^2+1}{4q}\epsilon^2 + \frac{(64\pi^2-720)\,q^4 + (660-60\pi^2)\,q^2 + 17\pi^2 - 192}{384q}\epsilon^4 + \mathcal{O}(\epsilon^6) \\
\rho &= \frac{\pi}{2}q\epsilon^2 - \frac{\pi}{24}q\left(\left(2\pi^2-18\right)q^2 + 6 - \pi^2\right)\epsilon^4 + \mathcal{O}(\epsilon^6) \\
m &= \frac{\pi}{4}\epsilon^2 - \frac{\pi}{96}\left(\left(4\pi^2-42\right)q^2 + 9 - 2\pi^2\right)\epsilon^4 + \mathcal{O}(\epsilon^6) \\
\phi_c &= \epsilon - \frac{1}{16}\left(\pi^2-8\right)\left(2q^2-1\right)\epsilon^3 + \mathcal{O}(\epsilon^5).
\end{aligned} \tag{4.55}$$

Note that we have quoted here the results parametrised by the expectation value of the CFT operator, which is the natural parameter for the perturbation expansion. It is possible to set up the perturbation directly in terms of the core scalar value, ϕ_c, but that appears to be a bit more cumbersome.

It is interesting to ask whether solitons with multi-trace boundary conditions can be constructed using a similar perturbative expansion. One might naively have thought this to be possible; after all the multi-trace operators correspond to multi-particle states in the bulk via the AdS/CFT dictionary. Consider then the case where we impose a

double-trace boundary condition $\phi_2 = \varkappa \phi_1$. What we would like to do is find a regular two-particle wavefunction that in the linear approximation is regular at the origin and satisfies the asymptotic boundary condition mentioned above. This turns out to be impossible around the vacuum global AdS_4 solution, as we now explain.

Previously, we wrote down the linear eigenmodes for the scalar wave operator, where we had imposed regularity at the origin. It turns out that for $m_\phi^2 \ell^2 = -2$ the solutions to the linear wave equations for static spherically symmetric configurations about global AdS_4 are

$$\begin{aligned} \phi^{(2)}_{\rm lin}(r) &= \frac{1}{1+r^2}\left(\alpha_2 \frac{r^2-1}{r} + \beta_2\right) \ , \qquad \mu = \frac{2}{q} \\ \phi^{(1)}_{\rm lin}(r) &= \frac{1}{\sqrt{1+r^2}}\left(\alpha_1 + \frac{\beta_1}{r}\right) \ , \qquad \mu = \frac{1}{q} \end{aligned} \tag{4.56}$$

For the standard boundary condition (*i.e.* $\Delta = 2$) the ground state wavefunction is given by the first line with $\beta_2 = \phi_2$ and $\alpha_2 = 0$ while the alternate boundary condition (*i.e.* $\Delta = 1$) involved a seed solution with $\alpha_1 = \phi_1$ and $\beta_1 = 0$.

The double-trace deformation of the dual CFT involves $\mathcal{O}^2_{\phi_2}$ which should correspond to a two-particle state. The naive wavefunction for this appears to be simply $\phi_{\rm lin}(r) \simeq \frac{1}{1+r^2}$, which can be viewed for the moment as $(\phi^{(1)}_{\rm lin})^2$. Fortuitously, this is a static mode once we set $\mu = \frac{2}{q}$; this is natural since we are dealing with a two particle state (so the net charge is doubled). However, this cannot be the full story, as the mode in question does not satisfy the asymptotic boundary condition. Note that the double-trace boundary condition requires that we have $\phi_{\rm lin}(r) \to \frac{\phi_1}{r} + \frac{\varkappa \phi_1}{r^2}$. Inspecting (4.56) it is immediately clear that there is no linearised solution that is both regular at the origin and satisfies the asymptotic fall-off (for one we cannot simply set $\alpha_2 = \phi_1$ and $\beta_2 = \varkappa \phi_1$ as it is irregular at the origin).

The absence of a seed solution with correct boundary conditions makes it clear that it is not possible to set up a perturbation series analogous to the single-trace boundary condition. We believe this is because of the peculiar nature of the multi-trace boundary conditions: whilst they naively correspond to multi-particle state in the field theory, rather than being described by a new bulk effective field (which should roughly speaking be ϕ^2), such states are described by imposing a local relation between boundary fall-offs. This is somewhat reminiscent of issues arising with double-trace fermonic operators as recently discussed in [170]. We hope to return to a proper resolution of this issue in the future.

Conceptually, the breakdown of perturbation theory around global AdS_4 is not too

hard to understand. Whilst one can easily see this geometry (and the dual CFT vacuum) as being the appropriate state to expand around for single trace operators, it is no longer the case when we have an explicit deformation in the CFT Lagrangian. If one has a candidate ground state for the deformed CFT, then we would be able to undertake a perturbation analysis about it. The trouble is that constructing the appropriate bulk geometry usually involves numerical solving of the field equations. In the bulk of the chapter we have side-stepped this question by direct numerical integration of the field equations with the appropriate boundary conditions. It would indeed be interesting to find examples where we can adapt perturbation theory techniques to multi-trace deformed field theories.

Chapter 5

Superconducting instabilities of R-charged black branes

In this chapter, based on [171], we explore superconducting instabilities of black branes in $SO(6)$ gauged supergravity at finite temperature and finite R-charge densities. We compute the critical temperatures for homogeneous neutral and superconducting instabilities in a truncation of 20 scalars and 15 gauge fields as a function of the chemical potentials conjugate to the three $U(1)$ charges in $SO(6)$.

In the following section we present this consistent truncation and the three-chemical potential black brane solution we will be employing as the background normal phase. We will see that a study of this normal phase reveals basic lessons about the use of consistent truncations. We move on in section 5.2 to calculate the field equations for homogeneous fluctuations of the other fields in the truncation about this background that do not source gravitational fluctuations. The structure of the equations for the fluctuations and the instabilities found naturally leads to two different types of mode. Modes that are continuously connected to charged modes are discussed in section 5.3, while those that are continuously connected to neutral modes are discussed in section 5.4.

In both cases we map out the regions in the space of chemical potentials that are unstable to each mode and detail the critical temperatures. We find that despite the imbalance provided by multiple chemical potentials there is always at least one superconducting black brane branch, emerging at a temperature where the normal phase is locally thermodynamically stable.

5.1 Truncation and the normal phase

In addition to gravity, the bosonic sector of $\mathcal{N} = 8$ $SO(6)$ gauged supergravity in 5D [172, 173, 174] contains 42 scalars, 15 $SO(6)$ gauge fields as well as twelve 2-form gauge potentials. The scalars are organised into irreducible representations of $SO(6)$ and have masses $m_\phi^2\ell^2 = -4, -3, 0$ in an AdS_5 vacuum, the lightest of which saturates the BF bound. We will employ a further consistent truncation of this theory down to 15 gauge fields and 20 of the BF bound-saturating scalars. In 10D ingredients this truncation corresponds to retaining only the metric and 5-form of Type IIB supergravity [175].

This truncation provides a convenient starting point in our search for superconducting black brane branches. First, the truncation contains a three-parameter family of black brane backgrounds that we may employ as the normal phase. Second, only the lightest scalars remain and these should display a greater susceptibility to forming condensates in the black brane backgrounds.[1] Finally, we are able to make contact with special cases studied elsewhere at the nonlinear level.

The 20 scalars and 15 gauge fields can be packaged as a symmetric unimodular $SO(6)$ tensor T_{ij} and an antisymmetric $SO(6)$ tensor A_{ij}, respectively. The equations of motion for this consistent truncation may be derived from the following action, with the adjoint $SO(6)$ indices written in matrix form:

$$S = \frac{1}{16\pi G_5}\int d^5x\sqrt{-g}\left(R - \frac{1}{4}\operatorname{tr} T^{-1}\left(D_aT\right)T^{-1}\left(D^aT\right) + \frac{1}{8}\operatorname{tr} T^{-1}F_{ab}T^{-1}F^{ab} - V\right). \tag{5.1}$$

We have omitted a Chern-Simons term that will not be important for the electric, homogeneous superconductors sought here. The scalar potential is given by

$$V = \frac{g_c^2}{2}\left(2\operatorname{tr} T^2 - (\operatorname{tr} T)^2\right), \tag{5.2}$$

with the $SO(6)$ gauge-covariant derivative $D_aT = \nabla_aT + g_c\left[A_a, T\right]$ and field strength $F_{ab} = \partial_aA_b - \partial_bA_a + g_c\left[A_a, A_b\right]$. We set the dimensionful gauge coupling $g_c = 1$ throughout, which fixes the AdS length.

When written in 2×2 blocks, the background three-charge asymptotically AdS black

[1] Superconducting branches for special cases of the other scalar field sectors were investigated in [118].

brane solution [125] takes the form

$$T = T_0 \equiv \mathrm{diag}(X_1\mathbb{1}, X_2\mathbb{1}, X_3\mathbb{1}) \tag{5.3}$$

$$A = A_0 dt \equiv \mathrm{diag}(A_1\sigma, A_2\sigma, A_3\sigma)dt \tag{5.4}$$

where $\mathbb{1}$ is the 2×2 unit matrix and $\sigma \equiv i\sigma_2$. The unimodularity condition on T enforces $X_1X_2X_3 = 1$. The black branes are parametrised by three charge parameters q_I and take the form

$$\begin{aligned} ds^2 &= -H^{-2/3} f dt^2 + r^2 H^{1/3}\left(dx^2+dy^2+dz^2\right) + \frac{H^{1/3}}{f}\,dr^2 \\ X_I &= \frac{H^{1/3}}{H_I}, \quad A_I = \sqrt{\frac{r_+^4 H(r_+)}{q_I}}\left(\frac{1}{H_I(r)} - \frac{1}{H_I(r_+)}\right). \end{aligned} \tag{5.5}$$

We have defined

$$H_I(r) = 1 + \frac{q_I}{r^2}, \quad H(r) = H_1H_2H_3, \quad f(r) = -\frac{r_+^4 H(r_+)}{r^2} + r^2 H(r) \tag{5.6}$$

and $I = 1,2,3$ labels each 2×2 block. The horizon is at $r = r_+$; we use the coordinate freedom in r to fix $r_+ = 1$ and thus $\kappa_I = q_I$ in the conventions of [176].

The thermodynamics of these backgrounds was originally studied in [29, 177] in the context of holography, with the study of spinning D3-branes, their counterparts in the full 10D theory, initiated in [178, 179] and extended in [180, 181].

5.1.1 Multiple black brane branches

We work in the grand canonical ensemble throughout. The chemical potentials for this system can be expressed in terms of the charge parameters

$$\mu_I = \frac{\sqrt{q_I(1+q_1)(1+q_2)(1+q_3)}}{1+q_I} \tag{5.7}$$

and are conjugate to the three R-charges. In this ensemble the relevant thermodynamic potential is the Gibbs potential, Ω, with density $\omega = \frac{\Omega}{V_3}$, where V_3 is the (divergent) spatial volume of the dual theory. We employ a dimensionless expression $\hat{\omega}$:

$$\omega = -\frac{(1+q_1)(1+q_2)(1+q_3)}{16\pi G_5}, \qquad \hat{\omega} \equiv \frac{16\pi G_5\,\omega}{(\mu_1^2+\mu_2^2+\mu_3^2)^2}. \tag{5.8}$$

Similarly we employ a dimensionless version of the temperature, $\hat{T}$:

$$T = \frac{2 + q_1 + q_2 + q_3 - q_1 q_2 q_3}{2\pi\sqrt{(1+q_1)(1+q_2)(1+q_3)}}, \qquad \hat{T} = \frac{T}{\sqrt{\mu_1^2 + \mu_2^2 + \mu_3^2}}. \tag{5.9}$$

It is well known that this black brane family is not thermodynamically stable everywhere. For a stable thermodynamic equilibrium, the theory should lie at a local minimum of the thermodynamic potential, at fixed temperature and chemical potential. Constructing the Hessian matrix

$$\mathcal{H} = \frac{\partial^2 \varepsilon}{\partial s \partial \rho_I} \tag{5.10}$$

for variations of the energy density ε with respect to the entropy density s and the R-charge densities ρ_I following [176], a necessary condition for local thermodynamic stability is given by

$$\det \mathcal{H} \propto 2 - q_1 - q_2 - q_3 + q_1 q_2 q_3 > 0. \tag{5.11}$$

Note however that this is not a sufficient condition as there may be an even number of negative eigenvalues of $\mathcal{H}$.[2] At a fixed set of chemical potentials, (μ_1, μ_2, μ_3), we find that there is a minimum temperature for the existence of a thermodynamically stable dominant branch of solutions.

Without loss of generality we focus on $\mu_I \geq 0$ at which we only consider those solutions with $q_I \geq 0$. This ensures that the solutions are regular. For this ensemble we fix two dimensionless ratios of the chemical potentials, $\zeta_1 = \frac{\mu_1}{\mu_3}$ and $\zeta_2 = \frac{\mu_2}{\mu_3}$, or any function thereof, in addition to $\hat{T}$. In general there are four black brane solutions at any grand canonical coordinate, $(\zeta_1, \zeta_2, \hat{T})$. To explore the phases of the system we adopt the coordinates

$$p_1 = \frac{\mu_1 + \mu_2 - 2\mu_3}{\sqrt{6}\sqrt{\mu_1^2 + \mu_2^2 + \mu_3^2}}, \qquad p_2 = \frac{\mu_1 - \mu_2}{\sqrt{2}\sqrt{\mu_1^2 + \mu_2^2 + \mu_3^2}}, \tag{5.12}$$

which are dimensionless quantities and depend only on $\zeta_{1,2}$.

At a representative fixed (p_1, p_2) we show the free energy as a function of the temperature in the left panel of fig. 5.1, illustrating that the dominant line of black branes are only stable above a threshold temperature. This is the threshold for thermodynamic instability as described by the condition (5.11), as well as the positivity of the eigenvalues of $\mathcal{H}$. In appendix 5.A we show that there is always one dominant branch of black branes with a minimum temperature given by the threshold for thermodynamic instability.

[2] The author wishes to thank Mukund Rangamani for stressing this point.

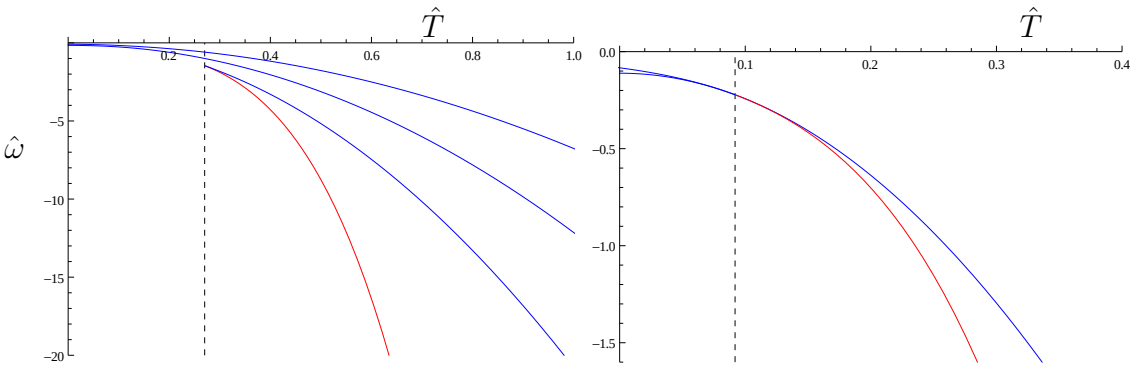

Fig. 5.1: *Left:* Gibbs free energy density for the various black brane branches that exist at fixed $(p_1, p_2) = (-0.2, -0.1)$, defined in (5.12). Solutions that are thermodynamically unstable are shown in blue. A locally thermodynamically stable branch has a minimum temperature marked by the dashed line. *Right:* Fixed $p_1 = p_2 = 0$. The equal-charge black brane is only thermodynamically stable above the temperature indicated by the dashed line, whilst below it is both thermodynamically unstable and subdominant in the grand canonical ensemble.

It is worth noting that in some cases there is a branch of black branes that satisfy the condition (5.11), but that are not thermodynamically stable due to an even number of negative eigenvalues of $\mathcal{H}$. For example, the three equal chemical potential case, where $p_1 = p_2 = 0$, is shown in the right panel of fig. 5.1. The dominant black brane above the critical temperature $\hat{T} \simeq 0.09$ is locally thermodynamically stable and has equal charges $q_1 = q_2 = q_3$ and is nothing but the Reissner-Nordström-AdS$_5$ (hereafter RN-AdS$_5$) black brane. Below this critical temperature $\mathcal{H}$ picks up two equal negative eigenvalues with eigenvectors $\delta(s, \rho_1, \rho_2, \rho_3) = (0, -1, 0, 1), (0, -1, 1, 0)$. These eigenvectors for this thermodynamic instability are naturally associated with a Gubser-Mitra dynamical instability [182, 183], as well as the generation of neutral zero modes at the threshold of stability that we discuss further in section 5.4.

On a different tack, the free energy analysis presented here reveals a worrisome issue associated with the RN-AdS$_5$ solution, as considered in this top-down approach. Working in the further consistent truncation of our theory corresponding to three equal charge parameters, RN-AdS$_5$ becomes the only black brane solution and therefore appears to be thermodynamically dominant. However, below the critical temperature for the thermodynamic instability discussed above, $\hat{T} \simeq 0.09$, RN-AdS$_5$ is not thermodynamically dominant in our more complete theory.

To understand the coordinates (5.12) better, we project the condition $\mu_I \geq 0$ into (p_1, p_2) space. This region is formed by the intersection of three ellipses, with equations

$$3p_1^2 + p_2^2 = 1, \quad 3p_1^2 + 5p_2^2 \pm 2\sqrt{3}p_1 p_2 = 2, \tag{5.13}$$

and is shown in fig. 5.2. Within this region we find there is always a stable branch that dominates the ensemble above some critical temperature, as in the explicit examples shown in fig. 5.1. The minimum temperature for this dominant stable branch as a function of p_1 and p_2 is illustrated in the right panel of fig. 5.2.

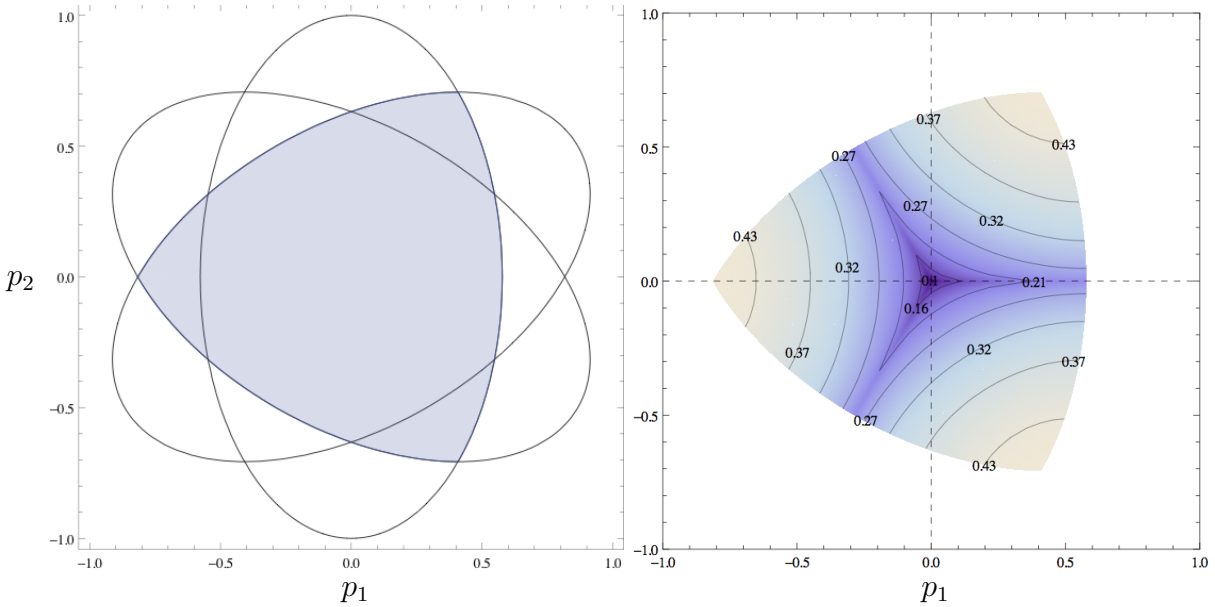

Fig. 5.2: *Left:* Region where black brane backgrounds with $\mu_I \geq 0$ exist. *Right:* Critical temperatures for the thermodynamic instability — *i.e.* the minimum temperature, $\hat{T}$, for which the dominant branch is thermodynamically stable.

5.2 Fluctuations about the normal phase

We now detail the fluctuations of the 20 scalars and 15 gauge fields about the background normal phase solution given in section 5.1. We parametrise deviations from the scalar field matrix T_0 (5.3) by the fluctuation matrix $\chi(r)$, and deviations about the gauge field matrix A_0 (5.4) with radial electric fluctuations $\alpha(r)$:

$$T = T_0 e^{\chi}\,, \qquad \operatorname{tr}\chi = 0\,; \qquad A = (A_0 + \alpha)dt. \tag{5.14}$$

The trace condition enforces unimodularity of T at all orders in the fluctuation. The action for the linearised fluctuations can be found in appendix 5.B. Since the background is block diagonal, the fluctuations in different 2×2 blocks do not couple.

In general the fluctuations χ and α source metric fluctuations. For general background

$\{q_I\}$ these may be switched off by enforcing the conditions

$$\operatorname{tr}\chi_{II} = \operatorname{tr}\sigma\alpha_{II} = 0, \tag{5.15}$$

where the trace is performed within the 2×2 block. In detail these conditions are so restrictive that we have $\alpha_{II} = 0$ and $\sigma\chi_{II} + \chi_{II}\sigma = 0$, leaving the only non-zero diagonal block fluctuation as $\sigma\chi_{II} - \chi_{II}\sigma$, which as we shall see shortly is a charged mode. For special cases of the background the conditions relax: for two or three equal charges we find

$$\sum_I \operatorname{tr}\chi_{II} = \sum_I \operatorname{tr}\sigma\alpha_{II} = 0, \tag{5.16}$$

where the sum is performed over equal q_I blocks, with any remaining diagonal blocks constrained by (5.15).

5.2.1 Diagonal fluctuations

Without loss of generality we focus on fluctuations living in the $(1,1)$ block,

$$\chi = \begin{pmatrix} \chi_{11} & 0 & 0 \\ 0 & 0 & 0 \\ 0 & 0 & 0 \end{pmatrix}, \qquad \alpha = \begin{pmatrix} \sigma\hat{\alpha}_{11} & 0 & 0 \\ 0 & 0 & 0 \\ 0 & 0 & 0 \end{pmatrix}, \tag{5.17}$$

where χ_{11} is a symmetric 2×2 matrix and $\hat{\alpha}_{11}$ is proportional to the 2×2 identity matrix. To satisfy the backreaction and unimodularity constraints away from equal charges we must impose $\operatorname{tr}\chi_{11} = 0$.

The equations of motion for these fluctuations may be partially diagonalised by moving to the new variables

$$\textbf{Neutral:} \quad \phi_{11}^{(+)} = \sigma\chi_{11} + \chi_{11}\sigma, \qquad \alpha_{11}^{(+)} = \sigma\hat{\alpha}_{11} + \hat{\alpha}_{11}\sigma, \tag{5.18}$$

$$\textbf{Charged:} \quad \phi_{11}^{(-)} = \sigma\chi_{11} - \chi_{11}\sigma, \qquad \alpha_{11}^{(-)} = \sigma\hat{\alpha}_{11} - \hat{\alpha}_{11}\sigma = 0. \tag{5.19}$$

The gauge potential for the $(-)$ mode vanishes due to the antisymmetry of $\sigma\hat{\alpha}_{11}$. Note that in what follows we define $\Box_r \equiv \frac{1}{\sqrt{-g}}\partial_r(\sqrt{-g}g^{rr}\partial_r)$ and write the gauge fields as one-forms with $F_I = dA_I$.

Charged equations of motion

The equation of motion for the charged scalar $\phi_{11}^{(-)}$ is

$$\Box_r \, \phi_{11}^{(-)} - 4 \left(X_1(X_1 - X_2 - X_3) + A_1^2 \right) \phi_{11}^{(-)} = 0. \tag{5.20}$$

Various special cases of this mode were considered nonlinearly in [118] for the one, two and three equal-charge background; for these cases we have numerically verified the critical temperatures quoted. The unimodularity and backreaction constraint $\operatorname{tr} \chi_{11} = 0$ can be imposed without trivialising this mode.

Neutral equations of motion

The equations of motion for the neutral scalar $\phi_{11}^{(+)}$ together with the gauge field fluctuation are

$$\Box_r \, \phi_{11}^{(+)} - 4X_1(X_1 - X_2 - X_3)\phi_{11}^{(+)} - \frac{F_1^2}{X_1^2}\phi_{11}^{(+)} + \frac{F_1 \cdot h}{X_1^2} = 0 \tag{5.21}$$

$$\frac{1}{\sqrt{-g}} \, \partial_r \left(\sqrt{-g} \, \frac{h^{rt} - 2F_1^{rt}\phi_{11}^{(+)}}{X_1^2} \right) = 0, \tag{5.22}$$

where we have defined $h = d\alpha_{11}^{(+)}$.

If the mode is to be considered alone as in (5.17), we must impose $\operatorname{tr} \chi_{11} = 0$ for which we have $\phi_{11}^{(+)} = 0$ by (5.18). In order to satisfy the backreaction and unimodularity constraints without trivialising these modes, we must therefore include other diagonal blocks, but this can only achieved if two or more of the background charges are equal. Such a sum of modes at two equal charges is closely related to the Gubser-Mitra instability [182, 183] — a connection that we explore further in section 5.4.

5.2.2 Off-diagonal fluctuations

Without loss of generality we focus on fluctuations living in the $(1,2)$ block (and $(2,1)$ by symmetry),

$$\chi = \begin{pmatrix} 0 & \chi_{12} & 0 \\ \chi_{12}^T & 0 & 0 \\ 0 & 0 & 0 \end{pmatrix}, \qquad \alpha = \begin{pmatrix} 0 & \sigma\hat{\alpha}_{12} & 0 \\ \hat{\alpha}_{12}^T\sigma & 0 & 0 \\ 0 & 0 & 0 \end{pmatrix}, \tag{5.23}$$

for which the condition $\operatorname{tr}\chi = 0$ and backreaction constraints are automatically satisfied.

As for the diagonal fluctuations, the equations of motion for these fluctuations may be partially diagonalised by moving to the new variables

$$\textbf{(+) mode:} \quad \phi_{12}^{(+)} = \sigma\chi_{12} + \chi_{12}\sigma, \qquad \alpha_{12}^{(+)} = \sigma\hat{\alpha}_{12} + \hat{\alpha}_{12}\sigma, \tag{5.24}$$

$$\textbf{(−) mode:} \quad \phi_{12}^{(-)} = \sigma\chi_{12} - \chi_{12}\sigma, \qquad \alpha_{12}^{(-)} = \sigma\hat{\alpha}_{12} - \hat{\alpha}_{12}\sigma, \tag{5.25}$$

where in contrast to the diagonal modes, here both the (+) mode and (−) mode are charged and couple to gauge field fluctuations in general. Dropping the indices and defining

$$A_\pm \equiv \frac{1}{2}(A_1 \mp A_2), \qquad F_\pm \equiv \frac{F_1}{X_1} \pm \frac{F_2}{X_2}, \qquad h_\pm \equiv d\alpha_\pm \tag{5.26}$$

we obtain the coupled equations of motion

$$\begin{aligned} &\Box_r\,\phi_\pm - \left(4A_\pm^2 - 2(X_1+X_2)X_3 + \frac{1}{4}F_\pm^2\right)\phi_\pm \\ &+\frac{X_1+X_2}{X_1X_2}\left((X_1-X_2)A_\pm\cdot\alpha_\pm + \frac{1}{4}F_\pm\cdot h_\pm\right) \;=\; 0, \end{aligned} \tag{5.27}$$

$$\begin{aligned} &\frac{1}{2\sqrt{-g}}\partial_r\left[\frac{\sqrt{-g}}{X_1X_2}\left(2h_\pm^{rt} - (X_1+X_2)F_\pm^{rt}\phi_\pm\right)\right] \\ &-\frac{(X_1-X_2)^2}{X_1X_2}g^{tt}\alpha_\pm + \frac{(X_1+X_2)(X_1-X_2)}{X_1X_2}A_\pm^t\phi_\pm \;=\; 0. \end{aligned} \tag{5.28}$$

When $q_1 = q_2$ we have that $\phi_{12}^{(-)}$ satisfies the same equation of motion as the charged mode $\phi_{11}^{(-)}$ (5.20), and $\phi_{12}^{(+)}$ satisfies the same equations of motion as the neutral mode $\phi_{11}^{(+)}$ (5.21) and (5.22).

5.2.3 Marginal modes

Collecting all the modes above we have

Type	Scalar field	See section
Charged diagonal	$\phi_{11}^{(-)}, \phi_{22}^{(-)}, \phi_{33}^{(-)}$	5.3
Off diagonal (−)	$\phi_{12}^{(-)}, \phi_{13}^{(-)}, \phi_{23}^{(-)}$	5.3
Neutral diagonal	$\phi_{11}^{(+)}, \phi_{22}^{(+)}, \phi_{33}^{(+)}$	5.4
Off diagonal (+)	$\phi_{12}^{(+)}, \phi_{13}^{(+)}, \phi_{23}^{(+)}$	5.4

Note that the equation of motion for the $I \neq J$ mode $\phi_{IJ}^{(\pm)}$ reduces to the equation of motion for the $\phi_{II}^{(\pm)}$ when the background charges on the legs coincide: $q_I = q_J$.

We seek time-independent solutions that are regular at the horizon and normalisable at the AdS boundary for each of the fluctuations detailed in the table above. Fluctuations of the gauge field at the boundary are required to vanish so that the chemical potentials are not perturbed. Such marginal modes indicate new branches of superconducting and normal black brane solutions. Developing series solutions we find the near-horizon behaviour (here the horizon position has been fixed to $r_+ = 1$)

$$\phi = a_1 + \ldots + \log(r-1)(a_2 + \ldots) \tag{5.29}$$

$$\alpha = a_3(r-1) + \ldots \tag{5.30}$$

where the parameters a_n are undetermined in the expansion and the ellipses denote determined higher order terms. For regularity we set $a_2 = 0$, and since the system of equations is linear we are free to scale $a_1 = 1$. Additionally, for the diagonal modes we have fixed a shift symmetry in α such that $\alpha(r_+) = 0$. The scalar fluctuations in the UV vacuum all have mass $m_\phi^2 = -4$, which saturates the BF bound. The boundary series takes the form

$$\phi = r^{-2}(b_1 + \ldots) + r^{-2}\log r\,(b_2 + \ldots) \tag{5.31}$$

$$\alpha = b_3 + \ldots + r^{-2}(b_4 + \ldots) \tag{5.32}$$

with data b_n. Normalisability demands that we set $b_2 = 0$ and we must also impose $b_3 = 0$ to preserve our choice of chemical potentials.

5.3 Sector $(-)$

In this section we consider fluctuations of the fields labelled by $(-)$. Before considering general ratios of the chemical potentials and general p_1, p_2 coordinates it is instructive to study a slice of the allowed region (fig. 5.2) at $\mu_1 = \mu_2$, for which $p_2 = 0$. We find marginal modes with critical temperatures illustrated in fig. 5.3.

On this slice we can consider the effect of an imbalance on the mode $\phi_{33}^{(-)}$, which is charged under A_3 and does not couple directly to any other gauge field. At $p_2 = 0$, p_1 becomes a function of the imbalance for this mode, $\zeta_{1,2} = \frac{\mu_{1,2}}{\mu_3}$. The imbalance $\zeta_{1,2} = 0$ at $p_1 = -\sqrt{2/3}$, $\zeta_{1,2} = 1$ at $p_1 = 0$ and $\zeta_{1,2} \to \infty$ as $p_1 \to \sqrt{1/3}$. As shown in fig. 5.3 the critical temperature as a function of this imbalance meets the temperature of thermodynamic instability at sufficiently high $\zeta_{1,2}$. Note however that before this value

of $\zeta_{1,2}$ is reached we see superconducting branches for the modes $\phi_{11}^{(-)}, \phi_{22}^{(-)}$ and $\phi_{12}^{(-)}$, which are charged under $A_{1,2}$.

Extending the analysis to the full allowed region of (p_1, p_2) space, we find the modes with the highest critical temperature as labelled in fig. 5.4.

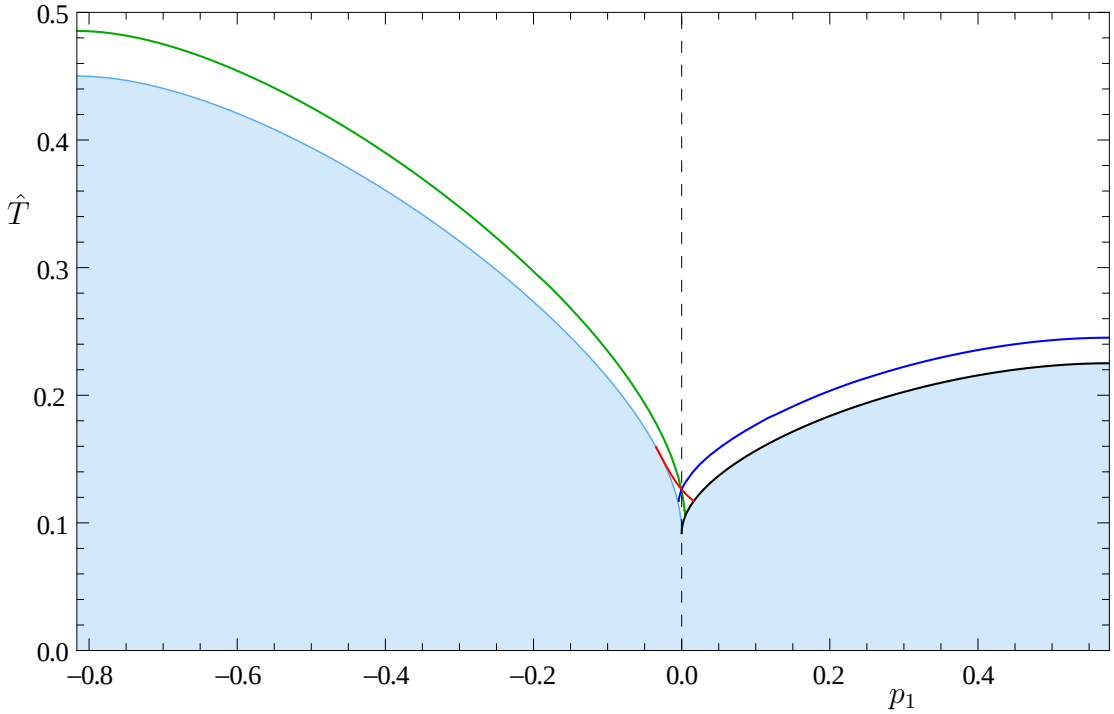

Fig. 5.3: A $\mu_1 = \mu_2$ slice ($\mu_3 \neq 0$) as a warm-up to the full (p_1, p_2) space of normal phase solutions. The light blue region is thermodynamically unstable. The lines indicate critical temperatures of *green:* $\phi_{33}^{(-)}$, *red:* $\phi_{13}^{(-)}, \phi_{23}^{(-)}$, *blue:* $\phi_{11}^{(-)}, \phi_{22}^{(-)}, \phi_{12}^{(-)}$. Finally we show the line of neutral scalar zero modes (see section 5.4) in *black:* $\phi_{11}^{(+)}, \phi_{22}^{(+)}, \phi_{12}^{(+)}$.

Charged diagonal modes

The critical temperatures for $\phi_{33}^{(-)}$ are plotted in fig. 5.5. It is important to emphasise that the region where $\phi_{33}^{(-)}$ is unstable is not restricted to the segment indicated in fig. 5.4 — there is a slight overlap of $\phi_{11}^{(-)}, \phi_{22}^{(-)}$ and $\phi_{33}^{(-)}$ near lines of equal chemical potential.

Off diagonal modes

We find that marginal modes exist in a window of allowed p_1 and p_2 values. This region and their critical temperatures are plotted in fig. 5.6. Note that the critical temperatures all lie below those found for the diagonal modes, except along the locus of equal chemical potentials on the two legs; for instance along $p_2 = 0$ the critical temperatures for $\phi_{12}^{(-)}$ and $\phi_{11}^{(-)}$ and $\phi_{22}^{(-)}$ coincide.

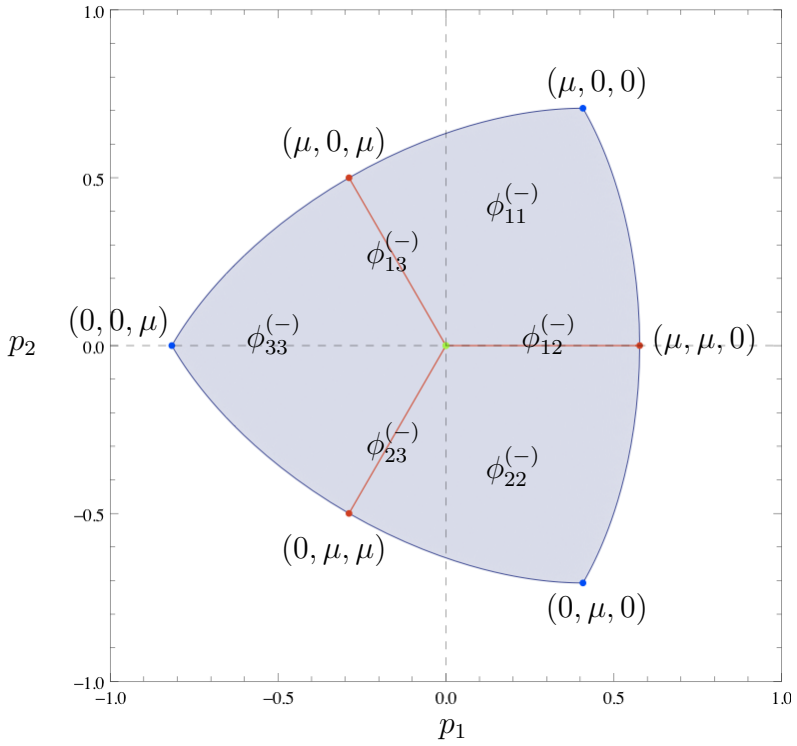

Fig. 5.4: Modes which give the highest critical temperature. The diagonal modes $\phi_{11}^{(-)}, \phi_{22}^{(-)}, \phi_{33}^{(-)}$ give the highest critical temperature in the blue regions as shown. In addition, along the red lines the modes $\phi_{12}^{(-)}, \phi_{13}^{(-)}, \phi_{23}^{(-)}$ linearly coincide with the diagonal modes and have the same critical temperature. Dots indicate special cases of the chemical potentials, (μ_1, μ_2, μ_3), with all equal at the origin.

5.4 Sector (+) and Gubser-Mitra instabilities

In this section we consider fluctuations of the fields labelled by (+). The three fields $\phi_{11}^{(+)}, \phi_{22}^{(+)}, \phi_{33}^{(+)}$ are neutral, while $\phi_{12}^{(+)}, \phi_{13}^{(+)}, \phi_{23}^{(+)}$ become neutral when two chemical potentials coincide. We find marginal modes along the loci

$$\left\{ \begin{array}{l} \mu_1 = \mu_2 > \mu_3 \\ \mu_1 = \mu_3 > \mu_2 \\ \mu_2 = \mu_3 > \mu_1 \end{array} \right\} \quad \text{for} \quad \left\{ \begin{array}{l} \phi_{11}^{(+)}, \phi_{22}^{(+)}, \phi_{12}^{(+)} \\ \phi_{11}^{(+)}, \phi_{33}^{(+)}, \phi_{13}^{(+)} \\ \phi_{22}^{(+)}, \phi_{33}^{(+)}, \phi_{23}^{(+)} \end{array} \right\} \tag{5.33}$$

where all fluctuations are neutral. The backreaction and unimodularity constraints for the diagonal modes can be satisfied by turning on two modes, *e.g.* $\phi_{22}^{(+)} = -\phi_{11}^{(+)}$.

It is perhaps surprising that unlike the (−) modes of section 5.3, these marginal modes exist only for one dimensional regions of the (p_1, p_2) plane. However, they do not indicate a true instability of the black brane background. Instead, as we shall demonstrate, they

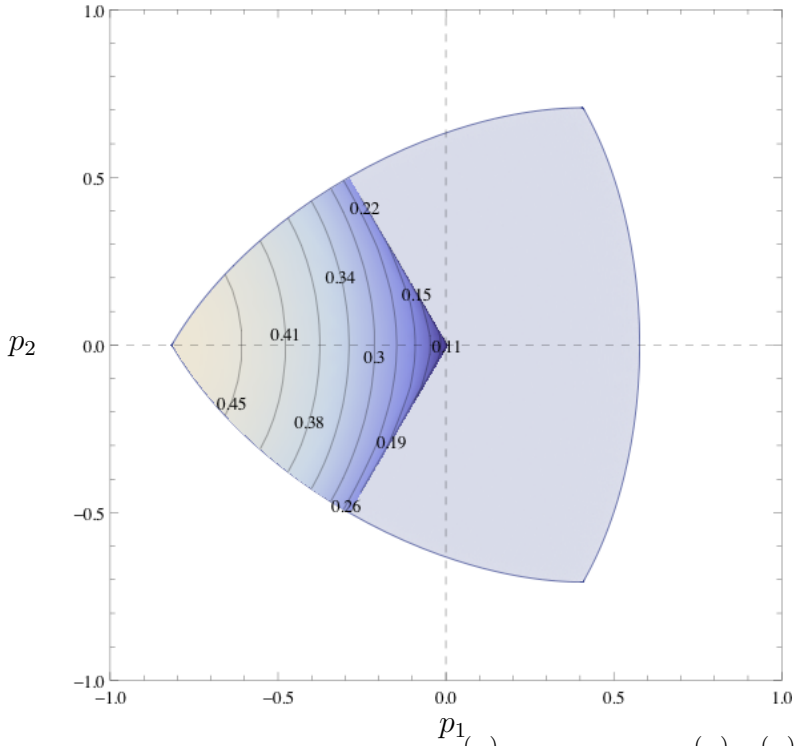

Fig. 5.5: Critical temperatures for the mode $\phi_{33}^{(-)}$. The modes $\phi_{11}^{(-)}, \phi_{22}^{(-)}$ can be obtained by permuting the labels and appear predominantly in the regions as labelled in fig. 5.4.

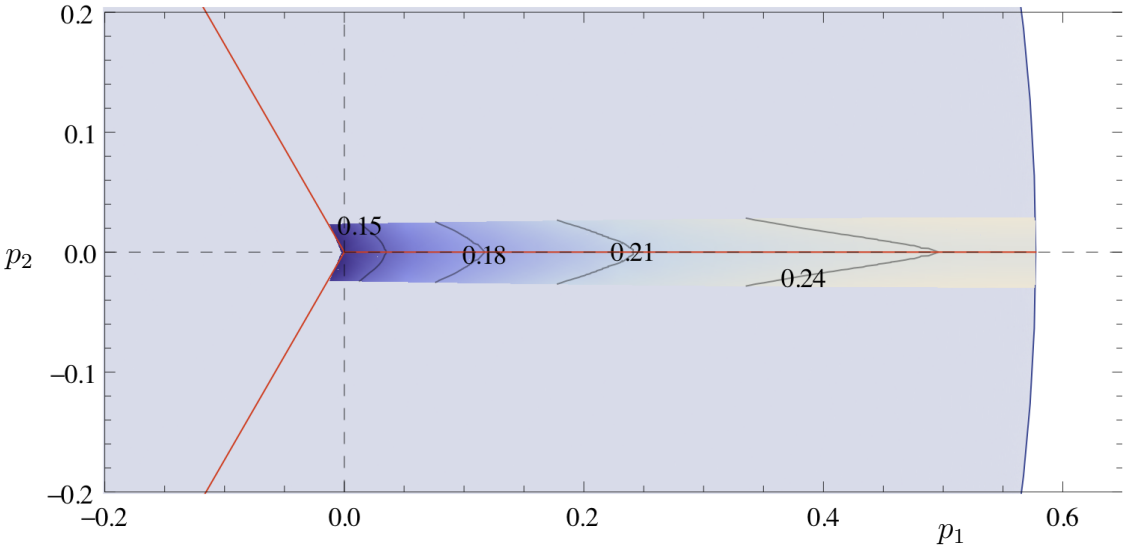

Fig. 5.6: Region where marginal modes for $\phi_{12}^{(-)}$ exist, with critical temperatures indicated by the contours. Regions for the other modes $\phi_{23}^{(-)}$ and $\phi_{13}^{(-)}$ can be found by permuting the indices. The blue shaded region is the region shown in fig. 5.2.

have a natural interpretation as zero modes that move in the family of background black branes. The existence of these zero modes is closely related to the threshold of

thermodynamic instability; indeed, the critical temperatures are given precisely by the lowest temperature at which the normal phase is locally thermodynamically stable.

We can analytically construct this class of marginal modes in the grand canonical ensemble by perturbing the charges and the horizon position whilst ensuring that the chemical potential and temperature remain fixed. A 4×4 matrix for this variation is

$$\mathcal{M} = \frac{\delta\{\mu_I, T\}}{\delta\{q_I, r_+\}} \tag{5.34}$$

and, if the fluctuations are to be marginal modes in the grand canonical ensemble, we require $\det \mathcal{M} = 0$, which is achieved for background values of q_I at the threshold of the thermodynamic instability given by $\det \mathcal{H} = 0$. We emphasise that this applies to modes that include gravitational fluctuations at any values of the chemical potentials and is easily derived in this way. For example, when $q_3 = \frac{2-q_1-q_2}{1-q_1 q_2} > 0$ we have a surface of zero modes generated by perturbations $H_I \to H_I + \delta H_I$, $f \to f + \delta f$ to (5.5), where

$$\delta H_i = \frac{q_i}{(q_i - 1)} \frac{1}{r^2}, \qquad i = 1, 2 \tag{5.35}$$

$$\delta H_3 = -\frac{q_1 + q_2 - 2}{(q_1 - 1)(q_2 - 1)} \frac{1}{r^2} \tag{5.36}$$

$$\delta f = 2 + \frac{q_1 q_2 (q_1 + q_2 - 2)}{(q_1 q_2 - 1)} \left(\frac{1}{r^2} - \frac{1}{r^4} \right). \tag{5.37}$$

Specialising to the non-gravitational modes of interest here, which exist only along loci of the chemical potentials, we obtain for example[3]

$$\frac{\delta X_1}{X_1} = -\frac{\delta X_2}{X_2} = \frac{1}{1 + r^2}, \qquad \delta X_3 = 0 \tag{5.38}$$

$$\delta A_1 = -\delta A_2 = \frac{\sqrt{(1 + q_3)}(r^2 - 1)}{(1 + r^2)^2}, \qquad \delta A_3 = 0 \tag{5.39}$$

at temperature $\hat{T} = \frac{1}{\pi\sqrt{2(1+4q_3+q_3^2)}}$. This zero mode corresponds to a redistribution of the black brane charges when two of them are equal. This mode satisfies equations (5.21) and (5.22) and consequently it is precisely this mode that gives rise to the black line in fig. 5.3. It is also the zero mode generated by the thermodynamically unstable directions discussed in section 5.1.1. We expect that there is also a true instability associated with these fluctuations [182, 183] but it is not captured by a zero mode analysis. We also

[3]The no-backreaction condition imposes that any two of the background charges are equal; let us here choose $q_1 = q_2$. Subsequent conditions on the fluctuations themselves become $\delta q_1 + \delta q_2 = 0$ and $\delta q_3 = 0$. Further imposing that the chemical potential is not perturbed we have $q_2 = 1$.

anticipate a true instability away from the lines of equal chemical potentials, provided gravitational fluctuations are included.

5.A Dominant branch

Using q_3 as a parameter along the branch of solutions and writing $s_i^2 = (1+q_3)^2 - 4q_3\zeta_i^2$ we find that q_1, q_2 are given by

$$q_1 = \frac{1+q_3-s_1}{1+q_3+s_1}, \qquad q_2 = \frac{1+q_3-s_2}{1+q_3+s_2}. \tag{5.40}$$

There are therefore up to four solutions coming from the sign choices for s_1 and s_2. In these coordinates the thermodynamic potential density becomes

$$\hat{\omega} = -\frac{(1+q_3)(1+q_3+s_1)(1+q_3+s_2)}{4q_3^2(1+\zeta_1^2+\zeta_2^2)^2} \tag{5.41}$$

and so we see that at some desired grand canonical coordinate, $(\zeta_1, \zeta_2, \hat{T})$, the dominant configurations live on the $s_1, s_2 > 0$ branch, provided it exists there. The temperature is stationary at the threshold for thermodynamic stability:

$$\left.\frac{\partial \hat{T}}{\partial q_3}\right|_{\zeta_1,\zeta_2} = -\frac{(1-q_3^2)(s_1+s_2)+2s_1s_2}{8\pi q_3 s_1 s_2\sqrt{q_3(1+\zeta_1^2+\zeta_2^2)}} \tag{5.42}$$

$$\det \mathcal{H} \propto 2\frac{(1-q_3^2)(s_1+s_2)+2s_1s_2}{(1+q_3+s_1)(1+q_3+s_2)} \tag{5.43}$$

and furthermore, on the $s_1, s_2 > 0$ branch the temperature is a minimum there: $\frac{\partial^2 \hat{T}}{\partial q_3^2} > 0$. This shows that there is a branch of black branes that only exists above the threshold temperature for thermodynamic stability, where it dominates the ensemble.

5.B Action for fluctuations

In this appendix we present the action to quadratic order for fluctuations of (5.1) of the form (5.14) that do not source metric fluctuations:

$$S_{(2)} = \frac{1}{16\pi G_5}\int d^5x\sqrt{-g}\,\mathrm{tr}\,(L_\chi + L_\alpha + L_{\mathrm{int}}) \tag{5.44}$$

with

$$L_\chi = -\frac{g^{rr}}{4}\chi'^2 - \frac{g_c^2 g^{tt}}{2}\left((A_0\chi)^2 - A_0^2\chi^2\right) + \frac{g^{rr}g^{tt}}{4}\left((T_0^{-1}A_0')^2\chi^2 + (T_0^{-1}A_0'\chi)^2\right) \\ - g_c^2\left(T_0^2 - \frac{1}{2}(\operatorname{tr} T_0)T_0\right)\chi^2 - g_c^2(T_0\chi)^2 \tag{5.45}$$

$$L_\alpha = -\frac{g_c^2 g^{tt}}{2}\left(\alpha^2 - T_0^{-1}\alpha T_0\alpha\right) + \frac{g^{rr}g^{tt}}{4}(T_0^{-1}\alpha')^2 \tag{5.46}$$

$$L_{\text{int}} = -\frac{g_c^2 g^{tt}}{2}T_0^{-1}\alpha T_0\left(A_0\chi - \chi A_0\right) - \frac{g^{rr}g^{tt}}{2}\left(\chi T_0^{-1}A_0' + T_0^{-1}A_0'\chi\right)T_0^{-1}\alpha'. \tag{5.47}$$

Chapter 6

Conclusion and outlook

The original work described in this thesis can be divided into two parts. In the first, we studied the real-time response of strongly-correlated states of quantum matter using holography. We started with a system at non-zero temperature and density, dual to a non-extremal RN-AdS$_4$ brane, and computed numerically the full retarded Green's functions for conserved currents in the shear channel [132] (chapter 2). Our results were consistent with those of [75], but we went beyond that treatment to show many interesting features. In particular, the linear response of the boundary theory was shown to exhibit rather peculiar behaviour beyond the hydrodynamic regime, which we would like to understand in more detail.

We moved on to study compressible states of the D3/D5 and D3/D7 theories that were not solids, superfluids, LFLs or NFLs [140] (chapter 3). In particular, we studied the effect of a non-zero magnetic field B on the collisionless/hydrodynamic crossover in these systems as we increased the temperature T, for values of B below any known phase transitions. We found that the crossover was simplest to understand by studying the spectrum of collective excitations of these systems with fixed frequency ω, where we could define the crossover for any value of B as the value of T where the dominant pole in $G^R_{tt}(\omega, k)$ becomes that of charge diffusion. Remarkably, this value of T is, to very good approximation, independent of B. In the high-frequency collisionless regime, for values of B above a value $B/T^2 \simeq O(1)$ estimated in (3.52) we also saw a suppression of spectral weight due to the magnetically-induced gap in the holographic zero sound dispersion relation. Our main results are summarised in fig. 3.21. We believe that, given our minimal ingredients, our results may be characteristic of compressible states described holographically by probe DBI actions with non-zero electric and magnetic flux, and hence may help in classifying them.

Various open questions remain about these, and other similar, holographic quantum liquids. Here we will list only a few such questions.

In the D3/D7 system we only studied excitations with momentum perpendicular to the magnetic field, but we have another option: the momentum can also have a non-zero component parallel to the magnetic field. How does the magnetic field affect the holographic zero sound mode that propagates *parallel* to the magnetic field? What happens to modes parallel to the magnetic field during the collisionless/hydrodynamic crossover?

We only considered values of B below any known phase transitions. What happens at higher values of B, in the symmetry-broken phases? Clearly the spectrum of excitations will then include the Goldstone bosons associated with the symmetry breaking. How do they affect the collisionless/hydrodynamic crossover?

More generally, an open question is whether these compressible states of the D3/Dp theories are the true ground states, *i.e. global* minima of the free energy. Indeed, as we mentioned in section 3.1, at one point in the phase diagram for the D3/D7 system in the grand canonical ensemble with non-zero B, these states are known to exhibit an instability towards an inhomogenous state. We hasten to add that even if the states we studied are not the true ground states, they are a useful theoretical laboratory that may reveal some guiding principle(s) to classify compressible states.

Another perspective on the collective excitations of these systems in the collisionless regime, which we have not explored here, is given by the semi-holographic approach [184, 64, 92, 93, 144]. This is an effective description in which some critical degrees of freedom, described by a (0+1)-dimensional CFT dual holographically to degrees of freedom in a near-horizon AdS_2, produce the dissipation of the holographic zero sound mode. Clearly in our D3/Dp systems the bulk geometry has no near-horizon AdS_2, unlike extremal RN-AdS. Nevertheless, quite generically the fluctuations of the Dp-brane worldvolume fields effectively 'see' AdS_2 deep in the bulk, due to the worldvolume electric flux [64, 92, 93, 144]. What aspects of the collisionless/hydrodynamic crossover, at either zero or non-zero B, can be understood using semi-holographic techniques?

The behavior of collective excitations with increasing T for the compressible state dual to RN-AdS_4 is qualitatively different from that of the D3/Dp systems. Although those states do exhibit a sound mode in the collisionless regime [76], as T increases no collision of poles in the complex ω plane occurs [61]. Does a non-zero magnetic field produce a gap in the sound dispersion relation in those states? If so, how does that affect the behavior of the collective modes as T increases?

In the second part we explored the space of solutions to gravity theories with a negative cosmological constant. First we studied the behaviour of charged scalar solitons in asymptotically global AdS_4 spacetimes [161] (chapter 4). The main objective was to obtain a better understanding of when such solutions admit a planar limit. In contrast to previous studies of compact objects in AdS geometries, we discovered new branches of solutions in bottom-up models that admit a planar limit even for 'small' amounts of matter repulsion. Furthermore, these were disconnected from the global AdS_4 vacuum. By examining scaling-invariant quantities we were also able to demonstrate explicitly that the planar limit of global solitons in these theories matched up with the zero-temperature limit of planar black holes with charged scalar hair. Whilst these results were obtained for a particular value of the scalar mass, we believe them to be generic for other masses and also to extend to higher dimensional AdS geometries. Evidence for this claim was found in [120].

An important result of our numerical studies was the unveiling of critical behaviour in the family of solitonic solutions. We found a very detailed pattern of branchings in the soliton solution space as a function of the scalar charge; solution branches underwent a series of deformations and even formed closed bubbles in solution space. Such rich structure signals a rather intricate interplay of the non-linearities in the system and it would be interesting to carry out a direct dynamical systems analysis to shed light on these features.

We also found many of these features in models that can be consistently embedded into eleven-dimensional supergravity, albeit with modifications due to the non-trivial matter interactions present in these examples. For such models, the ability to choose multiple boundary conditions for the scalar field provided us with a very useful dial to tune. In the context of holographic superconductors, [119] and [68] have already emphasised the role of this dial in providing access to new quantum critical behaviour. For the $SU(3)$ truncation we could show by using the double-trace deformations that the standard quantisation of the scalar field ($\Delta = 2$ boundary condition) was located at a critical point; specifically, it exhibited features seen for the special value of charge, $q = q_c$, in the Abelian-Higgs models. Similarly, this same method also allowed us to elicit critical behaviour (albeit of a slightly different kind) in the $U(1)^4$ truncation for the supersymmetric ($\Delta = 1$) boundary condition.

It should be emphasised that access to such dials allows one to explore the phase space of solutions more completely. For example, we would have struggled to find a new branch of non-supersymmetric solitons for $\Delta = 1$ operators in the M2-brane theory

without the ability to tweak the boundary conditions. More generally, solutions that are disconnected from the AdS_4 vacuum are most easily obtained if we can access deformations by tweaking Lagrangian parameters, boundary conditions, *etc.*, and then relaxing back to the undeformed theory.

There is by now a huge literature on asymptotically AdS solutions in both phenomenological models and consistent truncations of supergravity. We would like to propose that the method of constructing global solutions then 'blowing them up' into the planar limit is a useful diagnostic in general. In particular, it serves as an efficient technique to find new connections between various solutions, which should be explored further.

As an example of the utility of the global solutions, let us briefly mention an example on which we believe our results can shed some light. In a different sector of the $SU(3)$ truncation, studied in [116], the authors found charged planar domain walls for one choice of scalar boundary condition but not the other. Based on our results it seems likely that the two different choices should correspond to the planar limits of charged global soliton branches that have unbounded or bounded mass, respectively. It would indeed be interesting to verify this result, for while the specific truncation in question is more complicated than the single field truncations we have studied in this paper, it has the advantage that it allows interpolation between the AdS_4 vacuum of the M2-brane theory (which preserves $SO(8)$ R-symmetry) and a new supersymmetric vacuum preserving $SU(3) \times U(1)$. In particular, we should be able to again see emergence of new global domain wall solutions interpolating between the two vacua.

We have also discussed the location of solitons on the microcanonical phase diagram for various theories. For the supersymmetric quantisation of the M2-brane theory, it is clear that global solitons form the microcanonical phase boundary because they saturate the BPS bound. We have refrained however from making a similar conjecture for the Abelian-Higgs model because in certain cases one can find global hairy black holes that are lighter than a soliton at a given value of the charge. A more compete discussion of this issue appeared in [120]. Whilst we have not explicitly studied global hairy black holes in the $SU(3)$ truncation, it would be interesting to see whether the exponential scalar potentials encountered in consistent truncations necessitate the solitons being the minimal mass solution in a given charge sector.

The analysis of solutions in global AdS has the advantage of allowing one to explore finite size effects in a 'large N' field theory. While much of the recent literature of applications of AdS/CFT to condensed matter systems has been restricted to the Poincaré

patch, it would be useful to generalise these constructions to the global geometry where we have a covariant IR regulator in the spacetime. In particular, it would be interesting to undertake the study of low-temperature superfluid behaviour in a strongly-coupled theory on $\mathbb{R} \times S^2$. Similarly, it would be of interest to extend consideration of gravitationally interacting fermionic systems (*e.g.* [185]) to the global setting.

The solitonic solutions discussed here are coherent condensates of bosons carrying macroscopic charges in the dual field theory. One generically expects that a strongly-coupled system at finite volume should thermalise (in a microcanonical sense at fixed charges). Therefore it is rather curious that the nonlinear interactions of gravity allow for non-black hole solutions.[1] Evidence has emerged recently for the nonlinear instability of global AdS [187, 188]. One might expect that generic initial data for matter fields with asymptotically AdS boundary conditions would collapse into a black hole, as has been verified for neutral scalar fields in [187] and complex scalar fields in [189]. However, it can be argued [190] and demonstrated [191] that some non-black hole solutions asymptotic to global AdS are nonlinearly stable. It would be very interesting to delineate the class of fine-tuned initial data that does not thermalise in the strongly-coupled field theory dual.

We then went on to find new branches of superconducting black branes in $\mathcal{N} = 8$ $SO(6)$ gauged supergravity, coming from a truncation involving 20 scalar fields and 15 gauge fields [171] (chapter 5). It turns out that superconductivity persists to any values of the chemical potentials conjugate to the three R-charge densities of the background black brane. The critical temperatures at which these black brane solutions arise is always higher than the temperature at which the three-charge background becomes thermodynamically unstable.

It is known that in some special cases — such as two and three non-zero equal chemical potentials — one has 'retrograde condensation', *i.e.* the branch of superconducting black branes is thermodynamically subdominant and the condensate exists only above a critical temperature [118] (see also [192, 116] in four dimensions).[2] The other previously studied case of this system is that of one non-zero chemical potential, where the superconducting black brane is thermodynamically dominant [118]. Here, in all known cases of retrograde condensation, we find that there is an additional marginal mode with the same critical temperature (see figure 5.4). We suspect that a nonlinear investigation of this branch

[1] Note that our solitons are qualitatively different to the CFT states on $\mathbb{R} \times S^2$ that exhibit undamped collective oscillations (oscillons) of [186]; for one, our solutions are globally static.

[2] For systems exhibiting retrograde condensation, the expectation is that superconducting ground states do not exist in the planar theory, but can exist when the boundary has spherical topology [161].

would reveal it to be dominant, as in the '2+2 equal charged scalars' truncation in four dimensions studied in [116].

For a given mode we may interpret dialling the chemical potentials as introducing an imbalanced mixture, as initiated in [130, 131]. The critical temperature surface cannot be extended to arbitrarily low temperatures as the imbalance is dialled, due the presence of a thermodynamic instability in the normal phase at finite temperature. At a given set of chemical potentials, different modes in the consistent truncation experience a different effective imbalance. Interestingly, we find that before a superconducting instability vanishes as a function of its imbalance, another appears to take its place.

The difference of the chemical potentials sets a scale for the system. It would be interesting to see if this scale sets a value of spatial momentum in this truncation resulting in an inhomogeneous, FFLO-like phase [193, 194].[3] It would also be interesting to construct all of the superconducting branches found nonlinearly, away from the critical temperature. This would allow the direct comparison of the free energy with the normal phase, and consequently the identification of the true phase boundary for the spontaneous breaking of a $U(1)$ bulk symmetry.

For many of the linear modes studied in chapter 5, labelled by (+), we have found only neutral marginal modes, whose role is to move one infinitesimally within the family of background black branes. These modes occur precisely at the threshold temperature for thermodynamic instability. As such the marginal modes do not generate an actual instability of the black brane. We have shown that it is possible to populate the entire minimum temperature surface (as a function of chemical potentials) with zero modes of the background black brane, which can be found analytically and involve gravitational fluctuations in general. One expects to find a true instability associated with the thermodynamic instability in these cases.

Our work was motivated in part by the search for universal features in top-down holographic superconductivity. We wish to highlight a basic problem we have encountered when using consistent truncations: a subdominant solution in a given theory can appear as the dominant solution in a consistent truncation of that theory. This is exemplified by the normal phase solutions employed in this work.

In the case of three equal chemical potentials the normal phase solution is simply RN-AdS$_5$ at high temperatures. Whilst the RN-AdS$_5$ branch exists at low temperatures too, it is no longer the dominant contribution to the ensemble. This has important con-

[3] See [195] for examples of spatially modulated phases in a truncation of Type IIB supergravity on S^5.

sequences for the equal-q_I consistent truncation where RN-AdS$_5$ is the only normal phase solution remaining. Evidently in the equal-q_I truncation this appears as the dominant black brane branch at all temperatures, when in fact, at low temperatures in the full theory it is subdominant to a thermodynamically unstable black brane.

The work of chapters 4 and 5 can be viewed as part of a wider programme to explore the phase diagram of strongly-correlated condensed matter systems. Since finding the precise string theory embedding for the cuprates, for example, seems a little too much to hope for, instead one tries to extract general lessons by mapping out the space of solutions to gravity theories with the necessary ingredients. In the course of this study we have found some hints of generic connections in this solution space, but there are also many troubling features. Can we predict in advance whether a given truncation will have the qualitative behaviour we seek? Or, can we classify the coupling functions that appear in these theories? If modes outside a truncation give rise to preferred phases, then how are we to proceed?

It may be that the only way to find the highest critical temperature for an instability is to consider fluctuations of *all* the Kaluza-Klein modes in a given supergravity theory about a black hole solution. The search for the true ground state seems even more difficult, given the rich spectrum of instabilities that have been found in asymptotically AdS spacetimes. Rather than searching blindly, however, it may be that a new, more physical organising principle can be found that will guide us. One idea is to search for physically distinct ways of producing finite charge density in the bulk. For example, it is natural to associate horizon flux with 'fractionalised' phases of matter and explicit bulk sources with 'cohesive' phases [24]. Do different bulk mechanisms lead to distinct field theory features in general? Another approach is to classify all extremal charged black brane geometries with AdS asymptotics in the hope of finding the true ground state [196, 197].

One thing is clear: black holes can no longer be thought of as simple. As we grope towards a better understanding of strongly-coupled field theories, the more we learn about the rich structure of black holes in four and higher dimensions. Once again they provide the key to unlocking the toughest questions in theoretical physics.

Bibliography

[1] A. Ghez, S. Salim, N. Weinberg, J. Lu, T. Do, *et al.*, "Measuring Distance and Properties of the Milky Way's Central Supermassive Black Hole with Stellar Orbits," *Astrophys.J.* **689** (2008) 1044–1062, arXiv:0808.2870 [astro-ph].

[2] S. Gillessen, F. Eisenhauer, S. Trippe, T. Alexander, R. Genzel, *et al.*, "Monitoring stellar orbits around the Massive Black Hole in the Galactic Center," *Astrophys.J.* **692** (2009) 1075–1109, arXiv:0810.4674 [astro-ph].

[3] G. T. Horowitz and J. Polchinski, "Gauge/gravity duality," arXiv:gr-qc/0602037 [gr-qc].

[4] J. McGreevy, "Holographic duality with a view toward many-body physics," *Adv.High Energy Phys.* **2010** (2010) 723105, arXiv:0909.0518 [hep-th].

[5] J. M. Maldacena, "The Large N limit of superconformal field theories and supergravity," *Adv.Theor.Math.Phys.* **2** (1998) 231–252, arXiv:hep-th/9711200 [hep-th].

[6] O. Aharony, S. S. Gubser, J. M. Maldacena, H. Ooguri, and Y. Oz, "Large N field theories, string theory and gravity," *Phys.Rept.* **323** (2000) 183–386, arXiv:hep-th/9905111 [hep-th].

[7] J. L. Petersen, "Introduction to the Maldacena conjecture on AdS / CFT," *Int.J.Mod.Phys.* **A14** (1999) 3597–3672, arXiv:hep-th/9902131 [hep-th].

[8] E. D'Hoker and D. Z. Freedman, "Supersymmetric gauge theories and the AdS / CFT correspondence," arXiv:hep-th/0201253 [hep-th].

[9] J. Polchinski, "Introduction to Gauge/Gravity Duality," arXiv:1010.6134 [hep-th].

[10] S. Gubser, I. R. Klebanov, and A. M. Polyakov, "Gauge theory correlators from noncritical string theory," *Phys.Lett.* **B428** (1998) 105–114, arXiv:hep-th/9802109 [hep-th].

[11] E. Witten, "Anti-de Sitter space and holography," *Adv.Theor.Math.Phys.* **2** (1998) 253–291, arXiv:hep-th/9802150 [hep-th].

[12] L. Susskind and E. Witten, "The Holographic bound in anti-de Sitter space," arXiv:hep-th/9805114 [hep-th].

[13] A. W. Peet and J. Polchinski, "UV / IR relations in AdS dynamics," *Phys.Rev.* **D59** (1999) 065011, arXiv:hep-th/9809022 [hep-th].

[14] S. Grozdanov, "Wilsonian Renormalisation and the Exact Cut-Off Scale from Holographic Duality," *JHEP* **1206** (2012) 079, arXiv:1112.3356 [hep-th].

[15] K. Skenderis, "Lecture notes on holographic renormalization," *Class.Quant.Grav.* **19** (2002) 5849–5876, arXiv:hep-th/0209067 [hep-th].

[16] I. Papadimitriou and K. Skenderis, "AdS / CFT correspondence and geometry," arXiv:hep-th/0404176 [hep-th].

[17] N. Iqbal and H. Liu, "Real-time response in AdS/CFT with application to spinors," *Fortsch.Phys.* **57** (2009) 367–384, arXiv:0903.2596 [hep-th].

[18] P. Breitenlohner and D. Z. Freedman, "Stability in Gauged Extended Supergravity," *Annals Phys.* **144** (1982) 249.

[19] I. R. Klebanov and E. Witten, "AdS / CFT correspondence and symmetry breaking," *Nucl.Phys.* **B556** (1999) 89–114, arXiv:hep-th/9905104 [hep-th].

[20] G. Gibbons and S. Hawking, "Action Integrals and Partition Functions in Quantum Gravity," *Phys.Rev.* **D15** (1977) 2752–2756.

[21] S. A. Hartnoll, "Lectures on holographic methods for condensed matter physics," *Class. Quant. Grav.* **26** (2009) 224002, arXiv:0903.3246 [hep-th].

[22] C. P. Herzog, "Lectures on Holographic Superfluidity and Superconductivity," *J.Phys.A* **A42** (2009) 343001, arXiv:0904.1975 [hep-th].

[23] G. T. Horowitz, "Theory of Superconductivity," *Lect.Notes Phys.* **828** (2011) 313–347, arXiv:1002.1722 [hep-th].

[24] S. A. Hartnoll, "Horizons, holography and condensed matter," arXiv:1106.4324 [hep-th].

[25] N. Iqbal, H. Liu, and M. Mezei, "Lectures on holographic non-Fermi liquids and quantum phase transitions," arXiv:1110.3814 [hep-th].

[26] E. Witten, "Anti-de Sitter space, thermal phase transition, and confinement in gauge theories," *Adv.Theor.Math.Phys.* **2** (1998) 505–532, arXiv:hep-th/9803131 [hep-th].

[27] V. Balasubramanian and P. Kraus, "A Stress tensor for Anti-de Sitter gravity," *Commun.Math.Phys.* **208** (1999) 413–428, arXiv:hep-th/9902121 [hep-th].

[28] S. Sachdev, "The landscape of the Hubbard model," arXiv:1012.0299 [hep-th].

[29] A. Chamblin, R. Emparan, C. V. Johnson, and R. C. Myers, "Charged AdS black holes and catastrophic holography," *Phys.Rev.* **D60** (1999) 064018, arXiv:hep-th/9902170 [hep-th].

[30] S. S. Gubser, "Breaking an Abelian gauge symmetry near a black hole horizon," *Phys. Rev.* **D78** (2008) 065034, arXiv:0801.2977 [hep-th].

[31] S. A. Hartnoll, C. P. Herzog, and G. T. Horowitz, "Holographic Superconductors," *JHEP* **12** (2008) 015, arXiv:0810.1563 [hep-th].

[32] F. Denef and S. A. Hartnoll, "Landscape of superconducting membranes," *Phys.Rev.* **D79** (2009) 126008, arXiv:0901.1160 [hep-th].

[33] N. Iqbal, H. Liu, and M. Mezei, "Semi-local quantum liquids," *JHEP* **1204** (2012) 086, arXiv:1105.4621 [hep-th].

[34] A. Donos and J. P. Gauntlett, "Holographic striped phases," *JHEP* **1108** (2011) 140, arXiv:1106.2004 [hep-th].

[35] P. Basu, A. Mukherjee, and H.-H. Shieh, "Supercurrent: Vector Hair for an AdS Black Hole," *Phys.Rev.* **D79** (2009) 045010, arXiv:0809.4494 [hep-th].

[36] C. Herzog, P. Kovtun, and D. Son, "Holographic model of superfluidity," *Phys.Rev.* **D79** (2009) 066002, arXiv:0809.4870 [hep-th].

[37] I. Amado, M. Kaminski, and K. Landsteiner, "Hydrodynamics of Holographic Superconductors," *JHEP* **0905** (2009) 021, arXiv:0903.2209 [hep-th].

[38] J. Sonner and B. Withers, "A gravity derivation of the Tisza-Landau Model in AdS/CFT," *Phys.Rev.* **D82** (2010) 026001, arXiv:1004.2707 [hep-th].

[39] G. T. Horowitz, J. E. Santos, and D. Tong, "Optical Conductivity with Holographic Lattices," *JHEP* **1207** (2012) 168, arXiv:1204.0519 [hep-th].

[40] G. T. Horowitz, J. E. Santos, and D. Tong, "Further Evidence for Lattice-Induced Scaling," *JHEP* **1211** (2012) 102, arXiv:1209.1098 [hep-th].

[41] I. R. Klebanov and E. Witten, "Superconformal field theory on three-branes at a Calabi-Yau singularity," *Nucl.Phys.* **B536** (1998) 199–218, arXiv:hep-th/9807080 [hep-th].

[42] S. Benvenuti, S. Franco, A. Hanany, D. Martelli, and J. Sparks, "An Infinite family of superconformal quiver gauge theories with Sasaki-Einstein duals," *JHEP* **0506** (2005) 064, arXiv:hep-th/0411264 [hep-th].

[43] A. Butti, D. Forcella, and A. Zaffaroni, "The Dual superconformal theory for L**pqr manifolds," *JHEP* **0509** (2005) 018, arXiv:hep-th/0505220 [hep-th].

[44] O. Aharony, O. Bergman, D. L. Jafferis, and J. Maldacena, "N=6 superconformal Chern-Simons-matter theories, M2-branes and their gravity duals," *JHEP* **10** (2008) 091, arXiv:0806.1218 [hep-th].

[45] S. S. Gubser, C. P. Herzog, S. S. Pufu, and T. Tesileanu, "Superconductors from Superstrings," *Phys.Rev.Lett.* **103** (2009) 141601, arXiv:0907.3510 [hep-th].

[46] J. P. Gauntlett, J. Sonner, and T. Wiseman, "Holographic superconductivity in M-Theory," *Phys. Rev. Lett.* **103** (2009) 151601, arXiv:0907.3796 [hep-th].

[47] D. T. Son and A. O. Starinets, "Minkowski space correlators in AdS / CFT correspondence: Recipe and applications," *JHEP* **0209** (2002) 042, arXiv:hep-th/0205051 [hep-th].

[48] R. Kubo, "Statistical mechanical theory of irreversible processes. 1. General theory and simple applications in magnetic and conduction problems," *J.Phys.Soc.Jap.* **12** (1957) 570–586.

[49] M. Kaminski, K. Landsteiner, J. Mas, J. P. Shock, and J. Tarrio, "Holographic Operator Mixing and Quasinormal Modes on the Brane," *JHEP* **1002** (2010) 021, arXiv:0911.3610 [hep-th].

[50] C. Herzog and D. Son, "Schwinger-Keldysh propagators from AdS/CFT correspondence," *JHEP* **0303** (2003) 046, arXiv:hep-th/0212072 [hep-th].

[51] K. Skenderis and B. C. van Rees, "Real-time gauge/gravity duality," *Phys.Rev.Lett.* **101** (2008) 081601, arXiv:0805.0150 [hep-th].

[52] K. Skenderis and B. C. van Rees, "Real-time gauge/gravity duality: Prescription, Renormalization and Examples," *JHEP* **0905** (2009) 085, arXiv:0812.2909 [hep-th].

[53] E. Berti, V. Cardoso, and A. O. Starinets, "Quasinormal modes of black holes and black branes," *Class. Quant. Grav.* **26** (2009) 163001, arXiv:0905.2975 [gr-qc].

[54] G. T. Horowitz and V. E. Hubeny, "Quasinormal modes of AdS black holes and the approach to thermal equilibrium," *Phys. Rev.* **D62** (2000) 024027, arXiv:hep-th/9909056.

[55] D. Birmingham, I. Sachs, and S. N. Solodukhin, "Conformal field theory interpretation of black hole quasi- normal modes," *Phys. Rev. Lett.* **88** (2002) 151301, arXiv:hep-th/0112055.

[56] L. D. Landau, "Oscillations in a Fermi liquid," *Zh. Eksp. Teor. Fiz.* **32** (1957) 59. Soviet Phys. - JETP **5**, 101 (1959).

[57] A. A. Abrikosov and I. M. Khalatnikov, "The theory of a fermi liquid (the properties of ^{3}He at low temperatures)," *Rep. Prog. Phys.* **22** (1959) 329.

[58] D. Pines and P. Nozières, *The theory of quantum liquids*. W. A. Benjamin, New York, 1966.

[59] S. Sachdev and B. Keimer, "Quantum Criticality," *Phys.Today* **64N2** (2011) 29, arXiv:1102.4628 [cond-mat.str-el].

[60] F. Nogueira and J. B. Stang, "Density versus chemical potential in holographic field theories," *Phys.Rev.* **D86** (2012) 026001, arXiv:1111.2806 [hep-th].

[61] R. A. Davison and N. K. Kaplis, "Bosonic excitations of the AdS_4 Reissner-Nordstrom black hole," *JHEP* **1112** (2011) 037, arXiv:1111.0660 [hep-th].

[62] N. Evans, A. Gebauer, K.-Y. Kim, and M. Magou, "Holographic Description of the Phase Diagram of a Chiral Symmetry Breaking Gauge Theory," *JHEP* **1003** (2010) 132, arXiv:1002.1885 [hep-th].

[63] K. Jensen, A. Karch, and E. G. Thompson, "A Holographic Quantum Critical Point at Finite Magnetic Field and Finite Density," *JHEP* **1005** (2010) 015, arXiv:1002.2447 [hep-th].

[64] K. Jensen, A. Karch, D. T. Son, and E. G. Thompson, "Holographic Berezinskii-Kosterlitz-Thouless Transitions," *Phys.Rev.Lett.* **105** (2010) 041601, arXiv:1002.3159 [hep-th].

[65] N. Evans, A. Gebauer, K.-Y. Kim, and M. Magou, "Phase diagram of the D3/D5 system in a magnetic field and a BKT transition," *Phys.Lett.* **B698** (2011) 91–95, arXiv:1003.2694 [hep-th].

[66] K. Jensen, "More Holographic Berezinskii-Kosterlitz-Thouless Transitions," *Phys.Rev.* **D82** (2010) 046005, arXiv:1006.3066 [hep-th].

[67] N. Evans, K. Jensen, and K.-Y. Kim, "Non Mean-Field Quantum Critical Points from Holography," *Phys.Rev.* **D82** (2010) 105012, arXiv:1008.1889 [hep-th].

[68] N. Iqbal, H. Liu, and M. Mezei, "Quantum phase transitions in semi-local quantum liquids," arXiv:1108.0425 [hep-th].

[69] E. D'Hoker and P. Kraus, "Quantum Criticality via Magnetic Branes," arXiv:1208.1925 [hep-th].

[70] S. A. Hartnoll, J. Polchinski, E. Silverstein, and D. Tong, "Towards strange metallic holography," *JHEP* **1004** (2010) 120, arXiv:0912.1061 [hep-th].

[71] T. Faulkner, N. Iqbal, H. Liu, J. McGreevy, and D. Vegh, "Strange metal transport realized by gauge/gravity duality," *Science* **329** (2010) 1043–1047.

[72] A. Donos and S. A. Hartnoll, "Universal linear in temperature resistivity from black hole superradiance," *Phys.Rev.* **D86** (2012) 124046, arXiv:1208.4102 [hep-th].

[73] L. Huijse and S. Sachdev, "Fermi surfaces and gauge-gravity duality," *Phys.Rev.* **D84** (2011) 026001, arXiv:1104.5022 [hep-th].

[74] S. Sachdev, "What can gauge-gravity duality teach us about condensed matter physics?," *Ann.Rev.Condensed Matter Phys.* **3** (2012) 9–33, arXiv:1108.1197 [cond-mat.str-el].

[75] M. Edalati, J. I. Jottar, and R. G. Leigh, "Shear Modes, Criticality and Extremal Black Holes," *JHEP* **04** (2010) 075, arXiv:1001.0779 [hep-th].

[76] M. Edalati, J. I. Jottar, and R. G. Leigh, "Holography and the sound of criticality," *JHEP* **10** (2010) 058, arXiv:1005.4075 [hep-th].

[77] S. Bhattacharyya, V. E. Hubeny, S. Minwalla, and M. Rangamani, "Nonlinear Fluid Dynamics from Gravity," *JHEP* **02** (2008) 045, arXiv:0712.2456 [hep-th].

[78] G. Policastro, D. T. Son, and A. O. Starinets, "From AdS/CFT correspondence to hydrodynamics," *JHEP* **09** (2002) 043, arXiv:hep-th/0205052.

[79] G. Policastro, D. T. Son, and A. O. Starinets, "From AdS/CFT correspondence to hydrodynamics. II: Sound waves," *JHEP* **12** (2002) 054, arXiv:hep-th/0210220.

[80] P. K. Kovtun and A. O. Starinets, "Quasinormal modes and holography," *Phys. Rev.* **D72** (2005) 086009, arXiv:hep-th/0506184.

[81] V. E. Hubeny and M. Rangamani, "A Holographic view on physics out of equilibrium," *Adv.High Energy Phys.* **2010** (2010) 297916, arXiv:1006.3675 [hep-th].

[82] A. Karch and L. Randall, "Open and closed string interpretation of SUSY CFT's on branes with boundaries," *JHEP* **0106** (2001) 063, arXiv:hep-th/0105132 [hep-th].

[83] O. DeWolfe, D. Z. Freedman, and H. Ooguri, "Holography and defect conformal field theories," *Phys.Rev.* **D66** (2002) 025009, arXiv:hep-th/0111135 [hep-th].

[84] J. Erdmenger, Z. Guralnik, and I. Kirsch, "Four-dimensional superconformal theories with interacting boundaries or defects," *Phys.Rev.* **D66** (2002) 025020, arXiv:hep-th/0203020 [hep-th].

[85] A. Karch and E. Katz, "Adding flavor to AdS / CFT," *JHEP* **0206** (2002) 043, arXiv:hep-th/0205236 [hep-th].

[86] S. Kobayashi, D. Mateos, S. Matsuura, R. C. Myers, and R. M. Thomson, "Holographic phase transitions at finite baryon density," *JHEP* **0702** (2007) 016, arXiv:hep-th/0611099 [hep-th].

[87] V. G. Filev, C. V. Johnson, R. Rashkov, and K. Viswanathan, "Flavoured large N gauge theory in an external magnetic field," *JHEP* **0710** (2007) 019, arXiv:hep-th/0701001 [hep-th].

[88] A. Karch and A. O'Bannon, "Holographic thermodynamics at finite baryon density: Some exact results," *JHEP* **0711** (2007) 074, arXiv:0709.0570 [hep-th].

[89] A. Karch, D. Son, and A. Starinets, "Zero Sound from Holography," arXiv:0806.3796 [hep-th].

[90] M. Kulaxizi and A. Parnachev, "Comments on Fermi Liquid from Holography," *Phys.Rev.* **D78** (2008) 086004, arXiv:0808.3953 [hep-th].

[91] A. Karch, M. Kulaxizi, and A. Parnachev, "Notes on Properties of Holographic Matter," *JHEP* **0911** (2009) 017, arXiv:0908.3493 [hep-th].

[92] D. Nickel and D. T. Son, "Deconstructing holographic liquids," *New J.Phys.* **13** (2011) 075010, arXiv:1009.3094 [hep-th].

[93] M. Ammon, J. Erdmenger, S. Lin, S. Müller, A. O'Bannon, and J. Shock, "On Stability and Transport of Cold Holographic Matter," *JHEP* **1109** (2011) 030, arXiv:1108.1798 [hep-th].

[94] R. A. Davison and A. O. Starinets, "Holographic zero sound at finite temperature," *Phys.Rev.* **D85** (2012) 026004, arXiv:1109.6343 [hep-th].

[95] M. Ammon, M. Kaminski, and A. Karch, "Hyperscaling-Violation on Probe D-Branes," *JHEP* **1211** (2012) 028, arXiv:1207.1726 [hep-th].

[96] H.-C. Chang and A. Karch, "Novel Solutions of Finite-Density D3/D5 Probe Brane System and Their Implications for Stability," *JHEP* **1210** (2012) 069, arXiv:1207.7078 [hep-th].

[97] M. Ammon, K. Jensen, K.-Y. Kim, J. N. Laia, and A. O'Bannon, "Moduli Spaces of Cold Holographic Matter," *JHEP* **1211** (2012) 055, arXiv:1208.3197 [hep-th].

[98] T. Hertog and G. T. Horowitz, "Towards a big crunch dual," *JHEP* **0407** (2004) 073, arXiv:hep-th/0406134 [hep-th].

[99] M. Berkooz, A. Sever, and A. Shomer, "'Double trace' deformations, boundary conditions and space-time singularities," *JHEP* **0205** (2002) 034, arXiv:hep-th/0112264 [hep-th].

[100] E. Witten, "Multitrace operators, boundary conditions, and AdS / CFT correspondence," arXiv:hep-th/0112258 [hep-th].

[101] T. Hertog and G. T. Horowitz, "Designer gravity and field theory effective potentials," *Phys.Rev.Lett.* **94** (2005) 221301, arXiv:hep-th/0412169 [hep-th].

[102] A. J. Amsel and D. Marolf, "Energy Bounds in Designer Gravity," *Phys.Rev.* **D74** (2006) 064006, arXiv:hep-th/0605101 [hep-th].

[103] T. Faulkner, G. T. Horowitz, and M. M. Roberts, "New stability results for Einstein scalar gravity," *Class.Quant.Grav.* **27** (2010) 205007, arXiv:1006.2387 [hep-th].

[104] Z. W. Chong, H. Lu, and C. N. Pope, "BPS geometries and AdS bubbles," *Phys. Lett.* **B614** (2005) 96–103, arXiv:hep-th/0412221.

[105] P. Basu, J. Bhattacharya, S. Bhattacharyya, R. Loganayagam, S. Minwalla, *et al.*, "Small Hairy Black Holes in Global AdS Spacetime," *JHEP* **1010** (2010) 045, arXiv:1003.3232 [hep-th].

[106] S. Bhattacharyya, S. Minwalla, and K. Papadodimas, "Small Hairy Black Holes in $AdS_5 x S^5$," *JHEP* **1111** (2011) 035, arXiv:1005.1287 [hep-th].

[107] N. Bobev, A. Kundu, K. Pilch, and N. P. Warner, "Supersymmetric Charged Clouds in AdS_5," *JHEP* **1103** (2011) 070, arXiv:1005.3552 [hep-th].

[108] D. N. Page and K. Phillips, "Selfgravitating radiation in Anti-de Sitter space," *Gen.Rel.Grav.* **17** (1985) 1029–1042.

[109] V. E. Hubeny, H. Liu, and M. Rangamani, "Bulk-cone singularities & signatures of horizon formation in AdS/CFT," *JHEP* **0701** (2007) 009, arXiv:hep-th/0610041 [hep-th].

[110] J. de Boer, K. Papadodimas, and E. Verlinde, "Holographic Neutron Stars," *JHEP* **1010** (2010) 020, arXiv:0907.2695 [hep-th].

[111] X. Arsiwalla, J. de Boer, K. Papadodimas, and E. Verlinde, "Degenerate Stars and Gravitational Collapse in AdS/CFT," *JHEP* **1101** (2011) 144, arXiv:1010.5784 [hep-th].

[112] J. Hammersley, "A Critical dimension for the stability of radiating perfect fluid stars," arXiv:0707.0961 [hep-th].

[113] V. Vaganov, "Self-gravitating radiation in AdS(d)," arXiv:0707.0864 [gr-qc].

[114] S. S. Gubser and A. Nellore, "Ground states of holographic superconductors," *Phys.Rev.* **D80** (2009) 105007, arXiv:0908.1972 [hep-th].

[115] G. T. Horowitz and M. M. Roberts, "Zero Temperature Limit of Holographic Superconductors," *JHEP* **0911** (2009) 015, arXiv:0908.3677 [hep-th].

[116] A. Donos and J. P. Gauntlett, "Superfluid black branes in $AdS_4 \times S^7$," *JHEP* **1106** (2011) 053, arXiv:1104.4478 [hep-th].

[117] S. S. Gubser, C. P. Herzog, S. S. Pufu, F. Rocha, and T. Tesileanu, "unpublished,".

[118] F. Aprile, D. Roest, and J. G. Russo, "Holographic Superconductors from Gauged Supergravity," *JHEP* **1106** (2011) 040, arXiv:1104.4473 [hep-th].

[119] T. Faulkner, G. T. Horowitz, and M. M. Roberts, "Holographic quantum criticality from multi-trace deformations," *JHEP* **1104** (2011) 051, arXiv:1008.1581 [hep-th].

[120] O. J. Dias, P. Figueras, S. Minwalla, P. Mitra, R. Monteiro, and J. E. Santos, "Hairy black holes and solitons in global AdS_5," *JHEP* **1208** (2012) 117, arXiv:1112.4447 [hep-th].

[121] P. Kovtun, D. T. Son, and A. O. Starinets, "Holography and hydrodynamics: Diffusion on stretched horizons," *JHEP* **0310** (2003) 064, arXiv:hep-th/0309213 [hep-th].

[122] A. Buchel and J. T. Liu, "Universality of the shear viscosity in supergravity," *Phys.Rev.Lett.* **93** (2004) 090602, arXiv:hep-th/0311175 [hep-th].

[123] G. Dall'Agata and G. Inverso, "On the Vacua of N = 8 Gauged Supergravity in 4 Dimensions," *Nucl.Phys.* **B859** (2012) 70–95, arXiv:1112.3345 [hep-th].

[124] G. T. Horowitz and J. E. Santos, "General Relativity and the Cuprates," arXiv:1302.6586 [hep-th].

[125] K. Behrndt, M. Cvetic, and W. Sabra, "Nonextreme black holes of five-dimensional N=2 AdS supergravity," *Nucl.Phys.* **B553** (1999) 317–332, arXiv:hep-th/9810227 [hep-th].

[126] D. Yamada and L. G. Yaffe, "Phase diagram of N=4 super-Yang-Mills theory with R-symmetry chemical potentials," *JHEP* **0609** (2006) 027, arXiv:hep-th/0602074 [hep-th].

[127] D. Yamada, "Fragmentation of Spinning Branes," *Class.Quant.Grav.* **25** (2008) 145006, arXiv:0802.3508 [hep-th].

[128] T. J. Hollowood, S. P. Kumar, A. Naqvi, and P. Wild, "N=4 SYM on S**3 with Near Critical Chemical Potentials," *JHEP* **0808** (2008) 046, arXiv:0803.2822 [hep-th].

[129] Y.-i. Shin, C. H. Schunck, A. Schirotzek, and W. Ketterle, "Phase diagram of a two-component Fermi gas with resonant interactions," *Nature* **451** no. 7179, (Feb., 2008) 689–693. http://dx.doi.org/10.1038/nature06473.

[130] J. Erdmenger, V. Grass, P. Kerner, and T. H. Ngo, "Holographic Superfluidity in Imbalanced Mixtures," *JHEP* **1108** (2011) 037, arXiv:1103.4145 [hep-th].

[131] F. Bigazzi, A. L. Cotrone, D. Musso, N. P. Fokeeva, and D. Seminara, "Unbalanced Holographic Superconductors and Spintronics," *JHEP* **1202** (2012) 078, arXiv:1111.6601 [hep-th].

[132] D. K. Brattan and S. A. Gentle, "Shear channel correlators from hot charged black holes," *JHEP* **1104** (2011) 082, arXiv:1012.1280 [hep-th].

[133] H. Kodama and A. Ishibashi, "Master equations for perturbations of generalized static black holes with charge in higher dimensions," *Prog. Theor. Phys.* **111** (2004) 29–73, arXiv:hep-th/0308128.

[134] E. W. Leaver, "Quasinormal modes of Reissner-Nordstrom black holes," *Phys. Rev.* **D41** (1990) 2986–2997.

[135] F. Denef, S. A. Hartnoll, and S. Sachdev, "Quantum oscillations and black hole ringing," *Phys. Rev.* **D80** (2009) 126016, arXiv:0908.1788 [hep-th].

[136] A. S. Miranda, J. Morgan, and V. T. Zanchin, "Quasinormal modes of plane-symmetric black holes according to the AdS/CFT correspondence," *JHEP* **0811** (2008) 030, arXiv:0809.0297 [hep-th].

[137] W. Witczak-Krempa and S. Sachdev, "Dispersing quasinormal modes in 2+1 dimensional conformal field theories," arXiv:1302.0847 [cond-mat.str-el].

[138] M. Kaminski, K. Landsteiner, F. Pena-Benitez, J. Erdmenger, C. Greubel, and P. Kerner, "Quasinormal modes of massive charged flavor branes," *JHEP* **1003** (2010) 117, arXiv:0911.3544 [hep-th].

[139] X.-H. Ge, K. Jo, and S.-J. Sin, "Hydrodynamics of RN AdS_4 black hole and Holographic Optics," arXiv:1012.2515 [hep-th].

[140] D. K. Brattan, R. A. Davison, S. A. Gentle, and A. O'Bannon, "Collective Excitations of Holographic Quantum Liquids in a Magnetic Field," *JHEP* **1211** (2012) 084, arXiv:1209.0009 [hep-th].

[141] J. Polchinski, *String theory. Vol. 1: An introduction to the bosonic string*. Cambridge University Press, 1998.

[142] A. Karch and A. O'Bannon, "Metallic AdS/CFT," *JHEP* **0709** (2007) 024, arXiv:0705.3870 [hep-th].

[143] P. Benincasa, "Universality of Holographic Phase Transitions and Holographic Quantum Liquids," arXiv:0911.0075 [hep-th].

[144] M. Goykhman, A. Parnachev, and J. Zaanen, "Fluctuations in finite density holographic quantum liquids," *JHEP* **1210** (2012) 045, arXiv:1204.6232 [hep-th].

[145] D. E. Kharzeev and H.-U. Yee, "Chiral helix in AdS/CFT with flavor," *Phys.Rev.* **D84** (2011) 125011, arXiv:1109.0533 [hep-th].

[146] R. C. Myers and M. C. Wapler, "Transport Properties of Holographic Defects," *JHEP* **0812** (2008) 115, arXiv:0811.0480 [hep-th].

[147] M. C. Wapler, "Holographic Experiments on Defects," *Int.J.Mod.Phys.* **A25** (2010) 4397–4473, arXiv:0909.1698 [hep-th].

[148] S. S. Pal, "Approximate strange metallic behavior in AdS," arXiv:1202.3555 [hep-th].

[149] A. Gorsky and A. Zayakin, "Anomalous Zero Sound," *JHEP* **1302** (2013) 124, arXiv:1206.4725 [hep-th].

[150] W. Kohn, "Cyclotron Resonance and de Haas-van Alphen Oscillations of an Interacting Electron Gas," *Phys.Rev.* **123** (1961) 1242–1244.

[151] S. A. Hartnoll, P. K. Kovtun, M. Muller, and S. Sachdev, "Theory of the Nernst effect near quantum phase transitions in condensed matter, and in dyonic black holes," *Phys.Rev.* **B76** (2007) 144502, arXiv:0706.3215 [cond-mat.str-el].

[152] S. A. Hartnoll and C. P. Herzog, "Ohm's Law at strong coupling: S duality and the cyclotron resonance," *Phys.Rev.* **D76** (2007) 106012, arXiv:0706.3228 [hep-th].

[153] E. I. Buchbinder, S. E. Vazquez, and A. Buchel, "Sound Waves in (2+1) Dimensional Holographic Magnetic Fluids," *JHEP* **0812** (2008) 090, arXiv:0810.4094 [hep-th].

[154] J. Hansen and P. Kraus, "Nonlinear Magnetohydrodynamics from Gravity," *JHEP* **0904** (2009) 048, arXiv:0811.3468 [hep-th].

[155] E. I. Buchbinder and A. Buchel, "The Fate of the Sound and Diffusion in Holographic Magnetic Field," *Phys.Rev.* **D79** (2009) 046006, arXiv:0811.4325 [hep-th].

[156] E. I. Buchbinder and A. Buchel, "Relativistic Conformal Magneto-Hydrodynamics from Holography," *Phys.Lett.* **B678** (2009) 135–138, arXiv:0902.3170 [hep-th].

[157] J. Hansen and P. Kraus, "S-duality in AdS/CFT magnetohydrodynamics," *JHEP* **0910** (2009) 047, arXiv:0907.2739 [hep-th].

[158] K.-Y. Kim and I. Zahed, "Baryonic Response of Dense Holographic QCD," *JHEP* **0812** (2008) 075, arXiv:0811.0184 [hep-th].

[159] J. Mas, J. P. Shock, and J. Tarrio, "A Note on conductivity and charge diffusion in holographic flavour systems," *JHEP* **0901** (2009) 025, arXiv:0811.1750 [hep-th].

[160] N. Jokela, G. Lifschytz, and M. Lippert, "Magnetic effects in a holographic Fermi-like liquid," *JHEP* **1205** (2012) 105, arXiv:1204.3914 [hep-th].

[161] S. A. Gentle, M. Rangamani, and B. Withers, "A Soliton Menagerie in AdS," *JHEP* **1205** (2012) 106, arXiv:1112.3979 [hep-th].

[162] N. Bobev, N. Halmagyi, K. Pilch, and N. P. Warner, "Supergravity Instabilities of Non-Supersymmetric Quantum Critical Points," *Class.Quant.Grav.* **27** (2010) 235013, arXiv:1006.2546 [hep-th].

[163] N. Bobev, A. Kundu, K. Pilch, and N. P. Warner, "Minimal Holographic Superconductors from Maximal Supergravity," *JHEP* **1203** (2012) 064, arXiv:1110.3454 [hep-th].

[164] R. D. Sorkin, R. M. Wald, and Z. J. Zhang, "Entropy of selfgravitating radiation," *Gen. Rel. Grav.* **13** (1981) 1127–1146.

[165] J. M. Heinzle, N. Rohr, and C. Uggla, "Spherically symmetric relativistic stellar structures," *Class.Quant.Grav.* **20** (2003) 4567–4586, arXiv:gr-qc/0304012 [gr-qc].

[166] A. J. Amsel, T. Hertog, S. Hollands, and D. Marolf, "A Tale of two superpotentials: Stability and instability in designer gravity," *Phys.Rev.* **D75** (2007) 084008, arXiv:hep-th/0701038 [hep-th].

[167] C. Pope and N. Warner, "An SU(4) invariant compactification of d = 11 supergravity on a stretched seven sphere," *Phys.Lett.* **B150** (1985) 352.

[168] H. Elvang, D. Z. Freedman, and H. Liu, "From fake supergravity to superstars," *JHEP* **0712** (2007) 023, arXiv:hep-th/0703201 [hep-th].

[169] L. Romans, "Supersymmetric, cold and lukewarm black holes in cosmological Einstein-Maxwell theory," *Nucl.Phys.* **B383** (1992) 395–415, arXiv:hep-th/9203018 [hep-th].

[170] S. Bolognesi and D. Tong, "Magnetic Catalysis in AdS4," *Class.Quant.Grav.* **29** (2012) 194003, arXiv:1110.5902 [hep-th].

[171] S. A. Gentle and B. Withers, "Superconducting instabilities of R-charged black branes," *JHEP* **1210** (2012) 006, arXiv:1207.3086 [hep-th].

[172] M. Pernici, K. Pilch, and P. van Nieuwenhuizen, "Gauged N=8 D=5 Supergravity," *Nucl.Phys.* **B259** (1985) 460.

[173] M. Gunaydin, L. Romans, and N. Warner, "Gauged N=8 Supergravity in Five-Dimensions," *Phys.Lett.* **B154** (1985) 268.

[174] M. Gunaydin, L. Romans, and N. Warner, "Compact and Noncompact Gauged Supergravity Theories in Five-Dimensions," *Nucl.Phys.* **B272** (1986) 598.

[175] M. Cvetic, H. Lu, C. N. Pope, A. Sadrzadeh, and T. A. Tran, "Consistent SO(6) reduction of type IIB supergravity on S(5)," *Nucl. Phys.* **B586** (2000) 275–286, arXiv:hep-th/0003103.

[176] D. T. Son and A. O. Starinets, "Hydrodynamics of R-charged black holes," *JHEP* **03** (2006) 052, arXiv:hep-th/0601157.

[177] M. Cvetic and S. S. Gubser, "Phases of R charged black holes, spinning branes and strongly coupled gauge theories," *JHEP* **9904** (1999) 024, arXiv:hep-th/9902195 [hep-th].

[178] S. S. Gubser, "Thermodynamics of spinning D3-branes," *Nucl.Phys.* **B551** (1999) 667–684, arXiv:hep-th/9810225 [hep-th].

[179] R.-G. Cai and K.-S. Soh, "Critical behavior in the rotating D-branes," *Mod.Phys.Lett.* **A14** (1999) 1895–1908, arXiv:hep-th/9812121 [hep-th].

[180] M. Cvetic and S. S. Gubser, "Thermodynamic stability and phases of general spinning branes," *JHEP* **9907** (1999) 010, arXiv:hep-th/9903132 [hep-th].

[181] T. Harmark and N. A. Obers, "Thermodynamics of spinning branes and their dual field theories," *JHEP* **01** (2000) 008, arXiv:hep-th/9910036.

[182] S. S. Gubser and I. Mitra, "Instability of charged black holes in Anti-de Sitter space," arXiv:hep-th/0009126 [hep-th].

[183] S. S. Gubser and I. Mitra, "The Evolution of unstable black holes in anti-de Sitter space," *JHEP* **0108** (2001) 018, arXiv:hep-th/0011127 [hep-th].

[184] T. Faulkner and J. Polchinski, "Semi-Holographic Fermi Liquids," *JHEP* **1106** (2011) 012, arXiv:1001.5049 [hep-th].

[185] S. A. Hartnoll and A. Tavanfar, "Electron stars for holographic metallic criticality," *Phys.Rev.* **D83** (2011) 046003, arXiv:1008.2828 [hep-th].

[186] B. Freivogel, J. McGreevy, and S. J. Suh, "Exactly Stable Collective Oscillations in Conformal Field Theory," *Phys.Rev.* **D85** (2012) 105002, arXiv:1109.6013 [hep-th].

[187] P. Bizon and A. Rostworowski, "On weakly turbulent instability of anti-de Sitter space," *Phys.Rev.Lett.* **107** (2011) 031102, arXiv:1104.3702 [gr-qc].

[188] O. J. Dias, G. T. Horowitz, and J. E. Santos, "Gravitational Turbulent Instability of Anti-de Sitter Space," *Class.Quant.Grav.* **29** (2012) 194002, arXiv:1109.1825 [hep-th].

[189] A. Buchel, L. Lehner, and S. L. Liebling, "Scalar Collapse in AdS," *Phys.Rev.* **D86** (2012) 123011, arXiv:1210.0890 [gr-qc].

[190] O. J. Dias, G. T. Horowitz, D. Marolf, and J. E. Santos, "On the Nonlinear Stability of Asymptotically Anti-de Sitter Solutions," *Class.Quant.Grav.* **29** (2012) 235019, arXiv:1208.5772 [gr-qc].

[191] L. Lehner. Private communication (2013).

[192] A. Buchel and C. Pagnutti, "Exotic Hairy Black Holes," *Nucl.Phys.* **B824** (2010) 85–94, arXiv:0904.1716 [hep-th].

[193] A. Larkin and Y. Ovchinnikov, "Nonuniform state of superconductors," *Zh.Eksp.Teor.Fiz.* **47** (1964) 1136–1146.

[194] P. Fulde and R. A. Ferrell, "Superconductivity in a Strong Spin-Exchange Field," *Phys.Rev.* **135** (1964) A550–A563.

[195] A. Donos and J. P. Gauntlett, "Holographic helical superconductors," *JHEP* **1112** (2011) 091, arXiv:1109.3866 [hep-th].

[196] N. Iizuka, S. Kachru, N. Kundu, P. Narayan, N. Sircar, *et al.*, "Bianchi Attractors: A Classification of Extremal Black Brane Geometries," *JHEP* **1207** (2012) 193, arXiv:1201.4861 [hep-th].

[197] N. Iizuka, S. Kachru, N. Kundu, P. Narayan, N. Sircar, *et al.*, "Extremal Horizons with Reduced Symmetry: Hyperscaling Violation, Stripes, and a Classification for the Homogeneous Case," arXiv:1212.1948 [hep-th].